Analysis of Mantle Heterogeneity through Array Observations of Multipathing and its Expansion to a Global Scale

James Ashley Ward

Submitted in accordance with the requirements for the degree of
Doctor of Philosophy

The University of Leeds
School of Earth and Environment

September 2021

The candidate confirms that the work submitted is his own, except where work which has formed part of jointly authored publications has been included. The contribution of the candidate and the other authors to this work has been explicitly indicated below. The candidate confirms that appropriate credit has been given within the thesis where reference has been made to the work of others.

The work in Chapter 2 appears in the following publication:

Ward, J., Nowacki, A., & Rost, S. (2020). Lateral Velocity Gradients in the African Lower Mantle Inferred From Slowness Space Observations of Multipathing. *Geochemistry, Geophysics, Geosystems*, *21*(8), e2020GC009025
e2020GC009025 10.1029/2020GC009025

JW developed the methodology, particularly to correct for a curved wavefront, wrote the codes, acquired the data, performed the data analysis, made the figures and wrote the first draft of the manuscript which was then edited from suggestions by co-authors. AN and SR were involved in weekly discussions about the work providing suggestions along the way and the manuscript was edited in line with comments from two anonymous reviewers.

The work in Chapter 3 appears in the following publication:

Ward, J., Thorne, M., Nowacki, A., & Rost, S. (2021). Automatic slowness vector measurements of seismic arrivals with uncertainty estimates using bootstrap sampling, array methods and unsupervised learning. *Geophysical Journal International*, *226*(3), 1847–1857

JW developed the methodology, wrote the codes, acquired the data, performed the data analysis, made all figures and wrote the first draft of the manuscript which was then edited from suggestions by co-authors. MT, AN and SR were involved in frequent discussions which benefited the work greatly by providing suggestions along the way. The manuscript was edited in line with comments from reviewers Steve Gibbons and Yu Gu.

Chapter 4 is a draft manuscript ready for submission. Therefore, the format of my thesis is in compliance with the requirements for thesis submission with the use of published material.

JW developed the methodology, wrote all codes, performed all data analysis, made all figures and wrote the first draft of the manuscript which was then edited from suggestions by co-authors. MT provided the global SKS dataset which was then processed by JW to make sub arrays and apply the method from Chapter 3. AN and SR were involved in frequent discussions which benefited the work greatly by providing suggestions along the way.

Rationale for Alternative Format

The rationale for the alternative format thesis is that each of the three projects uses different datasets, methods and analyses such that it is more appropriate to be presented as three separate papers rather than the traditional format of having separate methods, results and discussion chapters. Furthermore, with two published papers, the chapters meet the requirement for an alternative format thesis.

Chapters 2, 3 are published manuscripts with the candidate as lead author and work in Chapter 4 is ready to submit with the candidate as the lead author. The chapters are the result of work from the candidate, with minor contributions of co-authors recognised earlier. These chapters meet the criteria for the alternative format thesis as described in the protocol for the submission of an alternative style doctoral thesis by the Faculty of Environment at the University of Leeds. A cohesive discussion on the main findings of the thesis and a general introduction is provided to add context to the work.

Acknowledgements

It's a strange feeling to write this section after what has been a long journey in terms of effort but feels like it only started a few months ago. I want to thank so many people and do so in an elegant way to articulate exactly what they mean to me. Alas, the contribution of those I thank later cannot be understated and, if I'm honest, I can't really do justice but I will try to do so.

A PhD is really made or destroyed by the supervisor team you have and the environment you are in. I feel so incredibly lucky to have had my supervisors and to have worked in Leeds with the colleagues there. My supervisors have been extremely knowledgeable and insightful while at the same time level headed, humorous and approachable. The number of times I have shared a story about them or quoted what they have said to other students and they reply "that's really good of them!" are countless which speaks volumes to their quality. Specifically, I would like to thank Andy Nowacki for, on top of everything else, always being positive in every interaction which makes such a big difference. For Sebastian Rost, I'd like to thank you for being extremely approachable, considerate, checking I have booked time off for holidays and looking out for the human side of supervision. I wish them all the best in future endeavours and really think they are fantastic supervisors.

My friends have a special place in this PhD story. They have been part of the journey for varying lengths of time and contributed in different ways. Some are inspirations or mentors, while others help me forget about my stresses and worries and for some, I can't describe their contribution but they were essential to me making it this far. Specifically, I'd like to thank Thirze, Rachel, Carl, Iain, Ita, Edna, Luke, Ben and Emma. I could give specific reasons for each of them and list all the memories we have shared, but then I'd go over the page limit. I hope these friendships stand the test of time, but if not this will hopefully be a reminder of how your characters and personalities helped me through the years and made it very enjoyable.

Although a more distant presence, my parents have given love and support that only they can. It speaks volumes that their unconditional enthusiasm and care throughout these years didn't waver despite often not knowing any of the details. Thank you Dad

for reading my papers, and most likely this thesis, to talk with me about my work, which is something I will always love. Thank you Mum for ordering edible gifts to my address, always being willing to look after me and welcoming me home with such warm arms. The one benefit of covid is I got to eat more of your cooking.

Finally, thank you to Mash (yes I will always call you that), who is off living his own incredible life and who I am proud to call my brother. See you soon.

For those who are interested in what I have done but feel they don't have the expertise to understand it all, I have tried to summarise what I have done and the findings of each chapter in Appendix D.

Abstract

Many mysteries remain about the inner workings of the Earth from what the origins of lower mantle structures to when did plate tectonics begin. Seismology provides observations of the Earth's interior by analysing phenomena such as the reflections of waves or anomalous timings of waves arriving at the recording stations. Through analysis of these phenomena, information such as the morphology, location and velocity perturbation of mantle heterogeneity has been constrained. Information about the velocity gradients, how quickly the seismic velocity of material changes with distance, at the boundaries of mantle heterogeneities has not been analysed to the same extent and can aid our understanding of its thermal and chemical properties. When a wave interacts with a sufficiently strong velocity gradient, the wave moves at two different speeds over a short distance leading to multiple arrivals arriving at the recording station. This phenomenon, called multipathing, has been analysed through the waveform complexity it creates and has led to estimations of the velocity gradients at the boundaries of mantle heterogeneity. In addition to the waveform complexity, the multiple arrivals should arrive with different directions and horizontal speeds through diffraction of the wave by the velocity gradient. The direction and horizontal speeds have seldom been used to analyse multipathed arrivals and could give more information about the heterogeneities. In this thesis, I use array seismology methods to analyse multipathing and diffraction of the wavefield by measuring the direction and speeds of the arrivals and expand the analysis to a global scale. First, I analyse multipathing caused by the African Large Low-Velocity Province (LLVP), a continent-sized anomaly at the core-mantle boundary beneath Africa, and show multipathing is frequency dependent and can be caused by relatively weak velocity gradients. Then, I develop a method to automate the identification of multipathing with array methods using cluster analysis which also provides uncertainty estimates of the measurements. Finally, this automated method is used to create a multi-regional map of SKS multipathing which motivates future studies analysing the conditions needed for multipathing and for comparison with other investigations into the Earth's current state and evolution.

Contents

List of Figures

Chapter 1

Introduction

This dissertation focuses on the use of seismic array methods to analyse mantle heterogeneities by measuring how they have perturbed the teleseismic wavefield through phenomena such as multipathing (Section 1.1.2) and scaling up the measurements from regional to global scale. To give context to the work presented later, I discuss why we should study the Earth's interior seismically and briefly outline what phenomena can be studied and why I focus on analysing the lateral velocity gradients of mantle heterogeneities (Section 1.1). Then, I summarise array methods used to measure the slowness vector properties (direction and horizontal velocity of a wave), their limitations and methods developed to overcome some of these limitations (Section 1.2).

1.1 Investigating the structure of the mantle seismically

The movement of Earth's tectonic plates driven by mantle convection is the cause of many of the most hazardous and extreme features of the surface including earthquakes, volcanoes and tsunamis. Although the dynamic interior of the Earth drastically affects the surface we live on, many questions concerning the structure and processes of the mantle remain. Such questions include: When did plate tectonics begin (Stern, 2007)? How do plumes or hotspots initiate (Koppers et al., 2021)? Does subducted lithosphere reach the core-mantle boundary? Why do some slabs stagnate and others not (Fukao and Obayashi, 2013)? Are there remnants of the primordial Earth in the mantle (Garnero et al., 2016)? Why are slabs (Fukao and Obayashi, 2013) and plumes (French and Romanowicz, 2015; Rickers et al., 2013) apparently impeded at 1000 km depth? What is the evolutionary history of the mantle? To address these and other uncertainties, seismology provides invaluable observations of the Earth's interior on scales ranging from global 1-D velocity models of the Earth (Dziewonski and Anderson, 1981) to tens of kilometre scale observations of the core-mantle boundary (e.g. Frost et al., 2013). Furthermore, as computational power and coverage of seismometers with novel de-

ployments (e.g. Simon et al., 2021) expands, further constraints on hypothetical Earth models such as that shown in Figure 1.1 can be made.

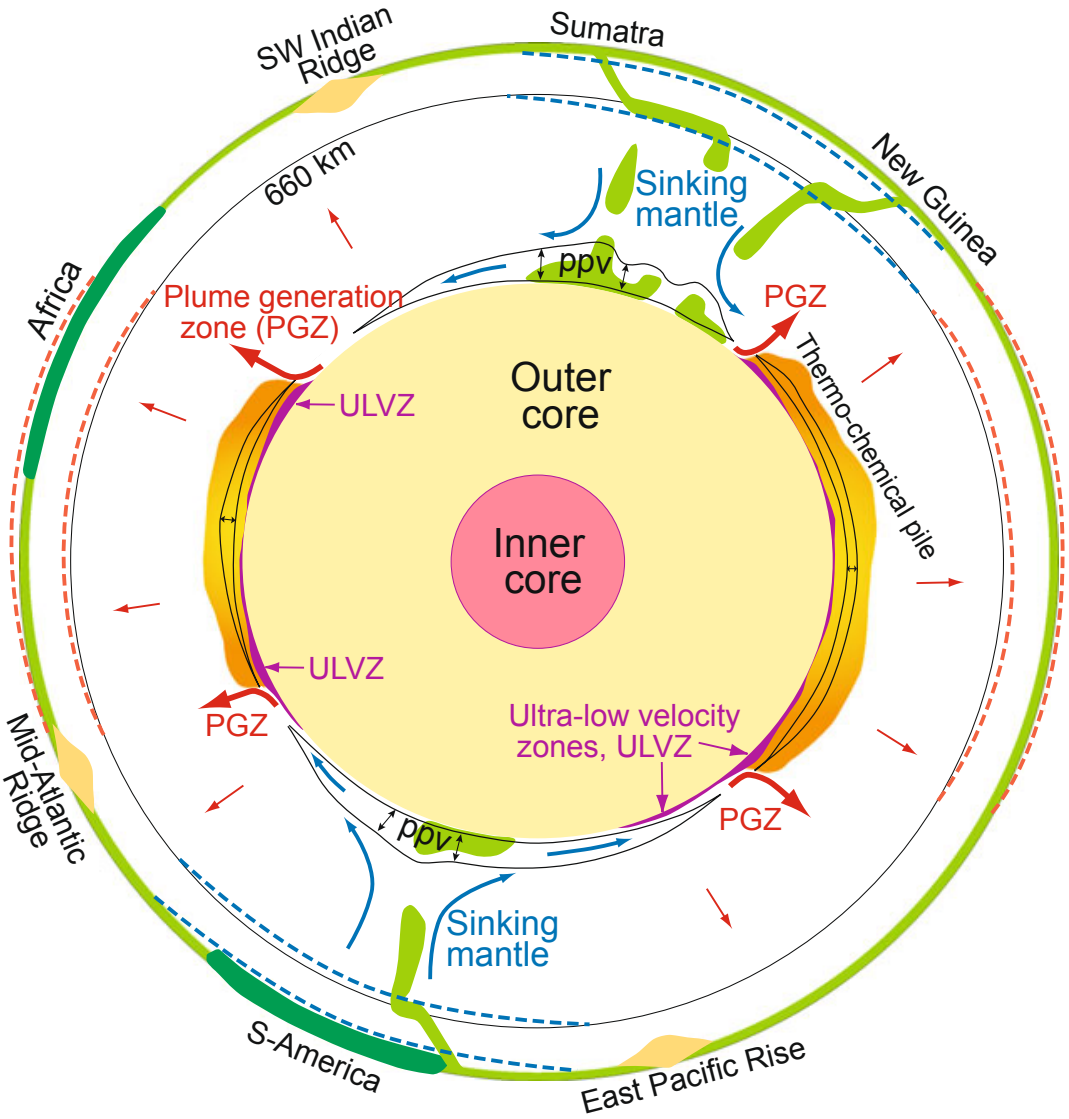

Figure 1.1: Figure 13 from Trønnes (2010) summarising a possible conceptual Earth model. In this hypothetical model, the LLVPs here are denoted as thermochemical piles causing large scale convection causing surface uplift. LLVPs are hypothesised to influence other mantle structures by possibly initiating mantle plumes at their boundaries as plume generation zones (PGZs) and Ultra Low Velocity Zones (ULVZs) collected at their boundaries. The sinking material reaches the core-mantle boundary and pushes the thermochemical material into the LLVP piles.

1.1.1 Seismic observations of the Earth

Seismologists have applied many techniques to the ever growing dataset of seismograms. Seismic tomography provides broad (>1000 kilometre scale) observations of 3-D elastic structure of the Earth (e.g. French and Romanowicz, 2014; Ritsema et al., 2011; Simmons et al., 2010), but cannot resolve finer scale structure on the order of

100s of kilometres. Regional studies focusing on a specific area of the Earth can have higher resolution and uncover structures invisible to tomography adding to the picture of what the Earth's internal structure is. Some of these regional studies employ array techniques outlined in Section 1.2 to observe weaker signals created through interaction with seismic heterogeneity such as from scattering in the mid mantle (Bentham and Rost, 2014; Li et al., 2014; Ritsema et al., 2020; Rost et al., 2008) and lower mantle (Cao and Romanowicz, 2007; Haddon and Cleary, 1974; Haddon et al., 1982; Ma and Thomas, 2020; Rost and Earle, 2010), reflected arrivals from transition zone (Day and Deuss, 2013; Lessing et al., 2014; Waszek et al., 2018) and mantle heterogeneity (Kito et al., 2007; Lay, 2007; Revenaugh and Meyer, 1997; Schumacher and Thomas, 2016; Schumacher et al., 2018) or diffraction and refraction of the wavefield (Cottaar and Romanowicz, 2012; Stockmann et al., 2019; Xu and Koper, 2009). Despite advances of seismic imaging of the Earth, standout questions of the most enigmatic features of the mantle remain.

1.1.1.1 Large Low-Velocity Provinces and Ultra Low Velocity Zones

Since the first seismic tomography models (Dziewonski et al., 1977), two extremely large low-velocity regions have been imaged beneath Africa and the Pacific labelled Large Low-Velocity Provinces (LLVPs) and have been a common feature in all S-wave tomography models (e.g. French and Romanowicz, 2014; Koelemeijer et al., 2015; Lu et al., 2019; Ritsema et al., 2011). Since their discovery, LLVPs have remained one of the most enigmatic and studied structures of the mantle with uncertainties remaining over their spatial scale, how 'sharp' the transition from the surrounding mantle to the LLVPs is, or their relationship with other mantle heterogeneity. Further uncertainties can be shown from the different hypotheses of what LLVPs are. Are they purely thermal structures or do they have some form of chemical heterogeneity? How old are LLVPs? Are they long lived features of the mantle or are they relatively short-lived features? Some of the differing conceptual models for LLVPs are shown in Figure 1.2 edited from Figure 2 in Garnero et al. (2016).

Seismic tomography typically shows LLVPs to spatially extend 1000s of km laterally and up to 1000 km above the CMB, have approximately 3% reduced S-wave velocity and approximately 2% reduced P-wave velocity relative to the surrounding mantle, although it has been shown tomography can underestimate seismic velocity anomalies in the lower mantle (Bull et al., 2009; Bull et al., 2010; Ritsema et al., 2007; Schuberth et al., 2009). The density of LLVPs has been a heavily discussed topic and knowledge of the density anomaly of LLVPs can potentially differentiate between the conceptual models shown in Figure 1.2. Initial estimates using gravity and normal mode (whole Earth oscillations) data suggested LLVPs may be 0.8% – 1.8% denser than the surrounding mantle (Ishii and Tromp, 1999; Trampert et al., 2004). Since these studies, other estimates have

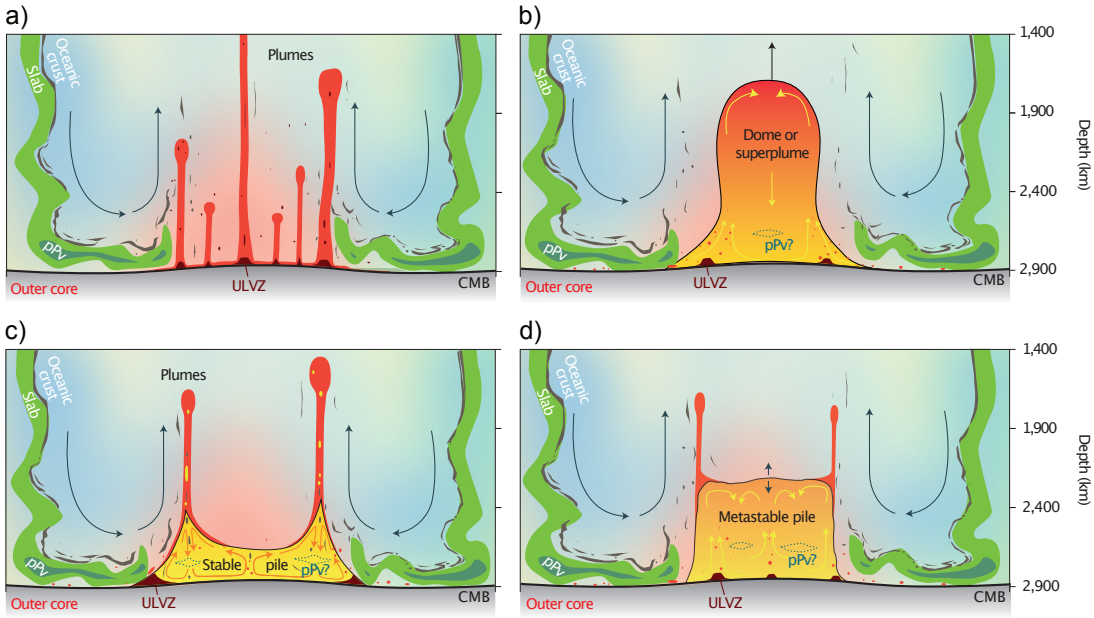

Figure 1.2: Edited from Figure 2 in Garnero et al. (2016). Four conceptual models of what LLVPs could be. **(a)**, a cluster of mantle plumes, **(b)** a superplume with chemical heterogeneity, **(c)**, a stable and long-lived dense thermochemical pile and **(d)**, a thermochemical pile with density similar to the surrounding mantle.

been made and suggest the LLVPs may be 0.88% less dense than the surrounding mantle (Koelemeijer et al., 2017) while others suggest they are 0.5% denser than the surrounding mantle (Lau et al., 2017). Work continues to consolidate the different results of Stonely modes and tide observations with an LLVP model with a more dense base and less dense tops (Richards et al., 2021). To infer whether chemical heterogeneity may be present, correlations between shear wave velocity (sensitive to the rigidity of the material) and bulk sound (sensitive to the compressibility of the material) can be made. Studies comparing these properties found a negative correlation between the two, which cannot be produced by thermal anomalies alone for the same phase (Masters et al., 2000) suggesting chemical heterogeneity is present, although, this could indicate locations of a phase change (Koelemeijer et al., 2017) and not necessarily constrain whether LLVPs are compositionally unique to the mantle. Seismic tomography provides broad-scale observations of LLVPs, but cannot resolve the spatial scale of the transition from the mantle to LLVP, which could give information about how distinct LLVPs are from the surrounding mantle. Studies analysing sharp changes in arrival times of waves over small spatial scales and identifying multipathing give estimates of a transition length of 10s of kilometres and a shear wave velocity reduction of between 3% and 5% (Bréger and Romanowicz, 1998; Ford et al., 2006; He and Wen, 2012; He et al., 2006; Ni and Helmberger, 2003a; Ni and Helmberger, 2003b; Ni et al., 2002; Ritsema et al., 1997; Sun et al., 2009; Sun and Miller, 2013; Wang and Wen, 2004; Wen, 2001; Zhao et al., 2015). Multipathing only occurs when a wave is incident on a sufficiently strong lateral

velocity gradient and leads to two arrivals which arrive at different times, directions and horizontal speeds. For further discussion of multipathing, see Section 1.1.2. Despite claims that sharp velocity gradients are evidence for chemical heterogeneity, it has been shown that purely thermal structures with no chemical heterogeneity can produce sharp velocity gradients and velocity reductions (Davies et al., 2012). At the moment, both purely thermal and thermochemical models of LLVPs can replicate the seismic observations made so far, therefore none of the conceptual models can be ruled out yet.

On a much smaller scale, Ultra Low Velocity Zones (ULVZs) have been imaged in various regions at the CMB with very strong reductions in S and P-wave velocity of up to 50% and 25% respectively (Garnero and Helmberger, 1996; Garnero et al., 1998; Idehara, 2011; Rondenay and Fischer, 2003; Rost et al., 2005; Yu and Garnero, 2018) and be up to 20% more dense than the mantle (Idehara, 2011; Rost et al., 2005). ULVZs are typically on the order of 10s of kilometres high and 100s of kilometres laterally (McNamara, 2019; Rost et al., 2005; Thorne and Garnero, 2004) although there have been observations of so called 'mega' ULVZs (Cottaar and Romanowicz, 2012; Thorne et al., 2013) which have lateral spatial scales of up to 1000 km. ULVZs have been detected using a variety of seismic techniques including scattering (e.g. Ma et al., 2019; Rondenay and Fischer, 2003; Rost and Garnero, 2006) and diffraction (Cottaar and Romanowicz, 2012) as well as by waveform analysis (e.g. Thorne and Garnero, 2004; Thorne et al., 2021; Thorne et al., 2019). Like LLVPs, ULVZs remain very enigmatic with uncertainty over their origins remaining and determining which hypotheses are correct is challenging. The hypotheses often involve partial melt, dense, compositionally distinct material, or some combination of the two. To be dense enough (10% denser McNamara et al. (2010)) to survive mantle mixing and not be limited to only the hottest regions of the mantle, ULVZs have been proposed to be compositionally distinct with a range of hypotheses proposed as sources for this compositional heterogeneity such as silicate sediments from the core (Buffett et al., 2000), iron enriched post perovskite (Mao et al., 2006; Mao et al., 2005), partial melt from subducted slab (Liu et al., 2016), iron-enriched oxides (e.g. Wicks et al., 2017).

ULVZs and LLVPs are likely related in some dynamic sense as ULVZs have been shown at the boundaries of LLVPs (Yu and Garnero, 2018). Understanding the relationship between ULVZs and LLVPs would give some insight into the origin of LLVPs and their role in global mantle convection. As it is unclear if either or both LLVPs and ULVZs are home to some heterogeneity it is challenging to constrain their relationship. Observations of ULVZ location, shape and sizes can further constrain their role in the mantle and with LLVPs and possibly the chemical nature of both structures (McNamara, 2019).

1.1.2 Why analyse multipathing, diffraction and refraction?

Of the phenomena analysed seismically, multipathing has not been analysed in the same detail or as widely applied as other seismic phenomena. Multipathing observations provide information about the lateral velocity gradients the wave has sampled and over what distance the properties change between the ambient mantle and the heterogeneity itself. Analysis of boundary structure has been focused on LLVPs using observations of waveform complexity and distinct changes in travel time anomalies (e.g. Ni et al., 2002). In addition to these observations, more information is available by using array-based methods to measure the slowness vector properties of the multipathed arrivals (Ward et al., 2020), see Section 1.2 for details. Furthermore, analysing the slowness vector properties of waves that have diffracted when interacting with the boundaries of mantle heterogeneities can also be used to constrain the velocity gradients. In this section, I outline in more detail what multipathing is, the progress that has been made in analysing the phenomenon and what analysing the slowness vectors of multipathing could contribute.

Multipathing occurs when a wave is incident on a sufficiently strong lateral velocity gradient. Figure 1.3 illustrates multipathing at the boundary of LLVPs and fast material and how they may be observed at the surface. The velocity gradient causes different parts of the wavefield to move at different speeds depending on whether they are travelling inside or outside of the structure. The different parts of the wave will diffract along the boundary and through the structure. This results in two or more wavefront segments that arrive at the station at different times and with different horizontal speeds and directions. Multipathing from mantle heterogeneity is often analysed in terms of their arrival times and waveform complexity (e.g. Ni and Helmberger, 2003a; Sun and Miller, 2013; Zhao et al., 2015) and later I show multipathed arrivals can be observed using their different direction and horizontal speeds.

Multipathing has been used to infer the morphology, location, velocity perturbation and lateral velocity gradient at the boundaries of mantle heterogeneity to understand processes active in the mantle. Silver and Chan (1986) identify multipathing in direct S waveforms by their broadening relative to ScS phases to identify a slab feature penetrating the 660 km discontinuity, verified using forward modelling to replicate the multipathing with a slab like feature. There have been several studies analysing multipathing caused by the LLVPs. As described earlier, a standout question about LLVPs is whether they are purely thermal features or if they are home to chemical heterogeneity. Observing multipathing at the boundaries of LLVPs and quantifying the possible gradients to compare with those in geodynamic models may constrain if chemical heterogeneity is required to produce strong enough velocity gradients to cause multipathing. A standout study on this was conducted by Ni et al. (2002) who analysed the waveforms of S, ScS, Sdiff and SKS waves recorded in southern African which is lo-

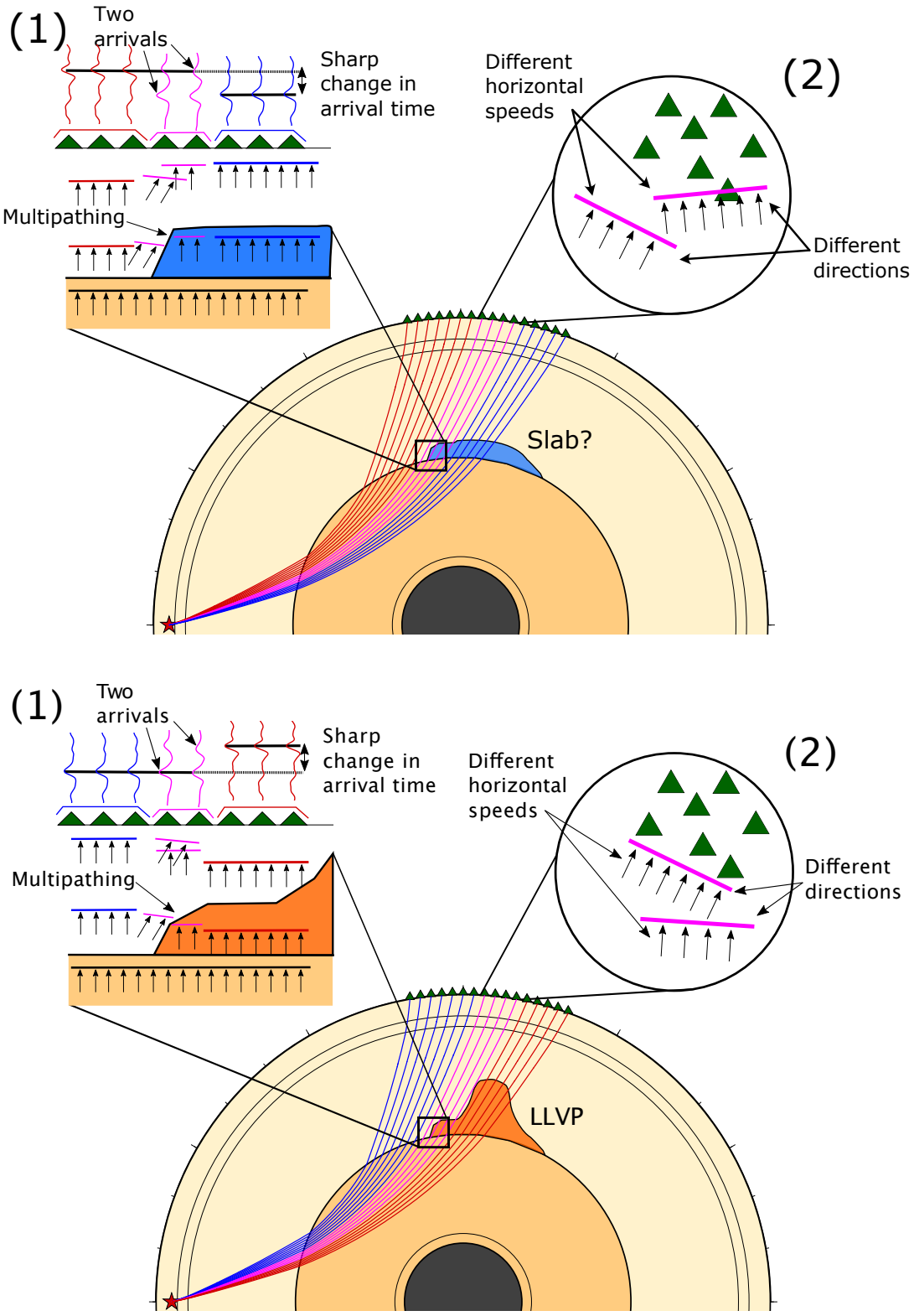

Figure 1.3: Cartoons of how SKS multipathing from an earthquake (red star) to a seismic array (green triangles) may occur at the boundaries of seismically fast material (top) and slow material (bottom). The raypaths are coloured by whether they are relatively slow (red), fast (blue) or if they will show multipathed arrivals (pink). These cartoons show how sharp boundaries and multipathing may be observed in seismograms recorded at an array. **(1)** of both subfigures shows the waveforms and an abrupt change in arrival times whereas **(2)** shows the difference in the vector properties of the arrivals, which is the focus of this thesis. The bottom subfigure is taken from Ward et al. (2020).

cated directly above the African LLVP. They find evidence for clear multipathing and, through a 2-D ray-tracing approach, estimated the velocity gradients as a reduction of 3% S-wave velocity over 50 km. Several other studies using similar approaches of waveform analysis and then replication using 2-D ray tracing synthetics (Ni and Helmberger, 2003a; Ni and Helmberger, 2003b; Sun et al., 2007) have found similar estimates for the lateral velocity gradients as have those expanding to 3-D ray tracing (Helmberger and Ni, 2005; Ni et al., 2005). Following this series of studies, efforts have been made to automate the identification of multipathing in the waveforms (Sun et al., 2009). In this algorithm, multipathing is identified by comparing the observed waveform to a synthetically generated seismogram where multipathing has been approximated as a difference in arrival times between the different sides of the Fresnel zone. The Fresnel zone describes the area at a point along the path of the wave between the source and receiver (for further discussion on Fresnel zones and array seismology see Rost and Thomas, 2009). This 'multipathing detector' (Sun et al., 2009) has since been used to analyse multipathing caused by plumes (Sun et al., 2010), African LLVP boundaries (Sun and Miller, 2013), ULVZs (Sun et al., 2019) and subducting slabs (Sun et al., 2017). Multipathing has been analysed using measurements of the multipathed arrivals' direction and horizontal speed, but the multipathed arrival is described as a post cursor to the main Sdiff arrival caused by sampling an ULVZ (Cottaar and Romanowicz, 2012).

It has often been proposed that the presence of 'sharp' velocity gradients capable of producing multipathing is evidence for chemical heterogeneity, particularly for lower mantle structure (e.g. Ni et al., 2002), however, it has been shown purely thermal structures are also capable of producing sharp velocity gradients (e.g. Davies et al., 2012). Studies analysing strong lateral velocity gradients have focused on LLVP boundary structure and the lateral velocity gradients of other mantle heterogeneities have not been fully explored. Therefore, multipathing observations to identify and quantify lateral velocity gradients are still valuable to understand mantle dynamics and history. Unlike other mechanisms for mantle heterogeneity to affect the seismic wavefield, multipathing has not been analysed on a global scale to identify where strong lateral velocity gradients exist and quantify their strengths. This is part of the motivation for the end goal of this thesis where I begin to create a global dataset of multipathing in different seismic phases starting with SKS.

1.2 Array methods: overview, limitations and developments

All of the work in this project uses a spatial distribution of recording stations to measure the properties of a teleseismic wave. It is therefore necessary to lay the foundation by describing what property I measure (Section 1.2.1), and introduce the techniques used

to measure it (Sections 1.2.2 and 1.2.3). Then, assumptions and limitations of the standard methods are outlined and the techniques I and others have used to address them are described (Section 1.2.4).

1.2.1 Slowness vector

All work in this thesis in some way involves making slowness vector measurements of a teleseismic wave arriving at receiver stations distributed spatially in close proximity called a 'seismic array' (Figure 1.4 shows an example of an array). Later in this section, I describe techniques to measure the slowness vector of a wave with a seismic array and, to understand the implications and results of Chapters 2, 3 and 4, I describe what a slowness vector represents.

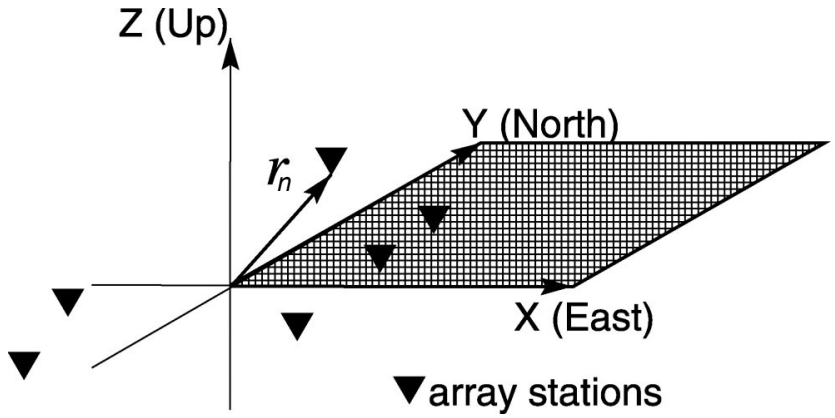

Figure 1.4: Edited from Figure 3 of Rost and Thomas (2002) showing a spatial distribution of stations (triangles). The position of the stations are recorded in the vector $\overrightarrow{r_m}$ with their x (east), y (north) and z (elevation) coordinates.

The slowness vector describes the horizontal direction and inclination of a wavefront. The horizontal direction (or backazimuth, θ) can be measured as the angle clockwise from north to the direction the wave is coming from (Figure 1.5). The inclination of the wave is inferred from the apparent horizontal velocity (v_{hor}) of the wave with

$$i = \arcsin\left(\frac{v_{med}}{v_{hor}}\right), \tag{1.1}$$

assuming the velocity of the material beneath the array (v_{med}). The apparent horizontal velocity can be calculated from the time taken for the wave to travel between stations at the surface. As these stations usually have very little elevation difference between them, relative to the seismic wavelength, only the horizontal component of the wave's velocity can be measured. Assuming similar velocity properties of the medium beneath the array, the faster the apparent horizontal velocity of the wave, the more steeply it is arriving. A completely vertical wave will arrive at all stations at the same time, thus having an infinite apparent velocity. In work presented later, the measurement made is not the apparent horizontal velocity but the horizontal slowness of the wave (p), which

is the inverse of the apparent horizontal velocity (v_{hor}),

$$p = \frac{1}{v_{hor}}, \tag{1.2}$$

of the wave moving over the array. From the horizontal slowness, the inclination (i) of the wave can be calculated by assuming a slowness of the wave u (the inverse of the velocity of the wave through the medium, v_{med}) travelling through the material beneath the stations with

$$i = \arcsin\left(\frac{p}{u}\right). \tag{1.3}$$

The slowness vector can be plotted in a polar coordinate system with horizontal slowness on the radial axis and the backazimuth on the azimuthal axis (Figure 1.5). The distance of a point on this plot from the centre gives the horizontal slowness and the angle from 0° (or north) gives the backazimuth. This can, if the velocity of the medium is known, be interpreted in 3D as a hemisphere beneath the array and a wave arriving from beneath. The closer the point is to the centre, the steeper the inclination of the arrival.

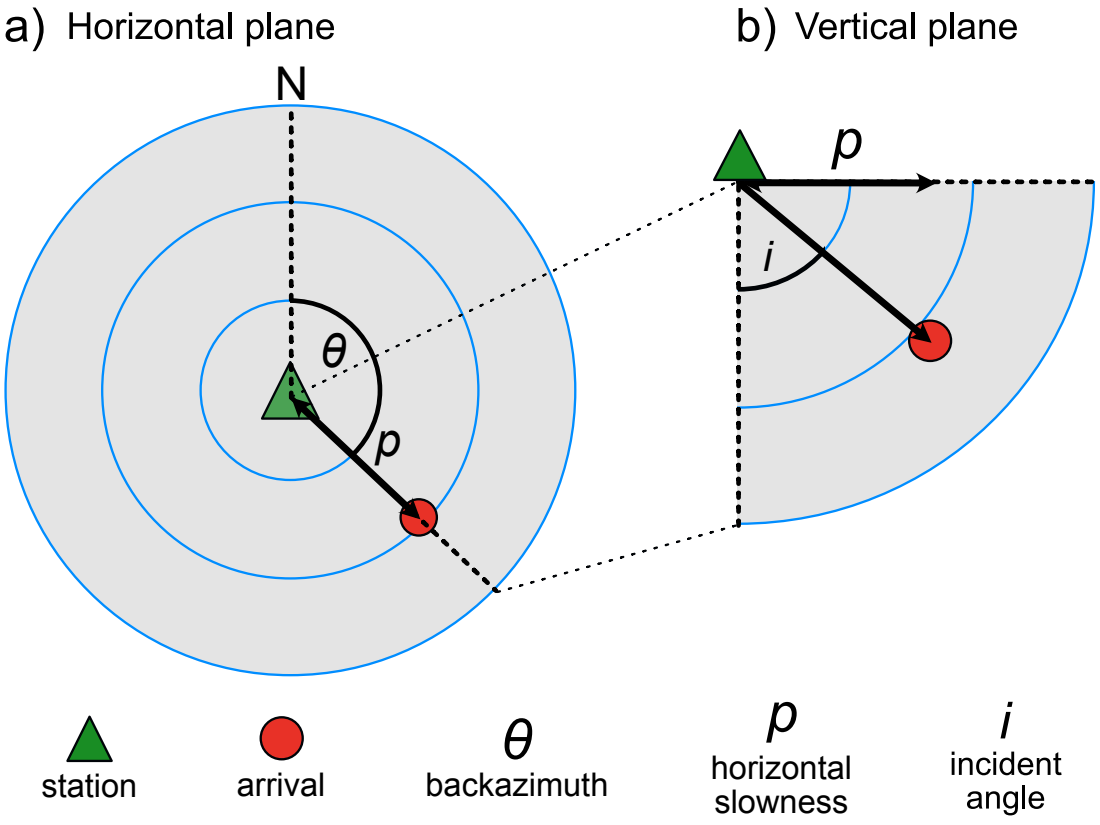

Figure 1.5: Cartoon explanation of making a slowness vector measurement when plotting horizontal slowness (p) on the radial axis and backazimuth (θ) on the azimuthal axis. **a)** shows the plot on the horizontal plane where the measurement can be made and **b)** shows how the horizontal slowness measurement on this plot relates to inclination angle.

When measuring the slowness vector of a wave using the methods described in Sections 1.2.2 and 1.2.3, one often searches over a range of different slowness vectors. For this search, the slowness vector can be defined through its p_x and p_y components which describe the slowness vector components in the East and North direction respectively. If searching over a range of slowness vectors in the polar system (backazimuth and horizontal slowness), the spacing between the vectors increases as a function of the horizontal slowness such that at very low horizontal slowness, the distance between the vectors is very small and at larger p values the distance is very large for the same backazimuth spacing. If the slowness vector is defined with p_x and p_y representation, the spacing between the slowness vectors in the search can be the same regardless. In all methods applied in this thesis, we search over a range of slowness vectors using their p_x and p_y representation, but for more intuitive interpretation we convert the measurements to backazimuth and horizontal slowness values.

1.2.2 Beamforming

In all methods used in this thesis, beamforming (Rost and Thomas, 2002) plays a crucial role. Beamforming is used to amplify the coherent signal and suppress incoherent noise for energy arriving from a particular backazimuth and horizontal slowness. Beamforming uses the fact that at a given array of stations distributed spatially, a wave arriving from a particular direction with a particular horizontal velocity will arrive at the stations at different times. Depending on the apparent horizontal velocity, the time taken to travel the horizontal distance between stations will be different and can be clearly seen as a moveout on a distance-time plot (Figure 1.6).

Given a backazimuth, horizontal slowness and station locations ($\overrightarrow{r_m}$), the estimated arrival times relative to a reference point assuming a plane wavefront can be calculated. The plane wavefront model assumes the curvature of the wavefront leads to negligible effects on the travel time estimates. This holds for a small seismic array but, for larger arrays and arrays which are close to the source or antipode, this assumption breaks down. This is discussed further in Section 1.2.4.1. Using the calculated delay times, the seismograms can be shifted in time. After the seismograms are shifted, they are 'stacked' which is essentially taking the mean amplitude at each time over all of the seismograms. The resultant stacked seismogram is the 'beam' that is formed. This whole process can be described by

$$b(t_{disc}, \overrightarrow{k}) = \frac{1}{M} \sum_{m=1}^{M} s_m(t_{disc} + \overrightarrow{r_m} \cdot \overrightarrow{k}), \tag{1.4}$$

where $b(t_{disc})$ is the amplitude of the beam at a discrete time t_{disc}, M is the number of seismograms, s_m is the mth seismogram, $\overrightarrow{r_m}$ is a vector describing the location of the seismograph which recorded the seismogram s_m and $\overrightarrow{k}$ is the horizontal slowness vector.

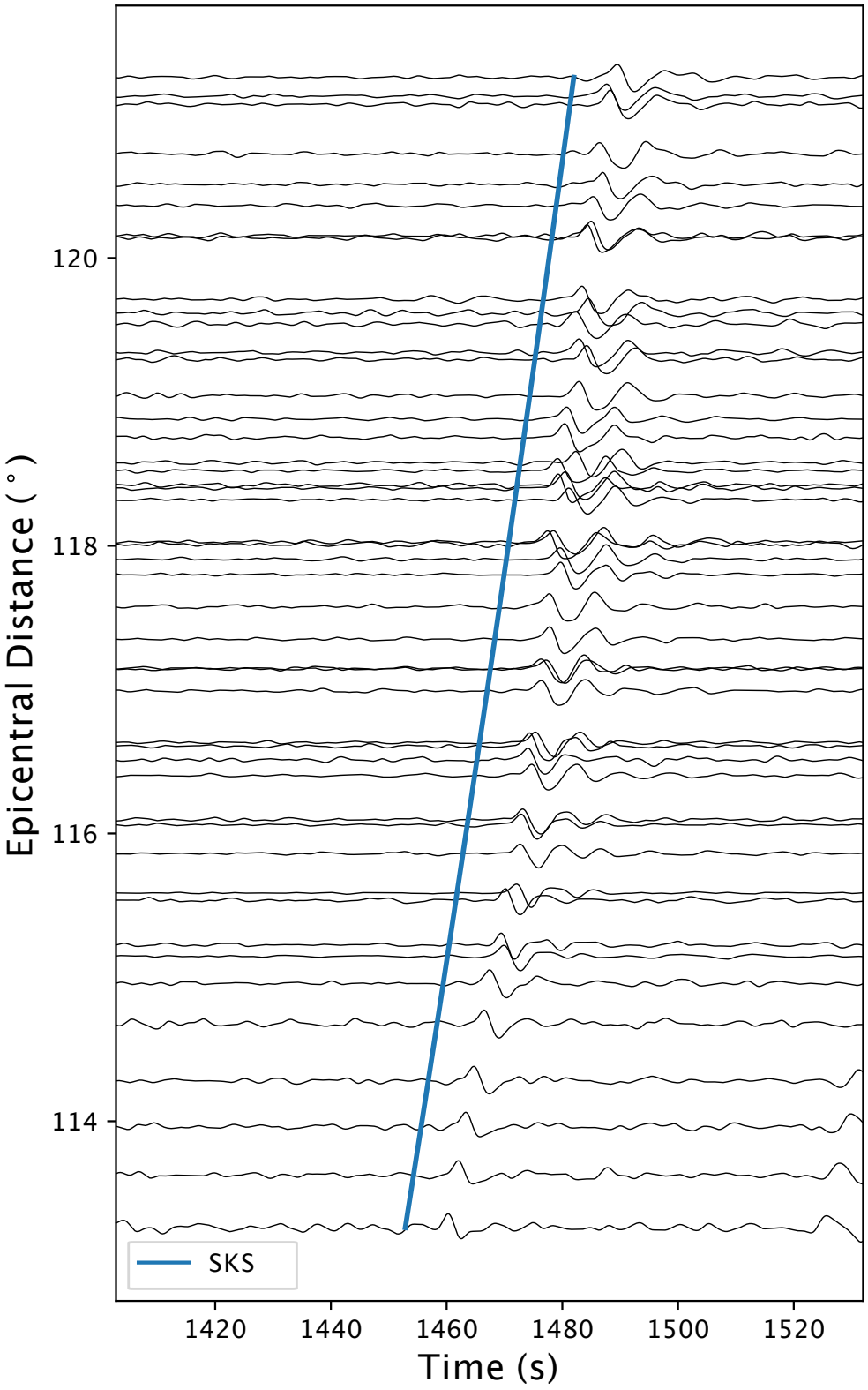

Figure 1.6: A distance-time plot of data from the 25 May, 1997 event recorded at the Kaapvaal array in South Africa. This plot illustrates the high amplitude waves generate by the earthquake arrives at about 1460s at an epicentral distance of 113.2° and then the wave arrives gradually later with epicentral distance until the top of the plot where the wave arrives at approximately 1490s. The blue line marks the expected arrival time if the wave travels through the 1-D Earth model PREM (Dziewonski and Anderson, 1981).

The full derivation for this equation and how the coherent signal separates from the incoherent noise can be found in Rost and Thomas (2002). The level to which the signal to noise (SNR) is increased from stacking is approximately $\sqrt{M}$ where M is the number of seismograms used in the beamforming assuming perfectly coherent signals and totally incoherent noise (Harjes and Henger, 1973). Beamforming can amplify the signal of coherent waves arriving from a particular backazimuth and horizontal slowness if it is known. What many techniques discussed in the next sections take advantage of is how beamforming can also be used to measure the coherent signal arriving from a particular backazimuth and horizontal slowness. Through this measurement of coherence, a range of slowness vector properties can be used to find which has the strongest coherent signal and therefore has the closest slowness vector properties to the arrival.

1.2.3 Vespagrams, beamforming grid searches and f–k analysis

It is rare to know the slowness vector properties of an arrival before using beamforming and it is often very useful to estimate these properties and study what may have caused them to deviate from the prediction of an Earth model. To estimate the slowness vector properties of arrivals in a given time section of seismograms recorded at a seismic array, velocity spectral analysis/vespagrams (Davies et al., 1971), beamforming and f–k analysis can be used. Here, I give a brief overview of these methods.

The vespa process takes advantage of the ability of beamforming to amplify the coherent signal and suppress the incoherent noise of a backazimuth and horizontal slowness of a wave. Vespagrams vary one of either backazimuth or horizontal slowness while keeping the other one constant and create beams at each combination of slowness vector properties. The result of the vespa process can be plotted as a vespagram which has the slowness vector property investigated on the y-axis and time on the x-axis (Figure 1.7). This example shows a vespagram where the horizontal slowness is varied and backazimuth is kept constant as the backazimuth between the source and the centre of the array. Alternatively, the horizontal slowness could be kept constant and vary the backazimuth. The value given to the constant slowness vector property is very important and may lead to misleading measurements of the other slowness vector property (Rost and Thomas, 2002). Furthermore, the array geometry, aperture and station spacing affect the resolution of the arrivals in the vespagram plot. Poor resolution on a vespagram is shown by high amplitudes at many horizontal slowness or backazimuth values making it difficult to measure the slowness vector property of the arrival. This is problematic when trying to isolate different arrivals based on their slowness vector properties. Strategies have been developed to improve the slowness resolution such as Nth-root stacking (McFadden et al., 1986), phase weighted stacking (Schimmel and Paulssen, 1997), F statistic (Blandford, 1974), or cross-correlation beamforming (Ruigrok et al., 2017).

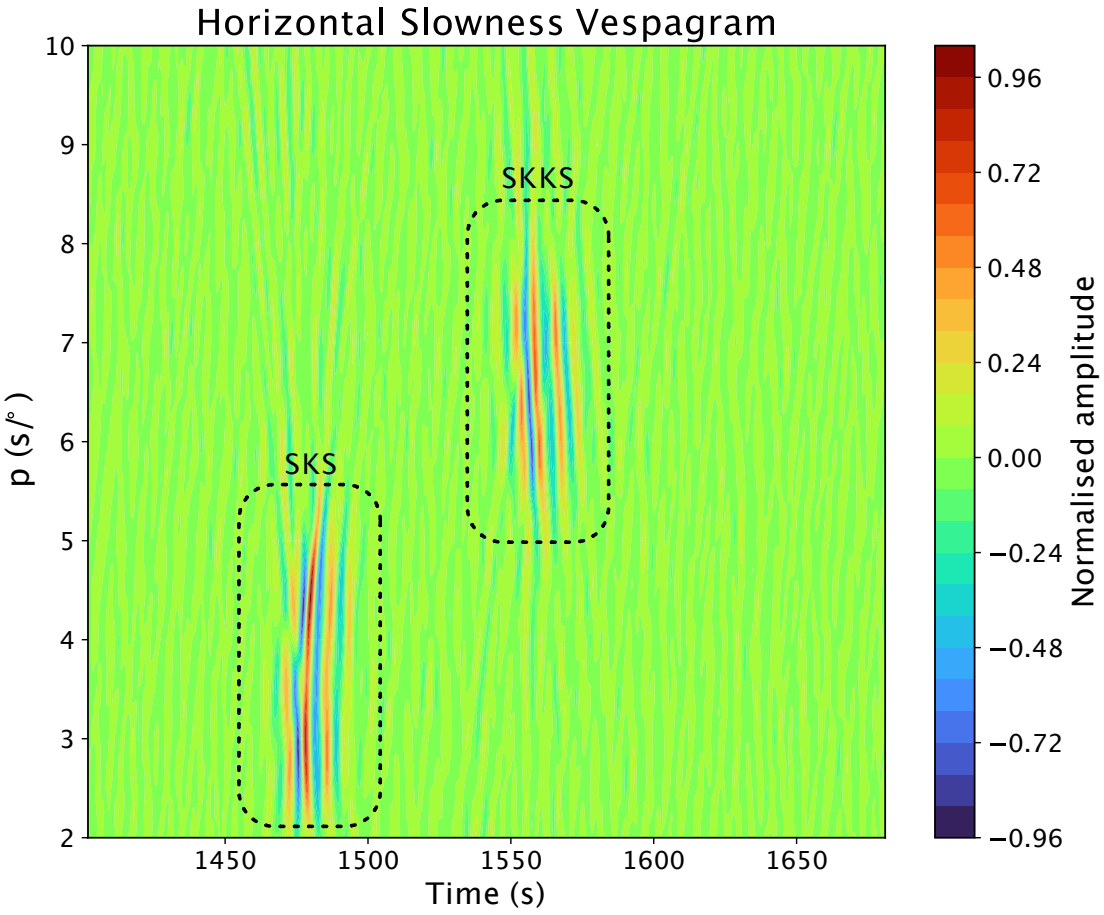

Figure 1.7: Example of a vespagram showing what times and horizontal slownesses have the most coherent signal. Data used are the same as in Figure 1.6. Notice that there are two clear regions where phases SKS and SKKS arrive (Figure 1.10). Furthermore, there may be two arrivals with different slownesses for both of these phases possible evidence for multipathing (Section 1.1.2).

The full slowness vector (finding both the backazimuth and horizontal slowness) of the coherent signal(s) in a time window can also be found using the beamforming approach. To do this, both backazimuth and horizontal slowness parameters are searched in a grid search. For each slowness vector, the beam is formed and a measure of the power in the beam with

$$P(\overrightarrow{k}) = \int_{t1}^{t2} b^2(t_{cont}, \overrightarrow{k})dt, \tag{1.5}$$

where $P(\overrightarrow{k})$ is the power value for a slowness vector $\overrightarrow{k}$ and is found by integrating along the power of the beam $b^2(t_{cont}, \overrightarrow{k})$ between times t_1 and t_2. Note, now time is a continuous variable. This gives a single value describing how coherent a signal is at a given slowness vector and therefore if you search over a range of slowness vectors, you can determine which have the strongest coherent signal. For example, Figure 1.8 shows the result of this grid search approach with the data in Figure 1.6 and there is clearly a region of high power values near the predicted SKS slowness vector value.

For the sake of efficiency, this grid search approach can be conducted in the frequency domain with the f–k method, which will calculate the coherent power distribution over frequency (f) and wavenumber (k) (Aki and Richards, 2002; Capon, 1969; Hinich, 1981) described as

$$P(\overrightarrow{k} - \overrightarrow{k_0}) = \int_{-\infty}^{\infty} b(t_{cont}, \overrightarrow{k})\ dt = \int_{-\infty}^{\infty} |S(\omega)|^2 \left| \frac{1}{M} \sum_{m=1}^{M} e^{2\pi i \cdot (\overrightarrow{k} - \overrightarrow{k_0}) \cdot \overrightarrow{r_m}} \right|^2 \frac{d\omega}{2\pi}, \tag{1.6}$$

where $P(\overrightarrow{k} - \overrightarrow{k_0})$ is the power at a particular slowness vector $\overrightarrow{k}$ relative to the slowness vector of the signal $\overrightarrow{k_0}$, $S(\omega)$ is the Fourier transform of the signal, $\overrightarrow{r_m}$ is the position vector of station m and ω is the angular frequency. From this expression of the power as a function of wave number, the power can be broken into the amplitude spectrum ($S(\omega)$) and the array response function

$$ARF(\overrightarrow{k} - \overrightarrow{k_0}) = \left| \frac{1}{M} \sum_{m=1}^{M} e^{2\pi i \cdot (\overrightarrow{k} - \overrightarrow{k_0}) \cdot \overrightarrow{r_m}} \right|^2. \tag{1.7}$$

The array response function describes the effect of array aperture and inter-station spacing on the wavenumber power spectrum. As the ARF can be calculated theoretically given an array geometry, studies have deconvolved the ARF from the power distribution to try and recover the signal $S(\omega)$. We discuss this alongside other limitations of using seismic arrays and methods developed to address them in the next section.

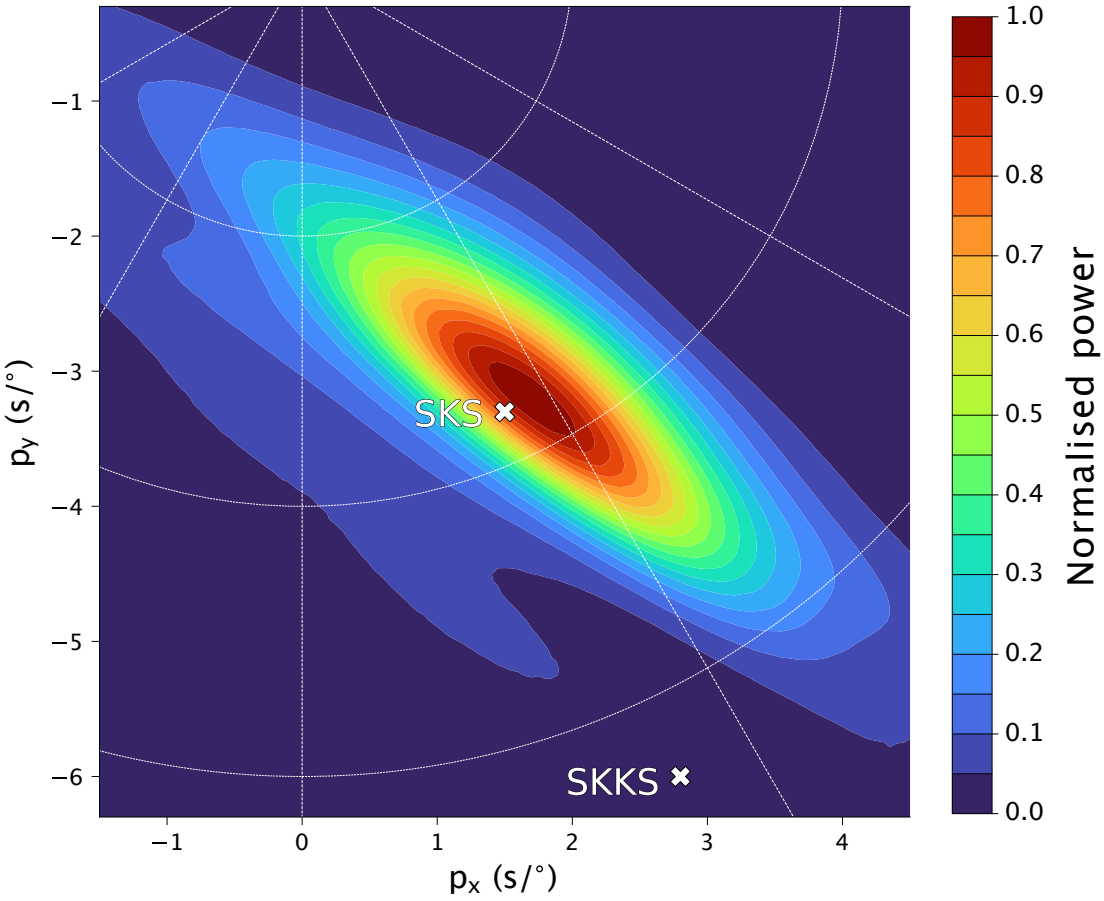

Figure 1.8: Example of a power distribution on a grid of different slowness vectors defined by their p_x and p_y components. The p_x is the easterly component of the slowness vector and p_y is the northerly component of the slowness vector. Data used are the same as in Figure 1.6 and the analysis is conducted between 1450 and 1500 seconds after event origin time in a frequency band between 0.10 – 0.40 Hz. Notice that there is one clear region with high power values and the centre of this region slightly deviates from the SKS predicted slowness vector (white cross). The shape of the high power region is determined by array geometry, spacing and aperture which can be calculated as the array response function.

1.2.4 Building on standard array processes

The techniques outlined in the previous section make assumptions about the wave speed, wavefront shape, near-surface geology, waveform shape, the contribution of noise and others. In this section, we describe these limitations and how studies have addressed these limitations and improved the resolution of slowness vector measurements.

1.2.4.1 Correcting for a curved wavefront

Conventional array methods assume the wave moving over the array can be approximated as a plane wave. A plane wavefront assumes the backazimuth and horizontal slowness of the wave are the same at all stations in the array. However, assuming a finite source and a spherical Earth, the backazimuth of the wave varies with location and the horizontal slowness varies with source-receiver distance. For arrays of a smaller aperture, the plane wave assumption holds and there is no effect of assuming a plane wavefront on the measured slowness vector. For large aperture arrays, such as the Kaapvaal array used for analysis in Chapter 2, the assumption breaks down and can affect the slowness vector measurement. Because of this, I change the beamforming methodology to correct for a curved wavefront.

To correct for a curved wavefront I alter the travel time estimation process given a backazimuth and horizontal slowness. To estimate the travel times, of a curved wavefront moving from an event to an array of stations, the radial distance over a spherical Earth is calculated using the Haversine formula,

$$a = (\sin(\frac{\Delta\phi}{2})^2 + \cos(\phi_1)\cos(\phi_2)\sin(\frac{\Delta\varphi}{2}))^2 \tag{1.8}$$

$$c = 2\arctan(\frac{\sqrt{a}}{\sqrt{1-a}}) \tag{1.9}$$

$$d = \frac{180}{\pi}c, \tag{1.10}$$

where d is the distance in degrees, $\Delta\phi$ is the latitudinal difference between the event and the station, $\Delta\varphi$ is the longitudinal difference between the station and the event, ϕ_1 is the latitude of the event, ϕ_2 is the latitude of the mean station location. From these distances, the arrival times are estimated by multiplying the distances by a horizontal slowness value, the traces are then shifted and stacked as in the conventional beamforming approach. For each backazimuth of interest, the event is relocated keeping the epicentral distance constant along the backazimuth in question from the centre of the array using

$$\phi_{new} = \left[\arcsin(\sin(\phi_{old})\cos(d) + \cos(\phi_{old})\sin(d)\cos(\theta))\right], \tag{1.11}$$

$$\varphi_{new} = \left[\varphi_{old} + \arctan\left(\frac{\sin(\theta)\sin(d)\cos(\phi_{old})}{\cos(d) - \sin(\phi_{old})\sin(\phi_{new})}\right)\right], \tag{1.12}$$

where ϕ_{new} is the new latitude, φ_{new} is the new longitude, ϕ_{old} is the old latitude, φ_{old} is the old longitude, d is the epicentral distance and θ is the backazimuth. From this new location, the distances and travel times can be recalculated. Figure 1.9 visualises the process of searching over backazimuths and calculating the radial distances as is also shown in Chapter 2.

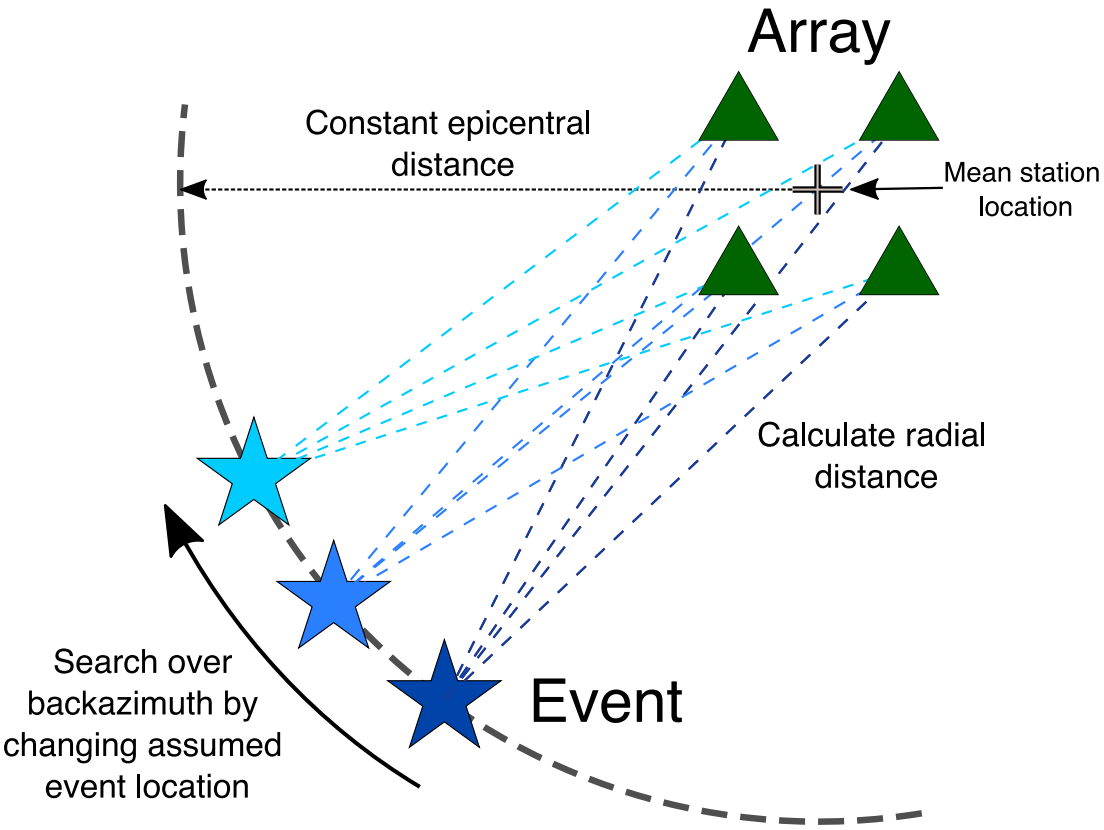

Figure 1.9: Figure 3 in Chapter 2 showing the process of correction for a curved wavefront and how the method searches over different backazimuths.

Rather than assuming the backazimuth is the same at all stations, this curved wavefront correction assumes the backazimuth of the wave at each station is the same as the theoretical backazimuth over a spherical Earth from the relocated point to the station. This accounts for the curved wavefront shape as it travels over an array. To test the correction, I apply the corrected beamforming method on synthetic data arriving from a known backazimuth and horizontal slowness (also shown in the supplementary material for Chapter 2 in Appendix Section A.1). The correction reduces the backazimuth error from 2.37° to 0.40° and the horizontal slowness error from 0.20 s/° to 0.03 s/°. It is still assumed the wave moves over the array with a constant horizontal velocity, which is not true for large arrays and may still account for the very small errors observed in slowness vector measurements observed from synthetic data.

1.2.4.2 Reducing the effect of array geometry

As discussed in Section 1.2.3 the power distribution can be described in the frequency domain as a convolution of the signal power and the array response function (ARF). The array response function describes how the array aperture and station distribution affects the resolution of the signal in the power distribution. As the ARF can be estimated theoretically using the array geometry, the ARF could be deconvolved from the power distribution output from beamforming or f–k analysis to improve the resolution.

I use the Richardson-Lucy (R–L) deconvolution algorithm (Lucy, 1974; Richardson, 1972) to deconvolve the theoretical ARF from the power distributions in Chapter 2 to better identify multipathed and single arrivals. The R–L algorithm restores an image that has been blurred by a known point spread function (psf). For this application, the blurred image is the beamforming power distribution and the point spread function is the ARF. Rather than directly deconvolve the point spread function from the image, which may increase the noise in the image, the R–L algorithm instead estimates what the deblurred image is by finding an image that, when convolved with the psf, is as close to the blurred image as possible. The algorithm assumes the blurred image (G) is described by

$$G = P * D, \tag{1.13}$$

where G is a matrix describing the blurred image, which is produced by the 2-D convolution ($*$) of P, a matrix describing the point spread function, with D, the unblurred image. The iterative deconvolution process is described in the following paragraph.

At each iteration, the algorithm calculates a correction factor matrix C, which is multiplied element-wise with each value in the current iteration's estimate of the unblurred image. If the estimated unblurred image is the same as the true unblurred image, the correction matrix will be filled with ones and the estimate of the unblurred image will not change.

The algorithm first convolves the point spread function matrix (P) with the previous iteration's image estimate matrix (D_{i-1}) as $P * D_{i-1}$. If the deblurred image estimate D_{i-1} is the true deblurred image, the result of this convolution will be the same as the observed image G. To quantify the deviation between the true deblurred image and the image estimate, the original image matrix G is divided element-wise by the output of the previous step as shown by $\frac{G}{P*D_{i-1}}$. To create the correction matrix C, the transpose of the point spread function (P^T) is convolved with the output of the previous step as shown by $P^T * \frac{G}{P*D_{i-1}}$. The correction factor is then multiplied element-wise with the image estimate of the previous iteration (D_{i-1}) to give an updated estimate (D_i) and the algorithm moves on to the next iteration. All of the above steps can be described

by

$$D_i = \alpha D_{i-1}(P^T * \frac{G}{P * D_{i-1}}), \tag{1.14}$$

where D_i is the deblurred image at iteration i, D_{i-1} is the deblurred image of the previous iteration, α is the inverse of the sum of the columns of the point spread matrix P and acts as a normalising vector, P is the point spreading function, P^T is the transpose of the point spreading function, $*$ indicates 2-D convolution, and G is the original observed image.

This technique has been applied to f–k power outputs in previous studies (Maupin, 2011; Picozzi et al., 2010) and I use this to deblur beamforming outputs in Chapter 2. For this application, the original image G is the beamforming output and the point spread function (P) is the ARF. A limitation of the R–L deconvolution technique in this application is the ARF accounts for array geometry, aperture and station spacing but not for the effect of the local geology. Therefore, the ARF may not be the same as the true point spread function which blurs the signal in the power distribution.

Other deconvolution algorithms have been implemented such as the CLEAN-PSF algorithm (for details see Gal et al., 2016) and algorithms which could be implemented such as blind deconvolution where the point spread function is not known to begin with and is updated alongside the deblurred image (Kundur and Hatzinakos, 1996). I do not explore these options further as the R–L deconvolution is satisfactory and improving the resolution further is not necessary or the focus of this work.

1.2.4.3 Reducing incoherent noise

In a linear stack, where seismograms are stacked with no weighting, only the time series of the amplitudes are used to create beams and search for the slowness vector properties. If incoherent noise is present in the traces with large amplitudes, it may, by chance, stack coherently and affect the slowness vector measurement. In this section, I outline methods often employed to reduce the power of incoherent noise and boost the signal of coherent arrivals. Through these processes, low amplitude but coherent arrivals may be identified and the resolution of the arrival of the power distributions are improved.

1.2.4.3.1 F statistic

The F statistic (Blandford, 1974; Frost et al., 2013) has been employed to improve the signal of coherent arrivals and reduce incoherent noise in the power distribution. The F statistic is calculated by dividing the total power of the beam by the total power of

the residual of the beam and the individual traces

$$F_{\theta,p} = (M-1)\frac{M\sum_{t_{disc}=1}^{T} b_{(\theta,p)}(t_{disc})^2}{\sum_{t_{disc}=1}^{T}\sum_{m=1}^{M}[s_{m(\theta,p)}(t_{disc}) - b_{(\theta,p)}(t_{disc})]^2}\,, \tag{1.15}$$

where $F_{\theta,p}$ is the F statistic at a particular backazimuth (θ) and horizontal slowness (p), M is the number of traces that form the beam, $b_{(\theta,p)}(t_{disc})$ is the beam at time t_{disc} (time is a discrete variable here) for a given backazimuth and horizontal slowness and $s_{m(\theta,p)}(t_{disc})$ is trace m at time t_{disc} shifted by the time calculated for a particular backazimuth and horizontal slowness. The F statistic gives a measure of the coherence of the signals in the time widow by measuring the similarity of the amplitude in time after the time shift from beamforming.

The F statistic assumes the signal waveform is the same on each trace and both the signal and noise are assumed to be stationary (their mean amplitude does not change over the time the signal is analysed) and spectrally white, the signal is perfectly correlated and noise completely uncorrelated (Blandford, 1974). The F statistic performs less well in instances where these assumptions are not met such as when the noise is correlated as found when using very small aperture arrays (station spacings of less than a kilometre) (Blandford, 1974), although techniques have been developed to use the F statistic on small arrays (Selby, 2008; Selby, 2011). The apertures of the arrays used in this work are much larger than those where the F statistic is less effective. Other assumptions in the beamforming process may make the signal appear less coherent such as not accounting for a curved wavefront at a large aperture array or from effects of the local geology. This would produce scatter in the time calculations leading to reduced coherence of the signal.

1.2.4.3.2 Phase weighted stacking

The methods described in Section 1.2.2 and 1.2.3 the stacking process is a linear stack where there is no additional weighting of the seismograms when they are summed. By weighting the seismograms or points of the seismograms, the signal-to-noise ratio of the beams can be improved, improving the resolution of the slowness vector power distribution and improving the relative amplitude of low amplitude but coherent arrivals. Phase weighted stacking (Schimmel and Paulssen, 1997) is a non-linear stacking method which weights each point of the linear stack by an amplitude independent measure of coherency described by

$$b_{pws}(t_{disc}) = b(t_{disc})\left|\frac{1}{M}\sum_{m=1}^{M} e^{(i\Phi_m(t_{disc}))}\right|^v\,, \tag{1.16}$$

where $b_{pws}(t_{disc})$ is the phase weighted stack at time t, M is the number of seismograms, $\Phi_m(t_{disc})$ is the mth instantaneous phase at time t_{disc}, $b(t_{disc})$ is the amplitude at time t_{disc} of the linear beam and v is the weighting power. Phase weighted stacking creates a 'phase stack' to weight the linear beam by. If the signal is coherent at a specific time, then the weighting from the phase stack is 1 and incoherent signals have a weighting closer to zero. The power value v in equation 1.16 controls how aggressively the incoherent signals are suppressed.

As phase weighted stacking is a non-linear stacking method, the waveforms are distorted and therefore the resultant phase weighted stack cannot be used for waveform analysis. Phase weighted stacking is very sensitive to the coherency of the wave over the array and therefore if an arrival is only present in some but not all of the traces it can be heavily down-weighted depending on v. Furthermore, the coherency measure means phase weighted stacking is very sensitive to time offsets which can greatly improve the slowness resolution of vespagrams or power distributions. However, errors in the travel time estimates during beamforming from effects of local geology or not correcting for a curved wavefront could offset arrivals in time making them less coherent and phase weighted stacking could erode them such that they are no longer visible.

1.2.4.3.3 Nth-root stacking

Although not used in this thesis, an approach used by some studies discussed later in Section 1.1 to improve the resolution of the vespa process is the Nth-root stack (McFadden et al., 1986). Like the F statistic and phase weighted stacking, Nth-root stacking is a non-linear stacking approach which enhances weak but coherent signals measured across the array. The Nth-root stack takes the Nth-root of each seismogram before creating the beam

$$b'_N(t_{disc}) = \frac{1}{M}\sum_{m=1}^{M}\left|s_m(t_{disc} + \overrightarrow{r_m}\cdot\overrightarrow{k})\right|^{1/N}\frac{s_m(t_{disc})}{|s_m(t_{disc})|}, \tag{1.17}$$

where $b'_N(t_{disc})$ is the temporary beam at time t_{disc}, M is the number of seismograms, $s_m(t_{disc} + \overrightarrow{r_m}\cdot\overrightarrow{k})$ is the time shifted seismogram of some slowness vector $\overrightarrow{k}$ and N is the order of the Nth-root stack. The Nth-root of the absolute amplitude is taken, therefore to retain the sign of the signal at time t_{disc} the Nth-rooted trace is multiplied by $\frac{s_m(t_{disc})}{|s_m(t_{disc})|}$. To create the Nth-root stack, the temporary beam is taken to the power N

$$b_N(t_{disc}) = \left|b'_N(t_{disc})\right|^N\frac{b'_N(t_{disc})}{\left|b'_N(t_{disc})\right|}, \tag{1.18}$$

$b_N(t_{disc})$ is the Nth-root stacked beam and again to retain the sign of the signal at time t_{disc}, the trace is multiplied by $\frac{b'_N(t_{disc})}{\left|b'_N(t_{disc})\right|}$. Taking the Nth-root of the single traces reduces the amplitude variance of the individual traces means the small amplitude but

coherent phases stack to a relatively greater amplitude than in a linear stack. This process puts greater importance on the coherence of the phase than the amplitude leading to more suppressed noise and greater enhancement of signal by reducing the signal amplitude variance. In Nth-root stacking, both the signal and the background noise are attenuated, but the background noise is much more attenuated relative to the signal (McFadden et al., 1986). When using a very high N value, even the signal itself begins to be attenuated, therefore a suitable value for N is essential in this application. The attenuation of the signal deforms the waveforms in the beam, therefore the resultant beams from Nth-root stacking cannot be used for waveform analysis.

1.2.4.4 Wavefield coherence assumption

Standard beamforming procedure assumes waveform coherence across the array or in other words the wavelet of the arriving signal is assumed to be the same across the array. Heterogeneities in the Earth which are sampled by some paths to the array but not all or complex source time functions recorded on a large enough array may result in waveform incoherence which can result in inaccurate measurements (Gibbons et al., 2018; Gibbons et al., 2008). Strategies to address the impacts of this assumption include using spectrogram beamforming (for details see Gibbons, 2014; Gibbons et al., 2008) or using the seismic envelopes, the instantaneous amplitude with the phase information removed (Eaton and Kendall, 2006). Other than the waveform shape, the effect of local geology on the wavefield as it moves across the array may result in scatter of the arrival times and lead to errors in the slowness vector measurement (Gibbons et al., 2018). Currently, there is no way to correct for the local structure without a velocity model of the near array structure. However, blind deconvolution (Kundur and Hatzinakos, 1996) and updating the array response function to better deblur the power distribution may contain some information about what may deform the signal in slowness space that is not included in the theoretical ARF.

Rather than trying to reduce or eliminate the effects of some of these assumptions about the local geology and waveform incoherence, the method presented in Chapter 3 estimates the combined uncertainty of these assumptions. This is because the array in question is bootstrapped (random sampling with replacement, Efron (1992)), therefore if local geology or differences in waveform shape does affect the measurement this will produce some scatter between the samples. The extent of the scatter of slowness vectors then gives the estimate of the uncertainty of the measurement when using all the stations in the array. This is discussed and demonstrated further in Chapter 3 and applied to a large dataset in Chapter 4.

1.3 Rationale of the thesis

The goal of this work is to quantify the effect mantle heterogeneity has on the teleseismic wavefield by using array methods to identify multipathing through slowness vector perturbation and to upscale the process to a global scale. This section outlines the strategy to achieve the goal of the thesis and discuss the reasoning behind decisions such as the choice of seismic phase I use (Section 1.3.2).

1.3.1 Strategy

Before trying to scale up the identification of multipathing and wavefield perturbation on a global scale, I investigate whether it is possible or worthwhile to investigate mantle heterogeneity through array analysis of multipathing and what can be learned from the observations. Chapter 2 investigates the use of array analysis of multipathing by gathering a large dataset of SKS and SKKS arrivals (Figure 1.10) and use beamforming (Section 1.2) to identify multipathing and wavefield perturbation by their slowness vector properties. The dataset samples the African LLVP which has been extensively studied and many studies have observed multipathing in the waveforms (e.g. Ni and Helmberger, 2003a; Ni et al., 2002; Sun and Miller, 2013; Wang and Wen, 2007) giving the best chance to observe and investigate the potential of using array methods with multipathing. This study also served to aid the automation of the process. Analysing the data by visual inspection and labelling the observations with multipathing, single arrival and noise helped to understand challenges such as identifying multipathing over spatial aliasing and misidentifying arrivals as noise.

After gaining an understanding of the process, I then try to automate the process as much as possible to make the analysis of large global datasets feasible. In addition to classifying seismic arrivals, the method in Chapter 3 also estimates the uncertainties of the slowness vector measurements of the arrivals, which typically are not included in slowness vector analysis. The uncertainty estimates account for many of the limitations discussed in Section 1.2.4. These uncertainty estimates allow for the properties such as the location of a structure or the depth of reflectors to have quantifiable uncertainty bounds. Other than SKS multipathing, the method is tested on other data such as PKPdf precursors and surface waves to show the parameters I find do generalise to other seismic arrivals. Challenges remain to reduce the misclassification of noise as an arrival and improvements to the method are discussed in Chapter 5.

Armed with this new method to automatically identify multipathed arrivals, I take the large dataset of SKS waveforms from Thorne et al. (2020) and apply the method and make global-scale observations of SKS multipathing. This final study essentially has started the journey towards global coverage of multipathing and slowness vector perturbation which can be used to infer locations, velocity perturbations and velocity

gradients of heterogeneities as well as make global scale interpretations of the frequency dependence of multipathing and wavefield perturbation. In Chapter 4, the process to make global-scale observations of SKS multipathing is outlined in more detail and basic interpretation are made to suggest possible causes of the observations. Even with simple statistical methods and smoothing the observations by binning, several structures found by comparing with findings from other approaches are visible. This motivates further study of what properties are capable of producing such observations and expanding the dataset to cover even more of the Earth.

1.3.2 Seismic phase choice

For all projects, I have used SKS and SKKS (Figure 1.10). I choose SKS because of the nearly vertical path it takes through the mantle after leaving the core. Having the wave exit the core at a near-vertical angle gives a greater chance for the wave to sample a vertically orientated lateral velocity gradient from structures such as mantle plumes or LLVPs for longer. Therefore, the velocity gradients of these structures can perturb the wavefield more and it is more likely to detect multipathing and the effects of diffraction. I collected a large dataset of over 2000 SKS and SKKS arrivals over several frequency bands to analyse in Chapter 2 of this thesis. I use this dataset of human-analysed observations to tune the method developed to automate the identification of multipathing and measurement of slowness vector properties in Chapter 3. Given the advantages of SKS described earlier, we then use an already collected global dataset of SKS waveforms from Thorne et al. (2020) to apply this method and begin to create a global map of multipathing and slowness vector deviations.

While using SKS has some advantages and I argue it is the best-suited phase to probe the lower and mid mantle for heterogeneity, there are some challenges to be noted. SKS is sensitive to some source side structure, but the extent of the perturbation remains to be fully explored and I argue large slowness vector deviations are unlikely to be caused by source side structure only because of the very large spatial deviation of the pierce points on the source side needed for a wave to arrive with the observed slowness vector properties. However, smaller slowness vector deviations may be caused by source side structure and this deviation will change the path taken on the receiver side.

1.3.3 Contribution and novelty

Each chapter of this thesis contributes to scientific knowledge differently. Chapter 2 demonstrates multipathed arrivals can be observed by their different slowness vector properties and slowness vector measurements of SKS waves alone can give real insight into the location, morphology and velocity gradient of LLVP boundaries. Forward modelling in the chapter uses the finite frequency code SPECFEM3D_Globe (Komatitsch

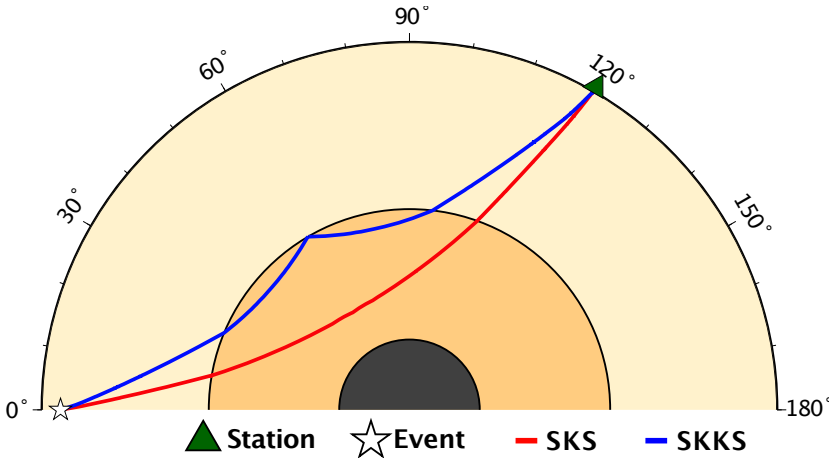

Figure 1.10: Ray paths of SKS (red) and SKKS (blue) from source (white star) to receiver (green triangle).

and Tromp, 2002a; Komatitsch and Tromp, 2002b) to model a full wavefield rather than ray tracing or coupled Earth mode–spectral element method approximations (Capdeville et al., 2003a; Capdeville et al., 2003b; Helmberger and Ni, 2005; Ni et al., 2000) to find lateral velocity gradients an order of magnitude lower than the strong gradients reported by Ni et al. (2002). In addition to suggesting LLVPs may have weaker velocity gradients than thought for the past 20 years or so, this also motivates a comparison between ray-tracing methods and finite frequency modelling to determine whether the inferred velocity gradients of the methods differ.

The implications of Chapter 3 come from providing the first method, to my knowledge, which both automatically identifies multiple arrivals in slowness space and gives the slowness vector measurements of those arrivals uncertainty estimates. The method makes global-scale measurements of slowness vector properties of seismic arrivals and identification of multipathing more feasible. Furthermore, the method allows uncertainty bounds on the location of structures such as the depth of a reflector or the location of scattering in the lower mantle. Even with applications on a smaller scale, knowing the uncertainty of the slowness vector measurement can allow the user to discriminate between measurements and determine which should be interpreted.

Finally, the novelty and contribution of the work in Chapter 4 is a global scale investigation locating mantle heterogeneities by their velocity gradients, which has not previously been conducted. The results of the study can already be used to identify several mantle heterogeneities in densely sampled regions unresolvable to global or regional tomographic studies. From this dataset, work can be done to expand the observations using phases such as Sdiff and ScS to get greater global coverage and can be used to compare the results of geodynamic studies as well as in tomographic studies. Furthermore, studies using forward modelling to quantify what velocity gradi-

ents, perturbations and height are needed to observe multipathing and slowness vector magnitudes now have a large number of observations to use for comparison. This multi-regional study shows each of the heterogeneities has unique characteristics in terms of the slowness vector pattern, magnitude and multipathing observations. These differing observations between heterogeneities show the value of these measurements to constrain the unique properties such as the geometry, velocity gradient magnitude and velocity perturbation of the structures. Having a global dataset of lateral velocity gradient properties can then be used to infer the differing thermal and chemical properties of the heterogeneities which then feed into inferences of their age and origin.

Overall the contribution of this work is to demonstrate the value of analysing the slowness vector properties of multipathing, developed an automated to identify multipathing and make slowness vector deviation measurements and applied the method to create large scale observations of mantle heterogeneities to improve our understanding of mantle structure and further constrain Earth's mantle dynamics.

References

Aki, K., & Richards, P. G. (2002). *Quantitative seismology.*

Bentham, H. L. M., & Rost, S. (2014). Scattering beneath Western Pacific subduction zones: Evidence for oceanic crust in the mid-mantle. *Geophysical Journal International*, *197*(3), 1627–1641.

Blandford, R. R. (1974). An automatic event detector at the Tonto Forest seismic observatory. *Geophysics*, *39*(5), 633–643.

Bréger, L., & Romanowicz, B. (1998). Three-dimensional structure at the base of the mantle beneath the central Pacific. *Science*, *282*(5389), 718–720.

Buffett, B. A., Garnero, E. J., & Jeanloz, R. (2000). Sediments at the top of Earth's core. *Science*, *290*(5495), 1338–1342.

Bull, A. L., McNamara, A. K., & Ritsema, J. (2009). Synthetic tomography of plume clusters and thermochemical piles. *Earth and Planetary Science Letters*, *278*(3), 152–162.

Bull, A., McNamara, A., Becker, T., & Ritsema, J. (2010). Global scale models of the mantle flow field predicted by synthetic tomography models. *Physics of the Earth and Planetary Interiors*, *182*(3-4), 129–138.

Cao, A., & Romanowicz, B. (2007). Locating scatterers in the mantle using array analysis of PKP precursors from an earthquake doublet. *Earth and Planetary Science Letters*, *255*(1), 22–31.

Capdeville, Y., To, A., & Romanowicz, B. (2003a). Coupling spectral elements and modes in a spherical Earth: an extension to the 'sandwich'case. *Geophysical Journal International*, *154*(1), 44–57.

Capdeville, Y., Chaljub, E., & Montagner, J. P. (2003b). Coupling the spectral element method with a modal solution for elastic wave propagation in global earth models. *Geophysical Journal International*, *152*(1), 34–67.

Capon, J. (1969). High-resolution frequency-wavenumber spectrum analysis. *Proceedings of the IEEE*, *57*(8), 1408–1418.

Cottaar, S., & Romanowicz, B. (2012). An unsually large ULVZ at the base of the mantle near Hawaii. *Earth and Planetary Science Letters*, *355-356*, 213–222.

Davies, D., Kelly, E. J., & Filson, J. R. (1971). Vespa Process for Analysis of Seismic Signals. *Nature Physical Science*, *232*(27), 8–13.

Davies, D. R., Goes, S., Davies, J., Schuberth, B., Bunge, H.-P., & Ritsema, J. (2012). Reconciling dynamic and seismic models of Earth's lower mantle: The dominant role of thermal heterogeneity. *Earth and Planetary Science Letters*, *353*, 253–269.

Day, E. A., & Deuss, A. (2013). Reconciling PP and P′P′ precursor observations of a complex 660km seismic discontinuity. *Geophysical Journal International*, *194*(2), 834–838.

Dziewonski, A. M., & Anderson, D. L. (1981). Preliminary reference Earth model. *Physics of the earth and planetary interiors*, *25*(4), 297–356.

Dziewonski, A. M., Hager, B. H., & O'Connell, R. J. (1977). Large-scale heterogeneities in the lower mantle. *Journal of Geophysical Research*, *82*(2), 239–255.

Eaton, D. W., & Kendall, J.-M. (2006). Improving seismic resolution of outermost core structure by multichannel analysis and deconvolution of broadband SmKS phases. *Physics of the Earth and Planetary Interiors*, *155*(1), 104–119.

Efron, B. (1992). Bootstrap Methods: Another Look at the Jackknife. In S. Kotz & N. L. Johnson (Eds.), *Breakthroughs in Statistics: Methodology and Distribution* (pp. 569–593). Springer.

Ford, S. R., Garnero, E. J., & McNamara, A. K. (2006). A strong lateral shear velocity gradient and anisotropy heterogeneity in the lowermost mantle beneath the southern Pacific. *Journal of Geophysical Research: Solid Earth*, *111*(B3).

French, S. W., & Romanowicz, B. (2015). Broad plumes rooted at the base of the Earth's mantle beneath major hotspots. *Nature*, *525*(7567), 95–99.

French, S., & Romanowicz, B. (2014). Whole-mantle radially anisotropic shear velocity structure from spectral-element waveform tomography. *Geophysical Journal International*, *199*(3), 1303–1327.

Frost, D. A., Rost, S., Selby, N. D., & Stuart, G. W. (2013). Detection of a tall ridge at the coreâmantle boundary from scattered PKP energy. *Geophysical Journal International*, *195*(1), 558–574.

Fukao, Y., & Obayashi, M. (2013). Subducted slabs stagnant above, penetrating through, and trapped below the 660 km discontinuity. *Journal of Geophysical Research: Solid Earth*, *118*(11), 5920–5938.

Gal, M., Reading, A., Ellingsen, S., Koper, K., Burlacu, R., & Gibbons, S. (2016). Deconvolution enhanced direction of arrival estimation using one- and three-component seismic arrays applied to ocean induced microseisms. *Geophysical Journal International*, *206*(1), 345–359.

Garnero, E. J., & Helmberger, D. V. (1996). Seismic detection of a thin laterally varying boundary layer at the base of the mantle beneath the central-Pacific. *Geophysical Research Letters*, *23*(9), 977–980.

Garnero, E. J., McNamara, A. K., & Shim, S.-H. (2016). Continent-sized anomalous zones with low seismic velocity at the base of Earth's mantle. *Nature Geoscience*, *9*(7), 481–489.

Garnero, E. J., Revenaugh, J., Williams, Q., Lay, T., & Kellogg, L. H. (1998). Ultralow velocity zone at the core-mantle boundary. *The core-mantle boundary region*, *28*, 319–334.

Gibbons, S. J. (2014). The Applicability of Incoherent Array Processing to IMS Seismic Arrays. *Pure and Applied Geophysics*, *171*(3), 377–394.

Gibbons, S. J., Näsholm, S., Ruigrok, E., & Kværna, T. (2018). Improving slowness estimate stability and visualization using limited sensor pair correlation on seismic arrays. *Geophysical Journal International*, *213*(1), 447–460.

Gibbons, S. J., Ringdal, F., & KvÃŠrna, T. (2008). Detection and characterization of seismic phases using continuous spectral estimation on incoherent and partially coherent arrays. *Geophysical Journal International*, *172*(1), 405–421.

Haddon, R. A. W., & Cleary, J. R. (1974). Evidence for scattering of seismic PKP waves near the mantle-core boundary. *Physics of the Earth and Planetary Interiors*, *8*(3), 211–234.

Haddon, R. a. W., Hide, R., Osmaston, M. F., Runcorn, S. K., Creer, K. M., & Jacobs, J. A. (1982). Evidence for inhomogeneities near the core-mantle boundary. *Philosophical Transactions of the Royal Society of London. Series A, Mathematical and Physical Sciences*, *306*(1492), 61–70.

Harjes, H., & Henger, M. (1973). Array-seismologie. *Zeitschrift fÃŒr Geophysik*, *39*, 865–905.

He, Y., & Wen, L. (2012). Geographic boundary of the âPacific Anomalyâ and its geometry and transitional structure in the north. *Journal of Geophysical Research: Solid Earth*, *117*(B9).

He, Y., Wen, L., & Zheng, T. (2006). Geographic boundary and shear wave velocity structure of the âPacific anomalyâ near the coreâmantle boundary beneath western Pacific. *Earth and Planetary Science Letters*, *244*(1), 302–314.

Helmberger, D. V., & Ni, S. (2005). Approximate 3D Body-Wave Synthetics for Tomographic Models. *Bulletin of the Seismological Society of America*, *95*(1), 212–224.

Hinich, M. J. (1981). Frequency-wavenumber array processing. *The Journal of the Acoustical Society of America*, *69*(3), 732–737.

Idehara, K. (2011). Structural heterogeneity of an ultra-low-velocity zone beneath the philippine islands: Implications for core–mantle chemical interactions induced by massive partial melting at the bottom of the mantle. *Physics of the Earth and Planetary Interiors*, *184*(1-2), 80–90.

Ishii, M., & Tromp, J. (1999). Normal-Mode and Free-Air Gravity Constraints on Lateral Variations in Velocity and Density of Earth's Mantle. *Science*, *285*(5431), 1231–1236.

Kito, T., Rost, S., Thomas, C., & Garnero, E. J. (2007). New insights into the P- and S-wave velocity structure of the Dâ³ discontinuity beneath the Cocos plate. *Geophysical Journal International*, *169*(2), 631–645.

Koelemeijer, P., Ritsema, J., Deuss, A., & Van Heijst, H.-J. (2015). SP12RTS: A degree-12 model of shear-and compressional-wave velocity for Earth's mantle. *Geophysical Journal International*, *204*(2), 1024–1039.

Koelemeijer, P., Deuss, A., & Ritsema, J. (2017). Density structure of Earth's lowermost mantle from Stoneley mode splitting observations. *Nature Communications*, *8*.

Komatitsch, D., & Tromp, J. (2002a). Spectral-element simulations of global seismic wave propagationâI. Validation. *Geophysical Journal International*, *149*(2), 390–412.

Komatitsch, D., & Tromp, J. (2002b). Spectral-element simulations of global seismic wave propagationâII. Three-dimensional models, oceans, rotation and self-gravitation. *Geophysical Journal International*, *150*(1), 303–318.

Koppers, A. A. P., Becker, T. W., Jackson, M. G., Konrad, K., MÃŒller, R. D., Romanowicz, B., Steinberger, B., & Whittaker, J. M. (2021). Mantle plumes and their role in Earth processes. *Nature Reviews Earth & Environment*, 1–20.

Kundur, D., & Hatzinakos, D. (1996). Blind image deconvolution. *IEEE Signal Processing Magazine*, *13*(3), 43–64.

Lau, H. C. P., Mitrovica, J. X., Davis, J. L., Tromp, J., Yang, H.-Y., & Al-Attar, D. (2017). Tidal tomography constrains Earthâs deep-mantle buoyancy. *Nature*, *551*(7680), 321–326.

Lay, T. (2007). Deep earth structure-lower mantle and D. *Seismology and Structure of the Earth*, 619–654.

Lessing, S., Thomas, C., Rost, S., Cobden, L., & Dobson, D. P. (2014). Mantle transition zone structure beneath India and Western China from migration of PP and SS precursors. *Geophysical Journal International*, *197*(1), 396–413.

Li, M., McNamara, A. K., & Garnero, E. J. (2014). Chemical complexity of hotspots caused by cycling oceanic crust through mantle reservoirs. *Nature Geoscience*, *7*(5), 366–370.

Liu, J., Li, J., Hrubiak, R., & Smith, J. S. (2016). Origins of ultralow velocity zones through slab-derived metallic melt. *Proceedings of the National Academy of Sciences*, *113*(20), 5547–5551.

Lu, C., Grand, S. P., Lai, H., & Garnero, E. J. (2019). TX2019slab: A New P and S Tomography Model Incorporating Subducting Slabs. *Journal of Geophysical Research: Solid Earth*, *124*(11), 11549–11567.

Lucy, L. B. (1974). An iterative technique for the rectification of observed distributions. *The Astronomical Journal*, *79*, 745.

Ma, X., Sun, X., & Thomas, C. (2019). Localized ultra-low velocity zones at the eastern boundary of Pacific LLSVP. *Earth and Planetary Science Letters*, *507*, 40–49.

Ma, X., & Thomas, C. (2020). Small-Scale Scattering Heterogeneities in the Lowermost Mantle From a Global Analysis of PKP Precursors. *Journal of Geophysical Research: Solid Earth*, *125*(3), e2019JB018736
e2019JB018736 2019JB018736.

Mao, W. L., Mao, H.-k., Sturhahn, W., Zhao, J., Prakapenka, V. B., Meng, Y., Shu, J., Fei, Y., & Hemley, R. J. (2006). Iron-rich post-perovskite and the origin of ultralow-velocity zones. *Science*, *312*(5773), 564–565.

Mao, W. L., Meng, Y., Shen, G., Prakapenka, V. B., Campbell, A. J., Heinz, D. L., Shu, J., Caracas, R., Cohen, R. E., Fei, Y. et al. (2005). Iron-rich silicates in the Earth's D" layer. *Proceedings of the National Academy of Sciences*, *102*(28), 9751–9753.

Masters, G., Laske, G., Bolton, H., & Dziewonski, A. (2000). The relative behavior of shear velocity, bulk sound speed, and compressional velocity in the mantle: Implications for chemical and thermal structure. *Earth's deep interior: mineral physics and tomography from the atomic to the global scale*, 63–87.

Maupin, V. (2011). Upper-mantle structure in southern Norway from beamforming of Rayleigh wave data presenting multipathing. *Geophysical Journal International*, *185*(2), 985–1002.

McFadden, P. L., Drummond, B. J., & Kravis, S. (1986). The Nthâroot stack: Theory, applications, and examples. *GEOPHYSICS*, *51*(10), 1879–1892.

McNamara, A. K. (2019). A review of large low shear velocity provinces and ultra low velocity zones. *Tectonophysics*, *760*, 199–220.

McNamara, A. K., Garnero, E. J., & Rost, S. (2010). Tracking deep mantle reservoirs with ultra-low velocity zones. *Earth and Planetary Science Letters*, *299*(1), 1–9.

Ni, S., Ding, X., & Helmberger, D. V. (2000). Constructing synthetics from deep earth tomographic models. *Geophysical Journal International*, *140*(1), 71–82.

Ni, S., & Helmberger, D. V. (2003a). Further constraints on the African superplume structure. *Physics of the Earth and Planetary Interiors*, *140*(1-3), 243–251.

Ni, S., & Helmberger, D. V. (2003b). Ridge-like lower mantle structure beneath south Africa. *Journal of Geophysical Research: Solid Earth*, *108*(B2).

Ni, S., Tan, E., Gurnis, M., & Helmberger, D. (2002). Sharp sides to the African superplume. *Science*, *296*(5574), 1850–1852.

Ni, S., V. Helmberger, D., & Tromp, J. (2005). Three-dimensional structure of the African superplume from waveform modelling. *Geophysical Journal International*, *161*(2), 283–294.

Picozzi, M., Parolai, S., & Bindi, D. (2010). Deblurring of frequencyâwavenumber images from small-scale seismic arrays. *Geophysical Journal International*, *181*(1), 357–368.

Revenaugh, J., & Meyer, R. (1997). Seismic Evidence of Partial Melt Within a Possibly Ubiquitous Low-Velocity Layer at the Base of the Mantle. *Science*, *277*(5326), 670–673.

Richards, F., Hoggard, M., Ghelichkhan, S., Koelemeijer, P., & Lau, H. (2021). Geodynamic, geodetic, and seismic constraints favour deflated and dense-cored llvps.

Richardson, W. H. (1972). Bayesian-Based Iterative Method of Image Restoration*. *Journal of the Optical Society of America*, *62*(1), 55.

Rickers, F., Fichtner, A., & Trampert, J. (2013). The IcelandâJan Mayen plume system and its impact on mantle dynamics in the North Atlantic region: Evidence from full-waveform inversion. *Earth and Planetary Science Letters*, *367*, 39–51.

Ritsema, J., Deuss, a. A., Van Heijst, H., & Woodhouse, J. (2011). S40RTS: A degree-40 shear-velocity model for the mantle from new Rayleigh wave dispersion, teleseismic traveltime and normal-mode splitting function measurements. *Geophysical Journal International*, *184*(3), 1223–1236.

Ritsema, J., Garnero, E., & Lay, T. (1997). A strongly negative shear velocity gradient and lateral variability in the lowermost mantle beneath the Pacific. *Journal of Geophysical Research: Solid Earth*, *102*(B9), 20395–20411.

Ritsema, J., Kaneshima, S., & Haugland, S. M. (2020). The dimensions of scatterers in the lower mantle using USArray recordings of S-wave to P-wave conversions. *Physics of the Earth and Planetary Interiors*, *306*, 106541.

Ritsema, J., McNamara, A. K., & Bull, A. L. (2007). Tomographic filtering of geodynamic models: Implications for model interpretation and large-scale mantle structure. *Journal of Geophysical Research*, *112*(B1).

Rondenay, S., & Fischer, K. M. (2003). Constraints on localized core-mantle boundary structure from multichannel, broadband SKS coda analysis. *Journal of Geophysical Research: Solid Earth*, *108*(B11).

Rost, S., & Earle, P. S. (2010). Identifying regions of strong scattering at the coreâmantle boundary from analysis of PKKP precursor energy. *Earth and Planetary Science Letters*, *297*(3), 616–626.

Rost, S., & Garnero, E. J. (2006). Detection of an ultralow velocity zone at the core-mantle boundary using diffracted PKKPab waves. *Journal of Geophysical Research: Solid Earth*, *111*(B7).

Rost, S., Garnero, E. J., & Williams, Q. (2008). Seismic array detection of subducted oceanic crust in the lower mantle. *Journal of Geophysical Research: Solid Earth*, *113*(B6).

Rost, S., Garnero, E. J., Williams, Q., & Manga, M. (2005). Seismological constraints on a possible plume root at the coreâmantle boundary. *Nature*, *435*(7042), 666.

Rost, S., & Thomas, C. (2002). Array seismology: Methods and applications. *Reviews of geophysics*, *40*(3).

Rost, S., & Thomas, C. (2009). Improving Seismic Resolution Through Array Processing Techniques. *Surveys in Geophysics*, *30*(4-5), 271–299.

Ruigrok, E., Gibbons, S., & Wapenaar, K. (2017). Cross-correlation beamforming. *Journal of Seismology*, *21*(3), 495–508.

Schimmel, M., & Paulssen, H. (1997). Noise reduction and detection of weak, coherent signals through phase-weighted stacks. *Geophysical Journal International*, *130*(2), 497–505.

Schuberth, B., Bunge, H.-P., & Ritsema, J. (2009). Tomographic filtering of high-resolution mantle circulation models: Can seismic heterogeneity be explained by temperature alone? *Geochemistry, Geophysics, Geosystems*, *10*(5).

Schumacher, L., & Thomas, C. (2016). Detecting lower-mantle slabs beneath Asia and the Aleutians. *Geophysical Journal International*, *205*(3), 1512–1524.

Schumacher, L., Thomas, C., & Abreu, R. (2018). Out-of-Plane Seismic Reflections Beneath the Pacific and Their Geophysical Implications. *Journal of Geophysical Research: Solid Earth*, *123*(3), 2286–2302.

Selby, N. D. (2008). Application of a generalized F detector at a seismometer array. *Bulletin of the Seismological Society of America*, *98*(5), 2469–2481.

Selby, N. D. (2011). Improved Teleseismic Signal Detection at Small-Aperture Arrays. *Bulletin of the Seismological Society of America*, *101*(4), 1563–1575.

Silver, P. G., & Chan, W. W. (1986). Observations of body wave multipathing from broadband seismograms: Evidence for lower mantle slab penetration beneath the Sea of Okhotsk. *Journal of Geophysical Research: Solid Earth*, *91*(B14), 13787–13802.

Simmons, N. A., Forte, A. M., Boschi, L., & Grand, S. P. (2010). GyPSuM: A joint tomographic model of mantle density and seismic wave speeds. *Journal of Geophysical Research: Solid Earth*, *115*(B12).

Simon, J. D., Simons, F. J., & Irving, J. C. (2021). A mermaid miscellany: Seismoacoustic signals beyond the p wave. *Seismological Research Letters*.

Stern, R. (2007). When and how did plate tectonics begin? Theoretical and empirical considerations. *Chinese Science Bulletin*, *52*(5), 578–591.

Stockmann, F., Cobden, L., Deschamps, F., Fichtner, A., & Thomas, C. (2019). Investigating the seismic structure and visibility of dynamic plume models with

seismic array methods. *Geophysical Journal International*, *219*(Supplement_1), S167–S194.

Sun, D., Helmberger, D., Lai, V. H., Gurnis, M., Jackson, J. M., & Yang, H.-Y. (2019). Slab Control on the Northeastern Edge of the Mid-Pacific LLSVP Near Hawaii. *Geophysical Research Letters*, *46*(6), 3142–3152.

Sun, D., Gurnis, M., Saleeby, J., & Helmberger, D. (2017). A dipping, thick segment of the Farallon Slab beneath central U.S. *Journal of Geophysical Research: Solid Earth*, *122*(4), 2911–2928.

Sun, D., Helmberger, D., & Gurnis, M. (2010). A narrow, mid-mantle plume below southern Africa. *Geophysical Research Letters*, *37*(9).

Sun, D., Helmberger, D., Ni, S., & Bower, D. (2009). Direct measures of lateral velocity variation in the deep Earth. *Journal of Geophysical Research: Solid Earth*, *114*(B5).

Sun, D., & Miller, M. S. (2013). Study of the western edge of the African Large Low Shear Velocity Province. *Geochemistry, Geophysics, Geosystems*, *14*(8), 3109–3125.

Sun, D., Tan, E., Helmberger, D., & Gurnis, M. (2007). Seismological support for the metastable superplume model, sharp features, and phase changes within the lower mantle. *Proceedings of the National Academy of Sciences*, *104*(22), 9151–9155.

Thorne, M. S., & Garnero, E. J. (2004). Inferences on ultralow-velocity zone structure from a global analysis of spdks waves. *Journal of Geophysical Research: Solid Earth*, *109*(B8).

Thorne, M. S., Garnero, E. J., Jahnke, G., Igel, H., & McNamara, A. K. (2013). Mega ultra low velocity zone and mantle flow. *Earth and Planetary Science Letters*, *364*, 59–67.

Thorne, M. S., Leng, K., Pachhai, S., Rost, S., Wicks, J., & Nissen-Meyer, T. (2021). The Most Parsimonious Ultralow-Velocity Zone Distribution From Highly Anomalous SPdKS Waveforms. *Geochemistry, Geophysics, Geosystems*, *22*(1), e2020GC009467 e2020GC009467 2020GC009467.

Thorne, M. S., Pachhai, S., Leng, K., Wicks, J. K., & Nissen-Meyer, T. (2020). New Candidate Ultralow-Velocity Zone Locations from Highly Anomalous SPdKS Waveforms. *Minerals*, *10*(3), 211.

Thorne, M. S., Takeuchi, N., & Shiomi, K. (2019). Melting at the Edge of a Slab in the Deepest Mantle. *Geophysical Research Letters*, *46*(14), 8000–8008.

Trampert, J., Deschamps, F., Resovsky, J., & Yuen, D. (2004). Probabilistic tomography maps chemical heterogeneities throughout the lower mantle. *Science*, *306*(5697), 853–856.

Trønnes, R. G. (2010). Structure, mineralogy and dynamics of the lowermost mantle. *Mineralogy and Petrology*, *99*(3-4), 243–261.

Wang, Y., & Wen, L. (2004). Mapping the geometry and geographic distribution of a very low velocity province at the base of the Earth's mantle. *Journal of Geophysical Research: Solid Earth*, *109*(B10).

Wang, Y., & Wen, L. (2007). Geometry and P and S velocity structure of the "African Anomaly". *Journal of Geophysical Research: Solid Earth*, *112*(B5).

Ward, J., Nowacki, A., & Rost, S. (2020). Lateral Velocity Gradients in the African Lower Mantle Inferred From Slowness Space Observations of Multipathing. *Geochemistry, Geophysics, Geosystems*, *21*(8), e2020GC009025 e2020GC009025 10.1029/2020GC009025.

Waszek, L., Schmerr, N. C., & Ballmer, M. D. (2018). Global observations of reflectors in the mid-mantle with implications for mantle structure and dynamics. *Nature Communications*, *9*(1), 385.

Wen, L. (2001). Seismic evidence for a rapidly varying compositional anomaly at the base of the Earthâs mantle beneath the Indian Ocean. *Earth and Planetary Science Letters*, *194*(1), 83–95.

Wicks, J. K., Jackson, J. M., Sturhahn, W., & Zhang, D. (2017). Sound velocity and density of magnesiowüstites: Implications for ultralow-velocity zone topography. *Geophysical Research Letters*, *44*(5), 2148–2158.

Xu, Y., & Koper, K. D. (2009). Detection of a ULVZ at the base of the mantle beneath the northwest Pacific. *Geophysical Research Letters*, *36*(17).

Yu, S., & Garnero, E. J. (2018). Ultralow velocity zone locations: A global assessment. *Geochemistry, Geophysics, Geosystems*, *19*(2), 396–414.

Zhao, L., Paul, A., Guillot, S., Solarino, S., Malusa, M. G., Zheng, T., Aubert, C., Salimbeni, S., Dumont, T., Schwartz, S., Zhu, R., & Wang, Q. (2015). First seismic evidence for continental subduction beneath the Western Alps. *Geology*, *43*(9), 815–818.

Chapter 2

Lateral Velocity Gradients in the African Lower Mantle Inferred from Slowness Space Observations of Multipathing

Abstract

Large Low-Velocity Provinces (LLVPs) are hypothesised to be purely thermal features or possess some chemical heterogeneity, but exactly which remains ambiguous. Regional seismology studies typically use travel time residuals and multipathing identification in the waveforms to infer properties of LLVPs. These studies have not fully analysed all available information such as measuring the direction and inclination of the arrivals. These measurements would provide more constraints of LLVP properties such as the boundary velocity gradient and help determine their nature. Here, we use array seismology to measure backazimuth (direction) and horizontal slowness (inclination) of arriving waves to identify structures causing multipathing and wavefield perturbation. Following this, we use full-wavefield forward modelling to estimate the gradients required to produce the observed multipathing. We use SKS and SKKS data from 83 events sampling the African LLVP, which has been extensively studied providing a good comparison to our observations. We find evidence for structures at heights of up to 600 km above the core-mantle boundary causing multipathing and wavefield perturbation. Forward modelling shows gradients of up to 0.7% δV_s per 100 km (0.0005 km s^{-1} km^{-1}) can produce multipathing with similar backazimuth and horizontal slowness to our observations. This is an order of magnitude lower than the previous strongest estimates of -3% δV_s per 50 km (0.0044 kms^{-1} km^{-1}). As this is lower than found

for both thermal and thermochemical structures, lateral velocity gradients capable of producing multipathing are not necessarily evidence for a thermochemical nature.

Plain Language Summary

Of the structures observed within the Earth, 'Large Low-Velocity Provinces' (LLVPs) have remained enigmatic in terms of their composition and origin. LLVPs have been hypothesised to affect the Earth from surface uplift to the magnetic field. Determining what LLVPs are remains a major question for those studying Earth structure.

Previous seismology studies analysing LLVPs used the time taken for the wave to travel from the earthquake to the recording station and what the seismic signals look like when they arrive. However, properties such as the direction and speed at which the waves arrive are not analysed in detail. The speed and direction of the waves can inform us about how LLVPs have perturbed the waves by phenomena such as refraction.

This study measures the direction and speed of the arriving waves that have sampled the LLVP beneath Africa. Analysing this information has lead to several structures to be identified. From modelling the full wavefield with different LLVP models, we estimate the distance over which the transition from the mantle to the LLVP happens. To replicate our observed changes in the direction and speed of the waves, the transition could be an order of magnitude larger than previous estimates.

2.1 Introduction

Large Low-Velocity Provinces (LLVPs) are roughly antipodal, low-velocity features of the lower mantle located beneath Africa and the Pacific and are surrounded by high-velocity material hypothesised to be slab remnants (Bijwaard et al., 1998; Grand et al., 1997; Grand, 2002), shown in Figure 2.1. Since first observed, LLVPs have remained enigmatic features of the lower mantle with their origin, composition and therefore their influence remaining uncertain.

The location of the LLVPs relative to other structures and phenomena such as surface uplift (Bull et al., 2010; Hager et al., 1985; Lithgow-Bertelloni and Silver, 1998), possible subducted slab remnants (Hager, 1984), mantle plumes (Davies et al., 2015b; Thorne et al., 2004), large igneous provinces (Torsvik et al., 2010), Ultra Low Velocity Zones (McNamara et al., 2010) and outer core stratification (Mound et al., 2019) suggests LLVPs are influential on whole Earth dynamics. Despite being very significant for our understanding of global dynamics, many properties of the LLVPs are still unknown and there are several hypotheses of their origin. These hypotheses can be approximately split into those where LLVPs are purely thermal features and those in which they are chemically distinct relative to the surrounding mantle (Garnero et al.,

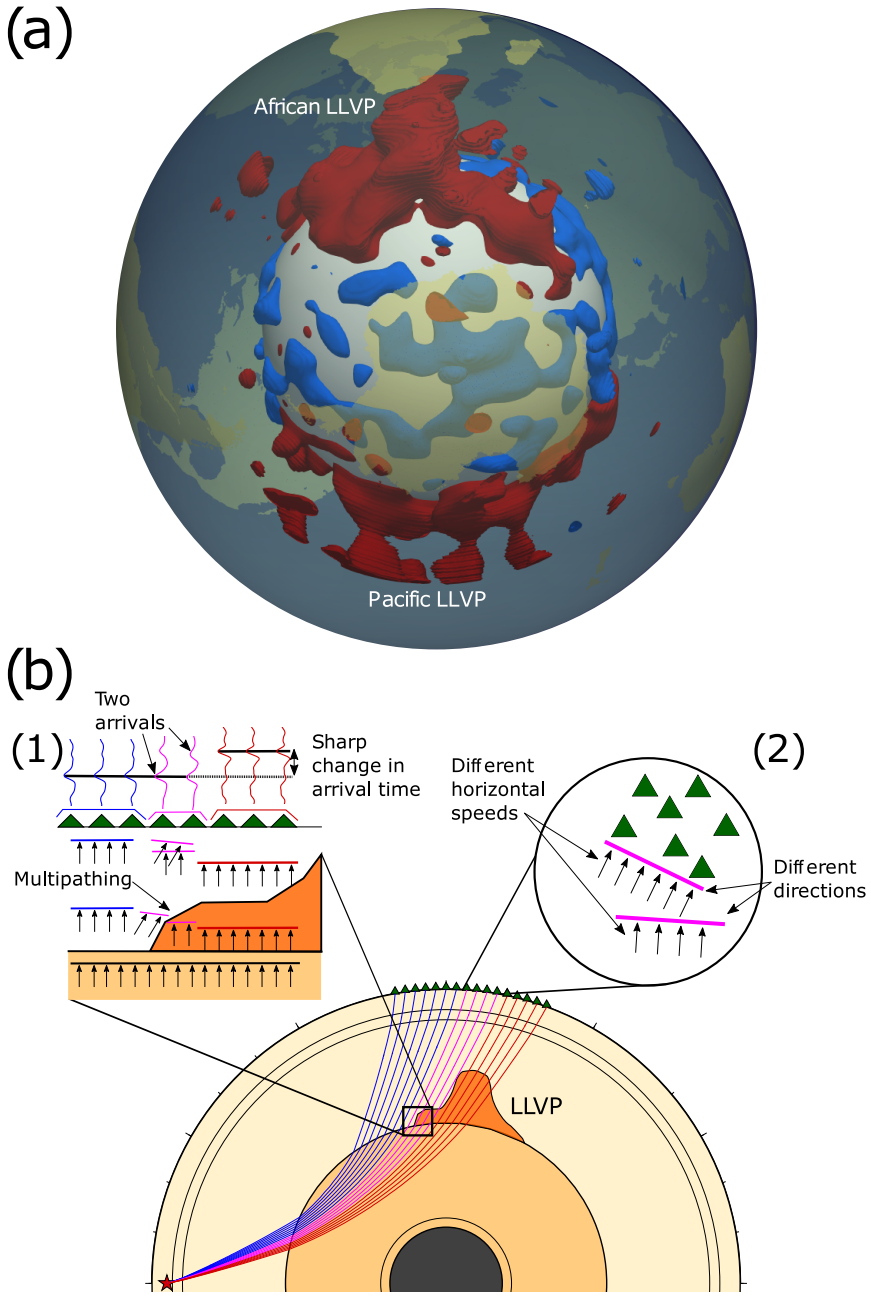

Figure 2.1: **(a)** 3D map of tomography model SEMUCB-WM1 (French and Romanowicz, 2014) with an isosurface of -1% δV_s shown in red and an isosurface of $+1\%$ δV_s in blue. The isosurface is plotted below 80% of the Earth's radius (5097 km, 2205 km above the CMB). **(b)** Multipathing at LLVP boundaries. As the wavefront moves over a strong lateral velocity gradient, different parts travel at different speeds and arrive at the stations at different times as two distinct arrivals **(1)**. The gradients can cause the wave to diffract and the structure can cause the wave to refract as it passes through it. As a result, multipathed arrivals can arrive from different directions and inclinations **(2)**.

2016). For a purely thermal feature, a common hypothesis is that LLVPs are a cluster of plumes (Schubert et al., 2004) which appear as one large slow feature because of the inherent resolution limitations from seismic tomography (Bull et al., 2009; Davies et al., 2015a; Davies et al., 2012; Ritsema et al., 2007). The thermochemical origin hypothesis requires a source of material chemically unique to the current lower mantle either from the primordial Earth or material that has accumulated over geological time. Material from the primordial Earth is hypothesised to start as a basal layer of material that is swept into piles forming the LLVPs. Mechanisms for the origin of this base layer include a basal magma ocean (Labrosse et al., 2007), accumulation of dense melts (Lee et al., 2010) or an ancient, iron-enriched crust which was then subducted and is stable at CMB conditions (Tolstikhin and Hofmann, 2005). This basal layer could then have been swept into piles observed as LLVPs which has been shown numerically (Tackley, 1998) and experimentally (Davaille, 1999). Alternatively, they could have accumulated over geological time as subducted lithosphere in the lower mantle (Christensen and Hofmann, 1994; Hirose et al., 1999; Hirose et al., 2005) which is swept into piles, forming the LLVPs (Mulyukova et al., 2015; Tackley, 2011). However, there is some question of the feasibility of producing negative velocity perturbations (Deschamps et al., 2012) and for the slab material to accumulate at the same rate as it is stirred into the mantle (Li and McNamara, 2013).

Depending on the origin of the LLVPs, our understanding of how the Earth evolved from its primordial state changes. If LLVPs are a short-lived cluster of mantle plumes, they do not need to exist in early Earth history. If they are long-lived piles of primordial Earth remnants, their formation and survival would need to be accounted for. Constraining the origin of LLVPs, therefore, has implications for our understanding of the Earth's history as well as whole Earth dynamics.

To reduce the number of hypotheses, there has been a focus on determining whether LLVPs are purely thermal or thermochemical features. Their relative density could provide constraints but conflicting observations have suggested both higher and lower relative density (Ishii and Tromp, 1999; Koelemeijer et al., 2017; Lau et al., 2017). Anticorrelation of S-wave velocity and bulk sound speed (Masters et al., 2000; Su and Dziewonski, 1997) is commonly used as evidence for compositional heterogeneity for LLVPs, but this has also been interpreted as the presence of post-perovskite (Davies et al., 2012; Koelemeijer et al., 2015). The presence of strong lateral velocity gradients has been attributed to a thermochemical origin (Ni et al., 2002; To et al., 2005), but these gradients can also be replicated with purely thermal structures (Davies et al., 2012; Schuberth et al., 2009).

Most of these studies use observations or constraints from seismological studies. Seismic tomography provides global, broad observations of LLVP location, morphology and relative velocity (e.g. French and Romanowicz, 2014; Grand et al., 1997; Grand,

2002; Koelemeijer et al., 2015; Ritsema et al., 2011; Simmons et al., 2010). The agreement of the long-wavelength structure of LLVPs in tomography models shows they are a result of the lower-mantle structure and not the different datasets or methodologies used (Lekic et al., 2012). In addition to these global observations, regional seismology studies combine travel time residuals, multipathing observations in the waveform and forward modelling to recover the location, gradient and inclination of LLVP boundaries (e.g. Frost and Rost, 2014; He and Wen, 2009; He and Wen, 2012; He et al., 2006; Ni et al., 2002; Ritsema et al., 1998; Roy et al., 2019; Sun and Miller, 2013; To et al., 2005). Multipathing occurs when a wavefront is incident on a strong lateral velocity gradient that causes the wavefront to move at different speeds and arrive at a recording station with different travel times as two arrivals. In addition to this, the boundary structure causes the wave to diffract and the structure causes the waves to refract as they pass through it, so the multipathed arrivals arrive from different directions and inclinations as well as arrival times. Figure 2.1 illustrates the multipathing phenomena at LLVP boundaries and how they can be observed at the surface.

LLVP boundary studies using travel time residuals and waveforms are common and, from their observations, have estimated the gradients at the boundaries of LLVPs to range from 3% δV_s per 50 km (0.0044 km s^{-1} km^{-1}) (Ni et al., 2002) to 2% δV_s per 300 km (0.00048 km s^{-1} km^{-1}) (Ritsema et al., 1998) (See Table 2.1 for published estimates of African LLVP S-wave velocity gradients). Combining travel time residuals, multipathing identification and forward modelling to observe and infer the properties of structures is well established and has been applied to a variety of structures (Silver and Chan, 1986; Sun et al., 2019; Sun et al., 2017; Sun et al., 2010) and algorithms developed to identify multipathing automatically in the waveforms (Sun et al., 2009; Zhao et al., 2015). Although regional seismology studies only use the waveform to infer the effects of deep Earth structure on the wavefield, they do not analyse all information available such as the direction and inclination of the arrival.

Study	Gradient (δV_s)	Gradient (kms^{-1} km^{-1})
Ni et al. (2002)	-3% per 50 km	0.0044
Ni and Helmberger (2003c)	-3% per 100–150 km	0.0022 – 0.0015
Ni and Helmberger (2003a)	-3% per 50 km	0.0044
Sun and Miller (2013)	-3.5% per 200 km	0.0013
Ritsema et al. (1998)	-2% per 300 km	0.00048
This study	-0.7% per 100 km	0.00050

Table 2.1: Table of lateral gradients of the African LLVP's boundaries in δV_s and kms^{-1}km^{-1}. The gradients for kms^{-1}km^{-1} were calculated using the V_s value for PREM (Dziewonski and Anderson, 1981) at the CMB.

Current observations have not been sufficient to constrain LLVP properties and therefore their composition, origin and influence remain ambiguous. Both purely ther-

mal and thermochemical structures can replicate properties such as the strong gradients, velocity reduction, morphology and anticorrelation between S-wave velocity and bulk sound speed (Davies et al., 2012; McNamara et al., 2010; McNamara and Zhong, 2004; McNamara and Zhong, 2005; Schuberth et al., 2009; Tackley, 1998). Because current seismic observations are not enough to constrain LLVP properties, we explore what can be inferred from analysing the direction and inclination of the arrivals.

This study uses array seismology to measure the backazimuth (direction) and horizontal slowness (a proxy for inclination) to identify multipathing and regions of diffraction and refraction. This is applied to data sampling the lower mantle beneath Africa, where several studies have identified multipathing and sharp travel time residuals (e.g. Ni et al., 2002; Sun et al., 2009; Wen et al., 2001). Different frequency bands are used to hypothesise differences in the African LLVP boundary structure such as gradient, depth and inclination. Using these observations, we estimate the gradients capable of producing multipathing with similar backazimuth and horizontal slowness deviations as our observations.

2.2 Methodology

2.2.1 Slowness vector grid search and beamforming

To measure the backazimuth and horizontal slowness, we search over a range of slowness vectors each with its own backazimuth and horizontal slowness and use beamforming (Rost and Thomas, 2002) to measure the power of the coherent signal. If there are multiple arrivals, we detect high power values at different backazimuths and horizontal slownesses. The results are referred to as $\theta - p$ plots as they describe how the power of coherent signal varies with backazimuth (θ) and horizontal slowness (p). Figure 2.2 shows examples of clear, possible and null multipathing observations in the $\theta - p$ plots and clear example of multipathing in the waveforms. The analysis is conducted within a time window selected from the visual inspection of the record section, typically on the order of tens of seconds. Information such as the time windows, stations, measurements, multipathing identification is available from 10.6084/m9.figshare.16573646.

Most array techniques assume energy propagates as a plane wavefront (Rost and Thomas, 2002). If the array aperture is small, this assumption holds and the effect of a curved wavefront is negligible. We use data from the Kaapvaal array (James et al., 2001), which has a large aperture (spread over approximately 20° in northwest-southeast orientation) so the plane wave assumption breaks down and can contribute to some deviation from the predicted backazimuth and horizontal slowness.

We alter the travel time calculation of beamforming to account for a circular wavefront given a backazimuth and horizontal slowness (Figure 2.3). To calculate the travel

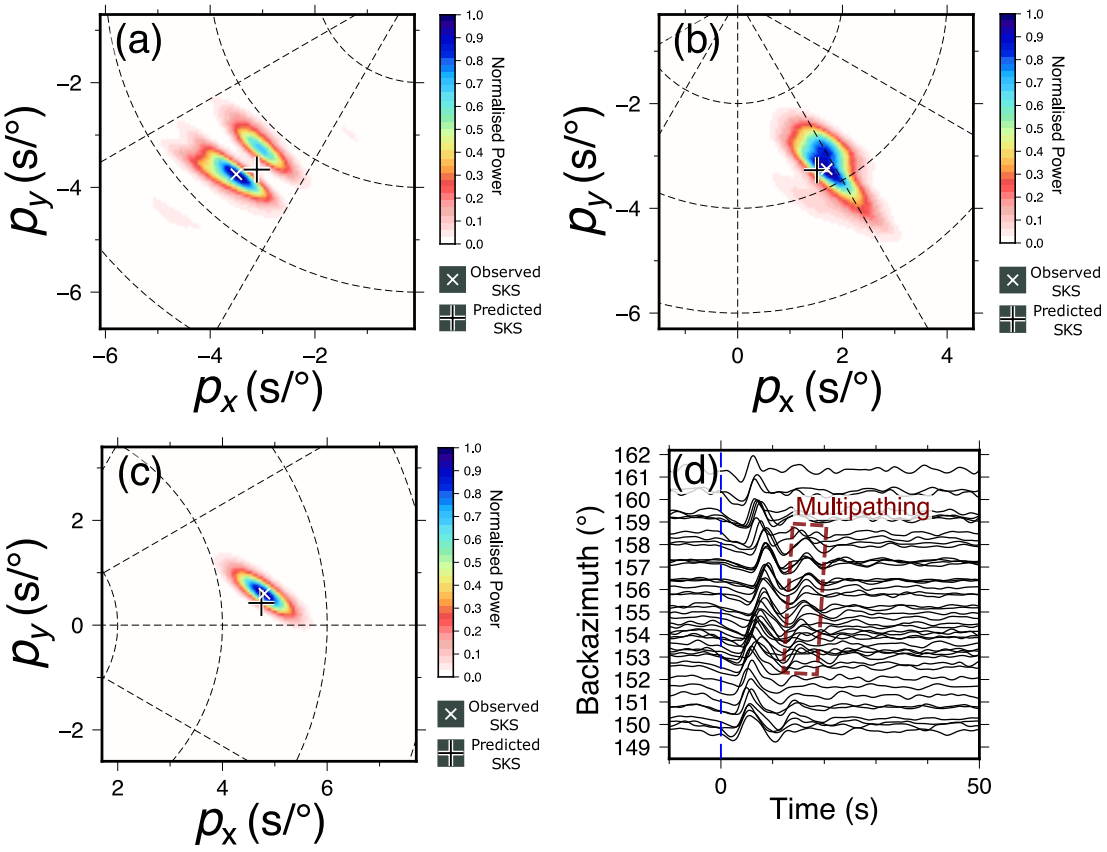

Figure 2.2: θ–p plots giving examples of arrivals classified as **(a)** clear multipathing using data from an event on 29 May, 1997, **(b)** potential multipathing using data from an event on 25 May, 1997 and **(c)** no multipathing using data from an event on 06 October, 1997. Details of event location and date are provided in the appendix Section A.8. All of these were filtered between 0.10 and 0.40 Hz and the power linearly normalised. **(d)** Waveforms from an event on 25 May, 1997 plotted by their great circle path backazimuth with a possible multipathed arrival highlighted.

times of a circular wavefront moving over a spherical Earth from event to station locations, the radial distances are calculated using the Haversine formula. This distance is then multiplied by an angular slowness value in $s/°$. From these estimates, the traces are shifted, stacked and the power of the coherent signal estimated. To search over backazimuth, the event is relocated keeping the epicentral distance constant. From this new location, the radial distance to each station is calculated relative to the mean distance and the travel times calculated (see Chapter 1 for details).

We test our correction on synthetic data arriving from a known backazimuth and horizontal slowness (see appendix section A.1). We find our correction reduces the backazimuth deviation from 2.37° to 0.40° and the horizontal slowness deviation from 0.20 $s/°$ to 0.03 $s/°$.

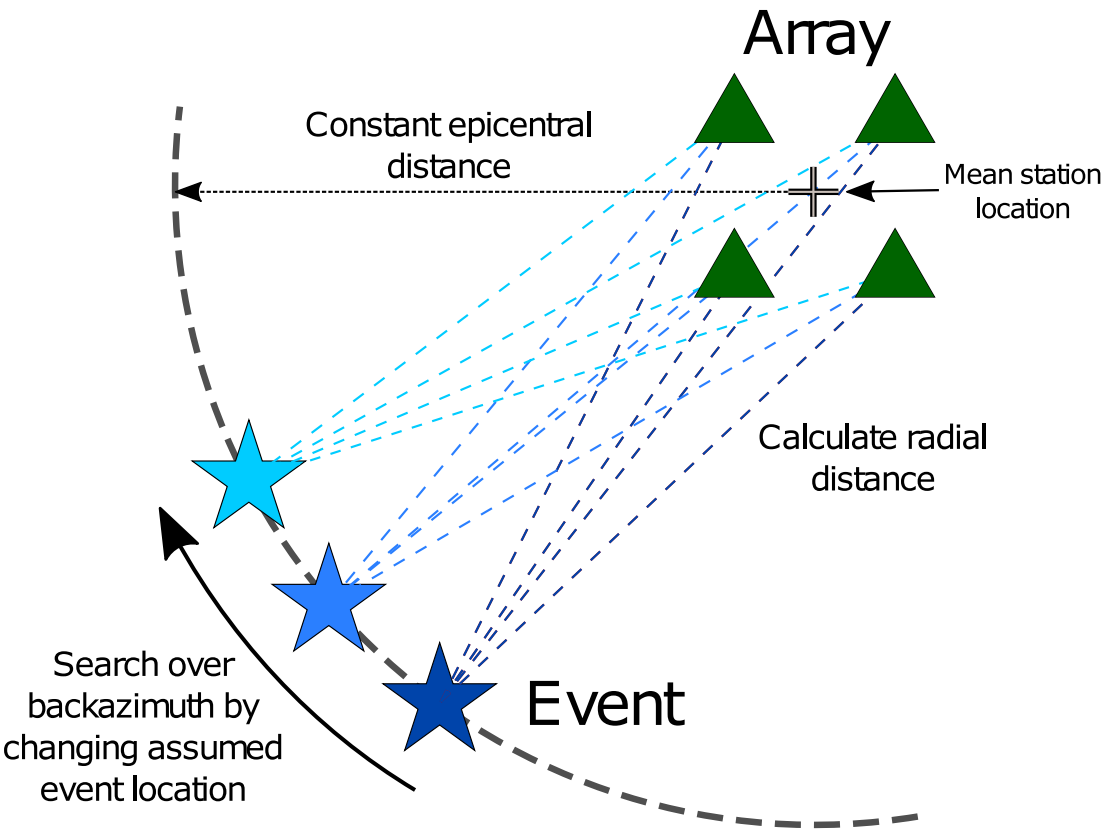

Figure 2.3: Illustration of the correction for a circular wavefront over a spherical Earth and how we search over backazimuth. The event location is changed depending on what backazimuth is tested with the epicentral distance kept the same. For each location, the radial distance to each station is calculated and the product of this with the angular slowness gives a travel time estimation.

2.2.2 Multipathing identification and slowness vector measurements

Multipathed arrivals are identified as power maxima separated in backazimuth and horizontal slowness and with a power value above the background noise and at least 10% of the maximum power value (Figure 2.2). We calculate the orientation of the locus between the multipathed arrivals clockwise from North where multipathing is identified. To calculate this, the locations of the multipathed arrivals in the $\theta - p$ observation are recorded and the angle of the vector connecting the two points from North is calculated. This angle is then rotated by 90° as the locus is orthogonal to the vector connecting the two points.

Our data set includes SKKS phases (Section 2.2.4) at distances where other phases such as S3KS could arrive at similar times and horizontal slownesses, which make it challenging to identify multipathing. For SKKS observations where multipathing could be present, we analyse synthetics generated using SYNGINE and the 1-D model prem_i_2s (Hutko et al., 2017; Krischer et al., 2017) as an estimate of the relative power of SKKS and S3KS. If there is any power for an S3KS arrival in the synthetic $\theta - p$ plots and there are multiple arrivals in the recorded data, the observation is labelled as "possible" multipathing. See Section A.2 for more details.

In addition to identifying multipathing, several measurements can be made from each observation. The backazimuth residual ($\Delta\Theta$) between the observed ($\Theta_{observed}$) and the backazimuth predicted by the great circle path between the event and mean station location ($\Theta_{predicted}$) is given by $\Delta\Theta = \Theta_{observed} - \Theta_{predicted}$. The horizontal slowness residual (Δp) between the observed ($p_{observed}$) and the PREM (Dziewonski and Anderson, 1981) predicted horizontal slowness ($p_{predicted}$) is given by $\Delta p = p_{observed} - p_{predicted}$. The vector from the predicted location to the observation location in the $\theta - p$ plot is recorded as a measure of the direction and strength of the perturbation the wave has experienced. Figure 2.4 illustrates the meaning of this vector residual, locus between the arrivals and visualises backazimuth and horizontal slowness deviations.

2.2.3 Frequency Analysis

To analyse the frequency dependence of multipathing and its wavefield effects, the data are filtered in five frequency bands and analysed separately (frequency bands: 0.07-0.28 Hz, 0.10-0.40 Hz, 0.13-0.52 Hz, 0.15-0.60 Hz, 0.18-0.72 Hz, 0.20-0.80 Hz) each with a width of two octaves. The frequencies will affect the size of the Fresnel zone, which gives an approximation of the area contributing to the observation. For both the main and multipathed arrival to have enough power to be observed, there needs to be a significant enough velocity change over the Fresnel zone. The frequency variation of multipathing could be indicative of differences in sharpness, depth or inclination between boundaries. Fresnel zones for each frequency band were calculated at the CMB using velocity values

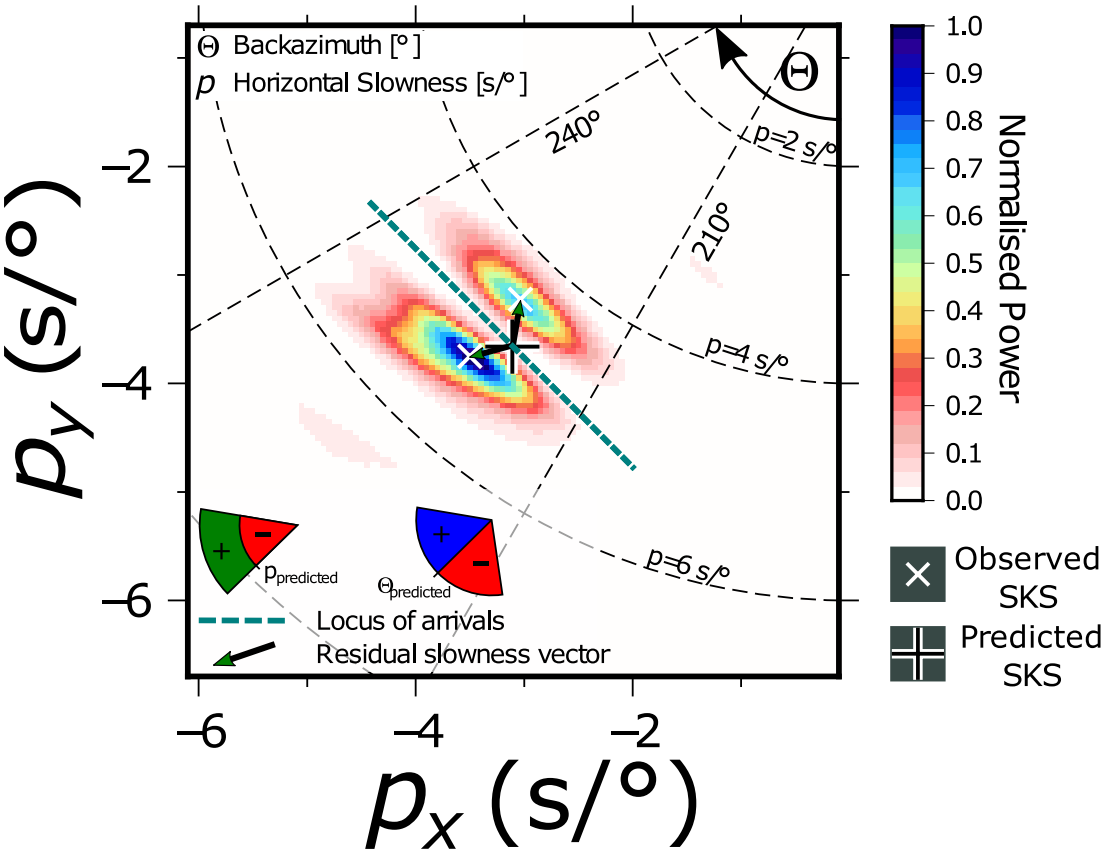

Figure 2.4: Annotations of the θ–p observation with data from an event on the 29 May, 1997 showing clear multipathing. The locus between the multipathed arrivals marked in blue gives an approximation of the boundary orientation. The residual slowness vector from the predicted backazimuth and horizontal slowness gives information of how the wavefield has been perturbed. Illustrations of positive and negative residuals for backazimuth and horizontal slowness are shown.

from PREM (Dziewonski and Anderson, 1981), details in Section A.9.

2.2.4 Data and preprocessing

SKS and SKKS data (Figure 2.5) from events located 70° to 140° away from the centre of the array and with magnitudes between 5.5 and 7.5 recorded at the Kaapvaal array are used to analyse Africa LLVP boundary structure (Figure 2.5). We deconvolve the instrument response, remove the mean amplitude, taper and apply a bandpass filter between 0.05 and 1.0 Hz (period of 1−20 s) for visual inspection. The horizontal components are rotated to radial and tangential components for clear SKS and SKKS identification. Following this, the signal-noise ratio (SNR) is estimated in a 70s time window around the predicted arrival time and used to roughly sort the data into traces that should be kept (SNR $>$ 3), removed (SNR $<$ 2.5) and could be used (2.5 $<$ SNR $<$ 3). Events with more than 10 traces sorted into "keep" or more than half between the "keep" and the potentially usable bins were sorted by hand after visual inspection of the record section aligned on the PREM (Dziewonski and Anderson, 1981) predicted SKS arrival. If there is a clear SKKS arrival, SKKS is also analysed. 83 events remain (see Appendix Section A.8 for event details).

The frequency bands we use are limited by the station spacing of the array. If the inter-station spacing is too large, spatial aliasing could occur in the $\theta - p$ plot and be misidentified as multipathing. The Nyquist criterion for the station spacing of each frequency band is used to limit the frequencies used. The lower frequencies will likely have higher amplitudes and influence the stacking significantly more than the higher frequencies, so we only limit the lower frequency cutoffs for the frequency analysis using this criterion. The lower frequency cut-off is limited to 0.20 Hz.

2.2.5 Noise reduction techniques

Multipathed arrivals could arrive with a lower SNR and stack to a similar power as incoherent signal at other backazimuths and horizontal slownesses. To aid multipathing identification, several techniques to improve the SNR of coherent arrivals are implemented. We use phase weighted stacking (Schimmel and Paulssen, 1997), F-statistic (Blandford, 1974) and deconvolve the array response function (ARF) using the Richardson-Lucy deconvolution method (Lucy, 1974; Richardson, 1972) as done in previous studies (Maupin, 2011; Picozzi et al., 2010). These are detailed further in Section A.3 with examples of their effectiveness. We use the outputs of all these methods to identify multipathing in the data with criteria for clear, potential and no multipathing explained in Section 2.2.2. Measurements of horizontal slowness and backazimuth deviations are taken using the phase-weighted (Schimmel and Paulssen, 1997) stack points as they most consistently have lower noise than the other methods.

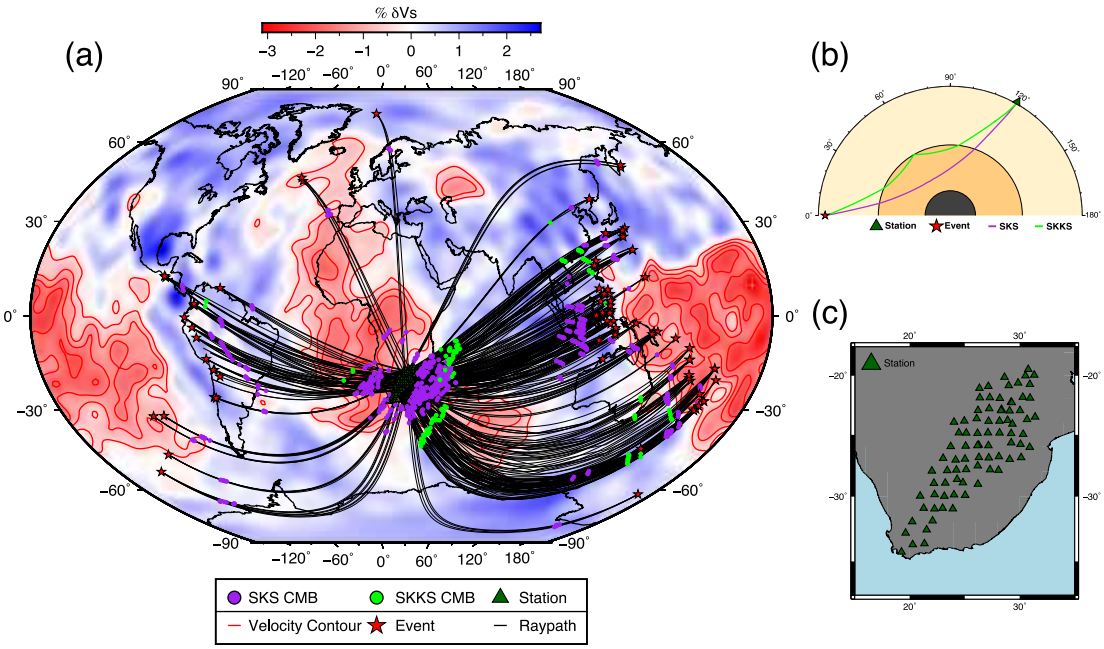

Figure 2.5: **(a)** The CMB pierce point locations for SKS and SKKS from events used in the analysis (Section 2.2.1) for whole array and sub-array observations (Section 2.2.6). The earthquakes, stations and ray paths are also plotted to show what other structures could have been sampled. The paths provide good coverage of the African LLVP, its boundaries and the surrounding mantle. The pierce points are shown on tomography model S40RTS (Ritsema et al., 2011) with shear wave velocity contours of −0.5%, −1.0%, −1.5% and −2.0% δV_s marked to highlight potential boundaries and structure. **(b)** Paths of SKS (purple) and SKKS (green) through the Earth. **(c)** Station coverage of the Kaapvaal array, chosen for its excellent station density and coverage.

2.2.6 Sub arrays

To better constrain the location of multipathing and its wavefield effects, the available stations in the Kaapvaal array are grouped into sub-arrays. Data from all available stations are also analysed. We group the traces using their waveform properties, back-azimuths and epicentral distances. We accept that we are adding our own bias to the observations by grouping the sub-arrays this way. Whole array observations are used to identify multipathing but, because the large area of the combined Fresnel zones of the Kaapvaal array, not used to analyse backazimuth and horizontal slowness deviations. 317 different sub-array geometries were used; stations for each sub-array and the data for each sub-array can be found from https://figshare.com/s/fbcb167ad15d581cfd4e.

2.2.7 Method strengths and limitations

Other studies have developed a method to automatically detect multipathing in the waveform (Sun et al., 2009). In comparison to this method, there are several limitations and advantages. The multipathed arrivals need to be present in enough traces to stack coherently and produce clear arrivals on the $\theta - p$ plot. Arrivals of similar slowness

may not be resolved as separate arrivals. On the other hand, noisier traces can be used because the stacking methods improve the SNR. The observations themselves also allow measurements of backazimuth and horizontal slowness deviations, which can be used to analyse structures affecting the wavefield.

2.3 Multipathing

This section describes our multipathing observations and discusses the frequency dependence (Section 2.3.1) and spatial variation (Section 2.3.2) with interpretations of possible boundary locations. Clear multipathing is observed in 16% of our whole array observations and 6.6% of our sub-array observations.

2.3.1 Frequency dependence

Figure 2.6 shows the variability of multipathing with different frequency bands. Some observations show clear multipathing within specific frequency bands while others in all frequency bands, which could be due to differences in boundary nature such as the velocity gradient, inclination or depth. As explained in Section 2.2.3, to observe multipathed arrivals, enough of the Fresnel zone needs to sample different velocities. This requires the lateral velocity gradient is sufficiently strong and sufficiently sampled by the wavefield. Analysing the power spectra of data with and without multipathing, using Welch's method (Welch, 1967), shows evidence for an increase in the power of higher frequencies (appendix Figures A.10 to A.14). We hypothesise this is caused by the focusing of higher frequencies due to diffraction from lateral velocity gradients. Further work is needed to constrain the exact relation between velocity gradient and frequency content and other possible causes, which is not the focus of this study.

Observations of multipathing at different frequencies could be due to differences in wavelength. Multipathing observations at higher frequencies could be indicative of strong velocity gradients while multipathing at low frequencies is indicative of a significant velocity change over a wider boundary. If the boundary is at an angle to the incidence of the wave, the boundary will not be sampled for as long and appear smoother.

Sampling boundaries at different depths could cause frequency variation in our observations due to changes of wavelength with velocity. At the same depth, and therefore the same 1-D velocity, the boundaries need to have different gradients or inclinations for multipathing to occur at different frequencies. At different depths, the boundaries could be the same sharpness and inclination but observed at different frequencies due to different Fresnel zone sizes.

The size and station density of the array could contribute to the frequency varia-

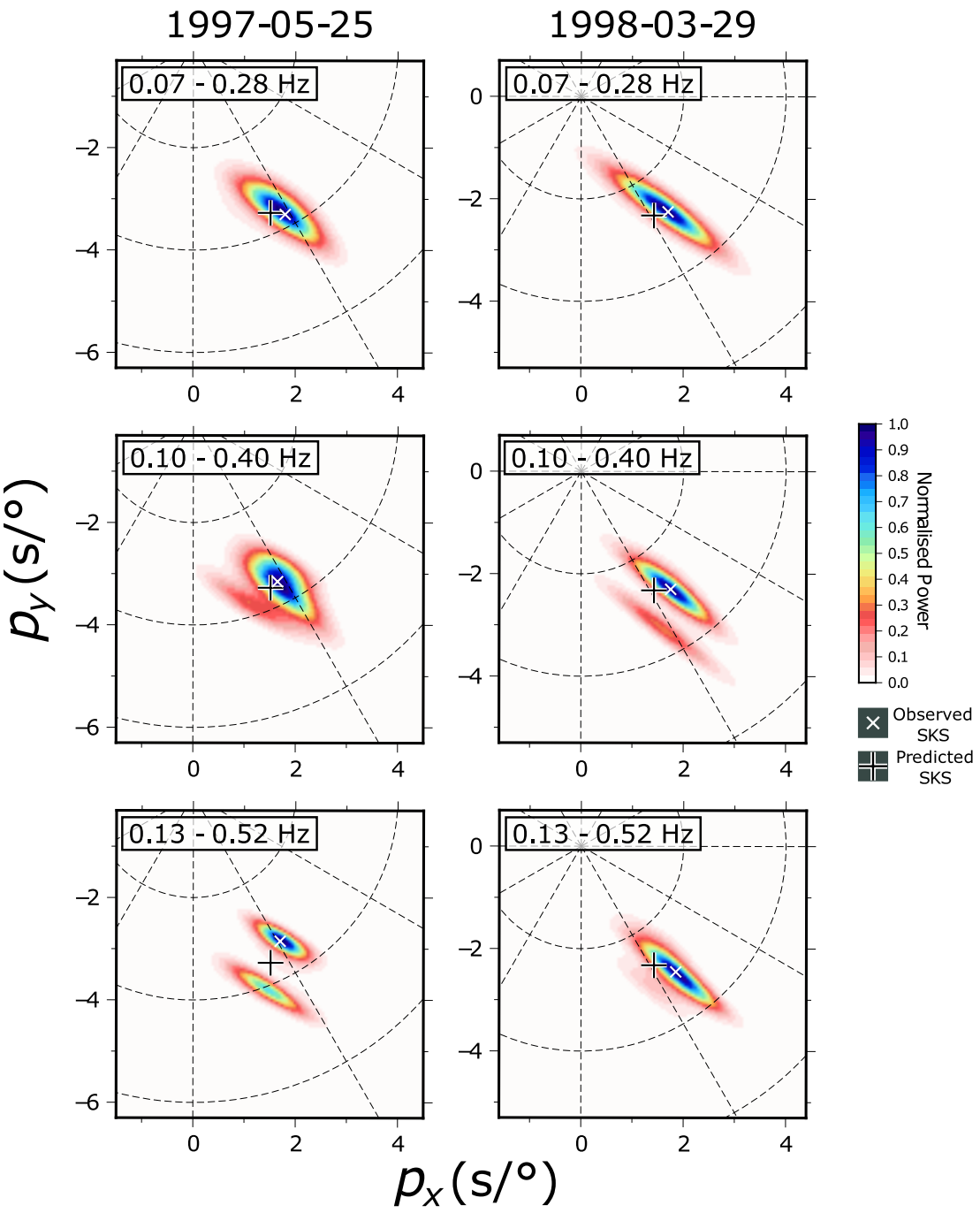

Figure 2.6: θ-p plots comparing the frequency bands in which clear multipathing is observed. The left column uses data from the 25 May 1997 event and clear multipathing is only observed in the 0.13 – 0.52 Hz band. The right column uses data from the 29 March 1998 event where clear multipathing is only observed in the 0.10 – 0.40 Hz frequency band.

tion. Larger, denser arrays will be sensitive to a larger area and will record multipathed arrivals in more waveforms. Lower frequencies with larger Fresnel volumes are more sensitive to weaker velocity gradients, but the weaker gradients may mean the multipathed arrivals will have a smaller amplitude also. Whole array observations should have more multipathing observations at lower frequencies (Figure 2.7) because weaker multipathed arrivals will be recorded in more waveforms and stack to an observable power.

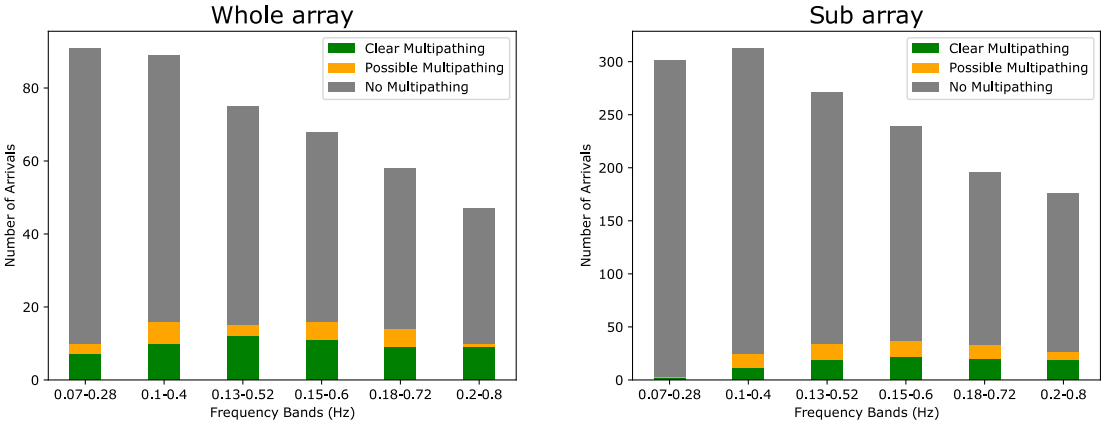

Figure 2.7: Number of observations of clear (green), possible (yellow) and no multipathing (grey) in different frequency bands for whole array and sub-array observations. The number of usable observations changes with frequency due to noise conditions and slowness resolution. At higher frequencies, the observations were noisier and at the lowest frequencies the slowness resolution is too poor to use.

2.3.2 Spatial analysis

Our observations show multipathing is not limited to one region and occurs in different frequency bands depending on the region. In Figure 2.8, the loci and the tomography velocity contours for both whole and sub-array observations align well to the east of Africa (25°S, 32°W) with a boundary trending northwest-southeast which then curves to trend approximately west-east as the boundary moves southward. Contours of S40RTS (Ritsema et al., 2011) and pierce points are mapped at 2400 km depth because for several paths this depth has an increase in lateral velocity gradient (e.g. Figure 2.12) and features at this depth provide possible explanations for most observations. It is possible, due to the 3-D nature of the structure, structures at other depths could explain our observations. However, we have tested several tomographic, and therefore data-based, models at different depths and found this to be the most satisfactory. In these regions, multipathing is observed in all frequency bands over both whole and sub-array observations. The range of frequencies could be interpreted as an LLVP boundary being sampled at several depths, or a boundary with both a strong lateral velocity gradients and a significant velocity change.

The circular low-velocity feature to the southeast of Africa (35°S, 30°W) is marked

by -1.5% δV_s velocity contour aligns well with the loci in the area. Multipathing is observed at a range of different frequencies here with arguably more observations at frequencies above the 0.15 – 0.60 Hz band. Observing multipathing at higher frequencies imply sampling of a relatively sharp gradient and observations in a broad frequency range suggest large and sharp velocity changes or sampling boundaries at several depths.

To the west of Africa (25°S, 15°W), particularly in the sub-array observations, there is a lot of scatter in loci orientations and multipathing is mainly observed in the higher frequency bands. The scattered loci are possibly due to the waves travelling through the body of the LLVP boundaries and sampling boundaries at several depths. Depending on the depth, the boundaries could have different orientations, therefore leading to scattered loci. Observing multipathing in higher frequency bands could be due to strong lateral velocity gradients or the depths the boundaries have been sampled.

There are significant differences between the whole and sub-array observations. Whole array observations will be sensitive to a larger area meaning small structures affecting a small part of the wavefield may not be resolved. This could explain why more multipathing is observed to the west in sub-array observations. Where multipathing is observed in whole array observations only, the velocity gradient may not be sampled for long enough along raypaths from the event to the sub-arrays. The multipathed arrivals would then not arrive with enough amplitude to stack to an observable power.

Studies using travel time and waveform observations have reported a boundary to the southwest of Africa with an approximate northwest-southeast strike (Ni et al., 2002). The orientation of the locus of our multipathed arrival in this region approximately agrees (Figure 2.8) supporting these previous results. Sun et al. (2010) find evidence for a mantle plume in the mid-mantle of this region too. We do not find evidence for this, most likely because of resolution and sampling limitations.

To further explore the spatial distribution of multipathing, we compare the locations of clear, possible and no multipathing observed at any frequency (Figure 2.8). Multipathing is not limited to one region and the pierce points of clear multipathing are very close to pierce points that show no or unclear multipathing. Our interpretation is the boundary structure needs to be sampled in a specific way for the multipathed arrivals to arrive with observable amplitudes.

2.3.3 Seismic anisotropy

There have been several studies analysing seismic anisotropy in the region of this study (e.g. Cottaar and Romanowicz, 2013; Ford et al., 2015; Lynner and Long, 2014; Reiss et al., 2019; Wang and Wen, 2007a). Shear wave splitting could complicate the waveforms and be misinterpreted as multipathing. Therefore, we measure SKS splitting in splitting

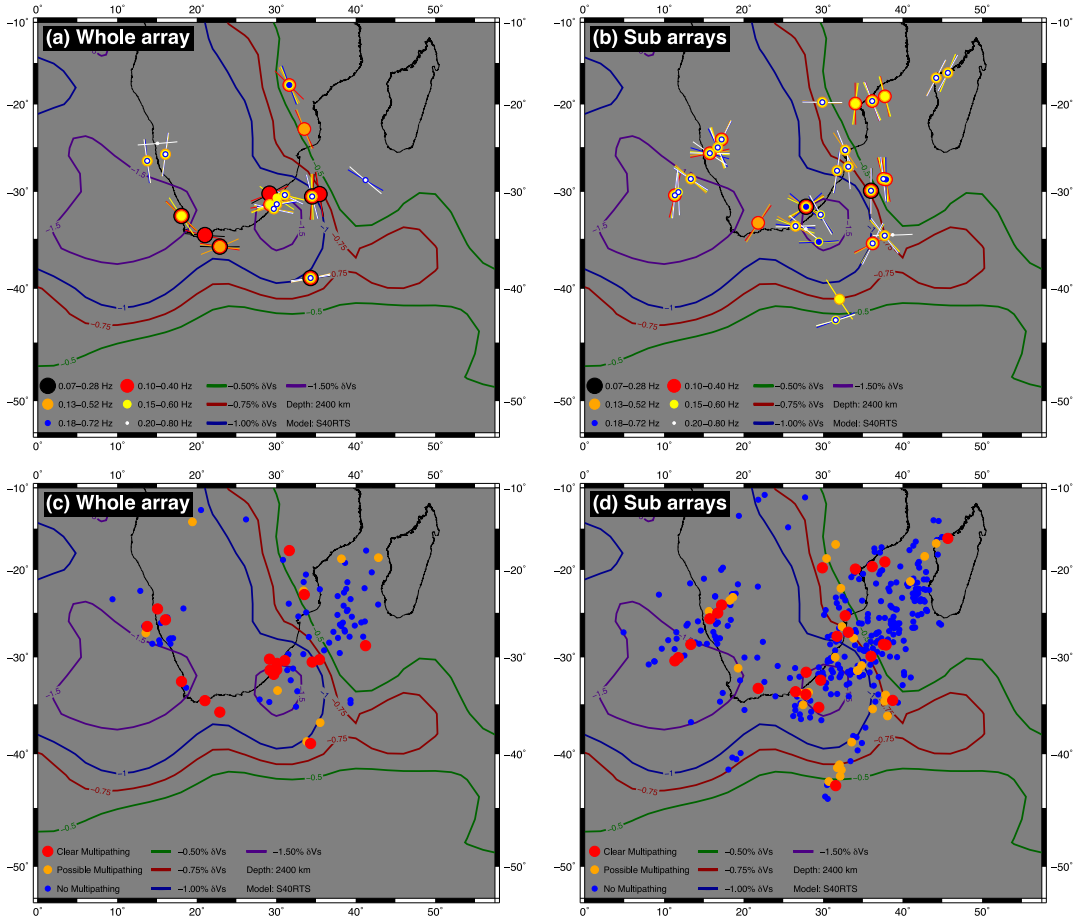

Figure 2.8: Subfigures **(a)** and **(b)** show 1-D ray path pierce points at 2400 km depth (approximately 500 km above the CMB) for events showing clear multipathing for whole array and sub-array observations respectively. The size and colour of the circles correspond to the frequencies at which multipathing is observed. The locus between the arrivals is marked for each frequency to represent the approximate orientation of the boundary causing the multipathing. Subfigures **(c)** and **(d)** show the pierce points at 2400 km depth for clear (red) possible (orange) and no (blue) multipathing for whole and sub-array observations respectively. Velocity contours are shown at 2400 km depth from tomography model S40RTS (Ritsema et al., 2011).

time and direction of the fast axis, remove the measured effect and repeat the analysis for a selection of events. After the anisotropy correction, we still observe multipathing (Figure A.16). For low SNR events, correcting for anisotropy reduced the quality of the observation. Since anisotropy alone is not the cause of observed multipathing and can reduce the quality of some observations, we do not correct for shear wave splitting.

2.4 Slowness Vector Residuals

This section analyses the slowness vector deviations and how they vary spatially. We focus our spatial analysis on the full slowness vector deviation from the predicted to the observed arrival in slowness space (Figure 2.4). Descriptions of backazimuth and horizontal slowness deviations are given in Section A.4. When spatially analysing these deviations, the pierce point location is moved to match observed backazimuth and horizontal slowness.

Backazimuth residuals show little variation between frequency bands (Figure A.5). The majority of the observations lie between 8° and −14° and maximum values are 10° to −22° for positive and negative deviations respectively. There are more negative residual observations with on average approximately 64% negative residual observations compared to 36% positive. This is possibly due to heterogeneous sampling from limited event-station configurations.

The horizontal slowness deviations vary little with frequency, with most observations lying between 1.2 s/° and −1.0 s/° (Figure A.7). Outliers are present in these observations but show no clear pattern and range from a maximum of 2.1 s/° and a minimum of −1.6 s/°. Like the backazimuth residuals, the observations are not evenly distributed about 0 s/° with 60% positive residuals and 40% negative. This variation could be due to the large-scale low velocity structures in the mantle beneath Africa causing them to refract and arrive at a shallower angle.

The magnitude of the slowness vector deviations does not vary greatly with frequency with slightly more high magnitude deviations at higher frequencies and with minimum and maximum observed values from less than 0.1 s/° to 2.1 s/° (Figure A.8).

2.4.1 Spatial analysis of slowness vector deviations

The full slowness vector deviation is a vector from the predicted arrival in the $\theta - p$ plot to the observed arrival. The azimuth of the vector indicates the direction of perturbation and the length is indicative magnitude. This vector combines the backazimuth and horizontal slowness perturbations giving a clear picture of how the wavefield is being affected. Figure 2.9 shows how these vectors vary spatially.

The radial pattern and magnitude of the vectors around the circular feature south-

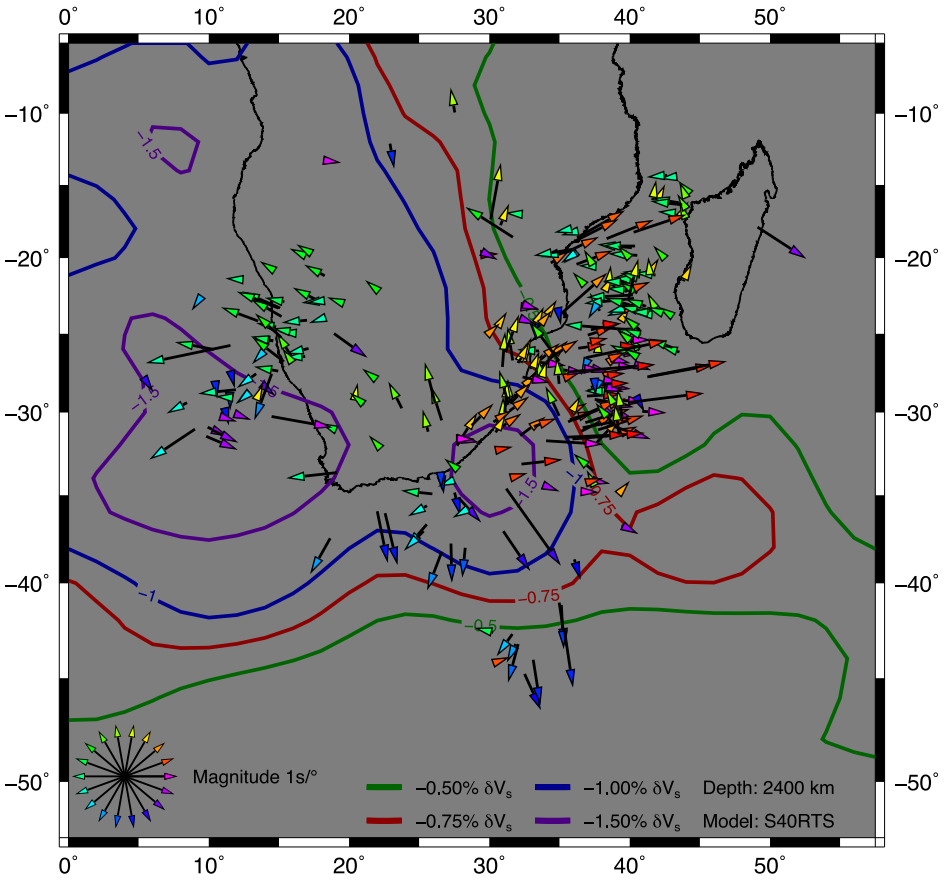

Figure 2.9: Pierce points for sub-array observations showing the full slowness vector deviation from the prediction to the observation in the θ-p plot coloured by azimuth (Figure 2.4). The slowness vector describes the full perturbation of the wavefield essentially combining the information from backazimuth and horizontal slowness. The contours from S40RTS (Ritsema et al., 2011) and the pierce points are marked at a depth of 2400 km to outline potential structures contributing to the observations. The frequency band used is from 0.13 Hz to 0.52 Hz. The pierce points have been relocated according to the observed backazimuth and horizontal slowness.

east of Africa (35°S, 30°W) support our interpretation that this structure is the cause of our observations. Northeast of this region, the azimuths change their orientation to be approximately orthogonal to the velocity contours striking northwest-southeast. The vector residuals west of Africa (25°S, 15°W) are more scattered than in other regions but generally have an azimuth pointing away from the array and arrive at a shallower inclination. The scattered vector residuals, the scattered loci and the presence of multipathing in this region suggest the wavefield is being affected by several boundaries at different depths. The trend of slowness vectors pointing away from the array suggest they are being refracted by the body of the LLVP.

East of Africa (25°S, 40°W) the vectors have opposite azimuths shown by the colour change from red to green in the vector heads. The paths of these waves suggest they may not sample the LLVP boundary. The arrivals sampling this region arrive with negligible backazimuth residuals but have opposite horizontal slowness residuals (Figure 2.10). We hypothesise the cause of these observations are adjacent fast and slow structures causing the wavefield to vertically refract. The location of fast structures relative to the LLVP boundary at the core-mantle boundary in tomography model SEMUCB-WM1 (French and Romanowicz, 2014) aligns well with the transition (Figure 2.10), implying these structures could be the cause of our observations. Given the size of the sub-arrays and the size of the Fresnel zone at these frequencies, it is possible this fast structure is causing the waves to refract and arrive at a steeper inclination with negligible backazimuth deviation.

Previous studies have analysed similar regions and show some evidence for similar structures. Sun et al. (2009) analyse regions of the lowermost mantle similar to areas where we find boundaries between slow and fast structures and a quasi-circular structure. Using their multipath detector method with S_{diff} data, they identify a region with strong gradients southeast of Africa similar to our hypothesised boundary in Figure 2.10. Their travel time residuals transition from negative to positive over this region supports our interpretation of a transition from slow to fast. Another Sun et al. (2009) event shows evidence for a smaller scale structure southeast of the Kaapvaal array with a similar structure and approximate location as our observed circular structure. Mega ULVZs have been shown to cause backazimuth deviations (Cottaar and Romanowicz, 2012) and are a possible explanation of our observations. However, a 20 km tall ULVZ with a 20% δV_s reduction lead to travel time residuals of 0.7s, which is well below the observed difference between multipathed arrivals. We tested travel time contributions of stronger ULVZ models (Yu and Garnero, 2018) and found they also can not explain our results.

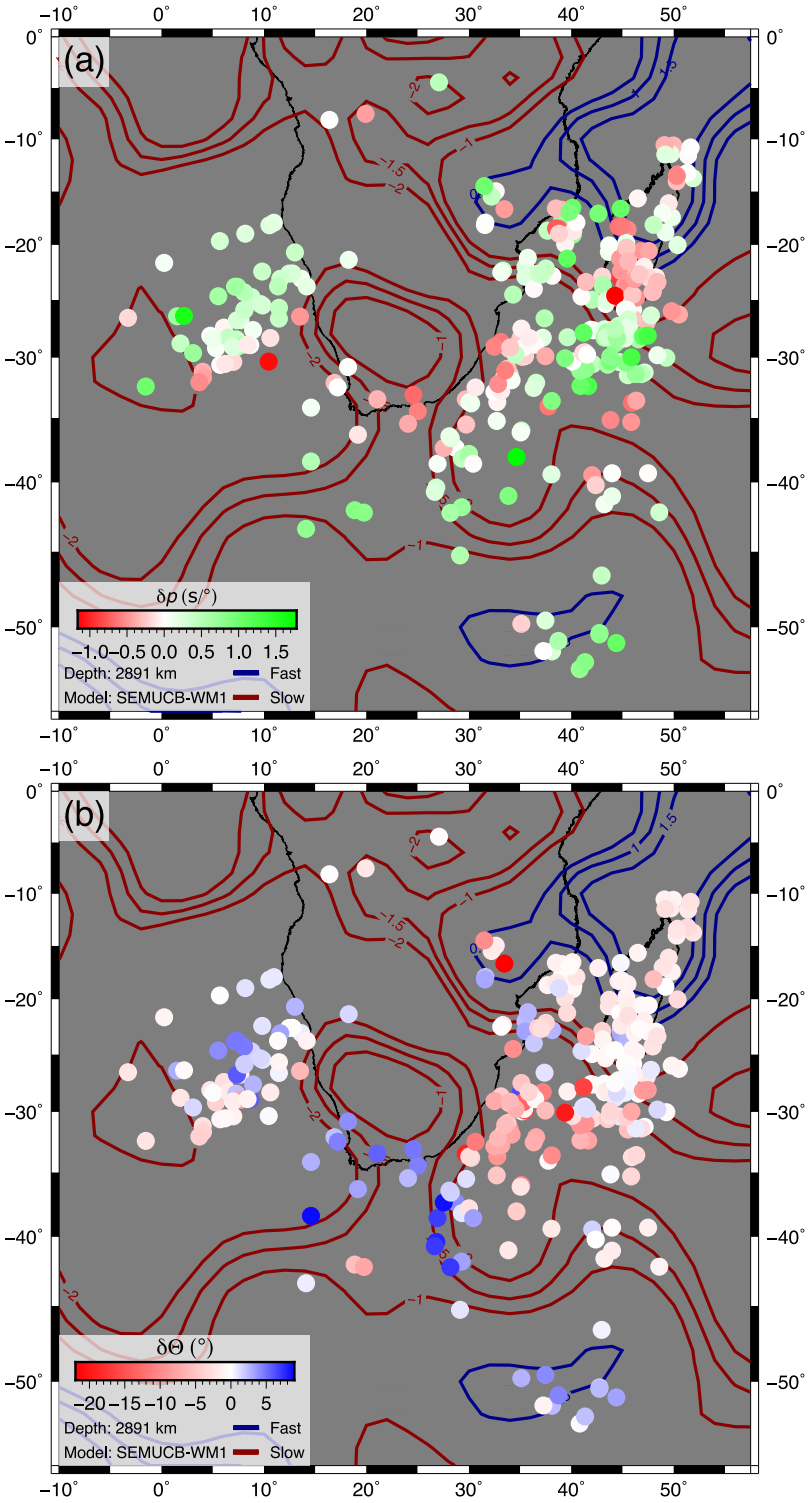

Figure 2.10: Pierce points at the CMB coloured with **(a)** horizontal slowness deviations and **(b)** backazimuth deviations. Negative contours −1.0%, −1.5%, −2.0% δV_s and positive contours 0.5%, 1.0%, 1.5% δV_s of tomography model SEMUCB-WM1 (French and Romanowicz, 2014) are shown to highlight the transition from fast to slow structures east of Africa. The events have been relocated so the 1-D paths arrive from the observed backazimuth and horizontal slowness.

2.5 Forward modelling and comparison to tomography models

In this section, we explore possible conditions for multipathing to be observed in slowness space and compare these to previous studies (Table 2.1).

Our observations are sensitive to 3D structure, show frequency dependence, and have been made at relatively high frequencies (up to ∼0.20 Hz). Therefore, forward-modelling strategies based on approximations, such as ray theory, are not appropriate to reproduce them. Instead, we must use a full-physics numerical method to capture the finite-frequency effects of wave propagation in a 3D medium, which is necessarily much more computationally costly. We use SPECFEM3D (Komatitsch and Tromp, 2002a; Komatitsch and Tromp, 2002b), to create synthetic data for three earthquakes (Section 2.5.1). These events were chosen as they show the clearest multipathing, and therefore likely sample the strongest gradients along their raypaths. As such, the analysis of these events will provide us with an upper bound of the seismic velocity gradients required to explain the data in this locale. As the modelling is computationally expensive, we limit ourselves to these events and model frequencies up to approximately 0.18 Hz. We test the effects of ellipticity and topography and find they have a negligible effect.

The loss of small-scale heterogeneity and reduction of velocity amplitude and gradients in seismic tomography from regularisation, smoothing and limited sampling coverage is well documented (Bull et al., 2009; Foulger et al., 2013; Ritsema et al., 2007; Schuberth et al., 2009). Given the large parameter space of a 3-D structure that could cause multipathing, we take the structure of tomography as an approximation of the long-wavelength Earth structure and accept the mentioned limitations. From this starting point, we increase the velocity perturbations and gradients linearly to approximately account for the reduction through tomographic filtering and recreate conditions for multipathing to be observed in our method.

S40RTS (Ritsema et al., 2011) is used as a starting point as the velocity contours shown in figures in Sections 2.3 and 2.4 provide possible explanations for our observations. In each model, the velocity perturbations have been amplified at depths greater than 1000 km with depths shallower than 660 km are unchanged. The transition from the amplified lower mantle to the upper mantle is tapered to avoid artefacts. No crustal model is used in our modelling as tests show no identifiable effect of crustal structure on our observations. Three models are used where perturbations at depths greater than 1000 km have been doubled (labelled as M2), trebled (M3), quadrupled (M4) and we use S40RTS (Ritsema et al., 2011) with no amplification (M1). Of course, any single mantle velocity model is not a unique fit to the data and many other possible models exist. However, using tomography-based, and therefore data-based, models means we

incorporate structures that other observations have already identified.

2.5.1 Gradients of boundaries

We compare observations of SKS data from events on the 25 May 1997, 28 March 1998 and 28 May 1997 to runs using all models described earlier. Figure 2.11 shows the $\theta - p$ plots of the synthetic data with the observations.

For these events, the S40RTS (Ritsema et al., 2011) velocity perturbations are not sufficient to cause detectable multipathing, indicating that stronger gradients are required. In models with stronger gradients, whether multipathing is observed and how similar it is to the observation varies with the event likely due to the different sampling geometry. Synthetic data for the 25 May 1997 in model M3 shows clear multipathing where the relative power and location of the two arrivals are similar to the observation. In model M2, there is no clear multipathing and the location of the arrival is approximately the average of the locations of the observed multipathed arrivals. As the only difference between M2 and M3 is the strength of amplitudes in the lower mantle, we argue it is lower mantle structure causing the observed multipathed arrivals in this event.

The 29 May 1997 event shows some weak multipathing in all amplified models in similar locations to the observation, but the arrivals do not have the same relative power in the $\theta - p$ plot. This suggests there is a boundary being sampled, but the gradient in the model is weaker or the path length along the boundary is shorter than in the data. The 29 March 1998 event shows no multipathing in most of the models except for M4, but this has much weaker multipathing and both arrivals are different to their location in the observation. The strength of the velocity gradient of the boundary or its location in the models is not enough to reproduce the observation.

These varying results are to be expected with the inherent limitations of tomography and show the models are not representative of the velocity gradients at the boundary of the African LLVP everywhere. Due to the good agreement between synthetic data from model M3 and real observation for the 25 May 1997 event, we analyse the gradients sampled along this path.

Figure 2.12 a shows a cross-section through model M3 between 70° and 140° distance along the great-circle path for the 25 May 1997 event. The 1-D raypath to the mean station location from the exit point is shown on the cross-section with the lateral velocity gradient and velocity perturbations sampled are shown in Figure 2.12b. The receiver-side cross-section and gradients sampled by the 25 May 1997 event along the raypath to the mean station location in model M3 are shown in Figure 2.12. The largest gradients sampled are not at the CMB but approximately 600 km above it, a similar depth to the maximum misfit found by Zhao et al. (2015) in their analysis of

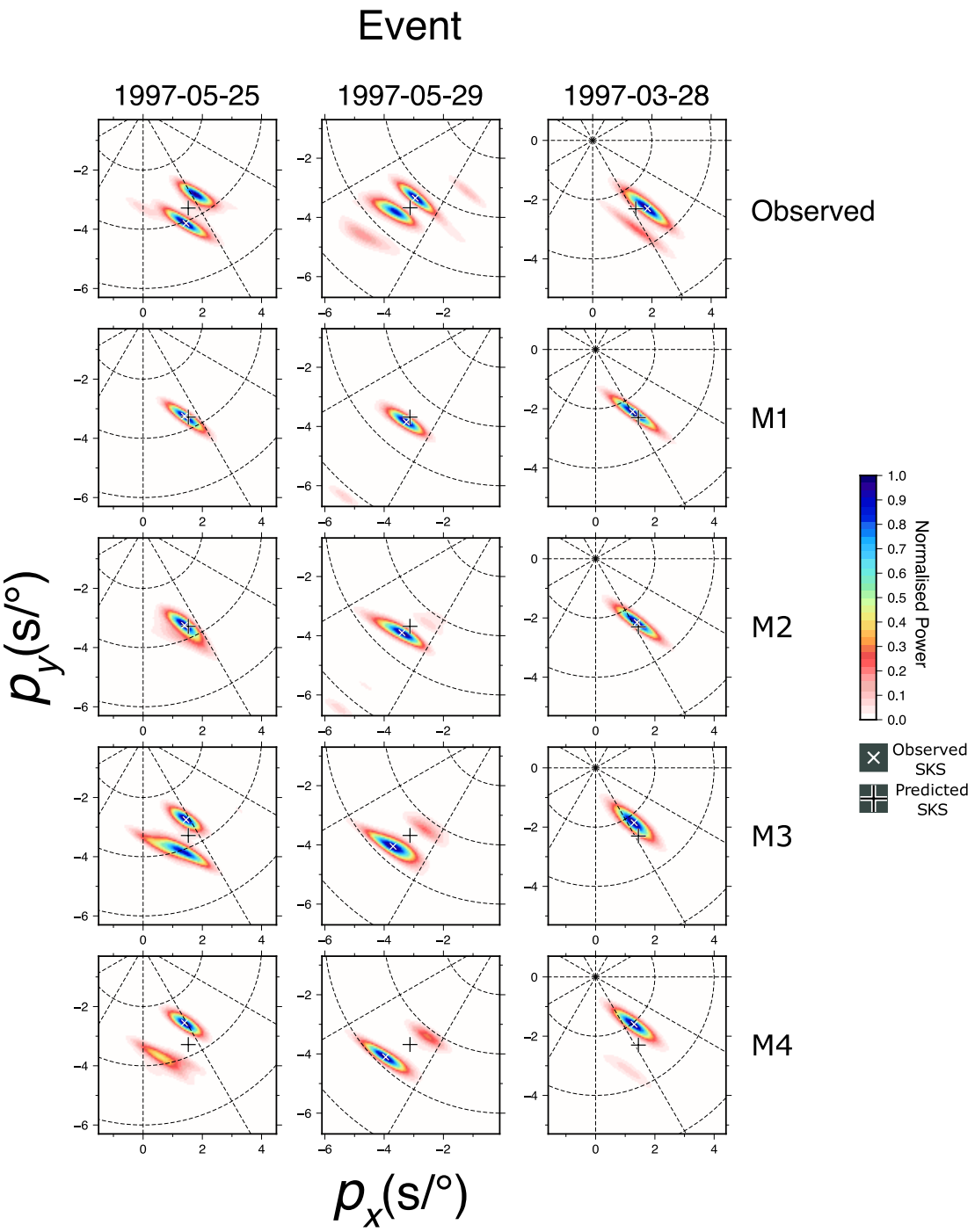

Figure 2.11: Analysis of multipathing for three events in the observed data (top row) with synthetics from models M1 to M4 in the rows beneath (labeled on the right). For each event, the same frequency bands are used for the observed and synthetic data.

waveform broadening and the Pacific LLVP. The path in the cross-section samples the edge of a particularly low-velocity region at 4100 km radius (shown by velocity contour of -4% δV_s), which we hypothesise is the same feature causing the circular contours shown previously. The maximum gradient sampled is 0.7% δV_s per 100 km (0.0005 km s^{-1} km^{-1}) about 600 km above the CMB. This is an order of magnitude lower than found in some previous studies, which we discuss further below.

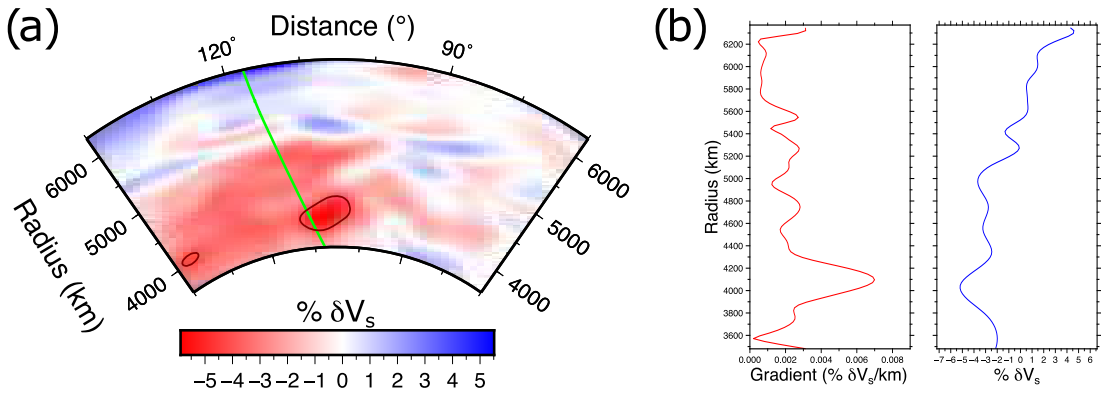

Figure 2.12: **(a)** Cross section of the receiver-side path of SKS from the 25 May 1997 event through M3. **(b)** two depth sections of the gradients and velocity perturbations sampled by the receiver-side 1-D path from event to average station location through model M3. Contour of -4% δV_s is shown to highlight the possible cause of our observations.

Although the modelled $\theta - p$ observation is similar, the modelled SKS data arrives much earlier than in the observations as shown in Figure 2.13. The difference in travel times is a reflection of the velocity perturbations sampled, whereas the observation of multipathing is indicative of the gradients sampled. For this example, the gradient sampled over the raypath is sufficient to create comparable multipathing to the observations, but the velocity perturbations are not sufficient to replicate the observed travel-time residuals.

In the synthetic waveforms, there is evidence for diffracted phases such as SPdKS. We do not think this is the cause of the second arrival in the $\theta - p$ plots. SPdKS is expected to arrive within a narrow slowness window, which the majority of our arrivals are not observed in. Furthermore, multipathed arrivals only appear in the $\theta - p$ plots once the velocity gradients have been increased. If SPdKS arrivals are present, they should be observed in the $\theta - p$ plots of all models and not just those with amplified gradients. We use a relative stack to isolate SPdKS using data in Figure 2.13 at distances larger than 119° where SPdKS is most clear and separated from SKS. We find SPdKS is not visible when SKS is included in the analysis time window (see Appendix Section A.7) and suggest it is because it arrives with a lower amplitude. When not including SKS, SPdKS is only visible in the synthetics using PREM (Dziewonski and Anderson, 1981) and not in the real data or synthetics from M3. Because of this, we are confident that the multiple arrivals observed are multipathing and not SPdKS.

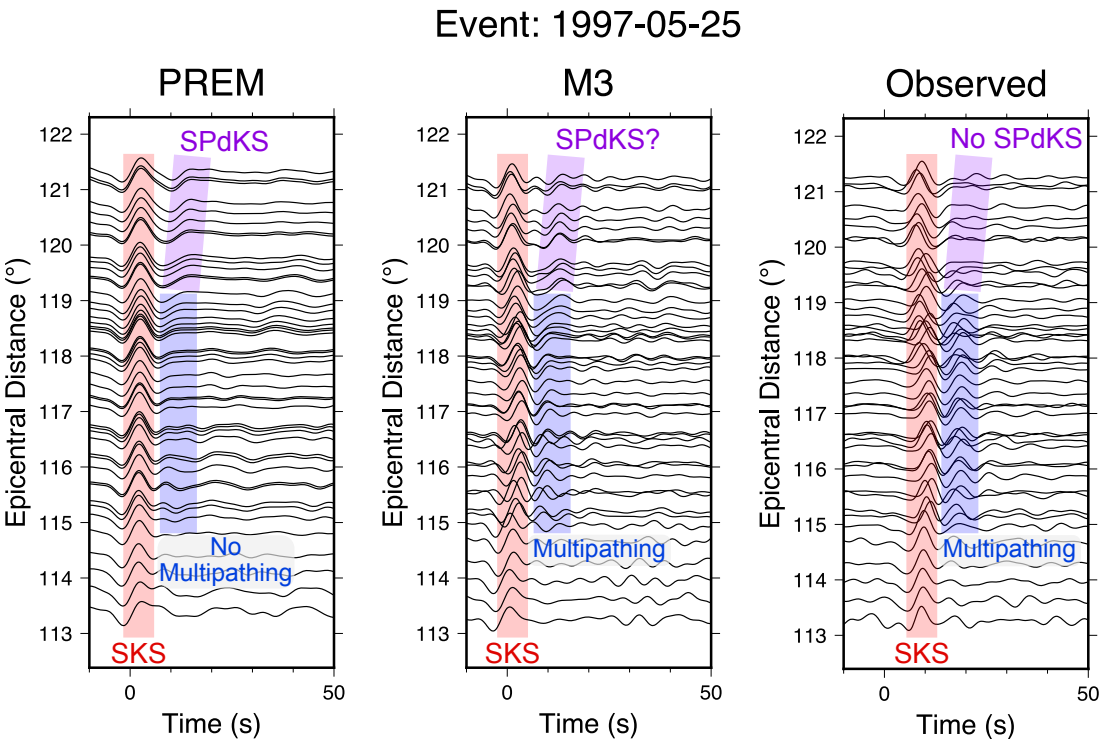

Figure 2.13: Record sections to illustrate the differences observed between the synthetic data from using the PREM (Dziewonski and Anderson, 1981) model (left), the M3 model (centre) and the observed data (right) for the 25 May 1997 event in terms of the effect of SPdKS on multipathing observations. Each of the record sections are annotated with shaded regions for the SKS arrival and the presence, or lack of, of multipathing or SPdKS. The multipathed arrivals in the observed data (right) and M3 synthetics (centre) have a visibly different moveout to SPdKS and in the observed data it is arguable SPdKS is not present where as in the M3 synthetics it is not clear. We discuss the possible presence of SPdKS further in Appendix Section A.7 and apply the same array processing technique to test the effects of SPdKS. The modelled waveforms arrive significantly earlier than the observations. We suggest this is a reflection of the velocity perturbations in the model rather than the lateral velocity gradients.

From travel time residuals and waveform analysis, several studies have inferred the velocity gradients at the boundaries and perturbations inside the African LLVP (Ni et al., 2002; Ritsema et al., 1998; Sun and Miller, 2013; Wang and Wen, 2007b). We assume the gradient of the boundary is the main cause of the observed multipathing. As only one of our models matches well with the observation, we only compare the gradient we found to produce multipathing for the 25 May 1997 event with other studies (See Table 2.1). Gradients up to 0.7% δV_s per 100 km (0.00050 km s^{-1} km^{-1}) can produce multipathing for the 25 May 1997 event which is an order of magnitude lower than the strongest estimated gradients of -3% δV_s per 50 km (0.044 km s^{-1} km^{-1}) (Ni et al., 2002), though similar to that found by Ritsema et al. (1998) -2% δV_s per 300 km (0.00048 km s^{-1} km^{-1}).

The apparent disparity between studies may be explained by the differing sensitivity of the methods used. Our observations analyse coherent signals across the array by stacking many waveforms together and not analysing them individually. Each measurement is sensitive to a larger region and could lead to boundary structures being sampled for longer, therefore weaker gradients are sufficient to produce multipathing. Most estimates of the stronger gradients used 2-D forward modelling to replicate their observations (Ni and Helmberger, 2003b; Ni et al., 2002), therefore estimate the gradients along the great-circle path. Any travel time delay or multipathing would have to be from in-plane structures and contributions from out of plane structure would not be accounted for. We use 3-D full wavefield modelling thus accounting for contributions from out of plane structures which more fully represents the ability of weaker gradients to lead to the same effect.

The presence of strong velocity gradients at LLVP boundaries causing multipathing and sharp changes in travel time residuals is commonly used as evidence for a thermochemical origin of LLVPs (Ni et al., 2002; Ritsema et al., 1998; To et al., 2005). We require gradients an order of magnitude lower than previous estimates to produce multipathing similar to our observations. The gradients of 0.7% δV_s per 100 km (0.00050 km s^{-1} km^{-1}) are well below those evident in purely thermal models (2.25% δV_s over 50 km (0.0032 km s^{-1} km^{-1}) (Schuberth et al., 2009) and 3.5 – 4.5% δV_s per 100 km (0.0025 – 0.0032 km s^{-1} km^{-1}) (Davies et al., 2012)). This modelling implies that the presence of lateral velocity gradients capable of producing observable multipathing cannot distinguish between thermal and thermochemical LLVPs.

2.6 Conclusions

Through measuring the backazimuth and horizontal slowness of SKS and SKKS data sampling the lower mantle beneath Africa, we identify clear multipathing in approximately 16% of our whole array observations and 8.0% of our sub-array observations.

We find evidence for wavefield perturbation from backazimuth deviations of up to 22° and horizontal slowness deviations of up to 1.2 $s/°$. Spatial analysis of these measurements relative to structure resolved by seismic tomography gives evidence for a circular feature to the southeast of Africa, adjacent fast and slow structures and an LLVP boundary. This suggests that tomography models can recover the shape but not the strength of the features explaining our observations.

We conduct full wavefield forward modelling to constrain what lateral velocity gradients are needed to observe multipathing in slowness space. We find gradients of up to 0.7% δVs per 100 km (0.00050 km s^{-1} km^{-1}) sampled approximately 600 km above the CMB can reproduce our multipathing observations. This is an order of magnitude lower than previous estimates of -3% δV_s per 50 km (0.0044 km s^{-1} km^{-1}) (Ni et al., 2002), commonly used to argue for a thermochemical origin of LLVPs. As the gradients we predict are well below the largest estimates for both thermal and thermochemical structures (Davies et al., 2012), we argue observing multipathing caused by lateral velocity gradients of LLVP boundaries is not necessarily evidence for a thermochemical composition.

Acknowledgments

This research is supported by the NERC DTP Spheres grant NE/L002574/1. Predictions were made using the Taup toolkit Crotwell et al., 1999. Figures made using GMT Wessel et al., 2013. Data was retrieved from IRIS Data Center (http://www.iris.edu) using ObspyDMT Hosseini and Sigloch, 2017, events used are provided in Appendix Section A.8. There are no financial conflicts of interest for any authors.

References

Bijwaard, H., Spakman, W., & Engdahl, E. R. (1998). Closing the gap between regional and global travel time tomography. *Journal of Geophysical Research: Solid Earth*, *103*(B12), 30055–30078.

Blandford, R. R. (1974). An automatic event detector at the Tonto Forest seismic observatory. *Geophysics*, *39*(5), 633–643.

Bull, A. L., McNamara, A. K., Becker, T. W., & Ritsema, J. (2010). Global scale models of the mantle flow field predicted by synthetic tomography models. *Physics of the Earth and Planetary Interiors*, *182*(3-4), 129–138.

Bull, A. L., McNamara, A. K., & Ritsema, J. (2009). Synthetic tomography of plume clusters and thermochemical piles. *Earth and Planetary Science Letters*, *278*(3), 152–162.

Christensen, U. R., & Hofmann, A. W. (1994). Segregation of subducted oceanic crust in the convecting mantle. *Journal of Geophysical Research: Solid Earth*, *99*(B10), 19867–19884.

Cottaar, S., & Romanowicz, B. (2012). An unsually large ULVZ at the base of the mantle near Hawaii. *Earth and Planetary Science Letters*, *355*, 213–222.

Cottaar, S., & Romanowicz, B. (2013). Observations of changing anisotropy across the southern margin of the African LLSVP. *Geophysical Journal International*, *195*(2), 1184–1195.

Crotwell, H. P., Owens, T. J., & Ritsema, J. (1999). The TauP Toolkit: Flexible seismic travel-time and ray-path utilities. *Seismological Research Letters*, *70*(2), 154–160.

Davaille, A. (1999). Simultaneous generation of hotspots and superswells by convection in a heterogeneous planetary mantle. *Nature*, *402*(6763), 756–760.

Davies, D. R., Goes, S., & Lau, H. C. P. (2015a). Thermally dominated deep mantle LLSVPs: a review. *The earth's heterogeneous mantle* (pp. 441–477). Springer.

Davies, D. R., Goes, S., & Sambridge, M. (2015b). On the relationship between volcanic hotspot locations, the reconstructed eruption sites of large igneous provinces and deep mantle seismic structure. *Earth and Planetary Science Letters*, *411*, 121–130.

Davies, D. R., Goes, S., Davies, J. H., Schuberth, B. S. A., Bunge, H.-P., & Ritsema, J. (2012). Reconciling dynamic and seismic models of Earth's lower mantle: The dominant role of thermal heterogeneity. *Earth and Planetary Science Letters*, *353*, 253–269.

Deschamps, F., Cobden, L., & Tackley, P. J. (2012). The primitive nature of large low shear-wave velocity provinces. *Earth and Planetary Science Letters*, *349*, 198–208.

Dziewonski, A. M., & Anderson, D. L. (1981). Preliminary reference Earth model. *Physics of the earth and planetary interiors*, *25*(4), 297–356.

Ford, H. A., Long, M. D., He, X., & Lynner, C. (2015). Lowermost mantle flow at the eastern edge of the African Large Low Shear Velocity Province. *Earth and Planetary Science Letters*, *420*, 12–22.

Foulger, G. R., Panza, G. F., Artemieva, I. M., Bastow, I. D., Cammarano, F., Evans, J. R., Hamilton, W. B., Julian, B. R., Lustrino, M., Thybo, H., & Yanovskaya, T. B. (2013). Caveats on tomographic images. *Terra Nova*, *25*(4), 259–281.

French, S. W., & Romanowicz, B. A. (2014). Whole-mantle radially anisotropic shear velocity structure from spectral-element waveform tomography. *Geophysical Journal International*, *199*(3), 1303–1327.

Frost, D. A., & Rost, S. (2014). The P-wave boundary of the large-low shear velocity province beneath the Pacific. *Earth and Planetary Science Letters*, *403*, 380–392.

Garnero, E. J., McNamara, A. K., & Shim, S.-H. (2016). Continent-sized anomalous zones with low seismic velocity at the base of Earth's mantle. *Nature Geoscience*, *9*(7), 481–489.

Grand, S. P., van der Hilst, R. D., & Widiyantoro, S. (1997). High resolution global tomography: a snapshot of convection in the Earth. *Geological Society of America Today*, *7*(4).

Grand, S. P. (2002). Mantle shear–wave tomography and the fate of subducted slabs. *Philosophical Transactions of the Royal Society of London A: Mathematical, Physical and Engineering Sciences*, *360*(1800), 2475–2491.

Hager, B. H. (1984). Subducted slabs and the geoid: Constraints on mantle rheology and flow. *Journal of Geophysical Research: Solid Earth*, *89*(B7), 6003–6015.

Hager, B. H., Clayton, R. W., Richards, M. A., Comer, R. P., & Dziewonski, A. M. (1985). Lower mantle heterogeneity, dynamic topography and the geoid. *Nature*, *313*(6003), 541.

He, Y., & Wen, L. (2009). Structural features and shear-velocity structure of the "Pacific Anomaly". *Journal of Geophysical Research: Solid Earth*, *114*(B2).

He, Y., & Wen, L. (2012). Geographic boundary of the "Pacific Anomaly" and its geometry and transitional structure in the north. *Journal of Geophysical Research: Solid Earth*, *117*(B9).

He, Y., Wen, L., & Zheng, T. (2006). Geographic boundary and shear wave velocity structure of the "Pacific anomaly" near the core–mantle boundary beneath western Pacific. *Earth and Planetary Science Letters*, *244*(1), 302–314.

Hirose, K., Fei, Y., Ma, Y., & Mao, H.-K. (1999). The fate of subducted basaltic crust in the Earth's lower mantle. *Nature*, *397*(6714), 53–56.

Hirose, K., Takafuji, N., Sata, N., & Ohishi, Y. (2005). Phase transition and density of subducted MORB crust in the lower mantle. *Earth and Planetary Science Letters*, *237*(1-2), 239–251.

Hosseini, K., & Sigloch, K. (2017). obspyDMT: a Python toolbox for retrieving and processing of large seismological datasets. *Solid Earth*, *8*.

Hutko, A. R., Bahavar, M., Trabant, C., Weekly, R. T., Fossen, M. V., & Ahern, T. (2017). Data products at the IRIS-DMC: Growth and usage. *Seismological Research Letters*, *88*(3), 892–903.

Ishii, M., & Tromp, J. (1999). Normal-Mode and Free-Air Gravity Constraints on Lateral Variations in Velocity and Density of Earth's Mantle. *Science*, *285*(5431), 1231–1236.

James, D., Fouch, M., VanDecar, J., Van Der Lee, S., & Group, K. S. (2001). Tectospheric structure beneath southern Africa. *Geophysical research letters*, *28*(13), 2485–2488.

Koelemeijer, P., Ritsema, J., Deuss, A., & Van Heijst, H.-J. (2015). SP12RTS: a degree-12 model of shear-and compressional-wave velocity for Earth's mantle. *Geophysical Journal International*, *204*(2), 1024–1039.

Koelemeijer, P., Deuss, A., & Ritsema, J. (2017). Density structure of Earth's lowermost mantle from Stoneley mode splitting observations. *Nature Communications*, *8*.

Komatitsch, D., & Tromp, J. (2002a). Spectral-element simulations of global seismic wave propagation–I. Validation. *Geophysical Journal International*, *149*(2), 390–412.

Komatitsch, D., & Tromp, J. (2002b). Spectral-element simulations of global seismic wave propagation–II. Three-dimensional models, oceans, rotation and self-gravitation. *Geophysical Journal International*, *150*(1), 303–318.

Krischer, L., Hutko, A. R., Van Driel, M., Stähler, S., Bahavar, M., Trabant, C., & Nissen-Meyer, T. (2017). On-demand custom broadband synthetic seismograms. *Seismological Research Letters*, *88*(4), 1127–1140.

Labrosse, S., Hernlund, J., & Coltice, N. (2007). A crystallizing dense magma ocean at the base of the Earth's mantle. *Nature*, *450*(7171), 866–869.

Lau, H. C., Mitrovica, J. X., Davis, J. L., Tromp, J., Yang, H.-Y., & Al-Attar, D. (2017). Tidal tomography constrains Earth's deep-mantle buoyancy. *Nature*, *551*(7680), 321.

Lee, C.-T. A., Luffi, P., Höink, T., Li, J., Dasgupta, R., & Hernlund, J. (2010). Upside-down differentiation and generation of a 'primordial' lower mantle. *Nature*, *463*(7283), 930–933.

Lekic, V., Cottaar, S., Dziewonski, A., & Romanowicz, B. (2012). Cluster analysis of global lower mantle tomography: A new class of structure and implications for chemical heterogeneity. *Earth and Planetary Science Letters*, *357*, 68–77.

Li, M., & McNamara, A. K. (2013). The difficulty for subducted oceanic crust to accumulate at the Earth's core-mantle boundary. *Journal of Geophysical Research: Solid Earth*, *118*(4), 1807–1816.

Lithgow-Bertelloni, C., & Silver, P. G. (1998). Dynamic topography, plate driving forces and the African superswell. *Nature*, *395*(6699), 269.

Lucy, L. B. (1974). An iterative technique for the rectification of observed distributions. *The Astronomical Journal*, *79*, 745.

Lynner, C., & Long, M. D. (2014). Lowermost mantle anisotropy and deformation along the boundary of the African LLSVP. *Geophysical Research Letters*, *41*(10), 3447–3454.

Masters, G., Laske, G., Bolton, H., & Dziewonski, A. (2000). The relative behavior of shear velocity, bulk sound speed, and compressional velocity in the mantle: implications for chemical and thermal structure. *Earth's deep interior: mineral physics and tomography from the atomic to the global scale*, 63–87.

Maupin, V. (2011). Upper-mantle structure in southern Norway from beamforming of Rayleigh wave data presenting multipathing. *Geophysical Journal International*, *185*(2), 985–1002.

McNamara, A. K., Garnero, E. J., & Rost, S. (2010). Tracking deep mantle reservoirs with ultra-low velocity zones. *Earth and Planetary Science Letters*, *299*(1), 1–9.

McNamara, A. K., & Zhong, S. (2004). Thermochemical structures within a spherical mantle: Superplumes or piles? *Journal of Geophysical Research: Solid Earth*, *109*(B7).

McNamara, A. K., & Zhong, S. (2005). Thermochemical structures beneath Africa and the Pacific Ocean. *Nature*, *437*(7062), 1136–1139.

Mound, J., Davies, C., Rost, S., & Aurnou, J. (2019). Regional stratification at the top of Earth's core due to core–mantle boundary heat flux variations. *Nature Geoscience*, *12*(7), 575–580.

Mulyukova, E., Steinberger, B., Dabrowski, M., & Sobolev, S. V. (2015). Survival of LLSVPs for billions of years in a vigorously convecting mantle: replenishment and destruction of chemical anomaly. *Journal of Geophysical Research: Solid Earth*, *120*(5), 3824–3847.

Ni, S., & Helmberger, D. V. (2003a). Further constraints on the African superplume structure. *Physics of the Earth and Planetary Interiors*, *140*(1-3), 243–251.

Ni, S., & Helmberger, D. V. (2003b). Ridge-like lower mantle structure beneath south Africa. *Journal of Geophysical Research: Solid Earth*, *108*(B2).

Ni, S., & Helmberger, D. V. (2003c). Seismological constraints on the South African superplume; could be the oldest distinct structure on Earth. *Earth and Planetary Science Letters*, *206*(1-2), 119–131.

Ni, S., Tan, E., Gurnis, M., & Helmberger, D. (2002). Sharp sides to the African superplume. *Science*, *296*(5574), 1850–1852.

Picozzi, M., Parolai, S., & Bindi, D. (2010). Deblurring of frequency–wavenumber images from small-scale seismic arrays. *Geophysical Journal International*, *181*(1), 357–368.

Reiss, M., Long, M., & Creasy, N. (2019). Lowermost Mantle Anisotropy Beneath Africa From Differential SKS-SKKS Shear-Wave Splitting. *Journal of Geophysical Research: Solid Earth*.

Richardson, W. H. (1972). Bayesian-based iterative method of image restoration. *JOSA*, *62*(1), 55–59.

Ritsema, J., Deuss, A. A., Van Heijst, H. J., & Woodhouse, J. H. (2011). S40RTS: a degree-40 shear-velocity model for the mantle from new Rayleigh wave dispersion, teleseismic traveltime and normal-mode splitting function measurements. *Geophysical Journal International*, *184*(3), 1223–1236.

Ritsema, J., McNamara, A. K., & Bull, A. L. (2007). Tomographic filtering of geodynamic models: Implications for model interpretation and large-scale mantle structure. *Journal of Geophysical Research: Solid Earth*, *112*(B1).

Ritsema, J., Ni, S., Helmberger, D. V., & Crotwell, H. P. (1998). Evidence for strong shear velocity reductions and velocity gradients in the lower mantle beneath Africa. *Geophysical Research Letters*, *25*(23), 4245–4248.

Rost, S., & Thomas, C. (2002). Array seismology: Methods and applications. *Reviews of geophysics*, *40*(3).

Roy, S. K., Takeuchi, N., Srinagesh, D., Ravi Kumar, M., & Kawakatsu, H. (2019). Topography of the western Pacific LLSVP constrained by S-wave multipathing. *Geophysical Journal International*, *218*(1), 190–199.

Schimmel, M., & Paulssen, H. (1997). Noise reduction and detection of weak, coherent signals through phase-weighted stacks. *Geophysical Journal International*, *130*(2), 497–505.

Schubert, G., Masters, G., Olson, P., & Tackley, P. (2004). Superplumes or plume clusters? *Physics of the Earth and Planetary Interiors*, *146*(1), 147–162.

Schuberth, B. S. A., Bunge, H.-P., & Ritsema, J. (2009). Tomographic filtering of high-resolution mantle circulation models: Can seismic heterogeneity be explained by temperature alone? *Geochemistry, Geophysics, Geosystems*, *10*(5).

Silver, P. G., & Chan, W. W. (1986). Observations of body wave multipathing from broadband seismograms: evidence for lower mantle slab penetration beneath the Sea of Okhotsk. *Journal of Geophysical Research: Solid Earth*, *91*(B14), 13787–13802.

Simmons, N. A., Forte, A. M., Boschi, L., & Grand, S. P. (2010). GyPSuM: A joint tomographic model of mantle density and seismic wave speeds. *Journal of Geophysical Research: Solid Earth*, *115*(B12).

Su, W.-j., & Dziewonski, A. M. (1997). Simultaneous inversion for 3-D variations in shear and bulk velocity in the mantle. *Physics of the Earth and Planetary Interiors*, *100*(1-4), 135–156.

Sun, D., Helmberger, D., Lai, V. H., Gurnis, M., Jackson, J. M., & Yang, H.-Y. (2019). Slab Control on the Northeastern Edge of the Mid-Pacific LLSVP near Hawaii. *Geophysical Research Letters*.

Sun, D., Gurnis, M., Saleeby, J., & Helmberger, D. (2017). A dipping, thick segment of the Farallon Slab beneath central US. *Journal of Geophysical Research: Solid Earth*, *122*(4), 2911–2928.

Sun, D., Helmberger, D., & Gurnis, M. (2010). A narrow, mid-mantle plume below southern Africa. *Geophysical Research Letters*, *37*(9).

Sun, D., Helmberger, D., Ni, S., & Bower, D. (2009). Direct measures of lateral velocity variation in the deep Earth. *Journal of Geophysical Research: Solid Earth*, *114*(B5).

Sun, D., & Miller, M. S. (2013). Study of the western edge of the African large low shear velocity province. *Geochemistry, Geophysics, Geosystems*, *14*(8), 3109–3125.

Tackley, P. J. (1998). Three-Dimensional Simulations of Mantle Convection with a Thermo-Chemical Basal Boundary Layer: D″? *The core-mantle boundary region*, 231–253.

Tackley, P. J. (2011). Living dead slabs in 3-D: The dynamics of compositionally-stratified slabs entering a "slab graveyard" above the core-mantle boundary. *Physics of the Earth and Planetary Interiors*, *188*(3-4), 150–162.

Thorne, M. S., Garnero, E. J., & Grand, S. P. (2004). Geographic correlation between hot spots and deep mantle lateral shear-wave velocity gradients. *Physics of the Earth and Planetary Interiors*, *146*(1), 47–63.

To, A., Romanowicz, B., Capdeville, Y., & Takeuchi, N. (2005). 3D effects of sharp boundaries at the borders of the African and Pacific Superplumes: Observation and modeling. *Earth and Planetary Science Letters*, *233*(1), 137–153.

Tolstikhin, I., & Hofmann, A. W. (2005). Early crust on top of the earth's core. *Physics of the Earth and Planetary Interiors*, *148*(2-4), 109–130.

Torsvik, T. H., Burke, K., Steinberger, B., Webb, S. J., & Ashwal, L. D. (2010). Diamonds sampled by plumes from the core-mantle boundary. *Nature*, *466*(7304), 352–355.

Wang, Y., & Wen, L. (2007a). Complex seismic anisotropy at the border of a very low velocity province at the base of the Earth's mantle. *Journal of Geophysical Research: Solid Earth*, *112*(B9).

Wang, Y., & Wen, L. (2007b). Geometry and P and S velocity structure of the "African Anomaly". *Journal of Geophysical Research: Solid Earth*, *112*(B5).

Welch, P. (1967). The use of fast Fourier transform for the estimation of power spectra: a method based on time averaging over short, modified periodograms. *IEEE Transactions on audio and electroacoustics*, *15*(2), 70–73.

Wen, L., Silver, P., James, D., & Kuehnel, R. (2001). Seismic evidence for a thermochemical boundary at the base of the Earth's mantle. *Earth and Planetary Science Letters*, *189*(3), 141–153.

Wessel, P., Smith, W. H., Scharroo, R., Luis, J., & Wobbe, F. (2013). Generic mapping tools: improved version released. *Eos, Transactions American Geophysical Union*, *94*(45), 409–410.

Yu, S., & Garnero, E. J. (2018). Ultralow velocity zone locations: A global assessment. *Geochemistry, Geophysics, Geosystems*, *19*(2), 396–414.

Zhao, C., Garnero, E. J., McNamara, A. K., Schmerr, N., & Carlson, R. W. (2015). Seismic evidence for a chemically distinct thermochemical reservoir in Earth's deep mantle beneath Hawaii. *Earth and Planetary Science Letters*, *426*, 143–153.

Chapter 3

Automatic Slowness Vector Measurements of Seismic Arrivals with Uncertainty Estimates using Bootstrap Sampling, Array Methods and Unsupervised Learning

Abstract

Horizontal slowness vector measurements using array techniques have been used to analyse many Earth phenomena from lower mantle heterogeneity to meteorological event location. While providing observations essential for studying much of the Earth, slowness vector analysis is limited by the necessary and subjective visual inspection of observations. Furthermore, it is challenging to determine the uncertainties caused by limitations of array processing such as array geometry, local structure, noise and their effect on slowness vector measurements. To address these issues, we present a method to automatically identify seismic arrivals and measure their slowness vector properties with uncertainty bounds. We do this by bootstrap sampling waveforms, therefore also creating random sub-arrays, then use linear beamforming to measure the coherent power at a range of slowness vectors. For each bootstrap sample, we take the top N peaks from each power distribution as the slowness vectors of possible arrivals. The slowness vectors of all bootstrap samples are gathered and the clustering algorithm DBSCAN (Density-Based Spatial Clustering of Applications with Noise) is

used to identify arrivals as clusters of slowness vectors. The mean of each cluster gives the slowness vector measurement for that arrival and the distribution of slowness vectors in each cluster gives the uncertainty estimate. We tuned the parameters of DBSCAN using a dataset of 2489 SKS and SKKS observations at a range of frequency bands from 0.1 Hz to 1 Hz. We then present examples at higher frequencies (0.5 to 2.0 Hz) than the example dataset, identifying PKP precursors, and lower frequency by identifying multipathing in surface waves (0.04 to 0.06 Hz). While we use a linear beamforming process, this method can be implemented with any beamforming process such as cross-correlation beamforming or phase weighted stacking. This method allows for much larger datasets to be analysed without visual inspection of data. Phenomena such as multipathing, reflections or scattering can be identified automatically in body or surface waves and their properties analysed with uncertainties.

3.1 Introduction

Seismic array techniques which measure the full horizontal slowness vector (backazimuth and inclination) of seismic arrivals have been used to investigate Earth structure for decades. These analyses have been applied to a wide variety of seismic arrivals and problems such as by using long-period surface waves to identify upper mantle and surface heterogeneity (Ji et al., 2005; Maupin, 2011; Xia et al., 2018), short period S-waves to analyse lower mantle structure (Cottaar and Romanowicz, 2012; Schumacher and Thomas, 2016; Stockmann et al., 2019; Ward et al., 2020), high-frequency P-waves to study scatterers in the mid and lower mantle (Bentham and Rost, 2014; Cao and Romanowicz, 2007; Frost et al., 2013; Niu and Kawakatsu, 1997; Ritsema et al., 2020; Thomas et al., 2002; Yang and He, 2015), event detection and spatial location (Chevrot et al., 2007; Landès et al., 2010; Liu et al., 2016), ambient noise (Behr et al., 2013; Roux and Ben-Zion, 2017), nuclear event detection (Bowers and Selby, 2009; Gibbons and Ringdal, 2011) and meteorological event spatial location (Gerstoft et al., 2006; Gerstoft et al., 2008).

Past studies which analysed slowness vector properties using array methods (for a review see: Rost and Thomas, 2002; Rost and Thomas, 2009) were limited in terms of the number of observations due to the usual requirement to visually inspect each observation to determine an arrivals slowness vector properties or if it is too noisy to use. In addition, several studies have discussed the limitations of using beamforming or f–k methodology to identify phases and estimate their slowness vector properties (Berteussen, 1976; Gibbons et al., 2008; Selby, 2011) and methods have been developed to correct slowness vector measurements for Earth structure when locating events (Bondár et al., 1999; Gibbons et al., 2011; Koch and Kradolfer, 1999; Schweitzer, 2001). To clarify what limitations the uncertainty estimate is accounting for, we first discuss the assumptions and limitations of making one slowness vector measurement.

Each slowness vector in the beamforming grid search assumes the wave moves over the array with a constant horizontal slowness and arrives at the stations with a backazimuth equal to that along the great circle path from the relocated event location (for details see: Ward et al., 2020). The beamforming process does not account for limitations in heterogeneous station distribution, which can lead to heterogeneous sampling of the wavefield, and interference from noise may contribute to errors in slowness vector measurement. The waveforms of the arrivals are assumed to be coherent across the array. Waveform incoherence of the signal across the array may result in deviations from the slowness vector prediction (Gibbons et al., 2008). Source complexity could lead to unusual waveforms recorded at the array, but should not affect the slowness vector measurement as source complexity should introduce consistent waveform complexity across the array. The local structure may deform the wavefield as it moves across the array such that the arrival times at the stations will deviate from the prediction (Gibbons et al., 2018). This may lead to slowness vector deviations depending on the geometry of stations distribution and local velocity and topography structure.

The predicted backazimuth of the arrival is assumed along the great circle path between the event and the mean station location assuming a spherical Earth. The predicted horizontal slowness of the arrival is taken from ray-tracing through a 1-D velocity model in a spherical Earth. Any structures local to the array or deeper with properties that differ from the 1-D velocity model may result in deviations from this prediction. It is difficult if not impossible to separate out these different contributions using just a single array measurement, let alone determine their relative contributions.

Automating the identification of arrivals and measuring their slowness vector properties would remove the time consuming and subjective process of visually inspecting each observation and could allow for larger data sets to be analysed. Estimating the uncertainty of these measurements allow for better interpretation of the observations, and the ability to rigorously accept or reject scientific hypotheses on Earth structure or its processes.

Previous efforts have been made in automating standard seismic processing techniques such as shear wave splitting (Teanby et al., 2004) and $H - \kappa$ stacking (Ogden et al., 2019). Methods also exist to estimate uncertainties in the beamforming methodology (Bear and Pavlis, 1997; Lin and Roecker, 1996; Ritsema et al., 2020) and to improve the detection of one or multiple arrivals (Gal et al., 2016; Gal et al., 2014; Schmidt, 1986). The method we propose differs from these by automatically identifying the number of arrivals with their slowness vector properties and uncertainties. To our knowledge, no method has been proposed that does all of these at once. The method we present later uses a linear relative beamforming process; however, this method can be applied with other techniques such as phase weighted stacking (Schimmel and Paulssen, 1997) or cross-correlation beamforming (Ruigrok et al., 2017).

Machine learning methodologies are becoming more prevalent in the geosciences (for a review see: Bower et al., 2013) and seismology (for a review see: Kong et al., 2019) with methods used to automate data selection (e.g. Thorne et al., 2020; Valentine and Woodhouse, 2010) and extracting properties from data by mapping seismograms to lower dimensional space using autoencoders (Valentine and Trampert, 2012) or sequence seismograms and identify features such as the presence of seismic scatterers (Kim et al., 2020). Here we use an unsupervised learning algorithm as part of our automation technique.

In the approach we present in this paper, we create subsets of waveforms using bootstrap sampling (Efron, 1992). For each sample, beamforming (Rost and Thomas, 2002) corrected for a curved wavefront (Ward et al., 2020) is used to search over a range of slowness vectors and recover the slowness vectors of potential seismic arrivals. The slowness vector measurements of all the individual bootstrap samples are collected and we use the DBSCAN (Density-Based Spatial Clustering of Applications with Noise) algorithm (Ester et al., 1996a) to identify clusters of slowness vectors as seismic arrivals. DBSCAN is an unsupervised learning algorithm that uses the density of points to classify them as part of a cluster or as noise. For further details, see Section 3.2.

By bootstrapping the traces, and therefore creating random subsets of the stations in the array, the scatter of the measurements in each cluster can give an estimate of the combination of some of the previously mentioned uncertainties. The uncertainty estimate will account for the following phenomena which cause different subsets of stations to have different slowness vector measurements:

- signal aberration where the arrival time of the wave at stations deviates from the prediction due to local array structure;
- incoherent or coherent noise;
- the horizontal slowness of the wave changing as it moves over the array, due to the size of the array, or unaccounted for velocity variations within the array;
- heterogeneous distribution of the stations causing heterogeneous sampling of the wavefield;
- slowness resolution limitations of the array aperture; and
- wavelet shape changing over the array.

All of these can relate to local structure or effects within the array and the uncertainty estimate describes the combination of all effects on the wavefield. If a measured slowness vector deviates from the 1-D Earth model prediction and is not within the uncertainty estimate, then the cause of this deviation must be external to the array and local structure. Determining the cause of these deviations to structures such as

a dipping Moho, or deeper structure requires additional information and might be resolvable through e.g. forward modelling. We do not try to measure the uncertainties of that aspect, only those listed above.

We tune the parameters of the DBSCAN algorithm on a visually inspected dataset where each observation is labelled as having either 0, 1, or 2 arrivals. More arrivals are possible, but in this dataset the maximum number confidently observed is 2. In this dataset, observations with more than one arrival are hypothesised to be caused by multipathing, one of many phenomena which can cause multiple arrivals. Multipathing occurs when the wavefront is incident of a sufficiently large velocity gradient causing different parts of the wavefield to move at different velocities, diffract and refract. Multipathing results in 2 arrivals arriving at the station at different times and different slowness vector properties. The predictions made by the method are compared to the labels given from visual inspection to find the best parameters for the DBSCAN algorithm. Following this, we show the effectiveness of this automated method on finding the slowness properties of short-period PKP scattering and long-period surface wave arrivals. Guidance on using the method is given in Section 3.5. We find the parameters work well for our example applications with a minor change needed for the surface wave example. Tuning the algorithm can be done for specific applications.

3.2 Method Overview

This section outlines the method to automatically measure the slowness vector properties with uncertainty estimates. The process can be roughly broken down into the following steps with more detail given below and a summary figure in Figure 3.1.

1. Create a number of bootstrap sub-samples (1000 here) through random sampling with replacement of a set of waveforms recorded at the seismic array in question.

2. For each bootstrap sample, use beamforming (Rost and Thomas, 2002) correcting for a curved wavefront (Ward et al., 2020) to search over a grid of slowness vectors and find how the power of coherent energy varies with backazimuth and horizontal slowness. Therefore, each bootstrap sample will have its own grid of power values.

3. Calculate a noise estimate for the bootstrap sample by shifting each trace in the bootstrap sample with a randomly generated time. These scrambled traces are then stacked and the power of the beam is measured. This is repeated 1000 times and the mean power is taken as the noise estimate.

4. Set all power values in the slowness grid below the noise estimate to zero.

5. From the resultant power distribution, take up to X peaks (in this study we take up to 3 peaks), which describe the slowness vectors of possible arrivals.

6. Gather the locations for these peaks of all the bootstrap samples.

7. Use DBSCAN, a density-based clustering algorithm, to identify the arrivals and measure their slowness properties with uncertainties.

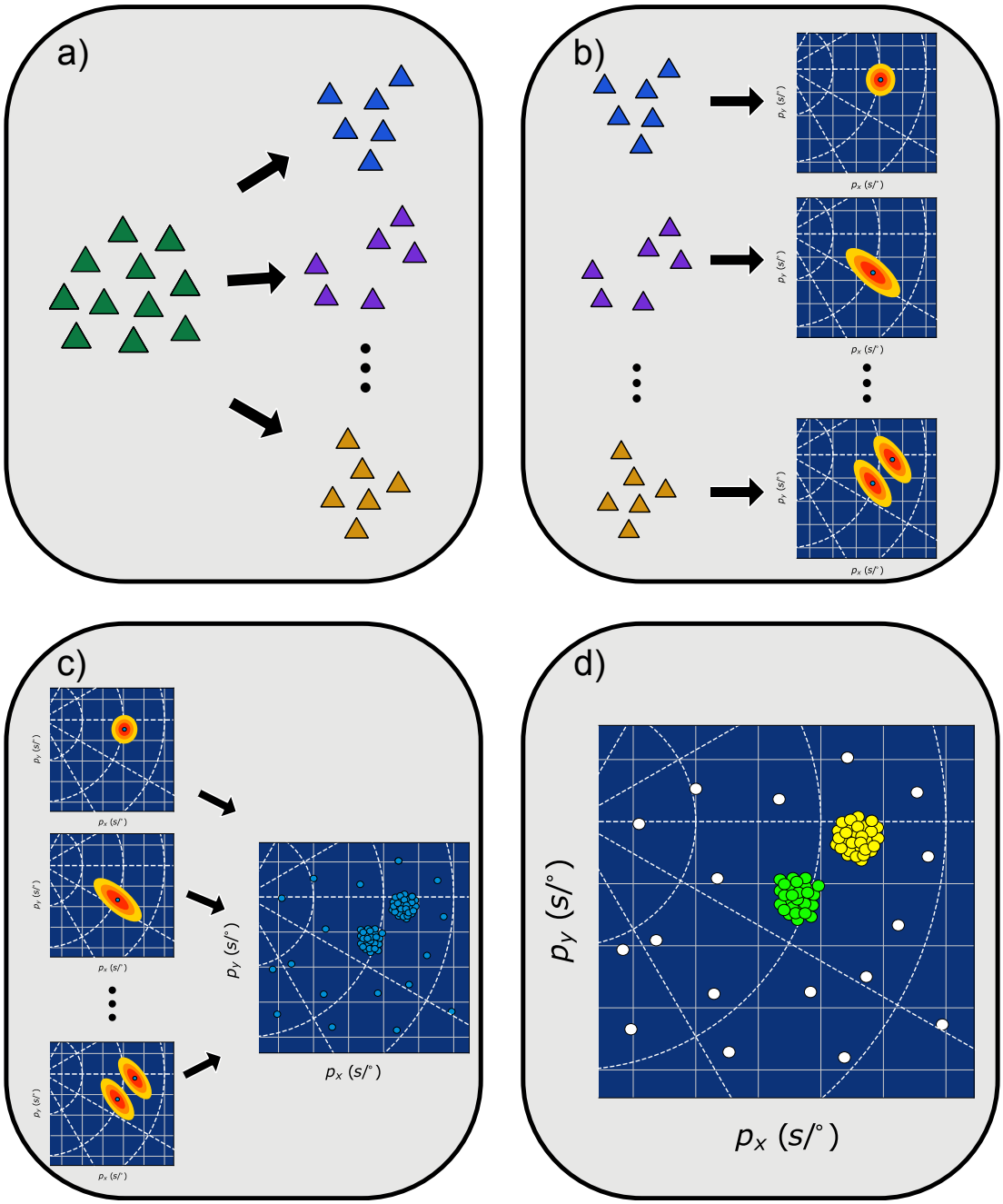

Figure 3.1: Cartoon illustrating the method to automatically identify arrivals in slowness space and measuring their slowness vector properties with uncertainty estimates. First bootstrap sample the traces recorded at an array N times creating N random sub arrays (a). Then, for each bootstrap sample, perform linear beamforming grid search and recover the top peaks (b). Once this is done, collect all the points from all N samples (c). Finally, apply clustering algorithm DBSCAN (Ester et al., 1996b) to identify regions dense enough to form clusters and, from their location, measure their slowness vector properties.

3.2.1 Bootstrapping and peak recovery

One advantage of the bootstrap sampling process is that bootstrap samples of the stations in the array are used. Beamforming subsets of the array lead to different peak power in the beams which leads to variations in the recovered slowness vectors for each arrival. When all of the slowness vectors are taken into account, using all of the bootstrap sampled arrays, we obtain uncertainty estimates in the slowness vector. These uncertainty estimates will include the effect that array geometry and local structure has on the slowness vector measurements. For each bootstrap sample, we use a relative beamforming method where the traces are aligned on a target slowness before searching over the slowness vectors. After the beamforming, we calculate a noise estimate using the traces in the bootstrap sample with a similar method to Korenaga (2013). The traces are aligned using the slowness vector with the highest power. Then, they are randomly shifted in time, stacked and the power of the stack calculated. This is repeated 1000 times and the mean of all power estimates is used for the noise power estimate. All power values in the beamforming plot (Fig 3.2) below three times this noise estimate are set to zero. Multiplying the estimate by three was determined by exploratory analysis and found to give the most satisfactory result. This can be changed depending on the application. To remove local power maxima, the power distribution is smoothed using a 2-D Gaussian filter. The 2-D Gaussian is formed by the product of two 1-D Gaussians. The standard deviation of the 1-D Gaussians is equal to the grid spacing (0.05 s/°), therefore will have a full width at half maximum of 0.12 s/°.

The 2-D Gaussian acts as a point spread function and is convolved with the power plot to smooth it and remove local maxima. After this, the top X peaks are taken from the power distribution. The peaks are found with a maximum neighbourhood filter which identifies points with higher power values than those in the surrounding neighbourhood. Fig 3.2 shows how the peaks are found for each bootstrap sample.

3.2.2 Identifying arrivals with cluster analysis

The peaks recovered for each bootstrap sample are then collected and the clustering algorithm DBSCAN (Ester et al., 1996a) is used to find clusters. DBSCAN is an unsupervised learning algorithm that uses the density of points to identify clusters and noise. The algorithm takes a radius ϵ and a minimum number of points (MinPts) to define a minimum density for points to be a cluster. Here, we define MinPts as a fraction of the number of bootstrap samples. DBSCAN sorts the data into three categories as visualised in Fig 3.3.

1. Core point: A point with at least MinPts points within its neighbourhood (i.e. within radius ϵ).

2. Boundary point: A point within the neighbourhood of a core point, but without

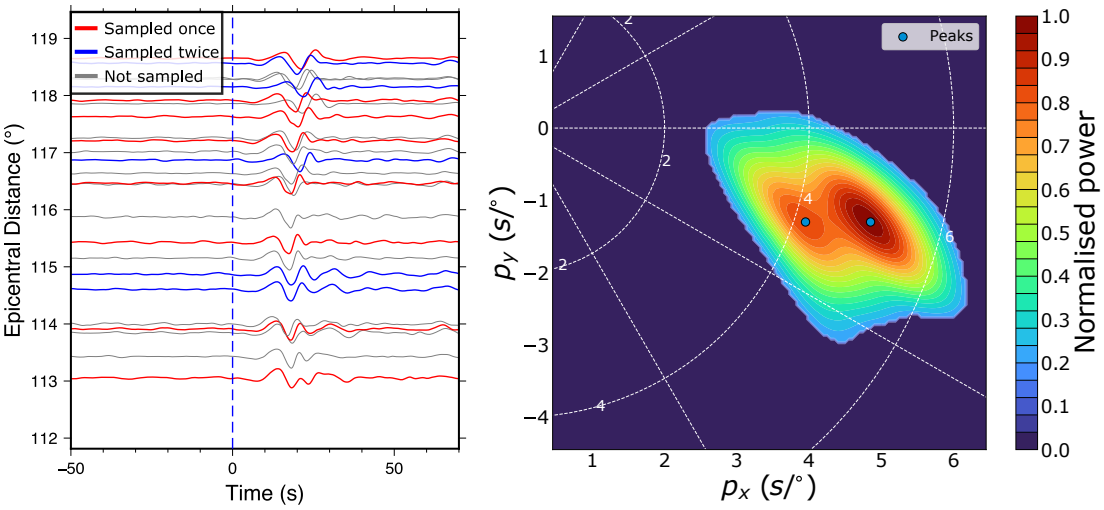

Figure 3.2: Example of recovery of peaks from a bootstrap sample of traces. The left figure shows a record section of data from the 05, April 1999 event recorded at the Kaapvaal array in Southern Africa (event metadata in the supplementary material). The traces are coloured by the number of times they have been sampled. The data had the instrument response removed and are filtered between 0.10 and 0.40 Hz before beamforming. The right figure shows the power distribution at each slowness vector with powers lower than the noise estimate set to zero and the 2-D Gaussian smoothing filter applied. Here each point on the grid represents a slowness vector described with their x (p_x) and y (p_y) components. In this example, two peaks have been recovered.

MinPts points in its own neighbourhood.

3. Noise: Points that are not within ϵ of a core point and does not have MinPts points within its neighbourhood.

The DBSCAN algorithm begins at a random point and measures its density by the number of points within the radius ϵ (Fig 3.3). If the density is lower than the threshold defined by ϵ and MinPts, the point is classified as noise (yellow points in Fig 3.3) and the algorithm moves on to another random point. If the density is higher than the defined threshold, the point is classified as a core point and cluster formation begins (red points in Fig 3.3). Points within ϵ of the core points then have the number of points in their neighbourhood measured. Those which do not have MinPts points within their neighbourhood are boundary points and are still part of the cluster (blue points in Fig 3.3). The points which do have MinPts points in their neighbourhood are classified as core points and added to the cluster. The points within ϵ of these new core points are also searched and the cluster expands until it finds no new core points to add to the cluster. Once no new core points can be added, an unexamined point is chosen at random and the process begins again. This process continues until all points have been examined. In this manner, DBSCAN can separate high-density clusters from low-density noise. Fig 3.4 shows the result of DBSCAN applied to the peaks recovered after the bootstrapping process.

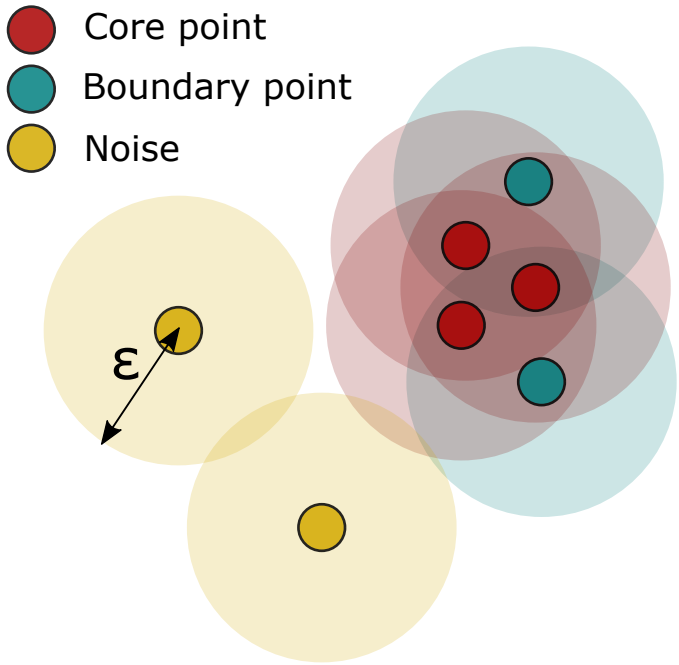

Figure 3.3: Cartoon illustrating what classifies as a core point, boundary point or noise. The neighbourhoods of the points are shown as a lighter colour of the point itself. The minimum number of points needed for a core point is 4 in this example. The red points all have at least 4 points in their neighbourhood, so are defined as core points. The blue points are within the neighbourhood of the core (red) points, but do not have 4 points in their own neighbourhood and are classified as boundary points. The yellow points are classified as noise because they are not in the neighbourhood of a core point and do not have 4 points within their own neighbourhood.

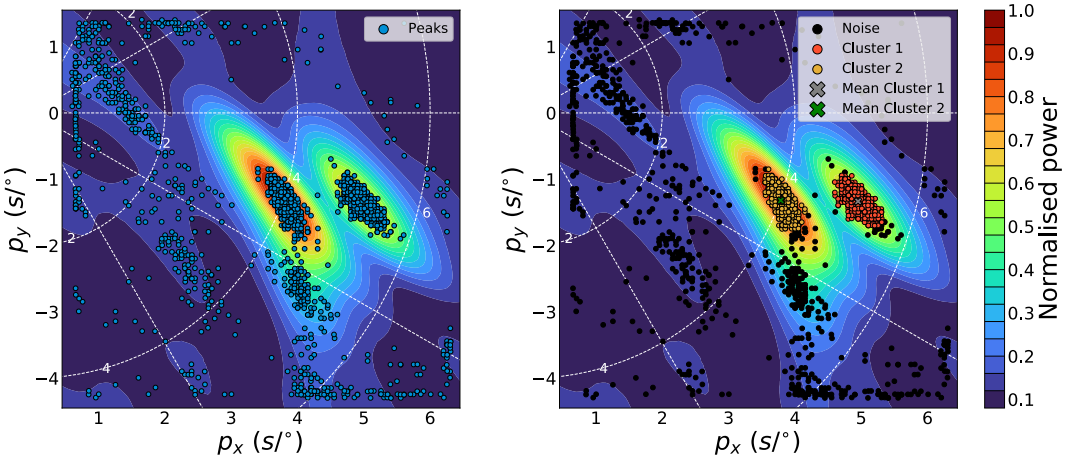

Figure 3.4: Cluster retrieval from points recovered through bootstrap sampling the traces (Fig 3.2). The left figure shows all the power peaks (blue dots) recovered using data from the 05 April 1999 event. The right image shows the clusters found by the DBSCAN algorithm (Ester et al., 1996a) where MinPts is 0.25 and ϵ is 0.2 $s/°$. The red and yellow points are classified as clusters 1 and 2 respectively and the black points are noise. The background power distribution is the mean of all the power distributions found from bootstrap sampling.

DBSCAN has advantages over other clustering algorithms such as k-means (MacQueen et al., 1967) for this application such as:

1. It does not take the number of clusters as input so visual inspection before the clustering is not required.

2. Not all points need to be part of a cluster allowing for noise.

3. If clusters are not well separated or the data is noisy, clusters of non-hyperspherical shape can still be recovered unlike k-means (Celebi et al., 2013; Ertöz et al., 2003).

There are also disadvantages to DBSCAN:

1. If the range and data are not well understood, choosing the parameters can be challenging.

2. Clustering data with large variations in density is challenging because there may be no combination of ϵ and MinPts which will find all of the clusters.

3. Clusters separated by a distance smaller than ϵ will be combined into one cluster.

We tested other density-based clustering algorithms such as HDBSCAN (Campello et al., 2013; Campello et al., 2015) and OPTICS (Ankerst et al., 1999) but found that both techniques have issues for this application. HDBSCAN (Hierarchical DBSCAN) searches over a range of ϵ values and measures over what length scales a cluster "persists" while containing a minimum number of points to form a cluster. Using how long each cluster survives and how many points it contains at each ϵ, clusters are extracted with the excess of mass algorithm (EOM) (McInnes and Healy, 2017). HDBSCAN will preferentially return a large, single cluster because one large cluster will usually contain more "mass" (for a detailed explanation, see McInnes and Healy, 2017). To avoid one large cluster being returned when multiple clusters exist, HDBSCAN by default will not return a single cluster as an output. If this default is kept, instances with one arrival (cluster) will be misidentified. Changing the default and allowing HDBSCAN to return one cluster will mean phenomena causing multiple arrivals (such as multipathing) may not be identified as EOM will preferentially return a single cluster.

OPTICS (Ordering Points To Identify the Clustering Structure) (Ankerst et al., 1999) is another density-based algorithm that specialises in identifying clusters of varying density. OPTICS orders the points to represent the clustering structure. From this, clusters can be extracted. When using OPTICS, we found the size of the clusters retrieved was too inconsistent to estimate the uncertainties of slowness vector properties. Because of these considerations, we decide to use DBSCAN instead of OPTICS or HDBSCAN.

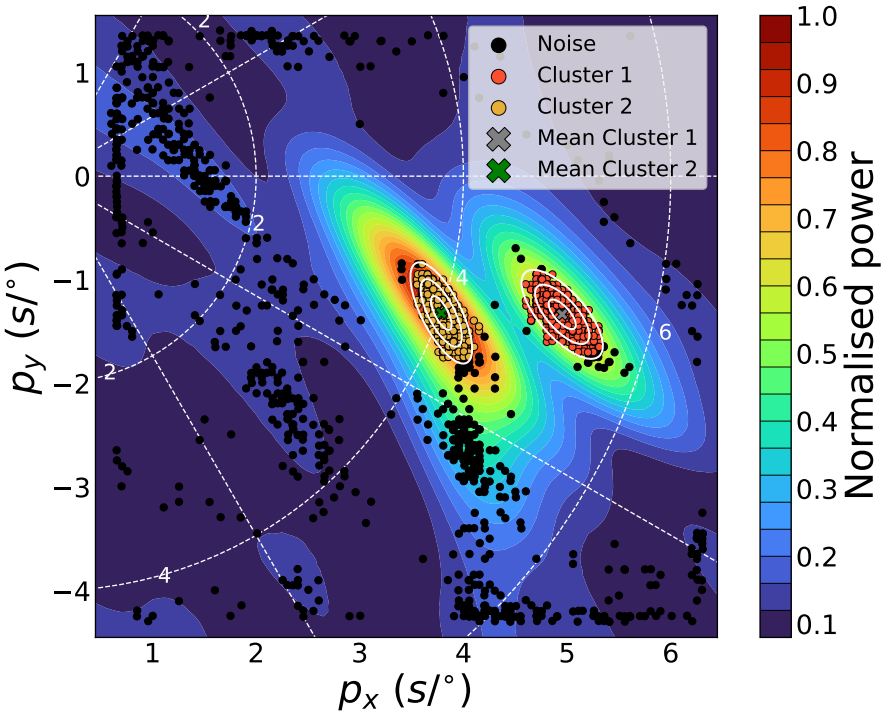

Figure 3.5: Example of error ellipses for 1,2 and 3 standard deviations. The data are the same as used in Figs 3.2 and 3.4. The background power plot is the mean of the power plots searching over a range of slowness vectors from each bootstrap sample.

3.2.3 Slowness Vector Uncertainty Estimates

We estimate the uncertainty with the standard deviation of backazimuths and horizontal slownesses in each cluster and also use the area of error ellipse of the clusters as a relative measure of uncertainty of each observation. The error ellipses are found by calculating the eigenvectors and eigenvalues of the covariance matrix for each cluster. These eigenvectors and eigenvalues give the directions and magnitudes of the maximum variances in the cluster which is used to determine the width, length and orientation of the ellipse. Fig 3.5 shows clusters plotted with their error ellipses for 1, 2 and 3 standard deviations. We would like to highlight the importance of the slowness grid dimensions; if the slowness grid is too small, the arrivals may be truncated at the edge leading to a smaller cluster and underestimate the uncertainty.

3.3 Parameter Tuning

To find the best parameters to use with the DBSCAN algorithm (ϵ and MinPts), we compare the number of arrivals predicted by the algorithm to the number of arrivals identified from visual inspection. We use the same dataset as Ward et al. (2020) which used SKS and SKKS data recorded at the Kaapvaal array in southern Africa. Ward

et al. (2020) make observations at a range of frequency bands (Table 3.1) using the whole Kaapvaal array and several sub-arrays. The data which have been labeled as having zero arrivals are where an SKS arrival is not observable due to noise. This is due to the frequency dependence of SKS amplitude. In the data where a human cannot identify a clear arrival, there will still be coherent signal in there which is a limitation of this test. We test the method on data with no coherent signal later in Section 3.3.1. The traces are first aligned on the predicted slowness of SKS or SKKS depending on the arrival of interest. The beamforming is conducted in a time window that is 20s before and 40s after the predicted arrival.

The dataset provides a good test for the algorithm since it has clear single arrivals, multipathed arrivals (2 arrivals) and observations that are too noisy to identify any arrivals (0 arrivals). Each observation is labelled from visual inspection of the distribution and density of the points collected from all the bootstrap samples and the mean power distribution of all the bootstrap samples. If the algorithm predicts a higher number of arrivals than the human given labels, we assume here the algorithm has identified noise as arrivals. If the algorithm predicts a lower number of arrivals, the density threshold is too high for arrivals to be identified. Due to the subjective nature of the labelling, this may not always be the case, but for the tuning process, we assume the human labels are a ground truth. Observations, where it was not clear whether there are one or two arrivals, are labelled as "1-2 arrivals" and excluded from this tuning process.

We searched over a range of ϵ and MinPts values and predict the number of arrivals in each observation. This is compared to the human labels in Table 3.1 and an accuracy score is calculated. The accuracy score is defined as the number of instances where the method correctly predicts the number of arrivals relative to the total number of instances ($\frac{No.\ correct\ predictions}{Total\ instances}$). Values of ϵ range from 0.05 to 1.0 s/° and MinPts is given as a fraction of the bootstrap samples (1000 here) and varies from 0.05 to 1.0. Fig 3.6 shows how the accuracy varies in the parameter space. The grid search shows the sensitivity of our method to the DBSCAN parameters chosen. With some parameters, the accuracy can exceed 90% while with others it can be less than 20%. The method performs the worst with small ϵ and high MinPts meaning the minimum density criteria will be very high and very few arrivals will be found.

We test how well the algorithm generalises using cross-validation. Cross-validation involves splitting the dataset into N representative subsets (5 here). One of the subsets is removed and the grid search is conducted on the remaining $N-1$ subsets and the best set of parameters recorded. The removed subset acts as a validation set. Then we take these best parameters and make predictions on the validation set. The accuracy of the predictions for the validation subset is measured and gives an indication of how well the algorithm generalises. The process is repeated by sequentially removing one subset and tuning the parameters on the remaining $N-1$ subsets. After the cross-validation

Table 3.1: The number of labels in each frequency band. Labels indicate the number of arrivals in that observation and 1-2 could be either 1 or 2. In total, there are 2628 labels with 2489 used in the tuning.

Frequency (Hz)	**Number of Arrivals**			
	1	**2**	**1-2**	**0**
0.07 - 0.28	403	18	10	7
0.10 - 0.40	378	21	20	19
0.13 - 0.52	326	33	25	54
0.15 - 0.60	308	28	23	73
0.18 - 0.72	280	27	27	104
0.20 - 0.80	253	35	28	122
Total	1948	162	133	379

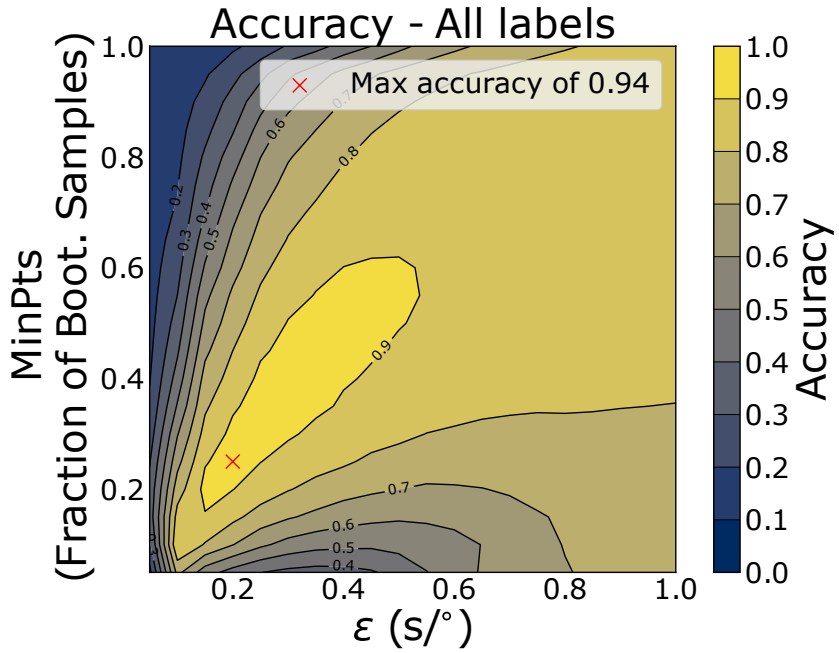

Figure 3.6: Grid search of DBSCAN parameters ϵ and MinPts (given as a fraction of bootstrap samples). For each combination, the number of arrivals in each observation are predicted, compared to the true labels (Table 3.1) and the accuracy calculated. The location of the highest accuracy value is plotted as a red cross where $\epsilon = 0.20$ $s/^\circ$ and MinPts = 0.25.

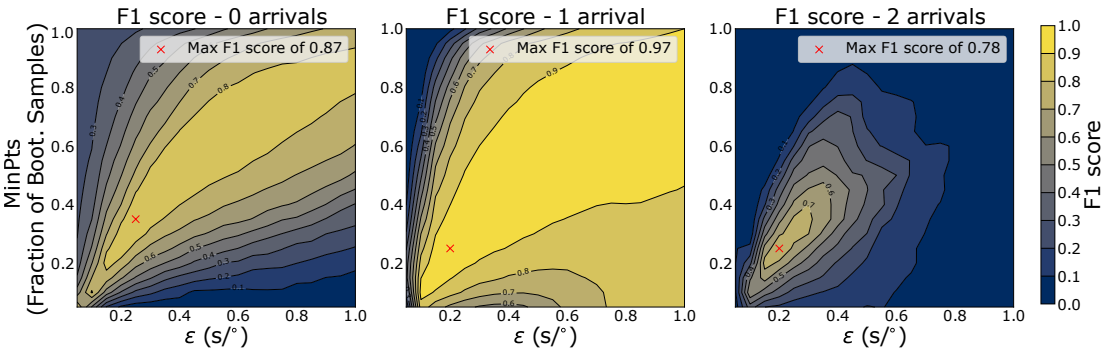

Figure 3.7: F_1 scores for combinations of DBSCAN parameters ϵ and MinPts where each plot represents a different target labels of 0 arrivals (left) one arrival (centre) and two arrivals (right). The location of the highest F_1 score is plotted as a red cross, which has parameters of $\epsilon = 0.20$ s/° and MinPts $= 0.25$ for 1 and 2 arrivals and $\epsilon = 0.25$ s/° and MinPts $= 0.35$.

process, there are N estimates indicating how well the algorithm performs on unseen data. Here we split the data into 5 subsets because of the low number of multipathed (2 arrivals) and 0 arrivals samples. Cross-validation and measuring the accuracy gave a mean accuracy of 0.939 with a standard deviation of 0.0090. In all the cross-validation samples, the best parameters were $\epsilon = 0.20$ s/° and MinPts $= 0.25$.

As there are many more instances of observations with one arrival, we also analyse each of the target labels (0,1 or 2 arrivals) individually using the precision, recall and F1 measures (defined below). These measures all depend on the number of true positive (TP), true negative (TN), false positive (FP) and false-negative (FN) instances. These are best understood with an example. If the target label is "2", true positives are instances where the algorithm correctly identifies 2 arrivals in an observation. True negatives are instances correctly identified as not having 2 arrivals (1 or 0 arrivals). False positives are those incorrectly identified as having 2 arrivals. False negatives are instances where 2 arrivals have not been identified when they should have been.

From these measures, the precision is defined by $P = \frac{TP}{TP+FP}$. This is essentially the proportion of the target labels which have been correctly identified. The recall, $R = \frac{TP}{TP+FN}$, is a measure of how many of the target labels has been recovered by the algorithm. The F_1 score is the harmonic mean of the precision and recall and can be described as $F_1 = \frac{2}{\frac{1}{P}+\frac{1}{R}}$. The F_1 score is only large if both the recall and precision are high. We only present the F_1 score as it shows which parameters have both high precision and recall. Fig 3.7 shows how the F_1 score varies with different parameter combinations for each target label.

Figures 3.6 and 3.7 show that the method is capable of greater than 90% agreement with the observations of a human. This is mainly from observations with one clear arrival, which makes up the majority of the observations. The algorithm also performs well with more complex observations of multipathing with a F_1 score of over 0.75. This

Table 3.2: Table of the cross-validation result for each of the labels (0,1 or 2 arrivals) where the F_1 score is the measure of success. Notice the standard deviation is an order of magnitude higher for labels 0 and 2, most likely because of the significantly fewer instances of those labels in the subsets created during cross-validation.

No. Arrivals	Mean F_1 score	Standard Deviation	Best Parameters
0	0.86	0.030	$\epsilon = 0.35$ s/° MinPts = 0.25
1	0.97	0.0063	$\epsilon = 0.20$ s/° MinPts = 0.25
2	0.78	0.035	$\epsilon = 0.20$ s/° MinPts = 0.25

method is quite insensitive to noise as it does not regularly incorrectly identify noisy observations as shown by a F_1 score of over 0.85 for observations with 0 arrivals. As with the accuracy, we use cross-validation to see how well the parameters generalise with new data. Table 3.2 shows the mean F_1 scores for the individual labels. As in Figure 3.6, there are DBSCAN parameters that perform very poorly showing the importance of the parameters used.

The cross-validation analysis of all the labels and F_1 score on the individual labels show the parameters $\epsilon = 0.20$ s/° and MinPts = 0.25 are consistently found to be the best. Inferring how well the parameters generalise from this analysis is limited because of the low number of cross-validation samples (5 here). The low sample number was necessary because of the small number of observations with 2 and 0 arrivals. Despite this, the mean values obtained for the accuracy score and F_1 scores from the cross-validation are very similar to that obtained by tuning with all the data (Figs 3.6 and 3.7). The standard deviations from the cross-validation are low suggesting similar performance on similar datasets.

Due to the subjective nature of labelling each observation with the number of arrivals, some difference between the method's prediction and the human labels is acceptable. To analyse how reasonable the predictions are when the technique disagrees with the human labels, we create a confusion matrix using the predictions with parameters of $\epsilon = 0.20$ s/° and MinPts = 0.25 (Fig 3.8). In the confusion matrix, each row represents a true label (number of arrivals in this case) and each column the predicted arrivals. The values at each point in the matrix indicates how many times that true label is identified as the corresponding predicted labels. For example, for all instances with the true label of 1 arrival, the confusion matrix will show how many are correctly classified as having one arrival and how many are incorrectly identified with 0, 2 or 3 arrivals. We normalise the values along each row of the confusion matrix so for each true label, the columns show the proportion of the predictions given to that label. For example, for the instances with a true label of '0 arrivals', 80 % of the predictions are

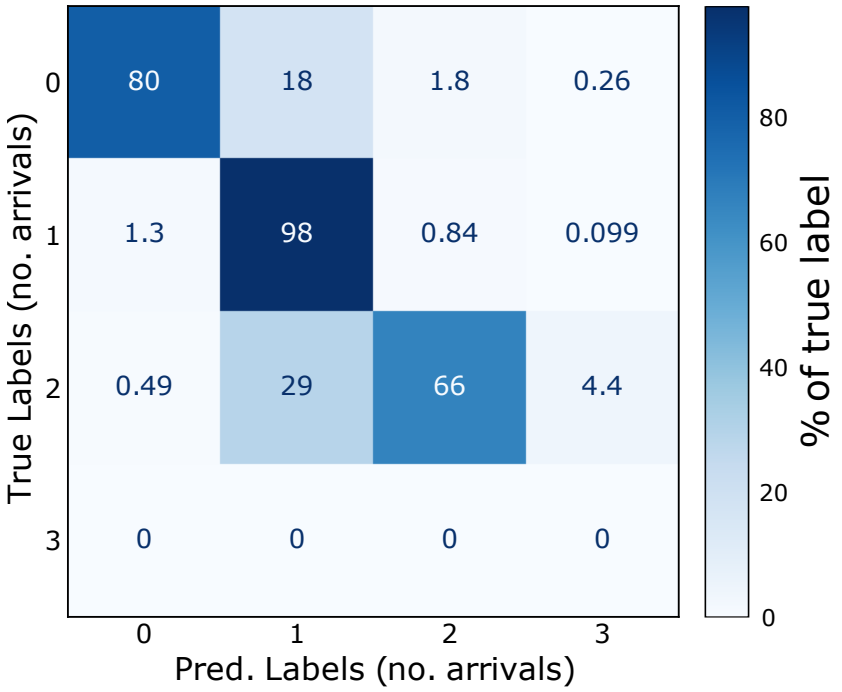

Figure 3.8: Confusion matrix for predictions made with $\epsilon = 0.20$ s/° and MinPts = 0.25. Each row represents a true label (number of arrivals) and each column the predicted arrivals. The values on the diagonal of the matrix show the percentage of correct predictions for the true label.

correctly identified as having 0 arrivals, 18 % are identified as having 1 arrival and so on.

The confusion matrix shows that when the method prediction differs from the human labels, the predictions it makes are not radically unreasonable. It is worth remembering the labelling process is quite subjective and just because the algorithm predicts a different number of arrivals to that labelled by a human, does not mean it is wrong. It is possible that some of the human labels with two arrivals only have one arrival or some have three arrivals. Equally, it is possible some instances labelled with no arrivals do have one arrival but a human could not confidently identify it above the noise. Fig 3.8 shows the algorithm makes reasonable predictions in the vast majority of the cases for this data set using the parameters found from the tuning process and cross-validation. Analysis of the uncertainty estimates shows the slowness vector measurements have small variation with the mean standard deviation for backazimuth measurements of 1.2° and horizontal slowness of 0.14 $s/°$. The mean area bounded by the 95% confidence ellipse is 0.14 $s^2/°^2$.

Analysis of the confusion matrix in addition to the findings from the cross-validation process shows the parameters $\epsilon = 0.20$ s/° and MinPts = 0.25 will give reasonable results that will generalise well. We use these parameters in other applications with a minor change for applications to surface waves (Section 3.4).

3.3.1 Test with incoherent data

As mentioned previously, the data used for the parameter tuning was analysed in several frequency bands and, after the analysis, labeled with the number of coherent arrivals. Where the observation was too noisy to identify, coherent arrivals is labeled as having zero arrivals. It should be restated; the lack of a clear arrivals is because at the higher frequencies the SKS arrival may have too low an amplitude to be observed. At lower frequencies, the same data may have a coherent arrival observable to a human. At higher frequencies, while the data may be too noisy for a human to identify coherent arrivals, there will be coherent signal in the traces. Therefore, it is not a true test of how the method will perform when there is no coherent signal to be found. In this section, we outline how we evaluate the performance of the method when applied to random data.

Using SKS data recorded at the Kaapvaal array from the 25 May 1997 event, we take a random 40 second time window from each of the traces. This is the random data used to test the method. We keep the array geometry the same and use the same parameters as outlined in the previous sections. Once the peaks have been collected, we apply DBSCAN to find the number of arrivals. The DBSCAN parameters we choose to use are those which performed best after the parameter tuning (Section 3.3). This then gives the number of arrivals found when given random noise. We repeated this process 500 times, each with different random data, and the method found 0 arrivals in total. This shows the effectiveness of this method in not finding arrivals when none are present.

3.4 Applications to PKP scattering and Rayleigh wave multipathing

This section provides two example applications of this method to study Earth structure. First, we show an example identifying a PKP precursor in the high-frequency teleseismic wavefield (0.5 to 2 Hz). Coherent precursors are indicative of scattering caused by small scale structures and our method can constrain uncertainties on their location. Then, we show an example of low frequency (0.04 to 0.06 Hz) Rayleigh wave multipathing. Using our method to identify Rayleigh wave multipathing, we can interpret possible causes of multipathing and provide uncertainties for phase velocity measurements. All measurements of backazimuth and horizontal slowness are shown with one standard deviation describing the uncertainties.

3.4.1 PKP precursors

Analysing the slowness vectors of PKP precursors is indicative of their location and whether they are caused by source or receiver side structure (Haddon and Cleary, 1974). We use PKP data from Thomas et al. (1999) who observe several scatterers beneath Europe and Eastern Asia. Of the data used in Thomas et al. (1999), we focus on a single event occurring on 15 September, 1992 which shows clear PKP precursors. We only use data recorded at the Gräfenberg array and not the larger GRSN array to avoid spatial aliasing. In this example, the PKP precursors appear to be coherent from visual inspection of the seismograms (Fig 3.9). Coherent precursors suggest they probably originate from localised scatterers such as an Ultra Low Velocity Zone (ULVZ) (Ma and Thomas, 2020).

Fig3.9 shows the traces used for this example and the clusters found by our algorithm. The data have the instrument response removed and are filtered between 0.5 and 2 Hz before the beamforming process. We used a time window of 10 s before the predicted PKIKP arrival and the same DBSCAN parameters found from the tuning (ϵ = 0.20 s/° and MinPts = 0.25). The method identifies a single precursor arriving with a backazimuth of 58.6° ± 2.3° and a horizontal slowness of 2.93 s/° ± 0.32 s/°. This is similar to the slowness vector properties of the dominant arrival found by Thomas et al. (1999) arriving 6.5 s before PKIKP with a horizontal slowness of 2.8 s/° and backazimuth of 53.6°. Unlike Thomas et al. (1999), we only identify one precursor rather than three. We believe this is because our time window encompasses all precursors meaning if one precursor has a significantly higher amplitude it may be the only one recovered. Furthermore, visual inspection of waveforms suggests a single dominant precursor (Fig 3.9). The range of possible horizontal slowness of this PKP precursor inferred from the uncertainty of the measurement (2.93 s/° ± 0.32 s/°) at a distance of approximately 140° means this precursor could originate from either source side or receiver side structure (Haddon and Cleary, 1974).

3.4.2 Rayleigh wave multipathing

The second example shows the identification of multipathed Rayleigh waves. From this observation, the phase velocities and backazimuths of the multipathed arrivals can be measured and analysed with uncertainty bounds. Xia et al. (2018) identify multipathing in Rayleigh waves in the western US and suggest this is caused by the transition from continental to coastal to oceanic structure each with unique velocity profiles. We analyse Rayleigh waves from an event on 05 January 2013 recorded at the Southern California Seismic Array (CI) to identify multipathing and hypothesise some potential causes. The instrument response is removed and traces are filtered between 0.04 and 0.06 Hz. The time window used in the relative beamforming is 200 s before and after the predicted arrival time assuming a velocity of 3.5 km/s. In this example,

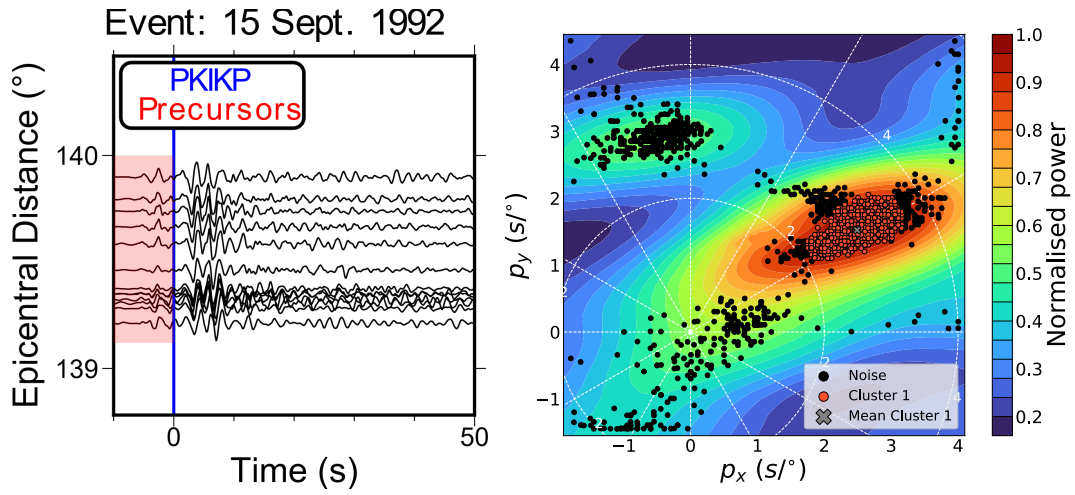

Figure 3.9: Example application of the method on PKP precursors. This example uses data from the 15 September, 1992 event recorded at the Gräfenberg array in Germany (GR) filtered between 0.5 and 2.0 Hz. The left subfigure shows the traces used in the example which are aligned on the predicted PKIKP arrival time and the time window for the analysis shown in red. On the right, the result of the algorithm with parameters of $\epsilon = 0.2$ s/° and MinPts = 0.25.

the points in each cluster are distributed over a different slowness-space scale that is an order of magnitude lower than in the body wave examples. The difference is due to the Rayleigh wave velocity and the change in units. p_x/p_y for body waves will vary on the order of 10^0, whereas for Rayleigh waves p_x/p_y vary on the order of 10^{-1}, an order of magnitude lower. Because of this, the ϵ parameter is also lowered by an order of magnitude from 0.20 $s/°$ found from tuning to 0.02 s/km.

Fig 3.10 shows the result of the clustering method, which identifies three multipathed arrivals with backazimuths of 319° ± 0.7°, 344° ± 1.3° and 299° ± 1.4° and velocities of 3.6 ± 0.025, 3.5 ± 0.032 and 3.8 ± 0.093 km/s respectively. For each arrival, we mark the path from the mean station location along the mean backazimuth (dashed white line in Fig 3.10) to determine a possible cause for the multipathing. Also shown are the paths showing the backazimuth uncertainty bounds (solid white lines in Fig 3.10), which suggest it is reasonable to hypothesise possible causes of the measurements. We investigate dispersion in the wave velocities by repeating the analysis in three frequency bands of 0.035 – 0.045, 0.045 – 0.055 and 0.055 – 0.065 Hz, finding differences in the number of arrivals and their backazimuths, but no absolute slowness variation between frequencies (See appendix Figure B.1). We argue this is a result of the different scale lengths of the structures which cause the observed multipathing, and not because of a property of the material the wave is travelling through.

The top and middle paths may come from interactions with the boundary between the continental and coastal regions, which agrees with the interpretation of Xia et al. (2018). The direction of the westernmost arrival suggests it could be caused by

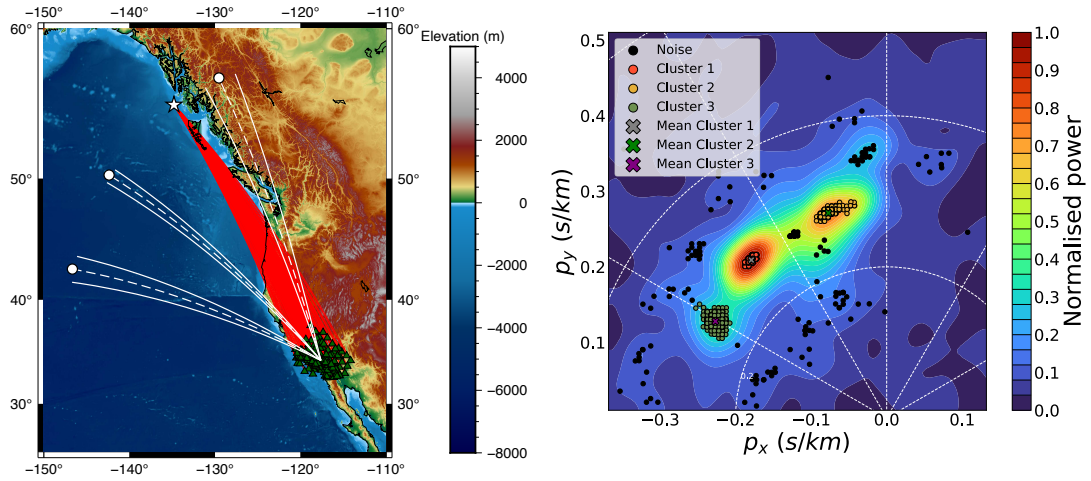

Figure 3.10: Example application of the method for identifying multipathing in surface waves. The left subfigure shows the raypaths (red lines) from the 05 January, 2013 event (white star) to the Southern California Seismic Array (CI) stations (green triangles). Before the beamforming, the data were filtered between 0.04 and 0.06 Hz. In this example, three arrivals have been identified by the algorithm (right subfigure). For each arrival, a path is marked from the mean station location along the mean backazimuth to a point with the same epicentral distance as the event (dashed white lines and circles). The solid white lines indicate the uncertainty bounds of the backazimuth for the measurement.

interacting with a coastal-ocean velocity transition or possibly due to more localised velocity variations. Further modelling is beyond the scope of this work, but our results demonstrate the potential of the method to investigate such phenomena efficiently.

The phase velocities of the arrivals may be indicative of azimuthal anisotropy beneath the array. The phase velocities of the central and easternmost arrival are the same within the uncertainties (3.6 ± 0.025 km/s and 3.5 ± 0.032 km/s respectively). The westernmost arrival moves with a significantly higher phase velocity over the array (3.8 ± 0.093 km/s) along a backazimuth of $299° \pm 1.4°$. While we do not have enough measurements to fully explore the nature of this azimuthal anisotropy beneath the array, our observation of a faster arrival from 299° is in line with that found by Alvizuri and Tanimoto (2011) who report a fast direction of approximately 290°. Further analysis would be needed to recover the anisotropic properties, but this example shows how our technique can be used to identify statistically significant differences in phase velocity measurements.

3.5 Code guidelines

This section outlines some guidance to use this technique in terms of parameter selection and computation time. There are many potential aspects of a study that can influence the method's effectiveness such as frequency bands, array size and configuration or local receiver side structure. The tuning process (Section 3.3) shows we cover a range

of frequency bands (Table 3.1) and array sizes ($10 - 50$ stations) and the sub-arrays have a wide range of configurations. For applications analysing body waves in similar frequency bands ($0.1 - 1$ Hz) with a similar array size ($10 - 50$), we recommend the parameters (MinPts = 0.25, $\epsilon = 0.2$ s/°) used here as a starting point and adjusted if necessary.

The number of peaks above the noise threshold should be equal to the maximum number of arrivals of interest or expect to be possible. The noise threshold was determined to be three times the noise estimate through exploratory analysis and found to give satisfactory results, but this can be changed depending on the application. DBSCAN parameters ϵ and MinPts of 0.20 $s/^\circ$ and 0.25 respectively will work well for identifying single arrivals and is relatively intolerant to noise. If the study is searching for multipathing, changing MinPts to 0.15 and keeping ϵ as 0.20 $s/^\circ$ increases the accuracy of the multipathed arrivals from 66 % to 75 % but decreases the accuracy of the noisy arrivals from 80 % to 44 %. These alternative parameters would require visual inspection of those identified as multipathing by the algorithm but would significantly reduce the amount of visual inspection as observations with one arrival need not be visually inspected.

For surface waves, the algorithm also works well after changing ϵ to 0.02 s/km. For applications with significantly different frequency bands or array sizes or searching for a very specific phenomenon, the DBSCAN parameters may need to be tuned to optimise performance (Section 3.3). The remaining parameters can be kept the same.

Sensible beamforming practice still applies when using this method and determining the cause of the deviation is up to the user. The effects of spatial aliasing should be taken into account and, if required, the effects of station elevation accounted for as it has been shown to affect slowness vector measurements (Jacobeit et al., 2013).

The computationally intensive part of the method is the bootstrap sampling and the beamforming on each sample, which must be performed for each observation; the cluster analysis is comparatively quick. However, the code is trivially parallelisable over observations since each is independent of all the others. The code is written in Python, is easily editable and freely available (https://github.com/eejwa/Array_Seis_Circle). The code has been parallelised so the bootstrap sampling can be spread over several cores and uses Numba (Lam et al., 2015) to compile the functions into machine code before execution. Further efficiency improvements could be made by rewriting the algorithm in more efficient languages such as Julia, C++ or Fortran, and investigating further performance improvements possible with the existing codebase. For an example array with 20 stations, a time window of 30 seconds, sampling rate of 0.05s and searching over a grid of slowness vector properties with 14641 vectors (a grid where each axis covers 6 s/° in increments of 0.05 s/°), each bootstrap sample

takes approximately 1.6 seconds to process. This makes tens of observations viable on a handful of cores such as on a desktop machine. Larger datasets (thousands of observations) can be processed on the order of hours using hundreds of cores.

3.6 Conclusions

Slowness vector measurements have been used to understand a variety of Earth structures and phenomena. They are typically used to identify wavefield perturbations, scattering and event/noise source localisation. While this analysis is a common tool used by seismologists, studies are limited because of the necessary and subjective visual inspection of observations. Interpretation of the measurements is limited by uncertainties such as the contribution of array geometry, noise and local structure. These may result in different slowness vector measurements depending on which stations are used in the analysis.

In this study, we described a method to automate slowness vector measurement, estimate the uncertainties and identify the number of possible arrivals. To do this, we bootstrap sample the waveforms and in each sample using a relative beamforming process to measure the coherent power and recover slowness vector properties of potential arrivals. These slowness vector properties are collected and the clustering algorithm DBSCAN is used to identify arrivals. The mean of the clusters gives the backazimuth and horizontal slowness and the spread of the cluster gives uncertainty estimates of phenomena that may vary the slowness vector measurement depending on which subset of stations are used. We use a linear beamforming approach but other beamforming methods such as phase weighted stacking (Schimmel and Paulssen, 1997) and cross-correlation beamforming (Ruigrok et al., 2017) can be used.

We tuned the DBSCAN parameters on a data set with 0, 1 and 2 arrivals and achieved $> 90\%$ accuracy in recovering these arrivals. We present examples of analysis of scattered P wave energy and Rayleigh wave multipathing. The advantage this method brings to these applications is the ability to automatically identify the arrivals and measure the slowness vectors with uncertainty estimates. The difference in spatial scale and wavelengths used in these examples shows that our approach is applicable to studying Earth properties at a wide variety of spatial scales. Using this method, it may be possible to analyse slowness vector properties on larger data sets with a reduced need for subjective visual inspection. In addition, uncertainties can also be quantified and used alongside the measurements. This technique makes 1000s of observations feasible in a matter of hours and allows for global-scale slowness vector observations to be made.

Acknowledgments

We thank reviewers Steve Gibbons and Yu Gu for their constructive reviews which have improved this manuscript. ObspyDMT (Hosseini and Sigloch, 2017) was used to download data. GMT (Wessel et al., 2013) was used to make some of the figures. Predictions from 1D velocity models were made using the TauP toolkit Crotwell et al. (1999). We thank the Department of Geology and Geophysics, the University of Utah for hosting a collaborative visit and the Centre for High-Performance Computing (CHPC) for computer resources and support. JW is supported by the NERC DTP Spheres grant NE/L002574/1, AN was funded by NERC standard grant NE/R001154/1 (REMIS: Reliable Earthquake Magnitudes for Induced Seismicity) and MT was partially supported by NSF grant EAR-1723081.

Data availability

Code to perform the analysis is available at: https://github.com/eejwa/Array_Seis_Circle. Data used for tuning and the examples is available to download from: https://figshare.com/s/fbcb167ad15d581cfd4e. Seismic arrays used were the Kaapvaal array (James et al., 2001), the Gräfenberg array (Federal Institute For Geosciences And Natural Resources (BGR), 1976) [https://doi.org/10.25928/mbx6-hr74] and the Southern California Seismic Network [https://doi.org/10.7914/SN/CI] (California Institute of Technology and United States Geological Survey Pasadena, 1926).

References

Alvizuri, C., & Tanimoto, T. (2011). Azimuthal anisotropy from array analysis of Rayleigh waves in Southern California. *Geophysical Journal International*, *186*(3), 1135–1151.

Ankerst, M., Breunig, M. M., Kriegel, H.-P., & Sander, J. (1999). OPTICS: ordering points to identify the clustering structure. *ACM Sigmod record*, *28*(2), 49–60.

Bear, L. K., & Pavlis, G. L. (1997). Estimation of slowness vectors and their uncertainties using multi-wavelet seismic array processing. *Bulletin of the Seismological Society of America*, *87*(3), 755–769.

Behr, Y., Townend, J., Bowen, M., Carter, L., Gorman, R., Brooks, L., & Bannister, S. (2013). Source directionality of ambient seismic noise inferred from three-component beamforming. *Journal of Geophysical Research: Solid Earth*, *118*(1), 240–248.

Bentham, H., & Rost, S. (2014). Scattering beneath Western Pacific subduction zones: evidence for oceanic crust in the mid-mantle. *Geophysical Journal International*, *197*(3), 1627–1641.

Berteussen, K. (1976). The origin of slowness and azimuth anomalies at large arrays. *Bulletin of the Seismological Society of America*, *66*(3), 719–741.

Bondár, I., North, R. G., & Beall, G. (1999). Teleseismic slowness-azimuth station corrections for the International Monitoring System seismic network. *Bulletin of the Seismological Society of America*, *89*(4), 989–1003.

Bower, D. J., Gurnis, M., & Seton, M. (2013). Lower mantle structure from paleogeographically constrained dynamic Earth models. *Geochemistry, Geophysics, Geosystems*, *14*(1), 44–63.

Bowers, D., & Selby, N. D. (2009). Forensic seismology and the Comprehensive Nuclear-Test-Ban Treaty. *Annual Review of Earth and Planetary Sciences*, *37*, 209–236.

California Institute of Technology and United States Geological Survey Pasadena. (1926). Southern California seismic network. *International Federation of Digital Seismograph Networks, Dataset/Seismic Network*.

Campello, R. J., Moulavi, D., & Sander, J. (2013). Density-based clustering based on hierarchical density estimates. *Pacific-Asia conference on knowledge discovery and data mining*, 160–172.

Campello, R. J., Moulavi, D., Zimek, A., & Sander, J. (2015). Hierarchical density estimates for data clustering, visualization, and outlier detection. *ACM Transactions on Knowledge Discovery from Data (TKDD)*, *10*(1), 1–51.

Cao, A., & Romanowicz, B. (2007). Locating scatterers in the mantle using array analysis of PKP precursors from an earthquake doublet. *Earth and Planetary Science Letters*, *255*(1-2), 22–31.

Celebi, M. E., Kingravi, H. A., & Vela, P. A. (2013). A comparative study of efficient initialization methods for the k-means clustering algorithm. *Expert systems with applications*, *40*(1), 200–210.

Chevrot, S., Sylvander, M., Benahmed, S., Ponsolles, C., Lefevre, J., & Paradis, D. (2007). Source locations of secondary microseisms in western Europe: Evidence for both coastal and pelagic sources. *Journal of Geophysical Research: Solid Earth*, *112*(B11).

Cottaar, S., & Romanowicz, B. (2012). An unsually large ULVZ at the base of the mantle near Hawaii. *Earth and Planetary Science Letters*, *355*, 213–222.

Crotwell, H. P., Owens, T. J., & Ritsema, J. (1999). The TauP Toolkit: Flexible seismic travel-time and ray-path utilities. *Seismological Research Letters*, *70*(2), 154–160.

Efron, B. (1992). Bootstrap methods: another look at the jackknife. *Breakthroughs in statistics* (pp. 569–593). Springer.

Ertöz, L., Steinbach, M., & Kumar, V. (2003). Finding clusters of different sizes, shapes, and densities in noisy, high dimensional data. *Proceedings of the 2003 SIAM international conference on data mining*, 47–58.

Ester, M., Kriegel, H.-P., Sander, J., Xu, X. et al. (1996a). A density-based algorithm for discovering clusters in large spatial databases with noise. *Kdd*, *96*(34), 226–231.

Ester, M., Kriegel, H.-P., Sander, J., Xu, X. et al. (1996b). A density-based algorithm for discovering clusters in large spatial databases with noise. *Kdd*, *96*, 226–231.

Federal Institute For Geosciences And Natural Resources (BGR). (1976). German Regional Seismic Network (GRSN).

Frost, D. A., Rost, S., Selby, N. D., & Stuart, G. W. (2013). Detection of a tall ridge at the core–mantle boundary from scattered PKP energy. *Geophysical Journal International*, *195*(1), 558–574.

Gal, M., Reading, A., Ellingsen, S., Koper, K., Burlacu, R., & Gibbons, S. (2016). Deconvolution enhanced direction of arrival estimation using one-and three-component seismic arrays applied to ocean induced microseisms. *Geophysical Journal International*, *206*(1), 345–359.

Gal, M., Reading, A., Ellingsen, S., Koper, K., Gibbons, S., & Näsholm, S. (2014). Improved implementation of the fk and Capon methods for array analysis of seismic noise. *Geophysical Journal International*, *198*(2), 1045–1054.

Gerstoft, P., Fehler, M. C., & Sabra, K. G. (2006). When katrina hit california. *Geophysical Research Letters*, *33*(17).

Gerstoft, P., Shearer, P. M., Harmon, N., & Zhang, J. (2008). Global P, PP, and PKP wave microseisms observed from distant storms. *Geophysical Research Letters*, *35*(23).

Gibbons, S. J., Näsholm, S., Ruigrok, E., & Kværna, T. (2018). Improving slowness estimate stability and visualization using limited sensor pair correlation on seismic arrays. *Geophysical Journal International*, *213*(1), 447–460.

Gibbons, S. J., & Ringdal, F. (2011). Seismic monitoring of the North Korea nuclear test site using a multichannel correlation detector. *IEEE transactions on geoscience and remote sensing*, *50*(5), 1897–1909.

Gibbons, S. J., Ringdal, F., & Kværna, T. (2008). Detection and characterization of seismic phases using continuous spectral estimation on incoherent and partially coherent arrays. *Geophysical Journal International*, *172*(1), 405–421.

Gibbons, S. J., Schweitzer, J., Ringdal, F., Kværna, T., Mykkeltveit, S., & Paulsen, B. (2011). Improvements to seismic monitoring of the European Arctic using three-component array processing at SPITS. *Bulletin of the Seismological Society of America*, *101*(6), 2737–2754.

Haddon, R., & Cleary, J. (1974). Evidence for scattering of seismic PKP waves near the mantle-core boundary. *Physics of the Earth and Planetary Interiors*, *8*(3), 211–234.

Hosseini, K., & Sigloch, K. (2017). obspyDMT: a Python toolbox for retrieving and processing of large seismological datasets. *Solid Earth*, *8*.

Jacobeit, E., Thomas, C., & Vernon, F. (2013). Influence of station topography and Moho depth on the mislocation vectors for the Kyrgyz Broadband Seismic Network (KNET). *Geophysical Journal International*, *193*(2), 949–959.

James, D., Fouch, M., VanDecar, J., Van Der Lee, S., & Group, K. S. (2001). Tectospheric structure beneath southern Africa. *Geophysical research letters*, *28*(13), 2485–2488.

Ji, C., Tsuboi, S., Komatitsch, D., & Tromp, J. (2005). Rayleigh-wave multipathing along the west coast of North America. *Bulletin of the Seismological Society of America*, *95*(6), 2115–2124.

Kim, D., Lekić, V., Ménard, B., Baron, D., & Taghizadeh-Popp, M. (2020). Sequencing seismograms: A panoptic view of scattering in the core-mantle boundary region. *Science*, *368*(6496), 1223–1228.

Koch, K., & Kradolfer, U. (1999). Determination of mislocation vectors to evaluate bias at GSETT-3 primary stations. *Journal of seismology*, *3*(2), 139–151.

Kong, Q., Trugman, D. T., Ross, Z. E., Bianco, M. J., Meade, B. J., & Gerstoft, P. (2019). Machine learning in seismology: Turning data into insights. *Seismological Research Letters*, *90*(1), 3–14.

Korenaga, J. (2013). Stacking with dual bootstrap resampling. *Geophysical Journal International*, *195*(3), 2023–2036.

Lam, S. K., Pitrou, A., & Seibert, S. (2015). Numba: A llvm-based python jit compiler. *Proceedings of the Second Workshop on the LLVM Compiler Infrastructure in HPC*, 1–6.

Landès, M., Hubans, F., Shapiro, N. M., Paul, A., & Campillo, M. (2010). Origin of deep ocean microseisms by using teleseismic body waves. *Journal of Geophysical Research: Solid Earth*, *115*(B5).

Lin, C.-H., & Roecker, S. (1996). P-wave backazimuth anomalies observed by a small-aperture seismic array at Pinyon Flat, southern California: Implications for structure and source location. *Bulletin of the Seismological Society of America*, *86*(2), 470–476.

Liu, Q., Koper, K. D., Burlacu, R., Ni, S., Wang, F., Zou, C., Wei, Y., Gal, M., & Reading, A. M. (2016). Source locations of teleseismic P, SV, and SH waves observed in microseisms recorded by a large aperture seismic array in China. *Earth and Planetary Science Letters*, *449*, 39–47.

Ma, X., & Thomas, C. (2020). Small-scale scattering heterogeneities in the lowermost mantle from a global analysis of PKP precursors. *Journal of Geophysical Research: Solid Earth*, *125*(3), e2019JB018736.

MacQueen, J. et al. (1967). Some methods for classification and analysis of multivariate observations. *Proceedings of the fifth Berkeley symposium on mathematical statistics and probability*, *1*(14), 281–297.

Maupin, V. (2011). Upper-mantle structure in southern Norway from beamforming of Rayleigh wave data presenting multipathing. *Geophysical Journal International*, *185*(2), 985–1002.

McInnes, L., & Healy, J. (2017). Accelerated hierarchical density based clustering. *2017 IEEE International Conference on Data Mining Workshops (ICDMW)*, 33–42.

Niu, F., & Kawakatsu, H. (1997). Depth variation of the mid-mantle seismic discontinuity. *Geophysical Research Letters*, *24*(4), 429–432.

Ogden, C., Bastow, I., Gilligan, A., & Rondenay, S. (2019). A reappraisal of the H–κ stacking technique: implications for global crustal structure. *Geophysical Journal International*, *219*(3), 1491–1513.

Ritsema, J., Kaneshima, S., & Haugland, S. M. (2020). The dimensions of scatterers in the lower mantle using USArray recordings of S-wave to P-wave conversions. *Physics of the Earth and Planetary Interiors*, *306*, 106541.

Rost, S., & Thomas, C. (2002). Array seismology: Methods and applications. *Reviews of geophysics*, *40*(3).

Rost, S., & Thomas, C. (2009). Improving seismic resolution through array processing techniques. *Surveys in Geophysics*, *30*(4-5), 271–299.

Roux, P., & Ben-Zion, Y. (2017). Rayleigh phase velocities in Southern California from beamforming short-duration ambient noise. *Geophysical Journal International*, *211*(1), 450–454.

Ruigrok, E., Gibbons, S., & Wapenaar, K. (2017). Cross-correlation beamforming. *Journal of Seismology*, *21*(3), 495–508.

Schimmel, M., & Paulssen, H. (1997). Noise reduction and detection of weak, coherent signals through phase-weighted stacks. *Geophysical Journal International*, *130*(2), 497–505.

Schmidt, R. (1986). Multiple emitter location and signal parameter estimation. *IEEE transactions on antennas and propagation*, *34*(3), 276–280.

Schumacher, L., & Thomas, C. (2016). Detecting lower-mantle slabs beneath Asia and the Aleutians. *Geophysical Journal International*, *205*(3), 1512–1524.

Schweitzer, J. (2001). Slowness corrections—One way to improve IDC products. *pure and applied geophysics*, *158*(1), 375–396.

Selby, N. D. (2011). Improved teleseismic signal detection at small-aperture arrays. *Bulletin of the Seismological Society of America*, *101*(4), 1563–1575.

Stockmann, F., Cobden, L., Deschamps, F., Fichtner, A., & Thomas, C. (2019). Investigating the seismic structure and visibility of dynamic plume models with seismic array methods. *Geophysical Journal International*, *219*(Supplement_1), S167–S194.

Teanby, N., Kendall, J.-M., & Van der Baan, M. (2004). Automation of shear-wave splitting measurements using cluster analysis. *Bulletin of the Seismological Society of America*, *94*(2), 453–463.

Thomas, C., Kendall, J.-M., & Weber, M. (2002). The lowermost mantle beneath northern Asia—I. Multi-azimuth studies of a D heterogeneity. *Geophysical Journal International*, *151*(1), 279–295.

Thomas, C., Weber, M., Wicks, C., & Scherbaum, F. (1999). Small scatterers in the lower mantle observed at German broadband arrays. *Journal of Geophysical Research: Solid Earth*, *104*(B7), 15073–15088.

Thorne, M. S., Pachhai, S., Leng, K., Wicks, J. K., & Nissen-Meyer, T. (2020). New Candidate Ultralow-Velocity Zone Locations from Highly Anomalous SPdKS Waveforms. *Minerals*, *10*(3), 211.

Valentine, A. P., & Trampert, J. (2012). Data space reduction, quality assessment and searching of seismograms: autoencoder networks for waveform data. *Geophysical Journal International*, *189*(2), 1183–1202.

Valentine, A. P., & Woodhouse, J. H. (2010). Approaches to automated data selection for global seismic tomography. *Geophysical Journal International*, *182*(2), 1001–1012.

Ward, J., Nowacki, A., & Rost, S. (2020). Lateral Velocity Gradients in the African Lower Mantle Inferred From Slowness Space Observations of Multipathing. *Geochemistry, Geophysics, Geosystems*, *21*(8), e2020GC009025.

Wessel, P., Smith, W. H., Scharroo, R., Luis, J., & Wobbe, F. (2013). Generic mapping tools: improved version released. *Eos, Transactions American Geophysical Union*, *94*(45), 409–410.

Xia, Y., Ni, S., & Tape, C. (2018). Multipathing Rayleigh Waves From Long-Distance Noise Cross Correlation Along an Ocean-Continent Boundary (Alaska to California). *Geophysical Research Letters*, *45*(12), 6051–6060.

Yang, Z., & He, X. (2015). Oceanic crust in the mid-mantle beneath west-central Pacific subduction zones: evidence from S to P converted waveforms. *Geophysical Journal International*, *203*(1), 541–547.

Chapter 4

Towards a Global Map of Multipathing and Slowness Vector Perturbations from Array Analysis of SKS Arrivals

Abstract

Global-scale observations of seismic reflections, scattered waves, waveform complexity and seismic tomography have provided multi-scale constraints of the seismic properties of heterogeneities in the Earth's interior. Of the seismic properties analysed on a global scale, inferences on the location, strength and geometry of lateral velocity gradients have yet to be made. Multipathing is a direct consequence of a wave interacting with strong lateral velocity gradients, therefore observing this phenomenon and replicating it through forward modelling can be used to constrain the properties of the lateral velocity gradients. Multipathing occurs when a seismic wave is incident on a sufficiently strong lateral velocity gradient which results in two arrivals that arrive at the surface with different slowness vector properties (direction and horizontal speed) and times. Array seismology can identify multipathed arrivals by their differing slowness vector properties, therefore locating strong lateral velocity gradients and quantifying the extent the heterogeneity may have perturbed the wavefield. Furthermore, the relative slowness vector properties of the multipathed arrivals and arrivals diffracted by the velocity gradient can constrain the geometry of the velocity gradient causing them. As the slowness vector measurements of multipathing and diffraction have not been analysed on a global scale, we apply an automated analysis technique for array data to identify regions of multipathing and diffraction from slowness vector

deviation measurements in a global dataset of SKS arrivals.

We conduct this analysis in three frequency bands (0.10 – 0.20, 0.15 – 0.30, 0.20 – 0.40 Hz), therefore varying the spatial scale lengths of velocity gradients we are sensitive to. The analysis results in a large dataset (>10,000 observations in total) sampling mainly beneath North America and Europe. We showcase the dataset by suggesting what heterogeneities could be causing the observations after some initial ray tracing modelling.

Each of the heterogeneities observed here shows its own unique combination of slowness vector patterns, slowness vector magnitudes and whether it causes multipathing. This shows the value of these measurements, in separating the different properties of these heterogeneities such as morphology, velocity perturbation and those of the lateral velocity gradients. This work is the beginning of the process towards a global map of multipathing and locations of heterogeneities with strong lateral velocity gradients. Our observations reported here and future maps of multipathing can be used in combination with forward modelling or statistical studies to constrain the properties of velocity gradients in the mantle. By mapping out the locations and strengths of lateral velocity gradients, different hypothetical Earth models will have more constraints to define the structures present and improve our overall understanding of the Earth's mantle system.

4.1 Introduction

Global or multi-regional scale observations of anomalous seismic phenomena give insight to the large- and small-scale processes of the mantle and improve our understanding of whole-Earth dynamics. Such global studies have analysed reflectors in the mid mantle (e.g. Bentham et al., 2017; Deuss, 2009; Deuss et al., 2006; Waszek et al., 2018), small-scale heterogeneity from scattering observed as PKP precursors (Hedlin and Shearer, 2000; Ma and Thomas, 2020; Waszek et al., 2015) and from waveform complexity (Thorne et al., 2021; Thorne et al., 2020), and travel times and waveforms through seismic tomography (Chang et al., 2015; French and Romanowicz, 2014; Koelemeijer et al., 2015; Lu et al., 2019; Ritsema et al., 2011; Simmons et al., 2010). While these studies have given many observations of heterogeneities in the Earth on spatial scales from 1000s to 10s of kilometres, global information about lateral velocity gradients and their effect on the wavefield through diffraction and multipathing are yet to be analysed. Multipathing occurs when a wavefield is incident on a sufficiently strong lateral velocity gradient such that, over a short lateral distance (100s km), the wave travels at different speeds and the lateral velocity gradient diffracts the wave. This results in multiple distinct arrivals at the seismic station each with different arrival times and, because of the diffraction, with different horizontal velocities and directions (backazimuths and horizontal slownesses). Observing multipathing is clear evidence for a strong velocity gradient indicative of mantle thermal or thermochemical heterogeneity and has been observed from wavefield interactions with subducting slabs (Silver and Chan, 1986; Sun et al., 2017), Large Low-Velocity Provinces (LLVPs) (Ni et al., 2002; Sun et al., 2010; Sun and Miller, 2013; Ward et al., 2020) and ancient slab–plume–ultra low-velocity zone (ULVZ) interactions (Sun et al., 2019). Observations of the velocity gradients by making slowness vector measurements of multipathing quantifying the effects of the gradients on the wavefield can give estimates of the properties of velocity gradients which could be translated to inferences on the thermal gradients, perturbations or chemical nature of the structures. If these observations are of a global scale, they can be used to evaluate conceptual Earth models of present-day structure which can then be used to understand the origin and history of many of the mantle structures.

In this study, we begin the process towards a global map of lateral velocity gradient properties by applying the automated array technique of Ward et al. (2021) to the global SKS dataset of Thorne et al. (2020) to constrain where strong lateral velocity gradients are and constrain the location and morphology of boundary structure of mantle heterogeneities such as mantle plumes and subducted slab material. We make 11829 observations over three frequency bands (Table 4.1) to identify velocity gradients of different spatial scales. There are many ways to analyse such a large dataset which may the base of further studies. Here, we provide a geological interpretation of what heterogeneities may be causing the observations and perform initial ray tracing modelling

to facilitate our qualitative interpretations. We find evidence for mantle heterogeneity everywhere we sample and use statistical analysis to constrain the depths of these structures. We find each of the heterogeneities has a unique slowness vector spatial pattern and whether they are in regions of high multipathing proportion. Each heterogeneity causing unique slowness vector and multipathing observations allows properties such as the geometry, and strength of the boundaries to be well constrained and differences between these structures analysed. Constraining the unique properties of the heterogeneities then give inferences on their different boundary structure and thermochemical properties. This dataset represents the beginning of a project to a map of where multipathing occurs and possibly velocity gradients strengths which then could translate into thermal gradients or regions of chemical heterogeneity.

4.2 Methods

4.2.1 Data and Sub Arrays

We use the global SKS dataset from Thorne et al. (2020) where events between 1990 and 2017 with magnitudes greater than 5.8, deeper than 75 km and with epicentral distances between 90° and 130° are collected. The raw data were processed by removing the mean, trend and instrument response. Low-quality data are removed first with an ensemble of neural networks each trained on the amplitude spectra of 10,000 traces and their respective labels of high or low quality following the approach of Valentine and Woodhouse (2010). Following this, all traces were visually inspected for quality and the high-quality traces were kept for analysis, for details of pre-processing, see Thorne et al. (2020). For each event, the high-quality data were divided into sub-arrays following the approach below.

To ensure high-quality observations, we require a sub-array to have a minimum of 15 stations with a maximum aperture of 400 km. To ensure all sub-arrays will meet this criterion, we first use DBSCAN (Ester et al., 1996) to identify stations that meet the criteria of having 15 stations within a 200 km radius of it and identify stations that do not meet the criteria. For the sake of ease of explanation, we describe how DBSCAN works in this specific application rather than in general terms. DBSCAN (Ester et al., 1996) is a density-based clustering algorithm that will classify the stations into 'core' stations, which have at least 15 other stations within 200 km of it, 'boundary' stations which do not meet the density criteria but are within the neighbourhood of a core station and 'outlier' stations which do not meet the density criteria and are not in the neighbourhood of a core station. The outlier stations can then be removed and not used to make sub-arrays. We spatially resample the core stations such that none are within 200 km of each other. The remaining stations will be centroids for the sub-arrays. For each of the centroid stations, we create a sub-array made up of all stations within 200

km of it. Figure 4.1 illustrates the steps to form sub-arrays and Figure 4.3 shows the resulting sub-array locations with the events and sampling of SKS in the lower mantle.

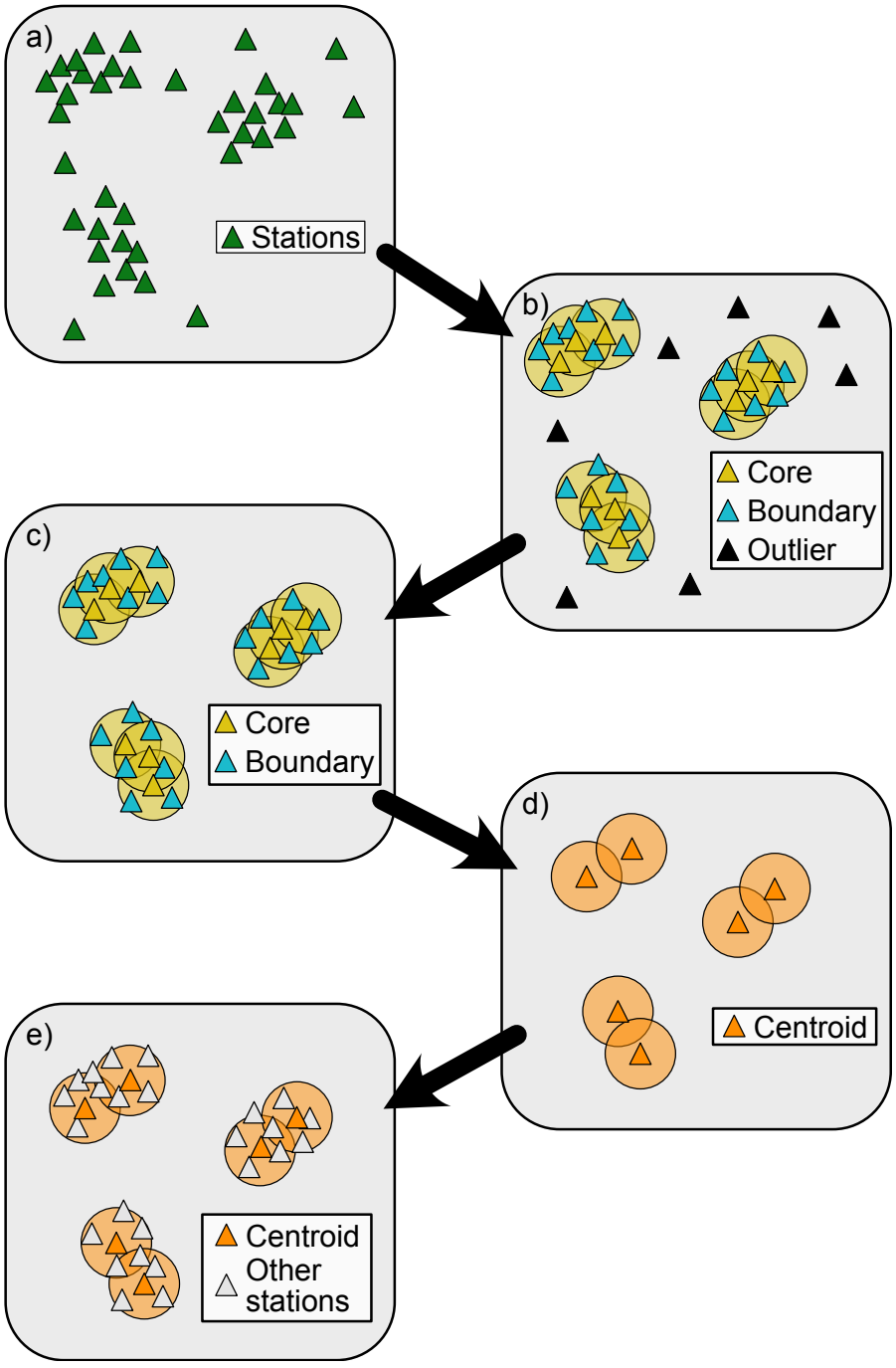

Figure 4.1: Cartoon describing the steps to automatically form a distribution of stations (a) into sub-arrays (e). (b) apply DBSCAN (Ester et al., 1996) to classify the stations into core, boundary and outlier stations. In the cartoon, a station needs 4 other stations in the neighbourhood to be a core station. (c) remove outlier stations. (d) from the core stations, resample them so none are within the desired spacing of each other, here the spacing is the same as the neighbourhood radius. (e) form sub-arrays by collecting the stations within the neighbourhood of the centroid stations.

4.2.2 Automatic multipathing and slowness vector measurements

For each event-sub array combination, we use the method of Ward et al. (2021) to automatically identify multipathed and single arrivals in slowness space and measure their slowness vector properties. Here, we provide a brief summary of the method but for details, such as searching for optimal parameters, see Ward et al. (2021). The waveforms recorded at a seismic array from which the measurement is to be made are bootstrap sampled (Efron, 1992) into N (1000 here) sub-samples. For each of the N bootstrap samples, we use beamforming (Rost and Thomas, 2002) corrected for a curved wavefront (Ward et al., 2020) to calculate the coherent power at a range of slowness vector properties. From this power distribution in slowness-space, take the top N power maxima (3 here) above a noise estimate. The location of the maxima in slowness space give their slowness vector properties. For the sake of ease of explanation, we describe these as points in a 2-D slowness-space. Each bootstrap sample will have its own power distribution and respective points. Gather all points from each of the bootstrap samples and use DBSCAN (Ester et al., 1996), a density-based clustering algorithm, to identify arrivals as dense clusters of the points. DBSCAN parameters ϵ and $MinPts$ define the density threshold to find the clusters where at least $MinPts$ points need to be within a radius ϵ for a region to be defined as a cluster. We set the DBSCAN parameters ϵ and $MinPts$ as 0.20 s/° and 250 points respectively in line with the tuning from Ward et al. (2021). The number of clusters found is taken as the number of arrivals, the mean of the location of the points in the cluster gives the slowness vector properties of the arrival and the scatter of the points in the cluster give the uncertainty estimates of the slowness vector measurement. Figure 4.2 illustrates the method.

By using this method, we can confidently make slowness vector measurements of a large dataset and identify multipathing. Observations classified as multipathed are visually inspected to check the classification and if necessary relabeled. Multipathing has been observed to be frequency-dependent (Ward et al., 2020) suggesting the Fresnel zone size relative to the velocity gradient sharpness of the boundary may impact whether multipathing is observable or not. Therefore, constraining which frequency band multipathing is observable in may give an indication of the velocity gradient sharpness or depths due to the sensitivity of the Fresnel zone with depth as well as frequency. To identify velocity gradients of different sharpness and strength, we conduct this analysis in three frequency bands (0.10 – 0.20 Hz, 0.15 – 0.30 Hz, 0.20 – 0.40 Hz). In total there are 11829 observations with the breakdown of the number of multipathed and single arrivals in each frequency band shown in Table 4.1.

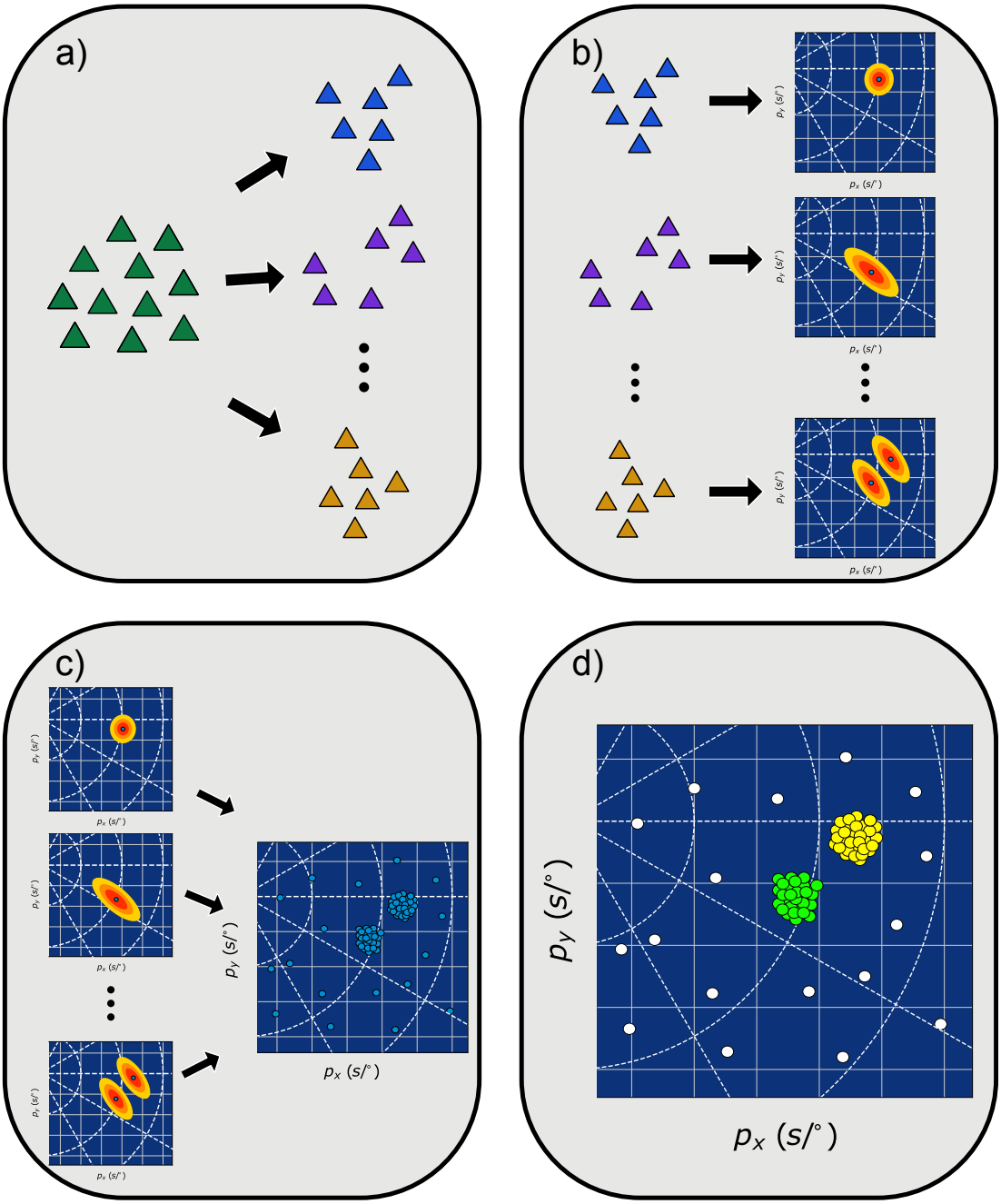

Figure 4.2: Same as Figure 3.1 in Chapter 3. Cartoon describing the steps to automatically identify arrivals in slowness space and measuring their slowness vector properties. First bootstrap sample the traces recorded at an array 1000 times creating 1000 random sub arrays (a). Then, for each bootstrap sample, perform linear beamforming grid search and recover the top peaks (b). Once this is done, collect all the points from all 1000 samples (c). Finally, apply clustering algorithm DBSCAN (Ester et al., 1996) to identify regions dense enough to form clusters and, from their location, measure their slowness vector properties.

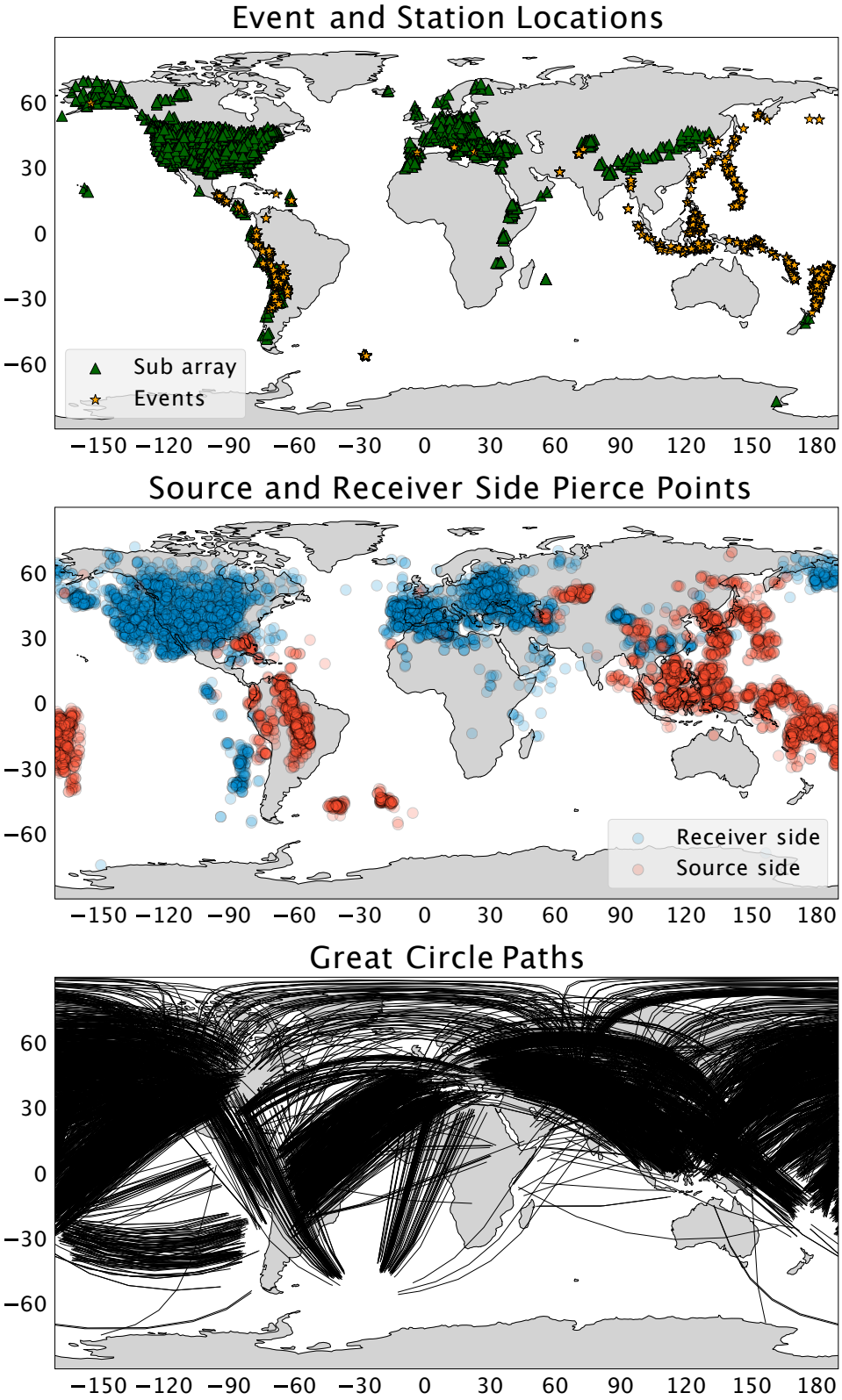

Figure 4.3: Top: Event (orange stars) and sub-array (green triangles) coverage of the usable observations after applying the method from Ward et al. (2021). Middle: map of SKS pierce point coverage at 2800 km depth for the observations after applying the method of Ward et al. (2021). Blue and red circles show the pierce point location on the receiver- and source-side, respectively. Bottom: great circle paths from event to stations.

Frequency Band (Hz)	Number of Arrivals Observed		
	1	2	3
0.10 – 0.20	4376	49	0
0.15 – 0.30	3580	269	0
0.20 – 0.40	3015	495	45

Table 4.1: Number of observations labelled as having 1,2 or 3 arrivals in each frequency band.

4.3 Forward modelling of slowness vector deviations

Before interpreting the observations of Section 4.4, we use the LLNL-Earth3D 3-D ray-tracing software (Simmons et al., 2011; Simmons et al., 2012; Zhao et al., 1992) to infer the expected pattern of slowness vector deviations of mantle heterogeneity on the scale of 100s of kilometres depending on whether they are fast or slow anomalies. Slowness vector deviation patterns may be able to discern whether the heterogeneity is fast or slow, something the observation of multipathing in slowness space alone may not be able to constrain.

We use two models to determine the qualitative pattern of the slowness vector measurements when the wave interacts with fast or slow heterogeneity. The modelling cannot be directly compared to the observations but can be used to determine the qualitative pattern of a seismically fast or slow structure. Inferring the properties of the heterogeneities may require finite frequency modelling to account for the full 3-D effect of the structure which, due to its computational expense, is unnecessary for this application. Figure 4.4 shows the setup of the modelling with the event and station distributions and two anomaly locations. The fast anomaly has a width and length of 1000 km and a height of 500 km above the CMB with a velocity perturbation of 5% δV_S and the slow anomaly is a cylinder with a diameter of 1000 km, height of 500 km above the CMB and a velocity perturbation of -5% δV_S relative to PREM (Dziewonski and Anderson, 1981). For the rest of the model, we assume the 1-D Earth model PREM (Dziewonski and Anderson, 1981).

We calculate the arrival times at each station using ray-tracing and insert a Ricker wavelet (Ricker, 1943; Ricker, 1944) with a frequency of 0.15 Hz at the arrival times creating synthetic seismograms. Using the synthetic data, a beamforming grid search is conducted over a range of slowness vectors for each sub-array. We record the slowness vector properties with the highest power value and calculate the deviation from PREM (Dziewonski and Anderson, 1981) predicted slowness vector properties. The differential slowness vector is plotted at the great circle path pierce points between the event and sub-array centre at the CMB. In addition to marking the slowness vector residuals at the great circle path pierce points, the vectors are relocated so the path they travel through a 1-D Earth is the same as a wave with the observed slowness vector properties. This

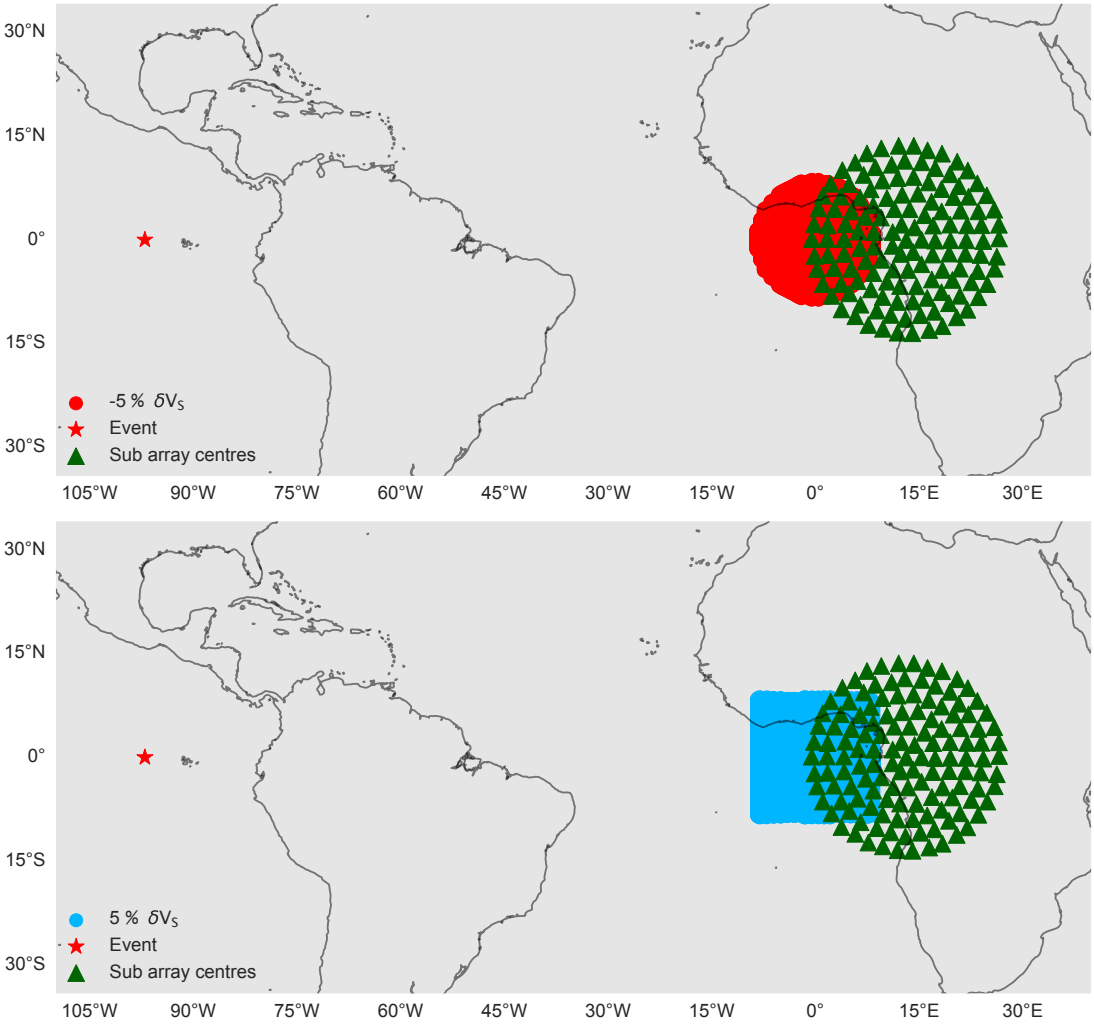

Figure 4.4: Model setups for the 3-D ray-tracing through a fast box (top) with length and width of 1000 km, a height of 500km and a velocity perturbation of $+5\%\delta V_S$ and a slow cylinder with a diameter of 1000 km, height of 500 km and a velocity perturbation of -5% δV_S. Also shown are the event location (red star) at $-97°$ longitude, $0°$ latitude and the mean station locations of the sub-arrays (green triangles).

is identical to the slowness vector plots in Section 4.4. The slowness vector deviations for both model setups with the relocated locations and the great circle path points plotted are shown in Figure 4.5. The modelling results clearly show a diverging pattern for the slow anomaly and a converging pattern for the fast anomaly. In both models, the slowness vector azimuths are perpendicular to the orientation of the boundary and are large at the edges of the structure and have a low magnitude in the centre of them. This suggests travelling through the centre of the heterogeneity does not refract the wave enough to cause slowness vector deviations. The magnitudes and azimuths cannot be directly compared to the observed slowness vectors without comparison to finite frequency forward modelling to determine whether the assumptions made by ray-tracing, such as the infinite frequency assumption, significantly affect the magnitudes and azimuths of the slowness vectors. Nonetheless, the ray-tracing results do allow for qualitative interpretation of the observations, which we discuss in the next section.

4.4 Spatial observations of slowness vectors and multipathing

Using the theoretical modelling results of Section 4.3, we now present the results of the dataset by analysing the slowness vector deviations and multipathing spatially and provide a geological interpretation. As the sampling of the dataset is heavily concentrated on paths sampling the mantle beneath North America and Europe, we focus our analysis there.

A challenge with interpreting SKS slowness vector measurements and multipathing locations is determining the depth of the structure causing the wavefield perturbations and whether the dominant signal is caused by source- or receiver-side structure. Furthermore, interpretation becomes more complex as there could be multiple structures affecting the wavefield at different depths and locations. Because of the dense sampling in this dataset, we try to determine the most likely depth and location (source or receiver) with the following approach.

For this analysis, we assume waves that sample similar regions should arrive with similar slowness vector properties if there is one dominant structure causing the perturbation. Essentially, we are assuming one structure for each region is the cause of a dominant pattern in our observations. When quantifying the coherence of slowness vector measurements in particular regions and depths, we relocate the pierce point such that it would arrive at the array with the same backazimuth and horizontal slowness as the observation. We calculate the relocated pierce points at 100 km depth intervals. At each depth, we create bins around each pierce point collecting all other slowness vector measurements within 100 km of that pierce point. Then the variance (σ^2) of the slowness vector measurements in each bin is calculated as the mean square distance

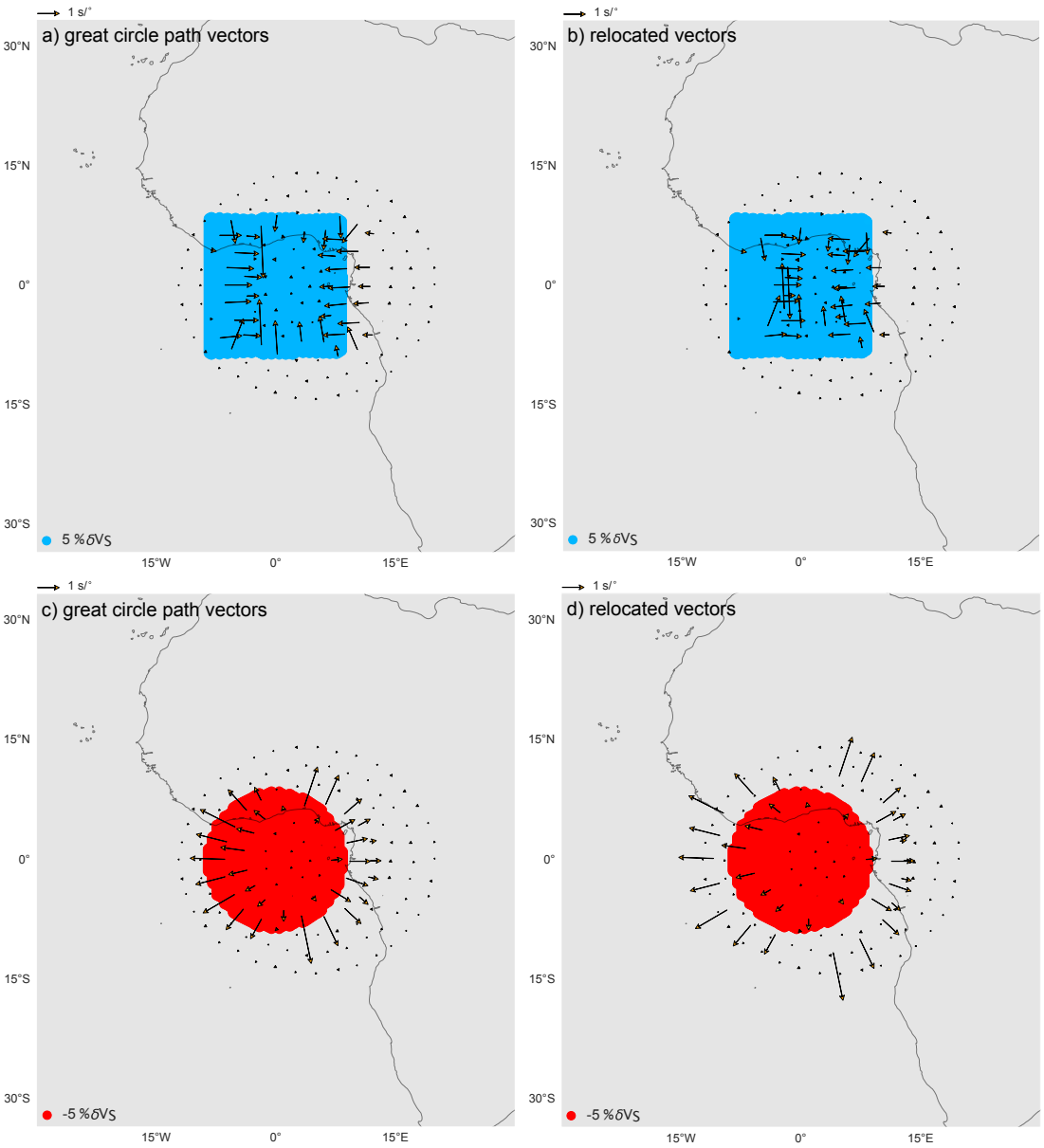

Figure 4.5: Slowness vector residuals for both model setups shown in Figure 4.4 with the fast box shown in subfigures (a) and (b) and the slow cylinder shown in (c) and (d). Slowness vectors shown in subfigures (a) and (c) plot the slowness vectors at their great circle path pierce points between the event and sub-array locations. Slowness vectors in subfigures (b) and (d) are marked at their relocated locations. Notice, the slowness vector patterns for the slow cylinder show a diverging pattern and for the fast box a converging pattern. In all instances, the slowness vector azimuth is orthogonal to the boundary of the structure.

between all the slowness vectors and the mean the slowness vector measurements in the bin as,

$$\sigma^2 = \frac{\sum_i^N (\sqrt{(\bar{p_x} - p_{ix})^2 + (\bar{p_y} - p_{iy})^2})^2}{N}, \tag{4.1}$$

where N is the number of vectors in the bin, $\bar{p}$ is the mean of slowness vectors in the bin and p_{ix}/p_{iy} are the east and north component respectively of the ith slowness vector measurement in the bin. The distances between the mean slowness vector and each of the slowness vector measurement is illustrated in Figure 4.6.

To infer which variances are statistically significantly low, we randomly take 20 slowness vector measurements from the whole dataset and calculate the variance. This is repeated 1000 times and the 5th percentile of these 1000 random variance estimates is recorded. Variances lower than the 5th percentile estimate are labelled as significantly low and included in the analysis. The depths where pierce points have a variance lower than the significant variance estimate are recorded and histograms of these depths are made. This process could be repeated with observations of the orientation of the multipathed arrivals in slowness space. We do not do this as most regions show few multipathed arrivals.

We now analyse the slowness vectors and multipathing locations at different depths and frequencies using the results of the modelling in Section 4.3 to suggest possible heterogeneities causing the observations. Multipathing and slowness vector deviation methods can constrain different information about the heterogeneity and, when combined, provide even more constraints. The presence or lack of multipathing in one or multiple frequency bands constrains the sharpness of the velocity gradient. The relative location of the multipathed arrivals in slowness space may give the orientation of the velocity gradient. It is challenging to recover the velocity anomaly of the heterogeneity through slowness space observations of multipathing alone. Slowness vector measurements on the other hand can give inferences on whether the heterogeneity is anomalously fast or slow and the azimuth of the vectors can be used to infer the orientation of the boundary also. As this dataset provides measurements of both multipathing and slowness vector deviations, the properties of velocity gradients sampled may be able to be well constrained in future forward modelling studies.

In our analysis, the vector deviations have been relocated so the ray path is the same as an arrival with the same slowness vector properties as the observation. We only analyse slowness vector measurements that have a variance lower than the significant variance estimate and are then binned in 200 km radius bins. The bin size was chosen to maximise clarity while retaining as much detail as possible. The multipathing observations are shown as the proportion of multipathing within 200 km bins with a minimum of 10 observations required to form a bin. We also plot the mean of the loci in each bin, again requiring 10 observations to form a bin. The locus is taken as the

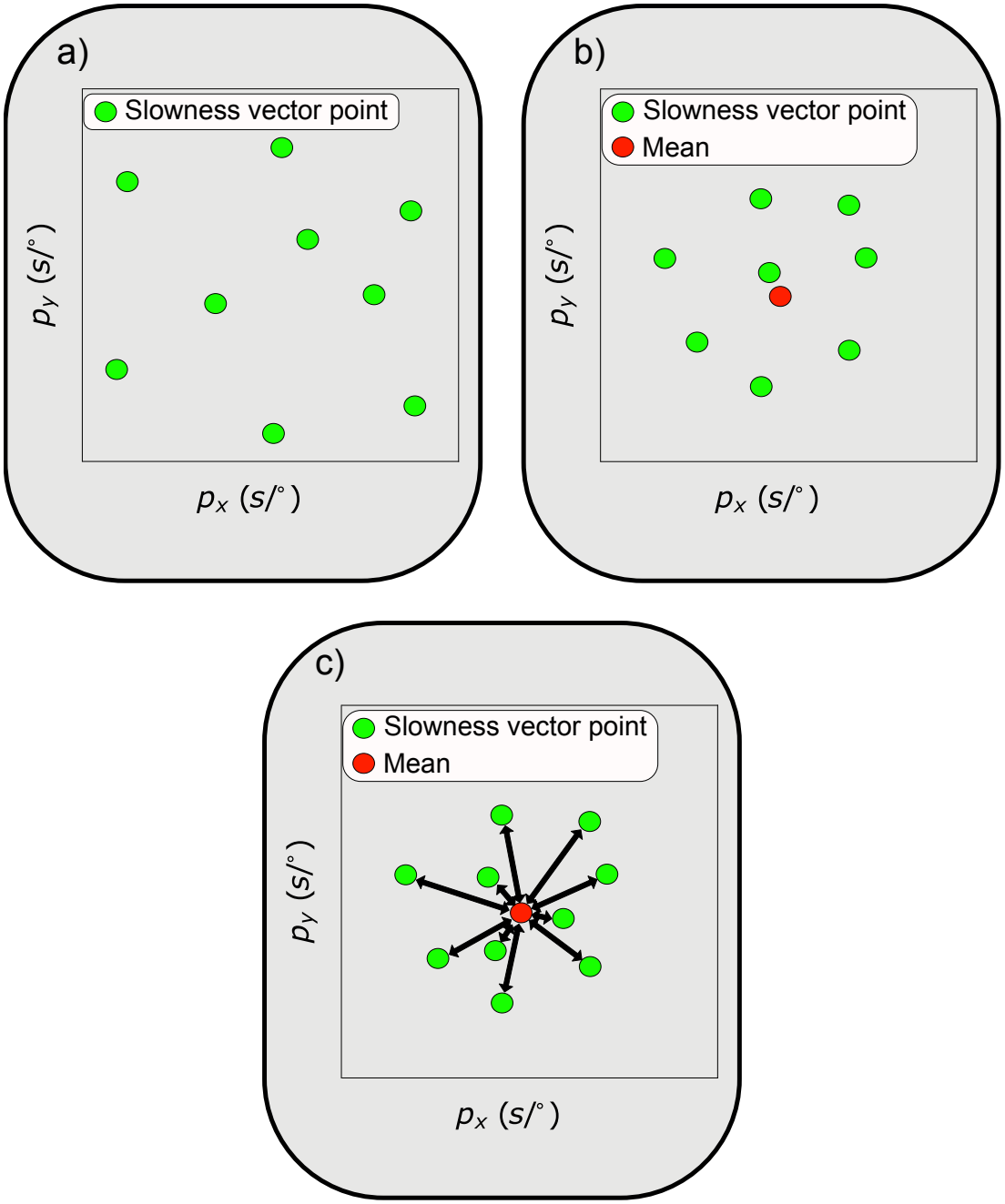

Figure 4.6: Cartoon of how from a cluster of slowness vector points in slowness space (a), the mean is measured (b) and the distances in slowness space are found (c). From these distances the RMS is calculated.

angle orthogonal to the segment connecting the multipathed arrivals in slowness space. The locus gives approximate information about the orientation of the velocity gradient causing the arrivals. Where multipathing is observed, we can estimate the maximum scale of the velocity gradient given the depth and frequency band it is observed in by taking the approach outlined in Section 4.4.1.

4.4.1 Estimating velocity gradient length scales

Without computationally expensive finite frequency forward modelling the exact strength, height and geometry of lateral velocity gradients cannot be inferred. We can, however, give an upper bound of the length scale of the transition from the ambient mantle to the interior of the heterogeneity by calculating the Fresnel zone diameter using

$$d = 2\sqrt{\frac{z\lambda}{2}}, \tag{4.2}$$

where d is the Fresnel zone diameter at depth z. The wavelength λ is calculated from the lower end of the frequency band in which multipathing has been observed (0.10, 0.15, or 0.20 Hz) and the PREM (Dziewonski and Anderson, 1981) velocity value at depth z. To find the upper bound of the velocity gradient length scale this needs to be added to the diameter of the sub-array used for the recording, which we set as 400 km (Section 4.2.1). The diameter the sub-array is sampling will change with depth, for example, a region spanning 400 km at the surface will become approximately 220 km when projected to the CMB. Therefore, this is accounted for before adding to the diameter of the Fresnel zone. With this, we propose maximum length scales for the lateral velocity gradients of heterogeneity observed.

4.4.2 Europe

Figure 4.7 shows the histograms of the number of receiver-side paths which have a significantly low variance at each depth for paths sampling the mantle beneath Europe. In all frequency bands, there is evidence for lower-mantle structure causing slowness vector deviation in our observations with the strongest evidence in the highest frequency band (0.20 – 0.40 Hz). This is shown by the trend of the number of low-variance observations increasing with depth in the bottom 500 km of the mantle.

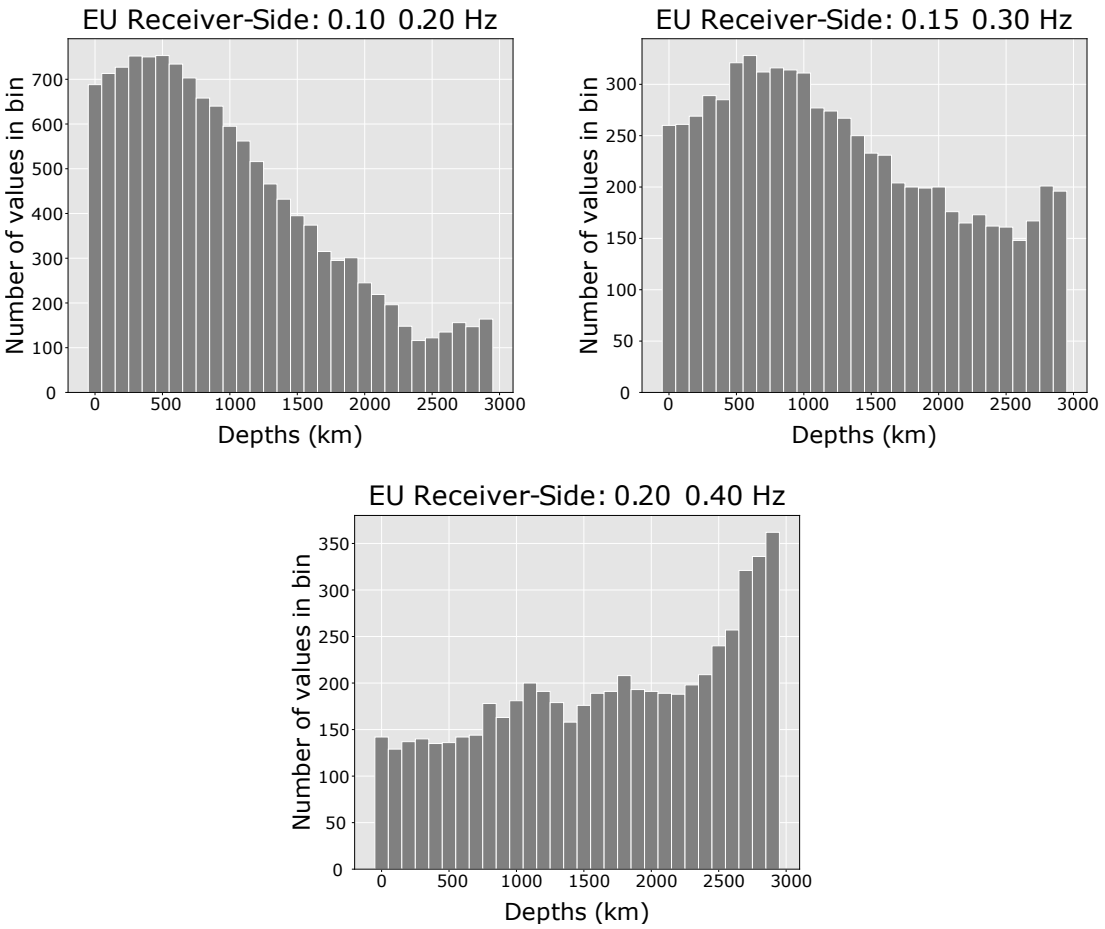

Figure 4.7: Histograms of the number of bins with a low variance slowness vector measurements. The different histograms represent the different frequency bands used. Top left is the lowest frequency band (0.10 – 0.20 Hz, top right is the central frequency band (0.15 – 0.30 Hz) and the bottom histogram is the highest frequency band (0.20 – 0.40 Hz). Receiver-side paths beneath Europe are used for this analysis for these histograms.

Other than this pattern in the lower mantle, each frequency band shows different depths with a high number of low variance slowness vector bins, suggesting different frequencies may be sensitive to heterogeneity at different depths. Based on these histograms, we select the depths to analyse in each frequency band. These are shown in Table 4.2.

We visually inspect the slowness vector deviation patterns, multipathing propor-

Frequency band (Hz)	Depths analysed
0.10 – 0.20	500 km, 2891 km
0.15 – 0.30	500 km, 800 km, 1000 km, 2891 km
0.20 – 0.40	1100 km, 1800 km, 2000 km, 2891 km

Table 4.2: Depths with possible mantle heterogeneity inferred from the slowness vector variances for the mantle beneath Europe.

tions and loci orientations at depths and frequency bands in Table 4.2 and in the following subsections describe our interpretations of the structures causing them. We selectively choose which depth slices of the results to show to avoid confusion or repeating similar observations (such as depth slices at 1800 km and 2000 km which show similar results). Those not presented in this chapter are shown in Appendix Section C.

4.4.2.1 Deep roots of European plumes

Evidence for mantle upwellings beneath Europe comes from a variety of observations such as geochemical evidence (Bell et al., 2004; Buikin et al., 2005; Cadoux et al., 2007; Wedepohl and Baumann, 1999), seismic tomography (Rickers et al., 2013; Ritter et al., 2001), and geodesy (Kreemer et al., 2020) and there is evidence that these upwellings have deep origins (Buikin et al., 2005; Goes et al., 1999). We have observed several radially diverging slowness vector patterns throughout the lower and upper mantle which, from inferences provided in Section 4.3, are evidence for low-velocity anomalies from structures such as mantle plumes.

In the lower mantle, we observe a clear radially diverging pattern of slowness vector residuals (P1 in Figure 4.8) with slowness vector magnitudes of up to 1.5 s/°. This, combined with the approximately circular pattern of the mean loci, a moderate proportion of multipathing (35%) in the region at the core-mantle boundary (G1 in Figure 4.9) and mid mantle suggests a structure with sharp velocity gradients at its boundaries rising 100s of kilometres through the mantle. Using the method outlined in Section 4.4, we estimate the maximum length scale for this velocity gradient at the CMB to cause multipathing in the highest frequency band (0.20–0.40 Hz) to be approximately 676 km.

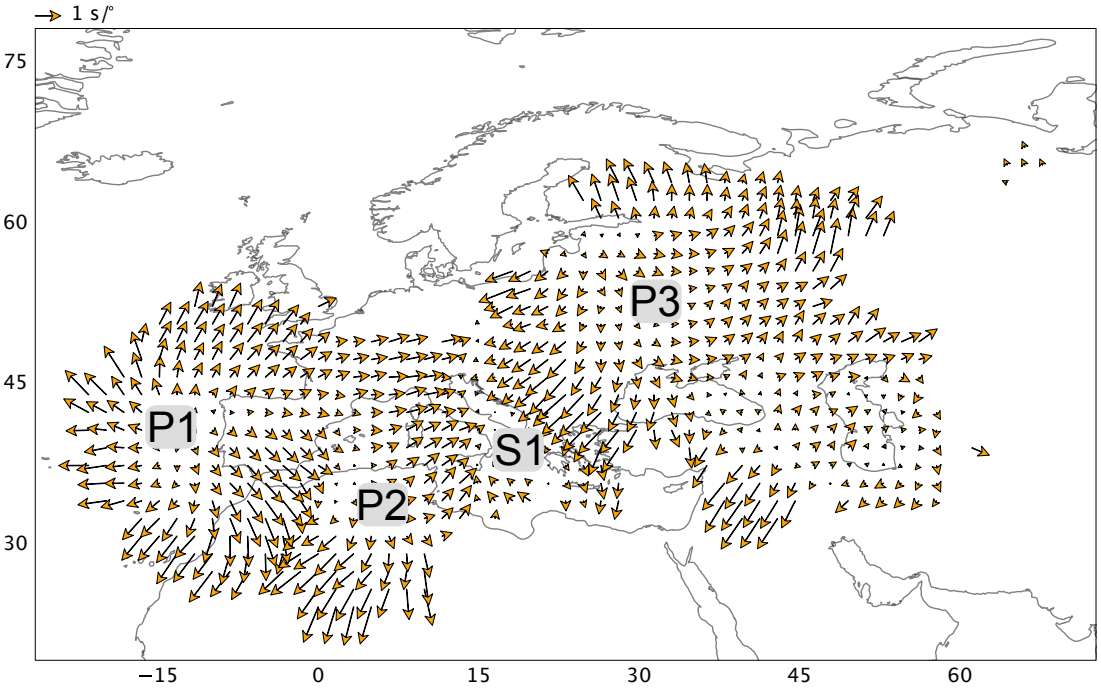

Figure 4.8: Map of slowness vector bins in the 0.20 – 0.40 Hz frequency band using pierce points at 2891 km depth beneath Europe. The bins have a radius of 200km with a spacing of 100 km.

The diverging slowness vector anomaly P1 begins at the CMB (Figure 4.8) and is present 1000 km above the CMB (Figure 4.10) and continues to migrate eastwards until

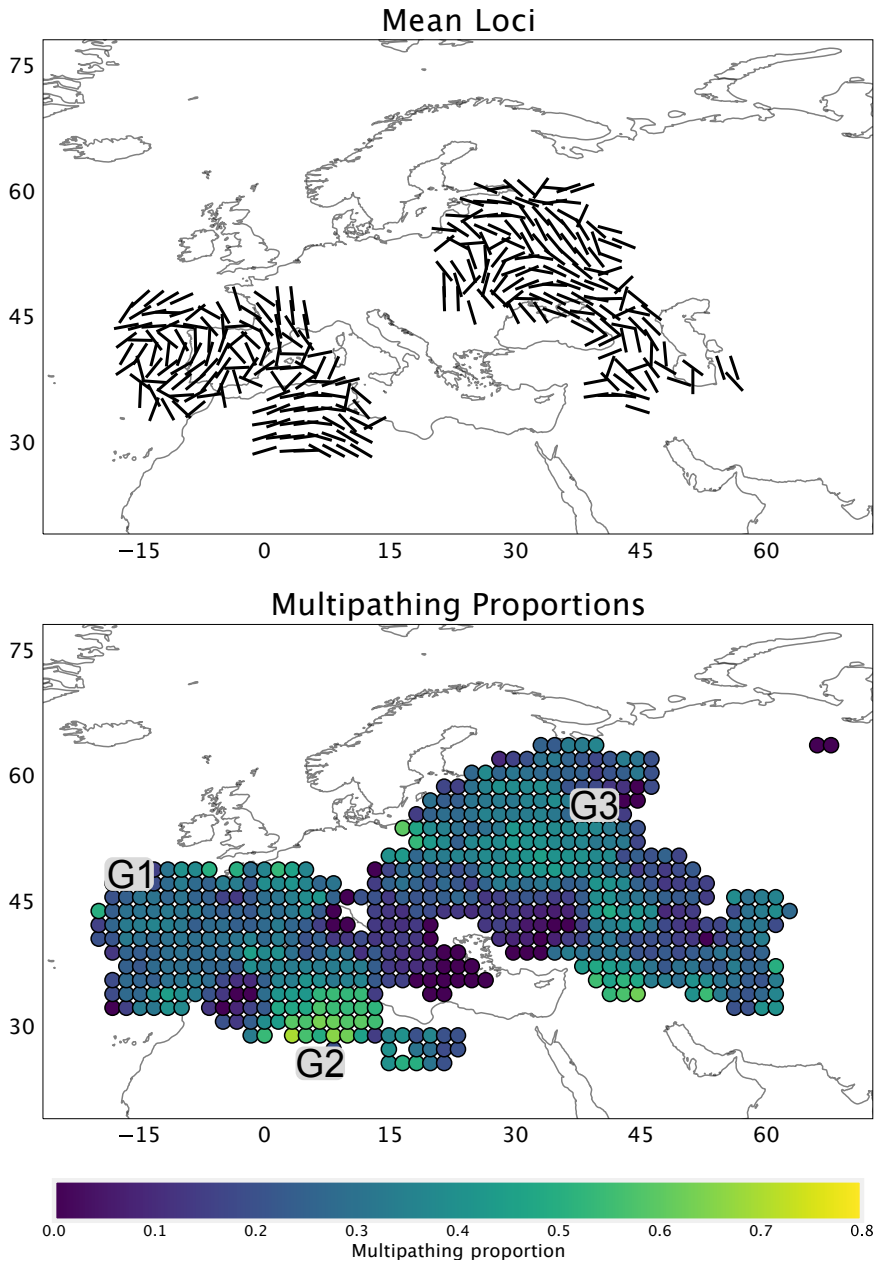

Figure 4.9: Binned multipathed arrival loci (top) and multipathing proportion (bottom) showing regions which may have strong lateral velocity gradients. The data used are from the 0.20 – 0.40 Hz frequency band and plotted at 2891 km depth. The bins have a radius of 200km with a spacing of 100 km.

it is beneath the Eifel region (Figure 4.13. We interpret the eastward migration of the radial pattern beginning at the CMB and its termination beneath the Eifel region as evidence that the Eifel plume has a lowermost mantle origin. There is little multipathing in the Eifel region in the upper mantle (Figure 4.12) which suggests the Eifel plume has strong enough gradients and perturbations to cause slowness vector deviation of approximately 0.6 s/° in the upper mantle, but the gradients are not strong enough to cause multipathing. The presence of an Eifel plume in the upper mantle and to depths of over 2000 km are supported by several studies (Buikin et al., 2005; Goes et al., 1999; Kreemer et al., 2020; Mathar et al., 2006; Rickers et al., 2013; Ritter et al., 2001) and shown by low-velocity anomalies in tomography models (Chang et al., 2015; French and Romanowicz, 2014; Lu et al., 2019; Ritsema et al., 2011; Simmons et al., 2010), although in the upper mantle the plume is not always resolved in tomography studies.

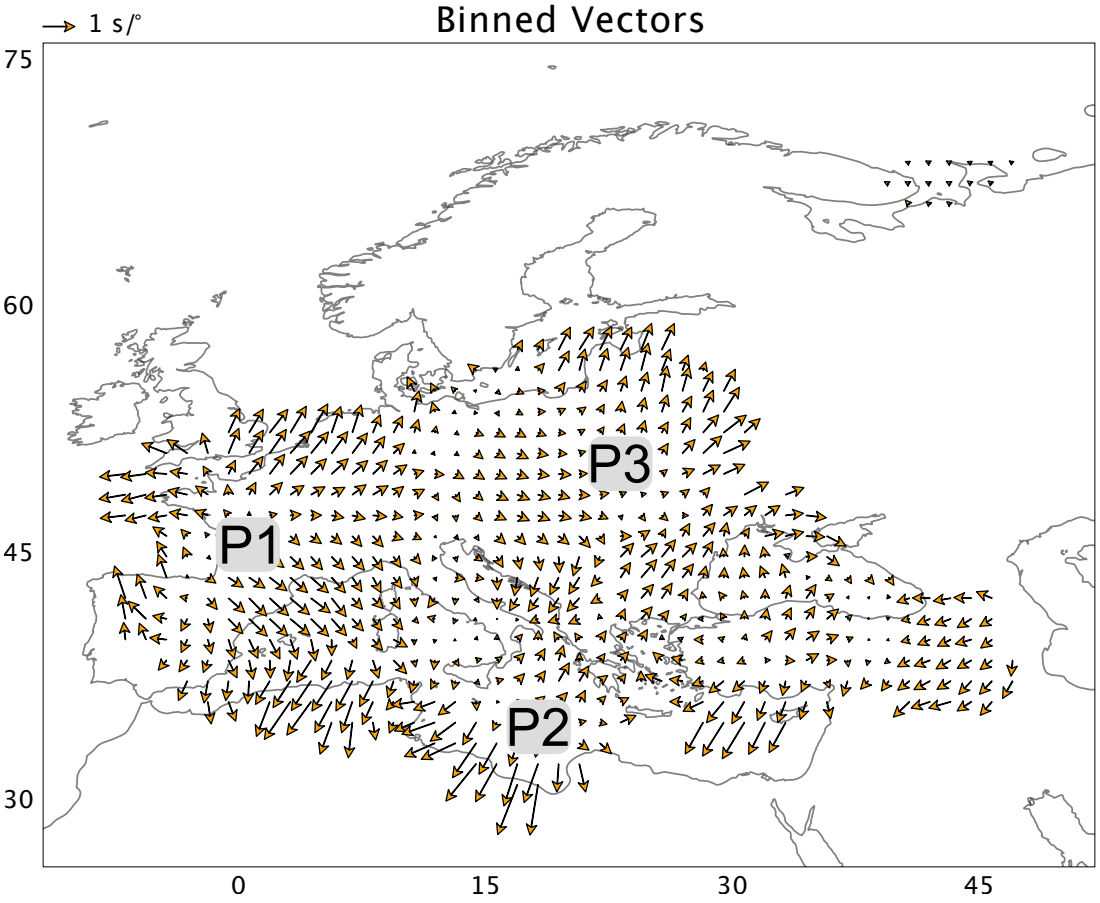

Figure 4.10: Map of slowness vector bins in the 0.20 – 0.40 Hz frequency band using pierce points at 1800 km depth beneath Europe. The bins have a radius of 200km with a spacing of 100 km.

In addition to the P1 heterogeneity, we observed clear radially diverging patterns south-east of Italy in the lower mantle (P2 in Figures 4.10 and 4.8) with large magnitudes (>2 s/°) and a high proportion of multipathing (60%) in this region (G2 in Figure 4.9), although, the same paths also have high multipathing proportion at shallower

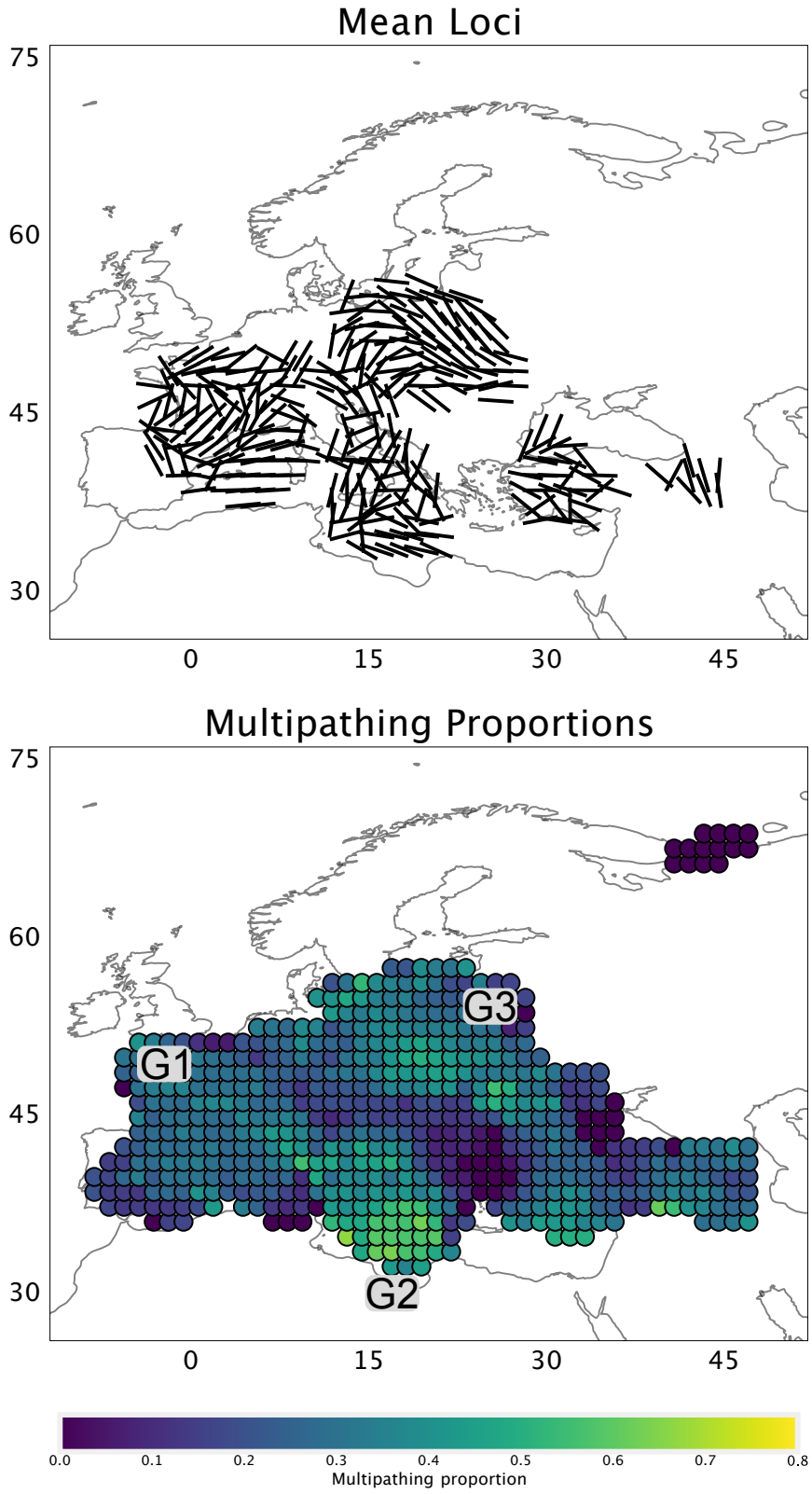

Figure 4.11: Binned multipathed arrival loci (top) and multipathing proportion (bottom) showing regions which may have strong lateral velocity gradients. The data used are from the 0.20 – 0.40 Hz frequency band and plotted at 1800 km depth. The bins have a radius of 200km with a spacing of 100 km.

depths (G4 in Figure 4.12). We interpret these observations as another low-velocity anomaly, possibly a mantle plume, extending from the CMB to the mid-mantle. The radial pattern does not reach the surface and could suggest the structure is impeded or may become more complex if it is present near slab structure. The possible interaction with a stagnating subducted slab has been suggested from geochemical studies (Bell et al., 2004), but we cannot confidently say if this is the case. The region shows high multipathing proportions in both the high and central frequency bands which, at the CMB, suggests the anomaly has velocity gradients over a maximum length of 747 km and at a depth of 1800 km suggest a maximum length of 686 km.

4.4.2.2 Wavefield perturbation from the Perm anomaly?

We observe large slowness vector deviations beneath northeastern Europe (40° longitude, 60° latitude) which is part of a broadly divergent pattern labelled as P3 in Figure 4.8). This region also shows a high proportion of multipathing (≈50%) at the CMB (G3 in Figure 4.9). At shallower depths (≈1800 km depth) there is a high proportion of multipathing (≈60%, G3 in Figure 4.11), a clear northwest-southeast trend in the mean loci in this region (Figure 4.11) and a diverging slowness vector pattern labeled as P3 in Figure 4.10. This is indicative of an anomaly rising more than 1000 km above the CMB. We find no evidence this anomaly is present at depths shallower than 1800 km suggesting it is being impeded by another structure, or, if it is an upwelling, may be in the process of making its way to the surface. Depending on the tomography chosen for comparison, this structure may be related to the Perm anomaly.

Depending on which tomography model is analysed, the exact location of the Perm anomaly varies. If following the interpretations of other regional studies (He et al., 2021; Long and Lynner, 2015) and compare our observations to GyPSuM (Simmons et al., 2010), the observations of the P3 anomaly align well (Figure 4.8) and we have measured the extent to which the Perm anomaly perturbs the wavefield and causes multipathing. On the other hand, many other tomography models locate the Perm anomaly further east (Chang et al., 2015; French and Romanowicz, 2015; Ritsema et al., 2011). Without sampling further eastwards to where most tomography models place the Perm anomaly (Lekic et al., 2012), we cannot determine whether we have observed the Perm anomaly or a different structure that causes slowness vector perturbations, multipathing and rises 1000 km into the mantle.

Regardless of whether this is the Perm anomaly or not, the potential Perm anomaly we have identified causes significant slowness vector deviations, multipathing and may extend to at least 1000 km above the CMB. We interpret these observations as a slow anomaly with velocity gradients of a maximum spatial scale of 676 to 747 km, possibly a mantle upwelling. This interpretation is in line with observations of discrepant SKS-SKKS anisotropy observations in the region (Grund and Ritter, 2019; Long and Lynner,

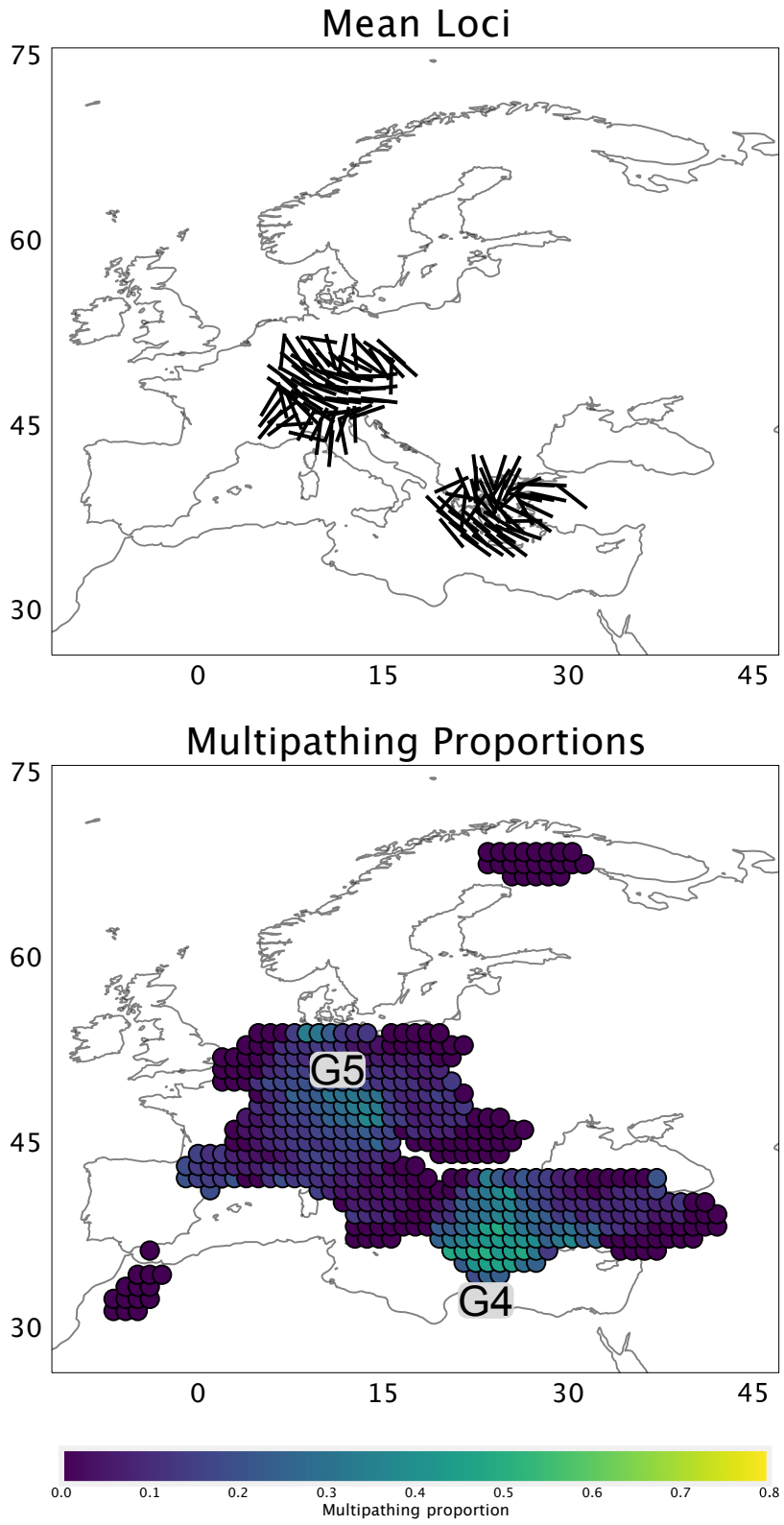

Figure 4.12: Binned multipathed arrival loci (top) and multipathing proportion (bottom) plotted at 500 km depth using data from the 0.15 – 0.30 Hz frequency band. The bins have a radius of 200km with a spacing of 100 km.

2015) which could indicate mantle flow around this anomaly.

4.4.2.3 Mid mantle slabs

We observe several converging slowness vector patterns throughout the mantle beneath Europe which, from the modelling in Section 4.3, are indicative of fast material. We interpret the converging vectors as fast, cold slab material.

The majority of the converging slowness vector patterns we observe beneath Europe are in the mid to upper mantle. We observe converging slowness vector pattern beneath the Alps (S3 in Figure 4.13) which also shows some multipathing suggesting that, while the structure has sufficient velocity gradients to cause strong slowness vector deviations of up to 1.5 s/° and some multipathing (40%, G5 in Figure 4.12). This complex pattern (S3 in Figure 4.13) has some converging aspect to it but the azimuths of the vectors are not perfectly reversed and have some offset to them (i.e. the vector azimuths are not separated by 180°). As the modelling in Section 4.3 suggested, the slowness vectors may be orientated orthogonal to the velocity gradient orientation. Having a convergence pattern where the slowness vectors are not pointing in opposite directions, suggests the velocity gradients are not parallel and may indicate the boundaries of one structure are deformed or the slowness vector pattern is caused by multiple structures. The region does show some evidence for multipathing, but it is unclear if it is from the S3 structure or the deeper P2 structure. If this presumed slab does cause multipathing, a transition from the mantle to heterogeneity may occur on a scale of up to 575 km. Our interpretation of slab material is supported by tomography (Wortel and Spakman, 2000; Zhu et al., 2012) and receiver function studies (Cottaar and Deuss, 2016). Future work could focus on recreating this unique slowness vector pattern and determine whether one structure can produce it or multiple anomalies are needed.

Southeast of S3 is a clear converging vector pattern (S4 in Figure 4.13) which, because of its location, we interpret as the Hellenic slab perturbing the wavefield. The Hellenic slab is shown in several P and S wave tomography models has been observed to descend from the upper 200 km to approximately 700 km depth (Bijwaard and Spakman, 2000; Hansen et al., 2019; Spakman et al., 1988; Wei et al., 2019). Like the Alpine anomaly, this region shows high proportion of high-frequency multipathing (55%, G4 in Figure 4.12), but smaller slowness vector magnitudes (approximately 0.5 s/°). Again, it is unclear if the multipathing in this region may be due to lower mantle contributions from the P2 anomaly. If the Hellenic slab is causing the multipathing it suggests the velocity gradient may be on the scale of up to 575 km at 800 km depth and 493 km at 200 km depth. The depth range for the structure was determined by the depths with the highest binned variances for this region (Figure 4.7). Comparing the slowness vector magnitudes of the Hellenic slab (1 s/°) to the magnitudes of the Alpine slab (relatively large $>$ 2 s/°) suggests some discrepancy in seismic velocity perturbation,

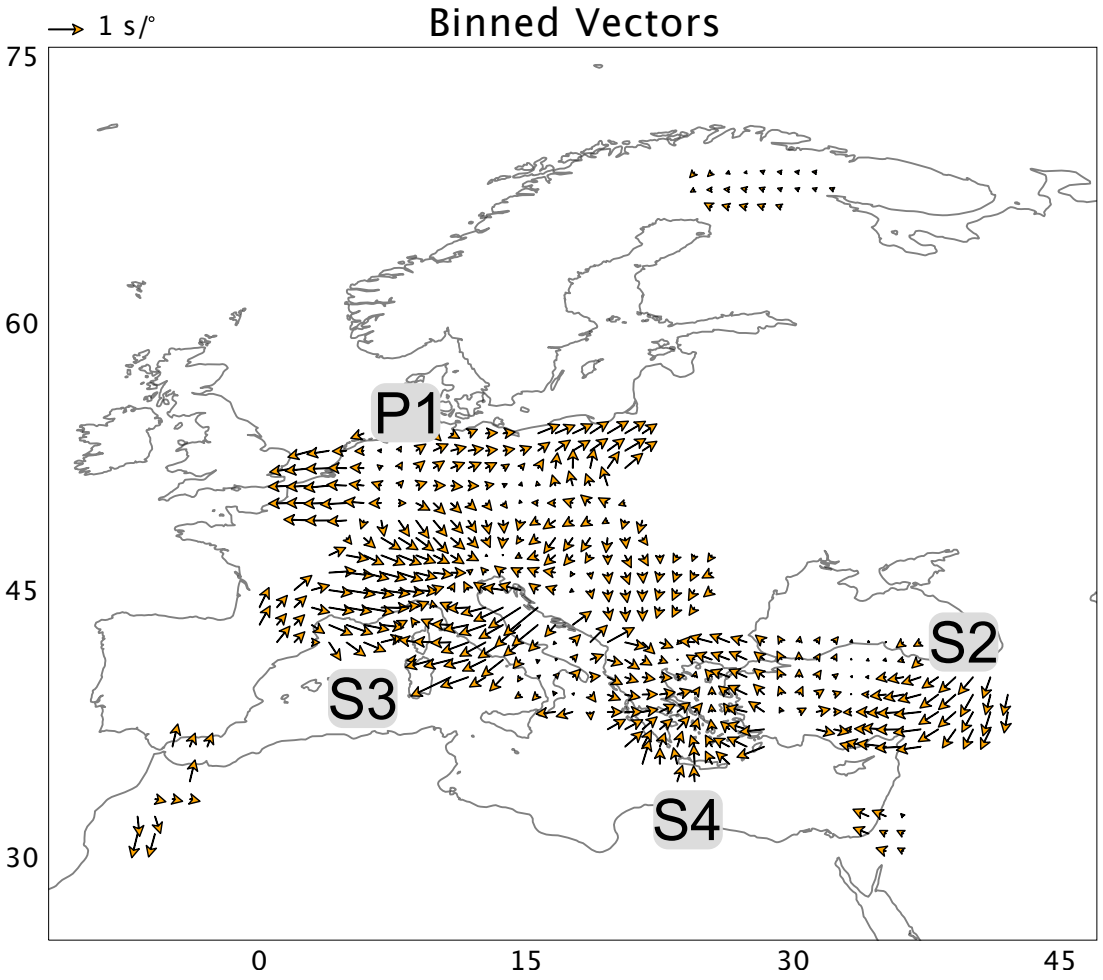

Figure 4.13: Map of slowness vector bins in the 0.10 – 0.20 Hz frequency band using pierce points at 500 km depth beneath Europe. The bins have a radius of 200km with a spacing of 100 km.

lateral velocity gradients, depth extent or morphology. Further extensive forward modelling studies would be needed to determine the differences in the subduction regimes but could infer differences in temperature or possible compositional differences.

While not showing a complete converging or diverging pattern, we observe a distinct change with slowness vectors with magnitudes of approximately 1 s/° pointing eastwards to a transition to very low slowness vector magnitudes (S2 in Figure 4.13) and a very low proportion of multipathing (Figure 4.12). Due to the location of this pattern we suggest the observations could be caused by the Cyprus slab. The sharp transition in slowness vector magnitude may be due to limited sampling of the structure, or velocity gradient strengths being different on different sides of the slab. If the latter is true, the eastern boundary has stronger velocity gradients suggesting it could be more intact or colder and the western boundary may have been deformed up or is closer to the temperature of the ambient mantle. Our observations of the Cyprus slab present in the mid mantle are also in agreement with P and S wave tomography (Berk Biryol et al., 2011; Wei et al., 2019) and receiver function studies (Taylor et al., 2019). With observations of differing lateral velocity gradients, P to S conversions from Taylor et al. (2019) and broad morphology from tomography (Berk Biryol et al., 2011; Wei et al., 2019) a forward modelling study could constrain the velocity structure in this region well, which in turn can be used to infer the thermal structure of the region and inform the interpretation of the evolution of the subduction zone.

In the lowermost mantle, we observe a very broad converging vector pattern (S1 in Figure 4.8) with magnitudes of up to 2 s/°, although the magnitude differs between the sides of the convergent pattern, and there are low magnitude vectors between them. The region has a low (10%) proportion of multipathing which could be due to relatively weak lateral velocity gradients unable to cause multipathing, one of the multipathed arrivals does not arrive with enough amplitude to be observed, or the gradient is not sampled for long enough. We interpret this as the location of the Balkan slab and suggest the slab has different velocity gradients on the east and west sides. The western side may have weaker velocity gradients possibly from interaction with the P1 and P2 structures causing weaker thermal gradients. How nearby slab and plume structures would appear in this analysis is unclear and possible geodynamic and seismological forward modelling studies would be needed.

4.4.2.4 Source side structure

We perform the same variance analysis on the source-side paths of the data recorded in Europe (Figure 4.14). For higher frequencies, there are very few bins that have a significantly low variance (<100), therefore we do not think source-side structure is contributing much to the slowness vector deviation for these frequencies along these paths. For the lowest frequency band (0.10 – 0.20 Hz), many bins have significantly

low variance and the number increases with depth. The trend suggests that likely only the lowermost mantle structure on the source-side is contributing to the perturbations.

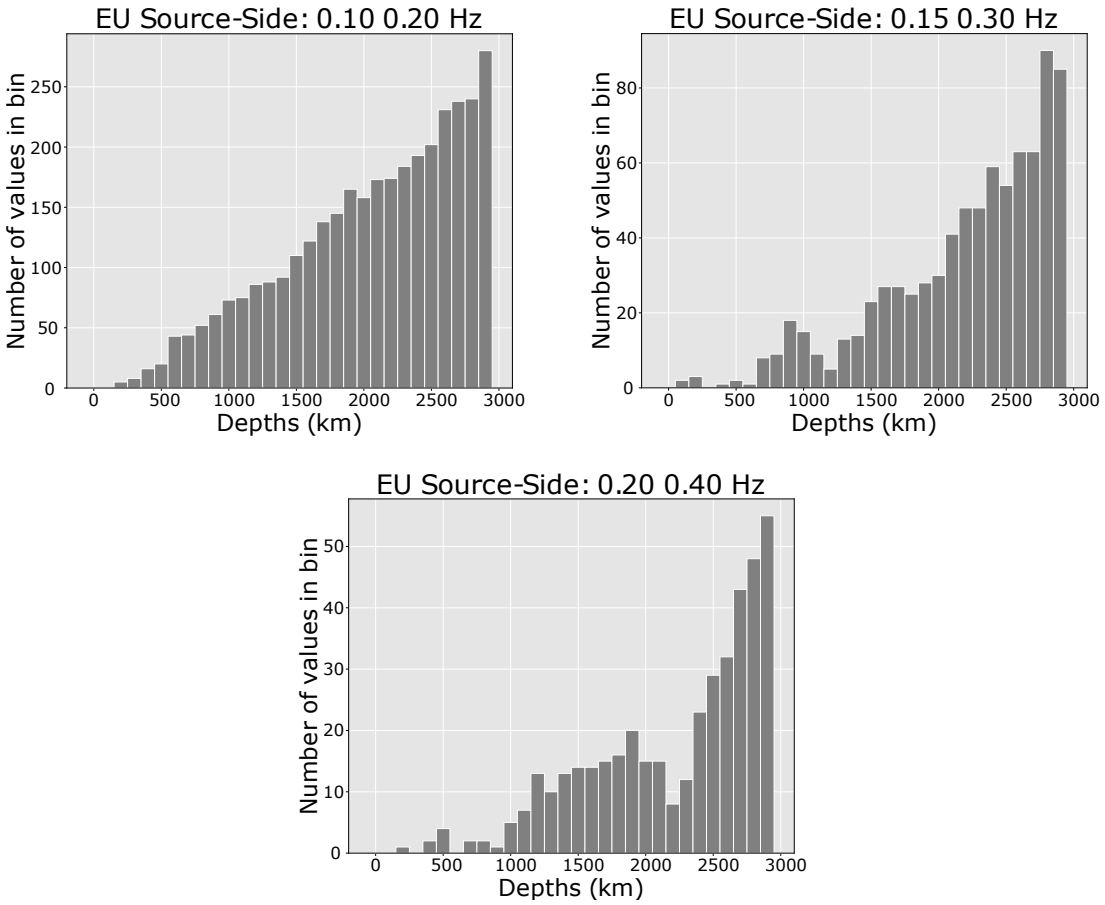

Figure 4.14: Histograms in different frequency bands of the number of bins with a low variance between the slowness vector measurement and slowness vector measurements within 200 km of it. Source-side paths for data recorded in Europe are used for this analysis for these histograms.

Visual inspection of the source-side slowness vector bins with low variance only shows a distinct pattern beneath South America (Figure 4.15). The vectors vary smoothly with a slight convergence in the north of the area and then generally trending south-east to the south with large slowness vector deviation magnitudes (>1.5 s/°). A very similar pattern is observed on the source-side when analysing the North American data (Section 4.4.3), where there is also fast upper mantle structure. This indicates this slowness vector pattern may be an artefact of upper mantle structure, but further analysis would be needed to determine the cause of this pattern.

4.4.2.5 Summary of findings for Europe mantle structure

To summarise, we find three diverging slowness vector patterns indicative of low velocity anomalies which we interpret to be the possible CMB roots of the Eifel and Italian plume and a third upwelling possibly related to the Perm anomaly (Lekic et al.,

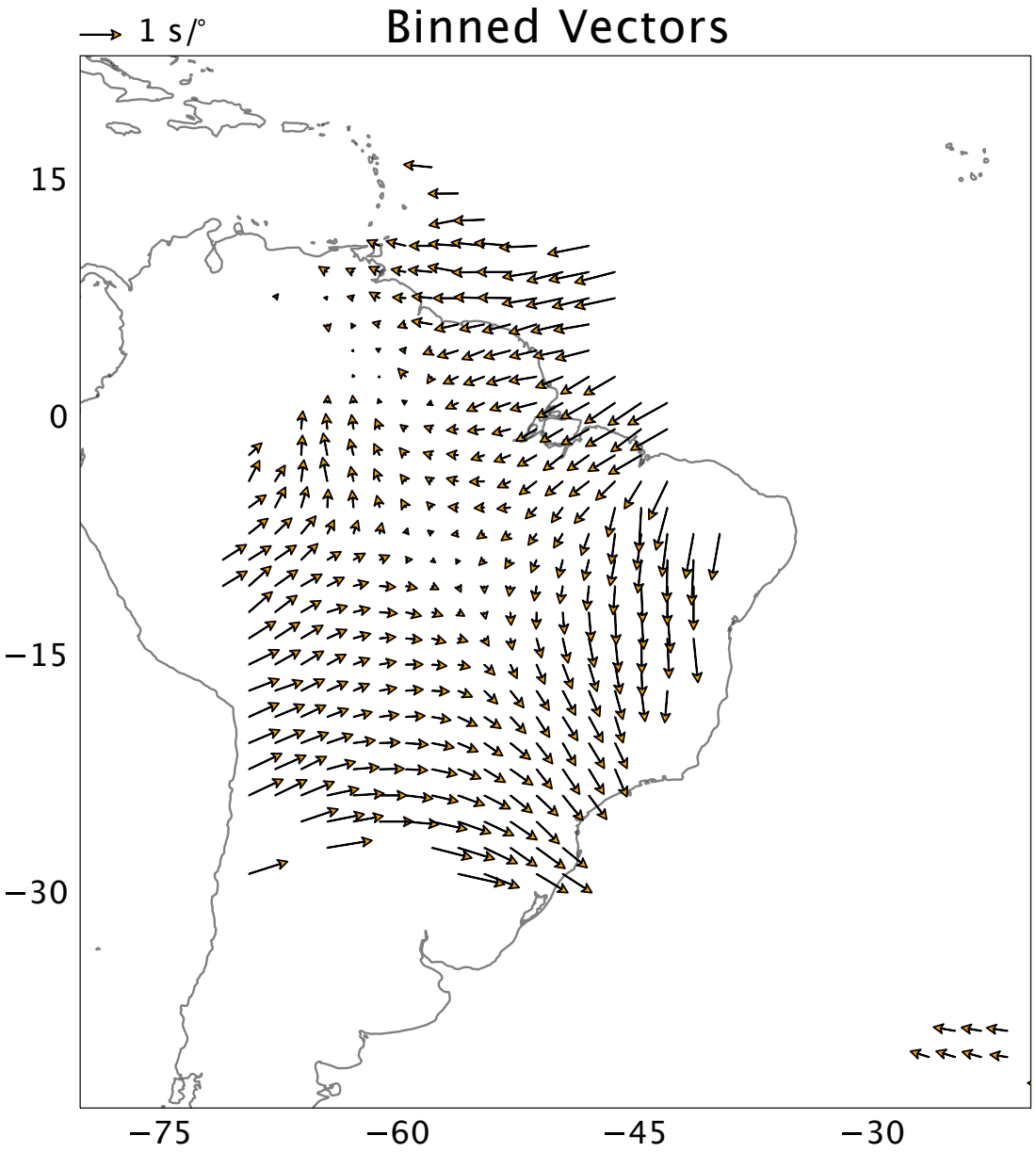

Figure 4.15: Map of slowness vector bins on the source-side beneath South America travelling to Europe. The bins used pierce points at 2891 km depth and use data from the 0.10 – 0.20 Hz frequency band.

2012). The Italian and Perm related anomaly show a high proportion of multipathing suggesting they have sufficiently strong velocity gradients at their boundaries, quantifying this requires further forward modelling. Also in the lowermost mantle, we find a large converging slowness vector pattern in a region with very little multipathing. The converging pattern suggests a fast anomaly is present in the region but the lack of multipathing suggests either the velocity gradients are not strong enough or not sampled for long enough to cause observable multipathing. Our interpretation is this is the remains of the Balkan slab and inferring the velocity perturbation required to produce the slowness vector deviations may give inferences to the thermal properties of the slab and possibly its age. Our interpretation of the lower mantle velocity structure beneath Europe broadly agrees with global tomography models, but we disagree with the morphology of the heterogeneities (Figure 4.16). Depending on the tomography model chosen, our interpretation of the Perm anomaly changes. Inline with previous studies analysing the Perm anomaly, if GyPSuM (Simmons et al., 2010) is chosen our observations agree well but this is not the case for all tomography models (Figure 4.16).

The upper mantle has several complex converging slowness vector patterns which we infer may be a result of the Alpine, Hellenic and Cyprus slab. The pattern we associate with the Cyprus slab has distinct change between large slowness vector deviations and negligible slowness vector magnitudes. This may be due to limited sampling of the Cyprus slab or there are differences in the velocity gradient magnitude between the edges of the slab. In addition to these converging patterns, there is a diverging pattern beneath the Eifel region which we infer to be the upper mantle signal of the Eifel plume and suggests the plume may extend from the CMB to the surface. In the upper mantle our observations broadly agree with the tomography but disagree with the morphology of the structures (Figure 4.17), which is to be expected from the differing resolutions of the observations. Figure 4.18 summarises the observations and interpretations of the heterogeneities in the region.

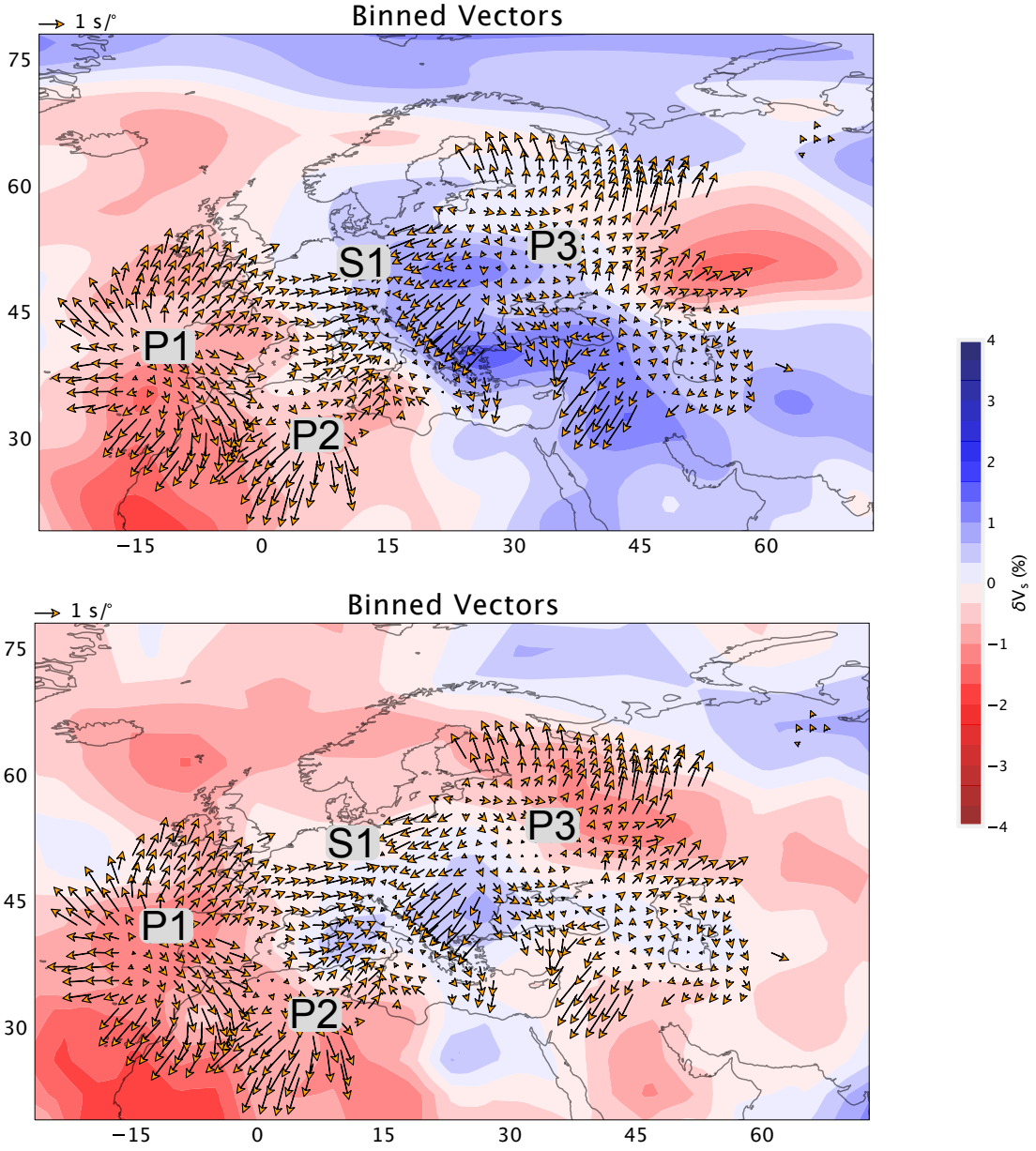

Figure 4.16: Slowness vector bins in the 0.20 – 0.40 Hz frequency band at 2891 km depth. The bins have a radius of 200 km with a spacing of 100 km. In the background, we show tomography models, S40RTS (Ritsema et al., 2011) (top) and GyPSuM (Simmons et al., 2010) (bottom) to highlight the difference in the possible locations of the Perm anomaly. Scale for slowness vector magnitude is given in top left.

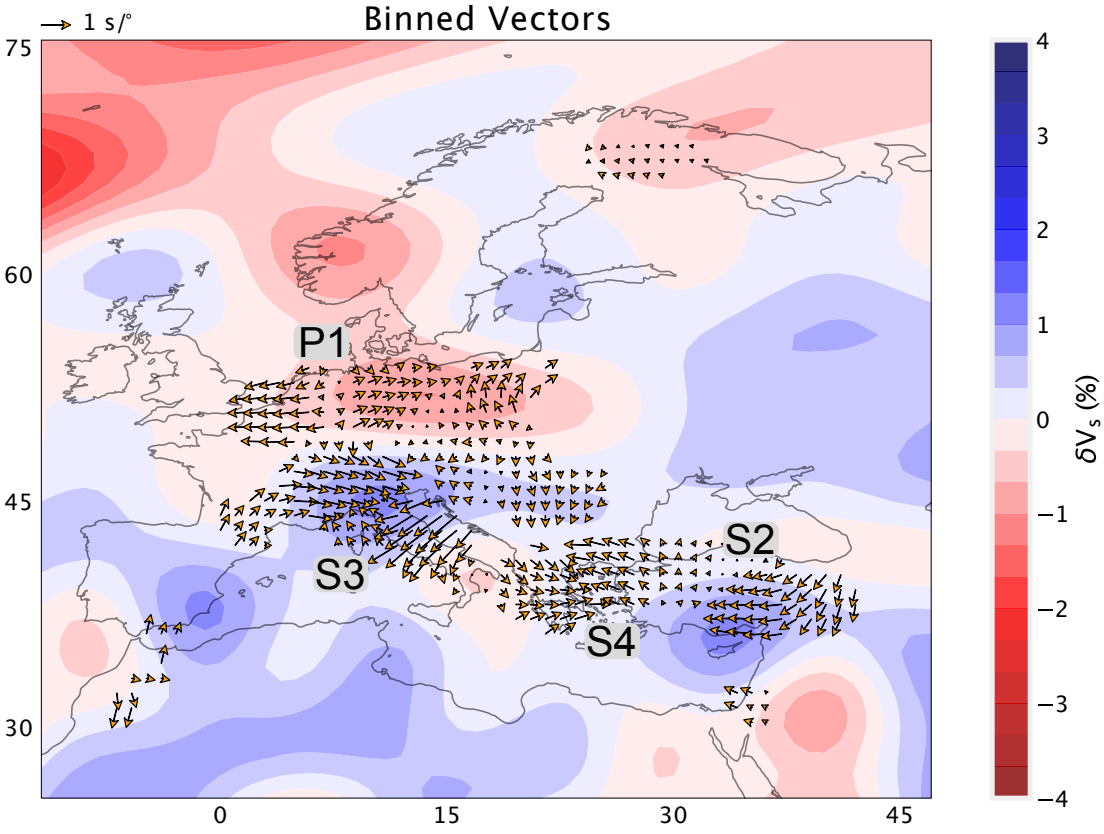

Figure 4.17: Slowness vector bins in the 0.10 – 0.20 Hz frequency band at 500 km depth. The bins have a radius of 200 km with a spacing of 100 km. In the background, we show tomography model S40RTS (Ritsema et al., 2011). Scale for slowness vector magnitude is given in top left.

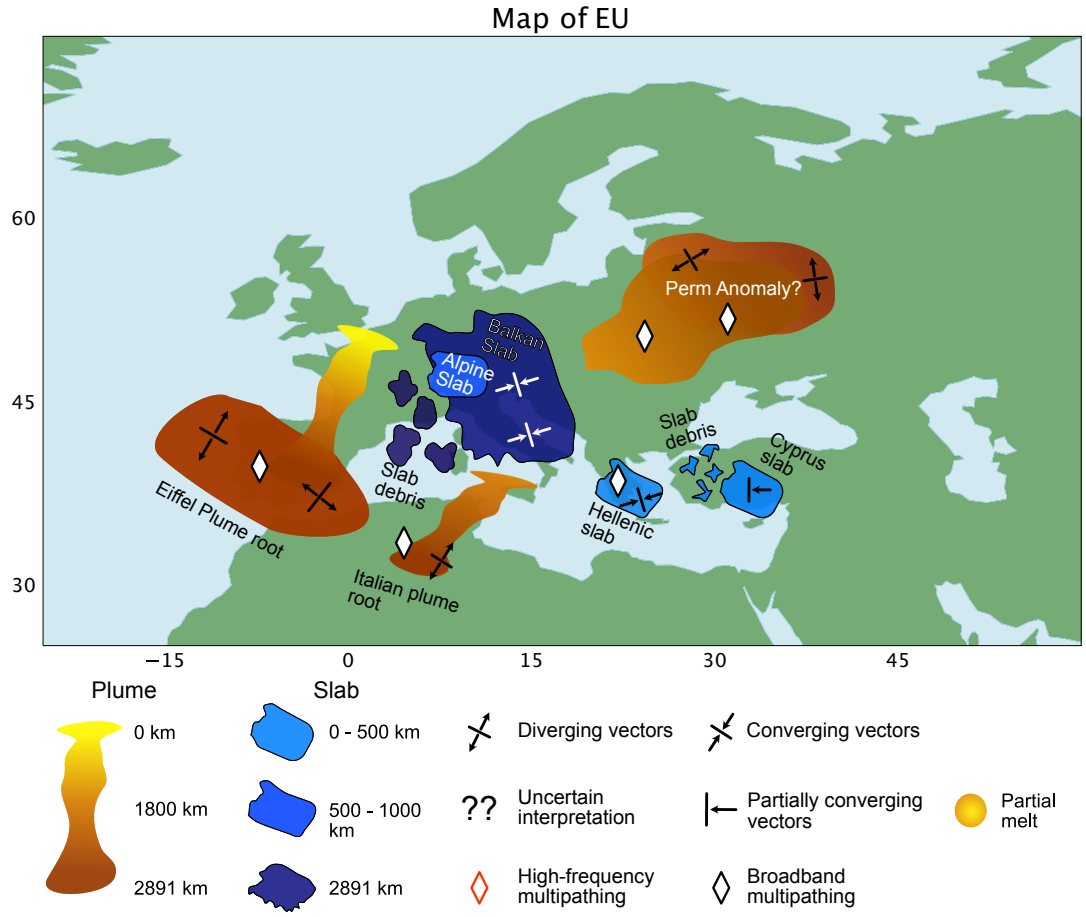

Figure 4.18: Cartoon summarising the interpretations of the spatial distribution of slowness vector deviation observations beneath Europe.

4.4.3 North America

Figure 4.19 shows the results of the variance-depth analysis of the sub-dataset sampling North America (NA). Unlike the European dataset, there is little evidence for lower-mantle structure causing slowness vector deviation in our observations in the low and central frequency bands (0.10 – 0.20 and 0.15 – 0.30 Hz). However, as observed in Section 4.4.2, the highest frequency band (0.20 – 0.40 Hz) appears to be most sensitive to lowermost mantle structure and the different frequency bands appear to be sensitive to structures at different depths. Table 4.3 shows which depths we think may have mantle heterogeneities beneath North America affecting the respective frequency bands.

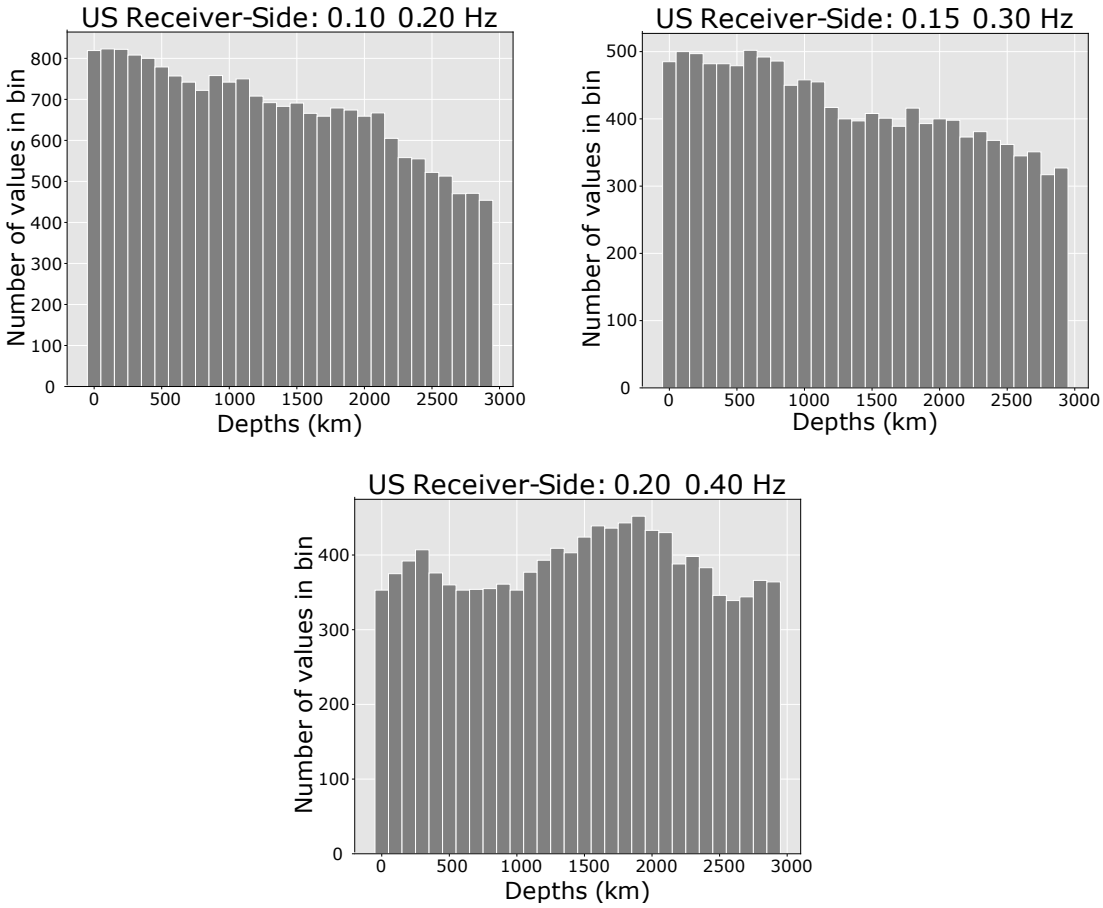

Figure 4.19: Histograms for the receiver-side paths beneath NA in different frequency bands of the number of bins with a low variance between the slowness vector measurement and slowness vector measurements within 200 km of it.

Frequency band (Hz)	Depths analysed
0.10 – 0.20	200 km, 1000 km, 1800 km, 2000 km
0.15 – 0.30	200 km, 500 km, 800 km, 1000 km, 1800 km
0.20 – 0.40	300 km, 1400 km, 1800 km, 2000 km, 2891 km

Table 4.3: Depths with possible mantle heterogeneity inferred from the slowness vector variances.

Like in Section 4.4.2 we visually inspect the slowness vector deviation patterns, multipathing proportions and loci orientations at depths and frequency bands in Table 4.3. In the following subsections we present our interpretations of the structures that may be causing them. We are selective with which depth slices to present with the rest presented in Appendix Section C.

4.4.3.1 Plumes and slabs of western US

The upper mantle of the western US is complex. It is broadly characterised by multi-scale low-velocity anomalies with high-velocity structures protruding through (Fichtner et al., 2018; Grand, 1994; Porritt et al., 2014; Schmandt and Lin, 2014). This, alongside observations of a thin low-velocity zone above the mantle transition zone at 410 km depth (Gao et al., 2006; Schmandt et al., 2011; Song et al., 2004; Vinnik et al., 2010), is interpreted as the Farallon slab subducting into the upper mantle, releasing water and causing partial melt and small scale upwellings in the upper mantle (Cao and Levander, 2010; Schmandt et al., 2012; Schmandt and Humphreys, 2010; Tian et al., 2009). The partial melt and plumes in the upper mantle are widely hypothesised to cause volcanic regions such as Yellowstone, Snake Valley Plane and Clear Lake volcanic field (Eagar et al., 2010; Obrebski et al., 2010; Pierce and Morgan, 2009; Smith et al., 2009). The Yellowstone plume is even speculated to affect the Farallon slab by causing tears and gaps in the slab observed as patches of high-velocity regions (Leonard and Liu, 2016; Obrebski et al., 2010; Pierce and Morgan, 2009; Sigloch et al., 2008; Tian et al., 2011; Xue and Allen, 2007). Furthermore, the Yellowstone plume is hypothesised to descend into the mid mantle with some recent studies imaging the plume from its core-mantle boundary root to the surface (Nelson and Grand, 2018).

In our observations, we find a large magnitude (>1 s/°) divergent slowness vector pattern (D1 in Figure 4.20) and moderately high multipathing proportion (40% M5 in Figure 4.21) in the upper mantle beneath the Yellowstone region. The slowness vector deviations are somewhat present in the mid mantle (D1 in Figure C.23), but with lower slowness vector magnitude suggesting the structure may extend into the mantle beneath Yellowstone, but this could be an artefact of some of the slowness vector measurements having similar paths through the mid and upper mantle. We interpret this diverging pattern (D1 in Figure 4.20) and moderately high multipathing proportion as evidence of a slow anomaly in the mantle, possibly the Yellowstone plume itself. The multipathing may be due to the depth extent of the Yellowstone anomaly, but if it is occurring in the upper mantle (300 km depth) suggests velocity gradients over at most 483 km. Some argue the Yellowstone plume may extend to the lowermost mantle and recently Nelson and Grand (2018) suggest the location of the Yellowstone plume lower mantle root at approximately -120° longitude and 35° latitude, in agreement with the diverging slowness vector pattern D6 in Figure C.25.

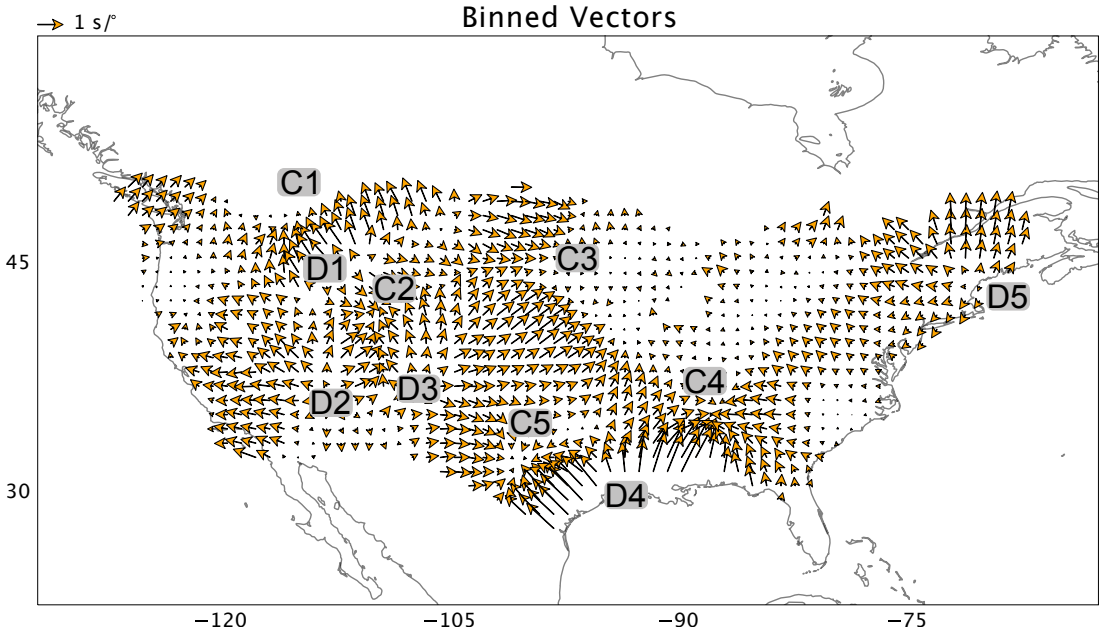

Figure 4.20: Map of slowness vector bins in the 0.10 – 0.20 Hz frequency band using pierce points at 200 km depth beneath the US. The bins have a radius of 200km with a spacing of 100 km.

In addition to the Yellowstone anomaly, we find evidence for several smaller scale low-velocity anomalies confined to the upper mantle as observed in previous studies (Eagar et al., 2010; Gilbert et al., 2003; Schmandt and Humphreys, 2010; Xue and Allen, 2007) as small diverging slowness vector patterns D2 and D3 in Figure 4.20. The D2 labelled diverging pattern is located east of where previous studies have identified a 'slab window' (Porritt et al., 2014; Sigloch et al., 2008; Tian et al., 2011). The slab window may be where the Farallon slab has broken apart possibly initiating small scale upwelling from the partial melt generated by hydration melting (Cao and Levander, 2010; Schmandt et al., 2012; Schmandt and Humphreys, 2010; Tian et al., 2009). In addition, we observe a divergent slowness vector pattern possibly an upwelling to the east of the slab window labelled as D3 in Figure 4.20. Despite the clear slowness vector patterns, there is a low multipathing proportion in this region (Figure 4.21). The difference in multipathing proportion and slowness vector magnitudes between these structures and the Yellowstone anomaly could be due to differences in velocity gradients or depth extents of the structures.

As mentioned, the western US is characterised by several high-velocity anomalies disconnected with each other which some interpret as the subduction of the Farallon slab being segmented into multiple different slab structures (Obrebski et al., 2010; Pierce and Morgan, 2009; Sigloch et al., 2008; Tian et al., 2009). We observe several converging patterns in the western upper mantle (C1 and C2 in Figure 4.20), which we interpret these converging patterns as clear fast anomalies in the upper mantle.

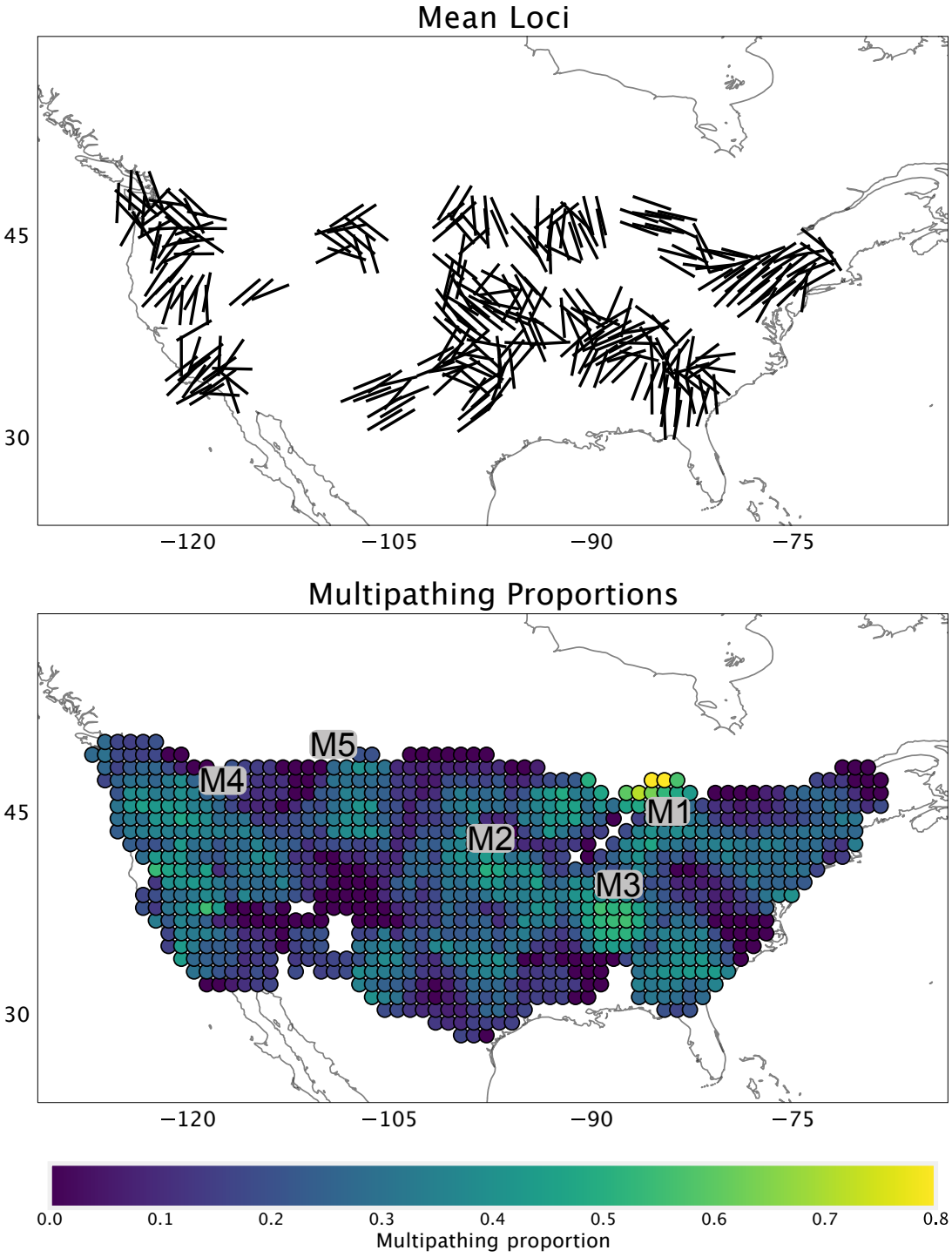

Figure 4.21: Figure summarising multipathing observations using data in the 0.20 – 0.40 Hz frequency band and pierce points at 300 km depth. The top figure shows the mean loci in bins of 200 km radius in increments of 100 km. The bottom figure shows the proportion of multipathing relative to the total number of observations in the bin. Bins for the multipathing proportion measurements are 200 km radius spaced with increments of 100 km.

The magnitudes of the slowness vectors around C1 vary depending on location with small magnitudes of < 0.5 s/° to the west of the pattern but other regions show large magnitudes of up to 1.5 s/°. This region also has high multipathing proportions in the high-frequency band (M4 in Figure 4.21) and in the central frequency band (M4 in Figure 4.22). The discrepancy in slowness vector magnitude may be a result of slowness vector deviations from the nearby diverging pattern (D1) being included in the binning process, or it could give some indication of the differing properties of the boundary structure of the heterogeneity. The multipathing proportions also may be influenced by the nearby Yellowstone anomaly where the change from one heterogeneity to another could cause the multipathing or the structure's velocity gradients and depth extent could be the cause. The C2 anomaly shows more consistent slowness vector magnitudes of approximately 1 s/° at all azimuths and is also near a region of high multipathing proportion in the central frequency band (M6 in Figure 4.22). The M6 region of high multipathing (50%) in the central frequency band has its highest proportion at depths shallower than 500 km and has a much lower proportion deeper in the mantle (Figure 4.23). The M6 feature lies between the C2 and D2 anomalies where a transition from fast to slow anomalies may exist which could create a sharp velocity gradient and cause multipathing. At this depth (200–300 km) and frequency band (0.15 – 0.30 Hz), we estimate the maximum transition length would be 482 km.

In the lowermost mantle beneath the western US, there is a broad diverging slowness vector pattern with magnitudes of up to 1.5 s/° (D7 in Figure 4.24) with relatively low multipathing proportion (Figure 4.25). This pattern is indicative of a slow anomaly at the CMB beneath the western US disagreeing with global seismic tomography models which often have a fast anomaly at this location (Chang et al., 2015; French and Romanowicz, 2014; Ritsema et al., 2011; Simmons et al., 2010).

4.4.3.2 Plumes and slabs of central end eastern US

The mantle beneath central and eastern US is characterised by a large cratonic structure with some studies suggesting the existence of upper mantle plumes beneath the Appalachian mountains (Menke et al., 2016; Schmandt and Lin, 2014; Tao et al., 2020) and potential Farallon slab and Kula slab remnants at depth (Bunge and Grand, 2000; Grand et al., 1997; Li et al., 2008; Sigloch et al., 2008; van der Lee and Nolet, 1997). We observe converging and diverging slowness vector patterns and high multipathing proportions in the eastern US indicative of mantle heterogeneity with slow and fast seismic velocities and strong lateral velocity gradients. Here, we discuss the possible heterogeneities we have observed in comparison to other studies.

We observe only one radially diverging pattern in the eastern US (D5 in Figure 4.20), which is indicative of a slow cylindrical anomaly beneath the Appalachians. Slowness vector magnitudes vary from 0.3 s/° at backazimuths of approximately 315°

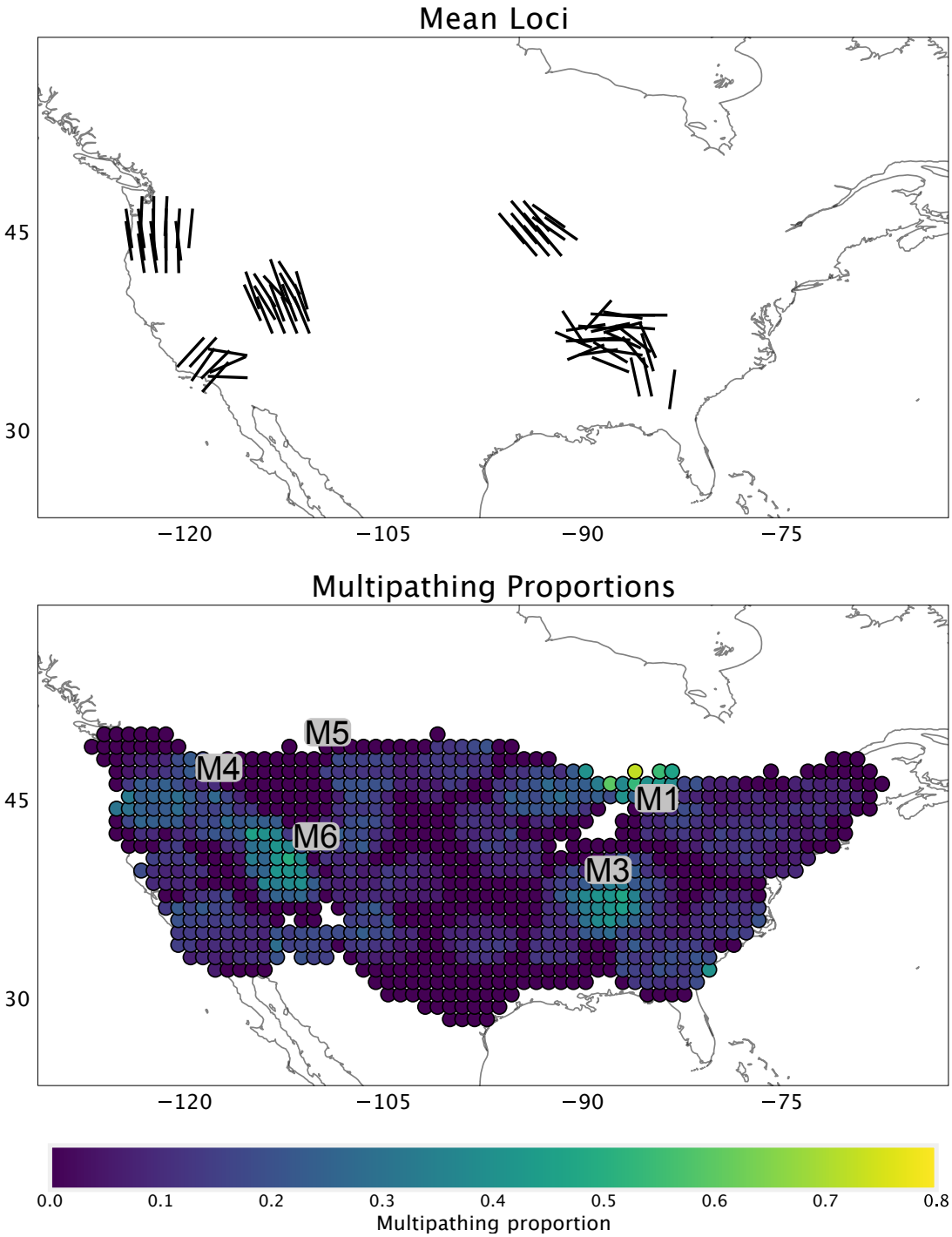

Figure 4.22: Figure summarising multipathing observations using data in the 0.15 – 0.30 Hz frequency band and pierce points at 300 km depth. The top figure shows the mean loci in bins of 200 km radius in increments of 100 km. The bottom figure shows the proportion of multipathing relative to the total number of observations in the bin. Bins for the multipathing proportion measurements are 200 km radius spaced with increments of 100 km.

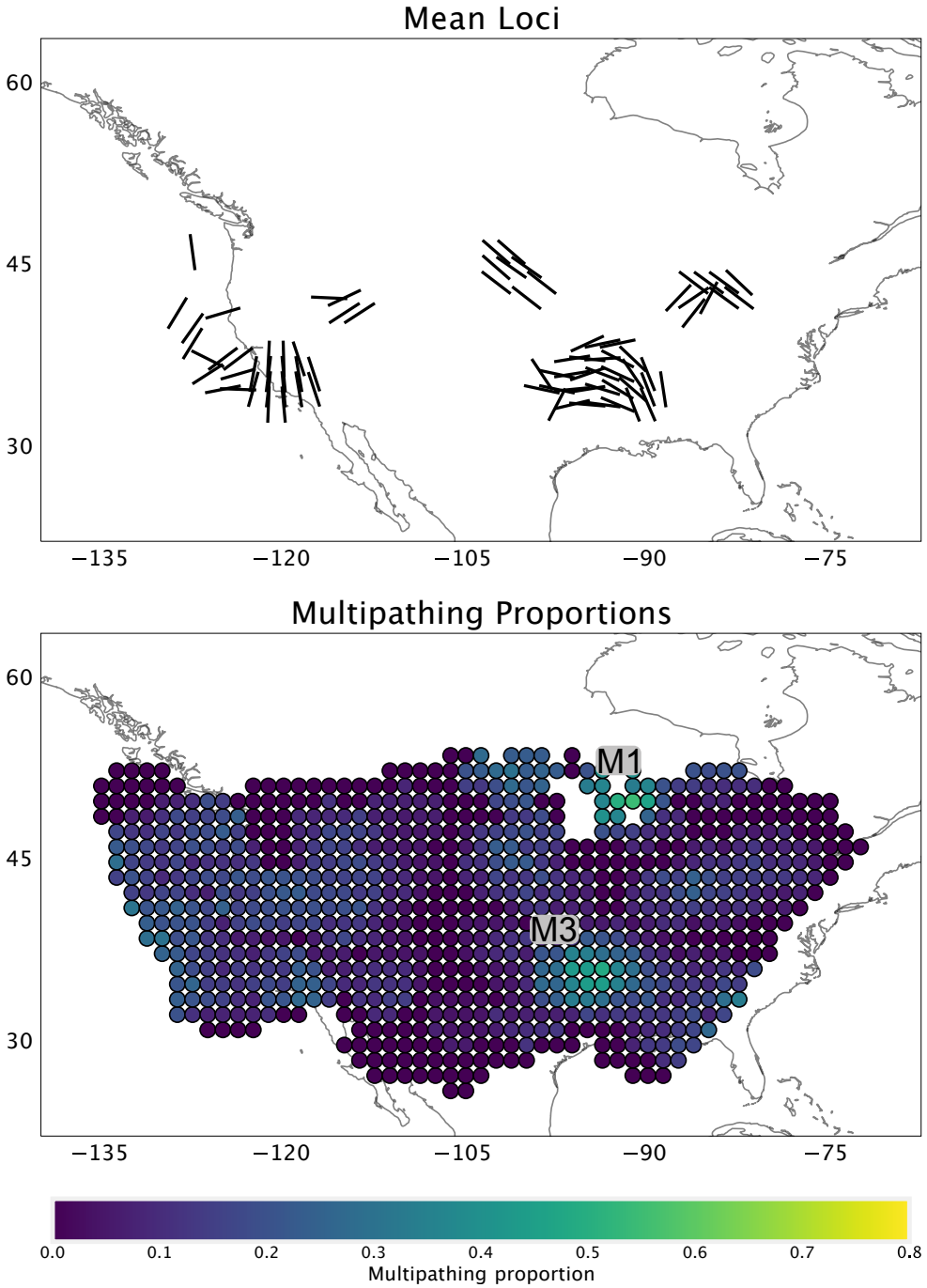

Figure 4.23: Figure summarising multipathing observations using data in the 0.15 – 0.30 Hz frequency band and pierce points at 1800 km depth. The top figure shows the mean loci in bins of 200 km radius in increments of 100 km. The bottom figure shows the proportion of multipathing relative to the total number of observations in the bin. Bins for the multipathing proportion measurements are 200 km radius spaced with increments of 100 km.

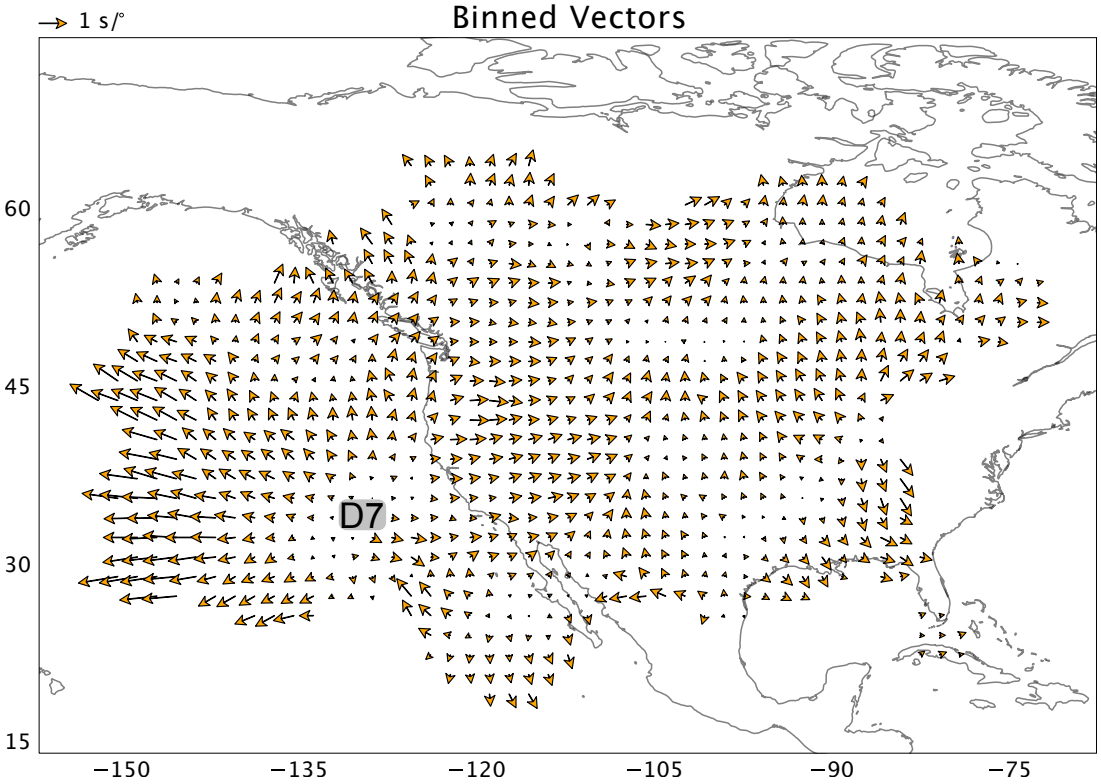

Figure 4.24: Map of slowness vector bins in the 0.20 – 0.40 Hz frequency band using pierce points at 2891 km depth beneath the US. The bins have a radius of 200km with a spacing of 100 km.

to >1 s/° at a backazimuth of 0° in all frequency bands. This pattern extends deep into the mantle, but we believe this is because the same slowness vectors are being binned as shown by a near-constant variance and not because the potential plume is deeply rooted. Our interpretation of a cylindrical slow anomaly is compatible with many studies who suggest the Appalachian plume is present in this region (Menke et al., 2016; Schmandt and Lin, 2014; Tao et al., 2020). The region does not show a high multipathing proportion, which may be due to the plume only existing in the upper mantle or it has weak velocity gradients.

East of the D5 anomaly, we observe a sharp change in slowness vector magnitudes from approximately 1 s/° to very small deviations and with no clear convergent or divergent pattern (C3 Figure 4.20). These large slowness vector magnitudes indicate a lateral velocity gradient or heterogeneity but, as there is a distinct transition to negligible magnitudes, only one strong velocity gradient may be present. The region does show some multipathing in the highest frequency band (M2 in Figure 4.21), which has been suggested to be Farallon slab remnants by some (Burdick et al., 2008; Porritt et al., 2014; Sigloch et al., 2008). If a single heterogeneity is causing the observations, there must be s significant discrepancy in the sharpness of the velocity gradients on either side of the structure to only cause large slowness vector magnitudes on one side. Such discrepancy could give insight into the thermal, chemical or relative deformation of the boundaries.

Southeast of the C3 feature, we observe a clear converging slowness vector pattern with magnitudes >1 s/° (C4 Figure 4.20). The azimuths of the vectors in the converging pattern are not completely opposite and are unique to any observations we have made here. Furthermore, there are no low magnitude slowness vectors in the pattern between the high magnitude vectors, which may suggest this is a relatively small structure. The pattern of the slowness vectors is not necessary linear and is somewhat radial suggesting the structure is more circular or cylindrical. In the same region, we observe a high proportion of multipathing in both the central and upper frequency bands labelled as M3 in Figures 4.22 and 4.21. The M3 multipathing anomaly is present at a range of depths, it is challenging to constrain the radial length scales of the velocity gradient. We interpret these observations as a fast anomaly with sufficiently sharp velocity gradients and perturbation difference over the velocity gradient to cause multipathing in multiple frequency bands. This interpretation is in line with previous studies suggesting a remnant of the Farallon slab in the mid mantle is present in the same region (Grand et al., 1997; Li et al., 2008; Sigloch et al., 2008; van der Lee and Nolet, 1997) which may be causing mantle downwelling in this region (Forte et al., 2007; Forte et al., 2010). Forward modelling would be needed to constrain the unique observations of this and other anomalies observed in this study, which shows the value of interrogating mantle structure in this way.

4.4.3.3 Distribution of multipathing

The spatial distribution of multipathing proportion is significantly different in the upper mantle between frequency bands. For the highest frequency band (0.20 – 0.40 Hz, Figure 4.21), there is a broad distribution of high multipathing proportion whereas, in the central frequency band (0.15 – 0.30 Hz, Figure 4.22), the high proportion regions are much more localised. We interpret the difference as the different frequency bands are sensitive to the different spatial and depth extents of the lateral velocity gradients.

The wide distribution of high multipathing proportion in the upper mantle in the higher frequencies only (Figure 4.21), suggests the heterogeneity causing the multipathing is sufficiently small scale to only be imaged by these short-wavelength observations. Not all multipathing will be caused at this depth, but we argue a significant proportion will be because of the high number of low variance bins in the upper mantle (Figure 4.19). We suggest this multipathing may be caused by structures not individually resolvable by seismic tomography or cause multipathing in lower frequency bands. We interpret these structures to have velocity gradients with scales of at most 483 km, which may be larger than some of the heterogeneities, but it is the best estimate we can make with the information available. The wide distribution of high frequency multipathing is also present throughout the lowermost mantle beneath North America although at a slightly lower proportion (Figure 4.25), but we do not observe large slowness vector magnitudes or patterns in this region. We suggest most of the multipathing observed is caused by structure in the upper and mid mantle, but some lower mantle structures may cause multipathing but it is challenging to discern the origin. Lower mantle anomalies may be contributing to some slowness vector deviations, but these may have been filtered out through the variance analysis and other, more regionally specific, studies would need to be conducted to infer the lower mantle structure on this length scale.

Alongside the broad distribution of multipathing, many depths and frequency bands show a very high proportion of multipathing at approximately -85° longitude and 45° latitude (M1 in Figures C.26, C.20, C.19 and 4.21), but very little slowness vector deviation in either the binned or the unbinned data. At present, we do not know what could be causing such high multipathing proportions with small slowness vector magnitudes and further work on a detailed regional analysis using forward modelling to investigate different mantle structures or investigating the region with different seismic phases is needed.

4.4.3.4 Gulf of Mexico anomaly

The highest magnitude slowness vectors (up to 2 s/°) were observed near the Gulf of Mexico (D4 in Figures 4.20), but with a very low proportion of multipathing (Figure

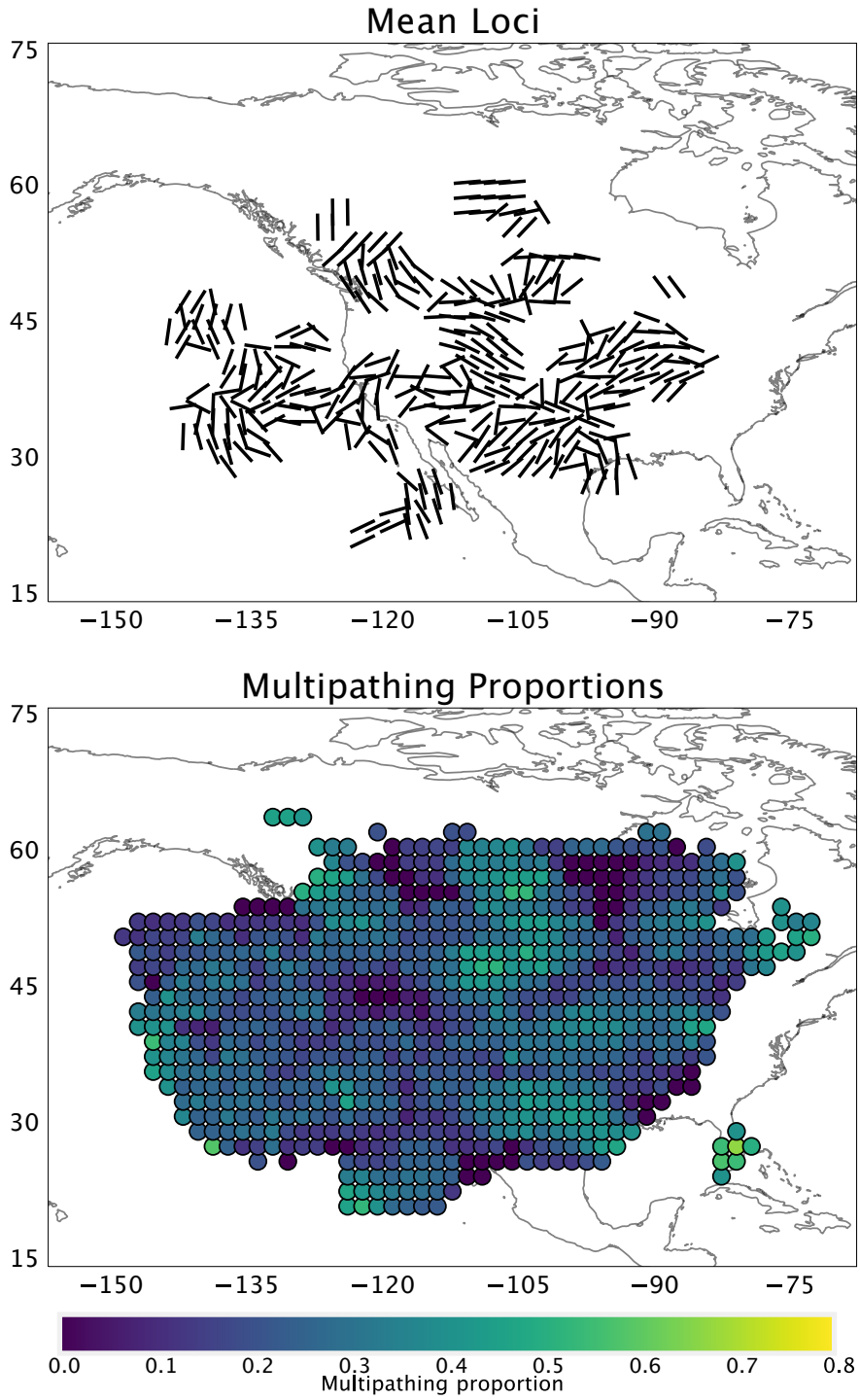

Figure 4.25: Figure summarising multipathing observations using data in the 0.20 – 0.40 Hz frequency band and pierce points at 2891 km depth. The top figure shows the mean loci in bins of 200 km radius in increments of 100 km. The bottom figure shows the proportion of multipathing relative to the total number of observations in the bin. Bins for the multipathing proportion measurements are 200 km radius spaced with increments of 100 km.

4.21). It is not clear whether shallow structures could cause such significant slowness vector deviations or whether a deeper structure needs to be sampled. We are not certain what could be the cause of such an anomaly and have not found an extensive discussion of this region in the literature. As with several other regions of interest identified in this study, further detailed analysis via forward modelling or a dedicated regional study is needed.

4.4.3.5 Source side structure

For source-side structure, while many bins have significantly low variance (Figure 4.26), most are low magnitude slowness vectors (< 0.5 s/°) and are not indicative of sampling mantle heterogeneity. We do observe a distinct slowness vector pattern very similar to that observed in Section 4.4.2 shown in Figure 4.27. As the slowness vector pattern on the source-side is very similar to that of data recorded in Europe (Figure 4.15), we hypothesise this is an artefact, possibly due to sampling subducted slab structure near the surface. Investigation with finite-frequency forward modelling would be needed to further investigate the cause of this slowness vector pattern.

4.4.3.6 Summary of findings for North America mantle structure

In summary, we find the heterogeneities in the upper and mid mantle beneath North America cause the majority of our observations of slowness vector deviations beneath the US. We observe several diverging slowness vector patterns which we interpret as low velocity anomalies and as evidence for the Yellowstone and possibly Appalachian plume in the upper mantle as well as small-scale upwellings in the western US. We observe several converging slowness vector patterns in the upper mantle which we interpret at fast anomalies caused by possible Farallon slab remnants. Our interpretations of the velocity structure agrees well with tomography model from Fichtner et al. (2018) (Figure 4.28).

There is a broad scattering of moderate multipathing proportion in the high frequency band which we suggest are caused by gradients on the spatial scale of up to 483 km, but we are not certain what structures may be causing it. Whether the heterogeneities identified through slowness vector deviation pattern cause multipathing varies depending on the heterogeneity. This, like the observations beneath Europe, highlights the unique slowness vector deviation observations and multipathing observations for each heterogeneity and the heterogeneities' properties can be greatly constrained if the observations can be replicated. The lower mantle offers fewer patterns but has a large diverging pattern west of the US possibly from low velocity anomalies, but this does not necessarily agree with global tomography models (e.g. Figure 4.29). Figure 4.30 summarises the interpretations and the observations made in this region.

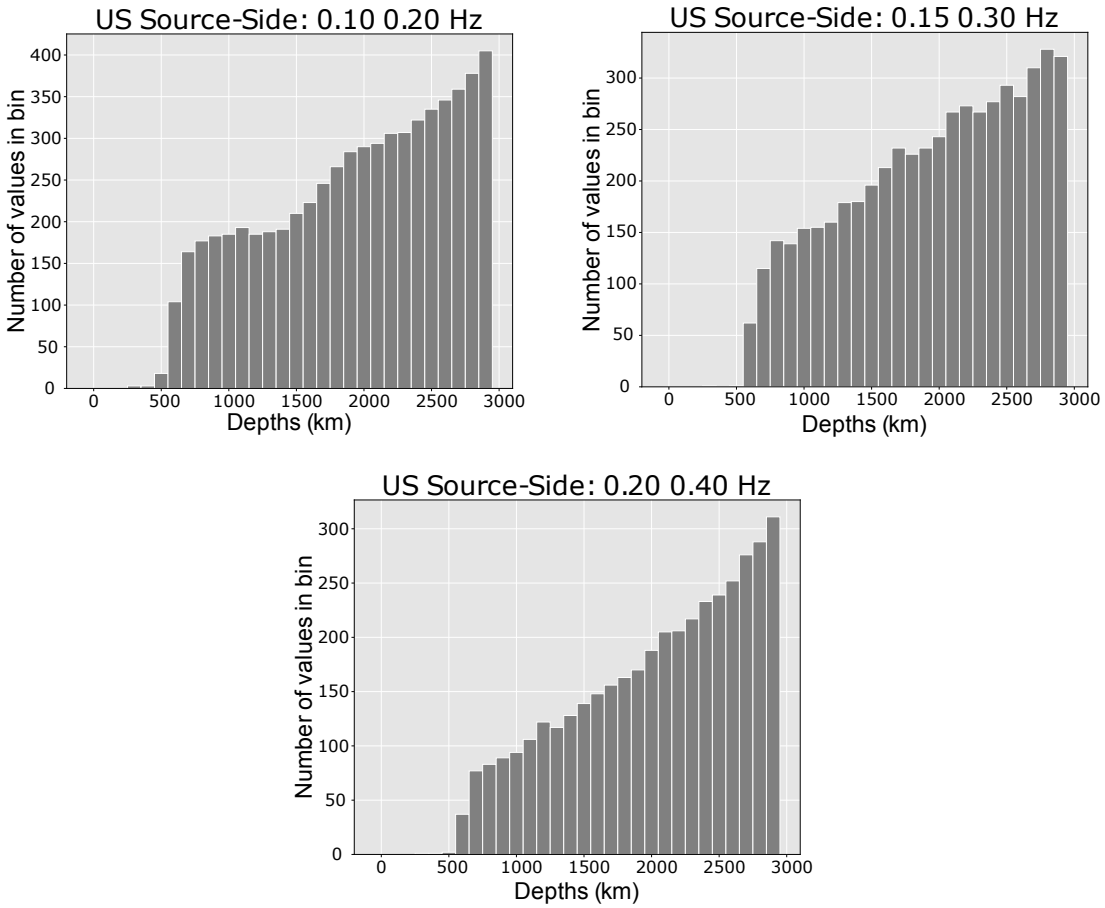

Figure 4.26: Histograms of source-side paths beneath NA in different frequency bands of the number of bins with a low variance between the slowness vector measurement and slowness vector measurements within 200 km of it for data recorded in NA.

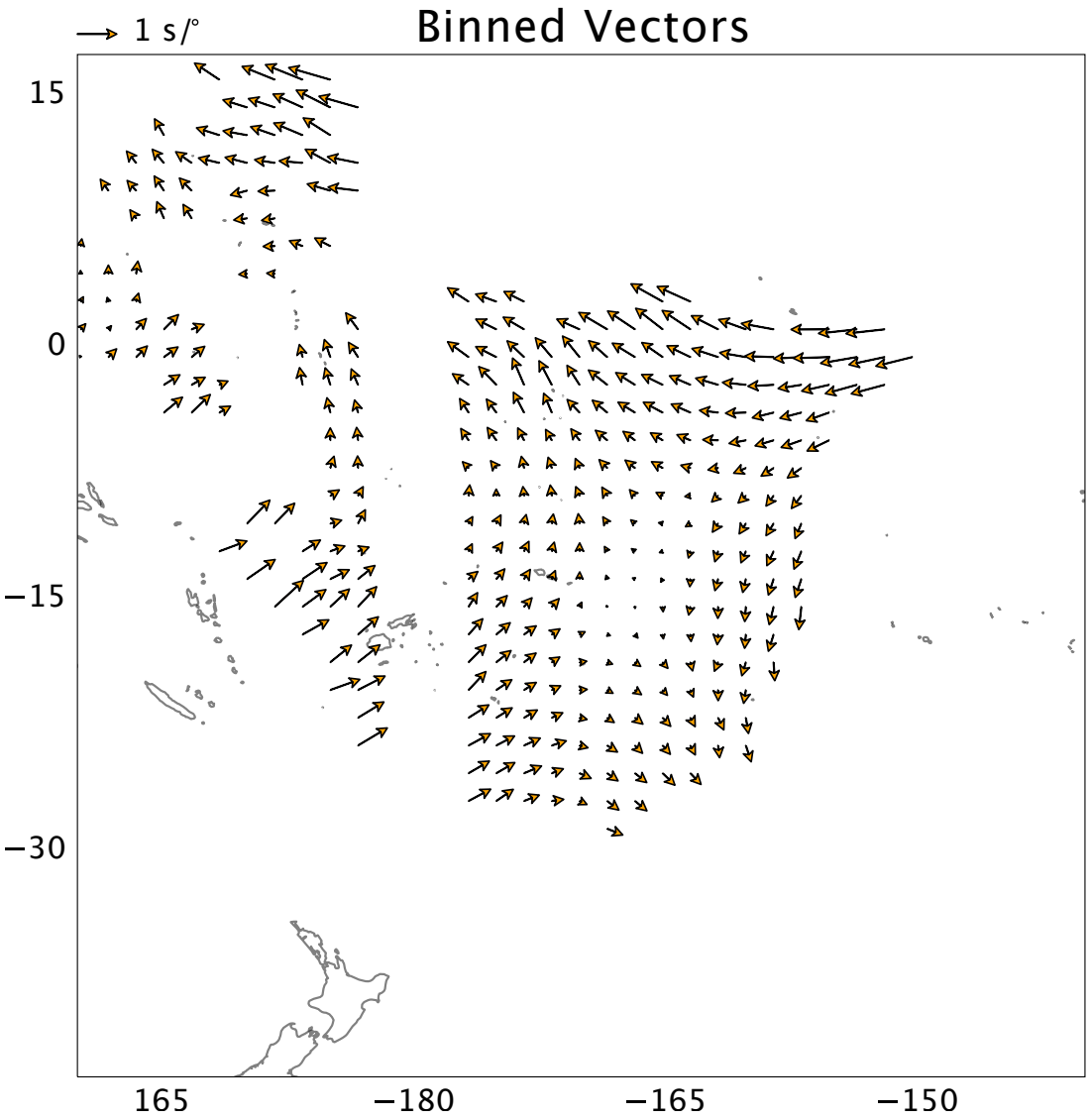

Figure 4.27: Map of slowness vector bins on the source-side beneath the southwest Pacific traveling to stations in North America. The bins use pierce points at 2891 km depth and use data from the 0.10 – 0.20 Hz frequency band.

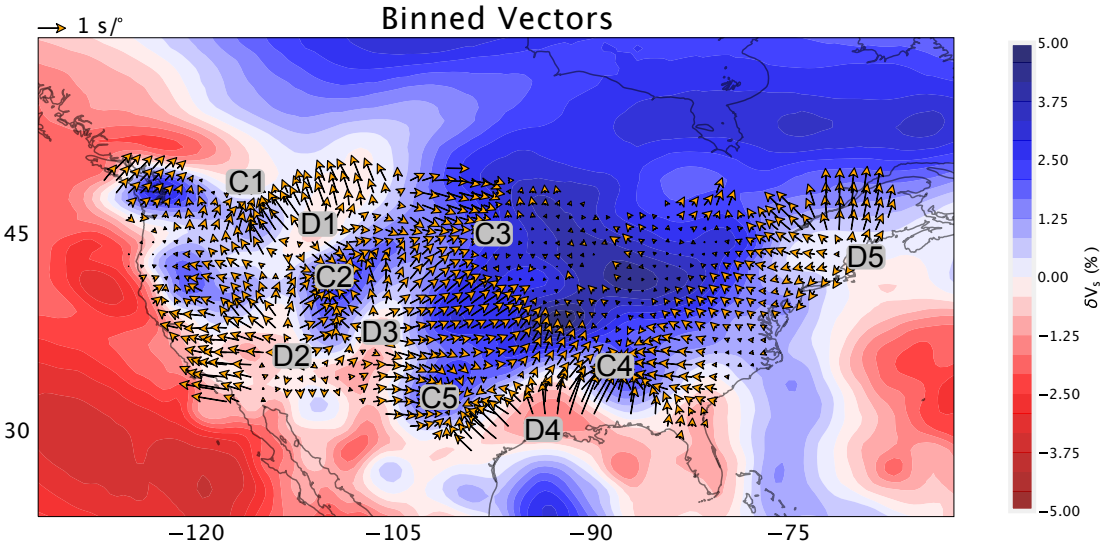

Figure 4.28: Map of slowness vector bins in the 0.10 – 0.20 Hz frequency band using pierce points at 200 km depth beneath the US. The bins have a radius of 200km with a spacing of 100 km. The vectors are plotted on top of the collaborative seismic earth model (Fichtner et al., 2018)

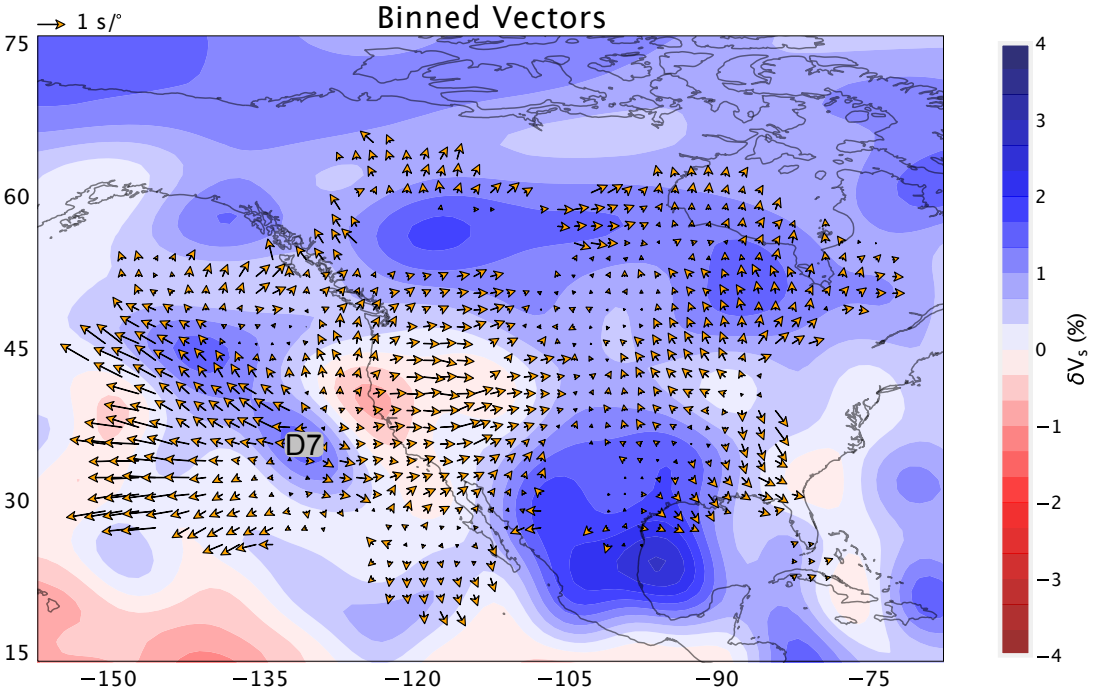

Figure 4.29: Map of slowness vector bins using observations in the the 0.20 – 0.40 frequency band. The bins have a radius of 200km with a spacing of 100 km. The pierce points are at 2891 km depth (CMB) plotted on top of tomography model is S40RTS (Ritsema et al., 2011).

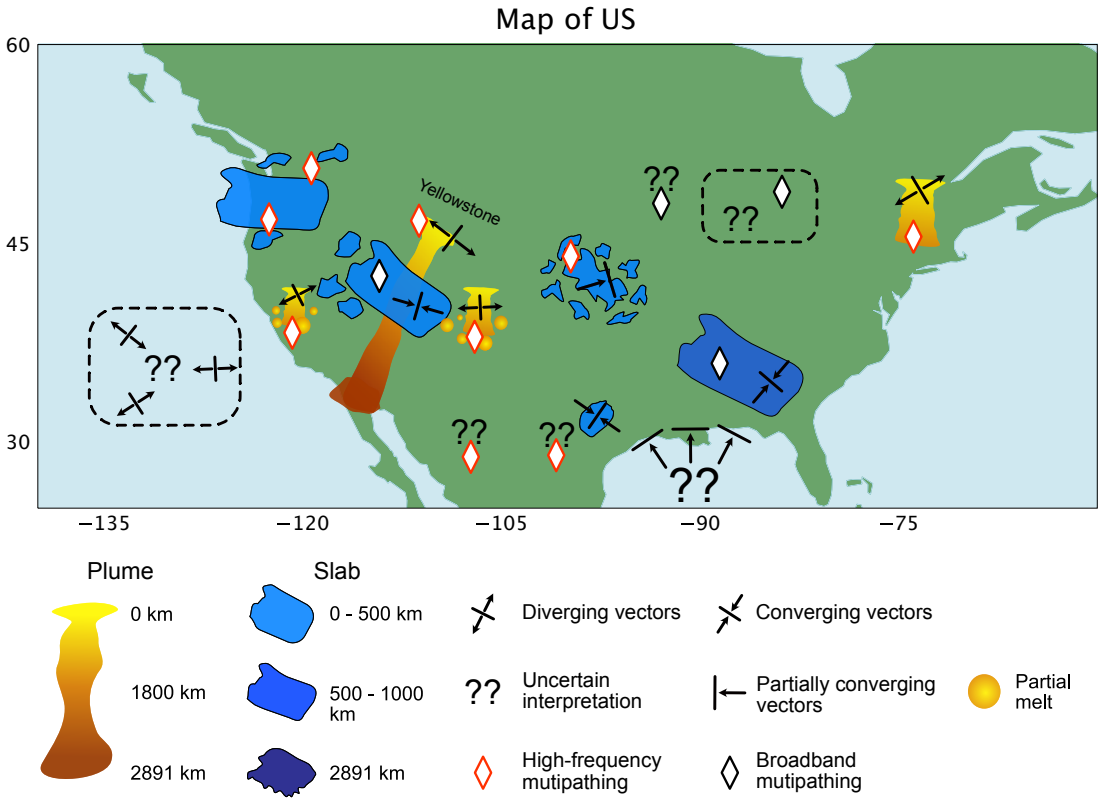

Figure 4.30: Cartoon summarising the interpretations of the spatial distribution of slowness vector deviation observations beneath North America. Note for the Yellowstone plume, we do not advocate for a linear feature from the CMB to the surface but this is to simply show the diverging pattern in the lower mantle may be related to the Yellowstone anomaly.

4.4.4 Future work

The results presented in this study are the beginning of a process to create a global map of multipathing and wavefield perturbation in the mantle which can then show regions where strong lateral velocity gradients exist. Future work building on this study will use other phases such as Sdiff, ScS and S wave arrivals with similar methodology and possibly expand to P, Pdiff and PcP wave arrivals also. Each of the heterogeneities has a unique combination of slowness vector patterns, slowness vector magnitude and whether they cause multipathing. These unique observations show the value of array analysis of waves sampling velocity gradients.

This work motivates future forward modelling studies to investigate the effect of sampling length, velocity gradient strength and velocity perturbation on the detectability of multipathing. This analysis can be expanded to infer what conditions cause multipathing in one or multiple frequency bands. Replicating the slowness vector patterns of the various heterogeneities would be able to constrain the geometry and strength of the velocity gradients as well as possibly the perturbation of the structure. Combining the inferences from modelling efforts investigating multipathing and slowness vector patterns, constraints on the possible depths, velocity gradients, velocity perturbations and morphologies of the heterogeneities observed in this study and future studies can be made. As the slowness vector and multipathing observations are unique for each structure, so to would be the properties recovered by the modelling. These estimates quantifying the perturbation and sharpness of the velocity gradients, and the global coverage of where lateral velocity gradients are, can be used in conjunction with conceptual Earth models to determine their accuracy and for parameterisation of tomographic inversions.

4.4.5 Limitations

This work is partly limited by the decisions made to automate the sub-array creation step and in the cluster analysis parameters used in the method of Ward et al. (2021). When breaking up the distribution of stations into different sub-arrays, the maximum size of the sub-arrays, the minimum number of stations needed for a sub-array and how closely spaced the sub-arrays are will affect the number and distribution of the sub-arrays. The parameters to create the sub-arrays were chosen to have sufficient stations in each sub-array to provide reliable observations while maximising the coverage of the mantle without such heavy sampling that some observations are nearly redundant.

The parameters given to the automated method of Ward et al. (2021) to make the slowness vector measurements and identify multipathing is another limitation. The method uses DBSCAN (Ester et al., 1996) to find clusters based on the density of the points (in this application points are the slowness vector estimates). The user

sets a minimum density for a cluster to exist as a minimum number of points needed within a radius of the point. In the context of identifying seismic arrivals, the lower the minimum density threshold, the more low amplitude arrivals may be recovered, but more noise may be misidentified as arrivals. On the other hand, if the density criterion is set very high, less noise will be identified as an arrival, however, the consequence of this is fewer low amplitude arrivals, such as multipathed arrivals, may be found. Choosing the DBSCAN parameters for the automation task of identifying multipathed arrivals requires a balance between finding as many low amplitude arrivals as possible while minimising the misclassification of noise as arrivals. The parameters used in this study were taken from the tuning in Ward et al. (2021) which performed well in both identifying multiple arrivals and limited the misidentification of noise as an arrival. Unfortunately, some multipathed arrivals will not be identified by the method, but this is a consequence of applying an automated method to a large dataset.

Another limitation is produced by the size of the bins chosen for the variance analysis and plotting. The variance analysis itself removes data from the analysis and is, therefore, a limitation as it removes data that could be interpreted. However, the variance analysis is necessary to remove incoherent measurements and allow the dataset to be interpreted at all. For the variance analysis, the size of the bin should be on the spatial scale expected for coherent slowness vector values to exist. A bin size that is too large may include many slowness vector values and may result in high variance and the removal of those observations. A bin size too small may not include enough slowness vectors to make a measurement as we impose the requirement of at least 10 observations in each bin. For plotting, too large a bin size or spacing would lose spatial resolution of the slowness vector measurements losing the effect of small scale structures on the slowness vector measurement. Like with the variance analysis, if the bin size is too small, then there may be too few measurements to form a bin limiting the spatial coverage of measurements making it difficult to interpret. To choose the bin size for the variance analysis and the plotting, the smallest bin size was chosen which retained enough coverage of measurements to be interpretable while providing as much detail as possible.

A further limitation includes using a constant time window of 20 s before and after the PREM (Dziewonski and Anderson, 1981) predicted arrival time. This value was chosen to avoid contamination by other arrivals, such as SKKS, but may suppress information about multipathed arrivals arriving much later or earlier than the predicted arrival time.

The outputs of the ray-tracing for our forward modelling holds no information about the amplitudes of the arrivals and are limited to travel times. Even if there are arrivals with the slowness vector perturbations arriving at the array, it is unclear if the arrivals will arrive with enough power to be observed. This motivates the need for finite

frequency modelling to compare the modelling results of the ray-tracing and determine if it is valid to use to investigate slowness vector perturbations. For the purpose of the modelling in this study, we assume the arrivals are observable and only want to infer the slowness vector pattern produced by fast and slow mantle heterogeneity.

4.5 Conclusions

Global observations of small-scale scatterers, mantle reflectors and 3-D velocity perturbations have helped to constrain the seismic velocity structure of the mantle and provide multi-scale constraints on seismic Earth models. Of the seismic phenomena analysed on a global scale, information on the lateral velocity gradients of mantle heterogeneity has been missing. Lateral velocity gradients at the boundaries of mantle heterogeneity can provide constraints about the length over which the transition between the ambient mantle and the heterogeneity occurs. Regional-scale studies analysing lateral velocity gradients use the presence of multipathing to locate the gradients and infer their properties. Multipathing results from an interaction between a strong lateral velocity gradient and an incident seismic wave. The wave moves at different speeds depending on whether it is inside the structure or stays in the surrounding mantle. The result of this interaction is two or more waves arriving at the station at different times and, due to diffraction at the boundary, with different slowness vector properties. Analysing multipathing and the slowness vector deviations from diffraction at lateral velocity gradients can provide information about the location and properties of boundary structure of mantle heterogeneity. The method from Ward et al. (2021) can be used to identify one or more arrivals in slowness space automatically and therefore can identify multipathing with slowness vector deviation measurement. This allows for the first multi-regional scale observations of multipathing and slowness vector deviation to be made giving information about strong velocity gradients in the mantle.

In this study, we applied the array method of Ward et al. (2021) to the global SKS dataset of Thorne et al. (2020) to create a dataset of multipathing and slowness vector deviation in multiple frequency bands. We then analyse the dataset spatially using 3-D ray tracing to interpret the observations. Due to the dense station coverage beneath North America and Europe, we focus our analysis there using statistical analysis of the slowness vector measurements to constrain the depths of structures affecting the wavefield. We also analyse the multipathing proportion spatially to infer which structures may have sufficiently sharp velocity gradients to cause observable multipathing and estimate what the upper bound of those length scales may be depending on the frequency band multipathing is observed in.

We find evidence for lowermost mantle roots for the Yellowstone, Italian, Eifel plumes from diverging slowness vector patterns indicative of a slow anomaly. We ob-

serve evidence for a low-velocity anomaly causing multipathing and strong slowness vector deviations (≈1.5 s/°) in northern Europe where some studies have interpreted as the Perm anomaly (Lekic et al., 2012). This region has been observed to have discrepant SKS-SKKS anisotropy (Long and Lynner, 2015) and coherent scattering (Ma and Thomas, 2020). This, with our observations suggesting the structure extends approximately 1000 km above the CMB, leads us to suggest this is a mantle upwelling rooted at the CMB. Our slowness vector and multipathing measurements show evidence for subducted slab material throughout the mantle. What we interpret as the Alpine, Cyprus and Hellenic slabs all show convergent slowness vector patterns and the Hellenic slab possibly shows multipathing but some multipathing may be caused by the Italian plume in the lower mantle. The lowermost mantle beneath Europe shows evidence for a large high-velocity anomaly from a converging slowness vector pattern with relatively little multipathing which we interpret as the Balkan slab.

Beneath the US, we find heterogeneities in the upper mantle may the the cause of the majority of multipathing and slowness vector deviation. We observe several converging slowness vector patterns in the upper mantle beneath the US which we interpret as possible subducted slabs. We find some of these cause multipathing in the central frequency band including in a location where previous studies have suggested a Farallon slab fragment exists (Bunge and Grand, 2000; Forte et al., 2007; Sigloch et al., 2008). Alongside these patterns we observe several smaller scale diverging slowness vector patterns indicative of a slow anomaly which we infer to be evidence for the Yellowstone plume and possibly the Appalachian plume and small scale upwellings beneath the western US. We find a broad spread of high proportion multipathing regions in the highest frequency band in the US upper mantle, which we interpret as smaller scale heterogeneities unresolvable to tomography with a maximum scale for the lateral gradients of 469 km.

This study provides the first steps towards global-scale observations of multipathing, slowness vector deviations and therefore global observations of the properties of the boundaries of mantle heterogeneity. Despite not being a fully global dataset, locations of strong lateral velocity gradients made in this study can be used in comparison with proposed Earth models, geodynamic simulation results and tomographic inversions. The resulting dataset facilitates forward modelling studies to determine what conditions are needed to produce observable multipathing, produce the frequency dependence of multipathing observations and produce similar slowness vector perturbations observed here. These observations begin to provide some constraints of the 'sharp' velocity gradients of structures in the mantle, a property not yet analysed on a global scale and which provides more constraints to the seismic velocity structure of the Earth.

Acknowledgments

JW is supported by the NERC DTP Spheres grant NE/L002574/1, AN was funded by NERC standard grant NE/R001154/1 (REMIS: Reliable Earthquake Magnitudes for Induced Seismicity), SR was supported by NE/R012199/1 and MT was partially supported by NSF grant EAR-1723081. ObspyDMT (Hosseini and Sigloch, 2017) was used to download data. Predictions from 1D velocity models were made using the TauP toolkit (Crotwell et al., 1999). SubMachine (Hosseini et al., 2018) was used to create some of the cross-sections through tomography models.

References

Bell, K., Castorina, F., Lavecchia, G., Rosatelli, G., & Stoppa, F. (2004). Is there a mantle plume below Italy? *Eos, Transactions American Geophysical Union*, *85*(50), 541–547.

Bentham, H. L. M., Rost, S., & Thorne, M. S. (2017). Fine-scale structure of the mid-mantle characterised by global stacks of PP precursors. *Earth and Planetary Science Letters*, *472*, 164–173.

Berk Biryol, C., Beck, S. L., Zandt, G., & Ãzacar, A. A. (2011). Segmented African lithosphere beneath the Anatolian region inferred from teleseismic P-wave tomography. *Geophysical Journal International*, *184*(3), 1037–1057.

Bijwaard, H., & Spakman, W. (2000). Non-linear global P-wave tomography by iterated linearized inversion. *Geophysical Journal International*, *141*(1), 71–82.

Buikin, A., Trieloff, M., Hopp, J., Althaus, T., Korochantseva, E., Schwarz, W. H., & Altherr, R. (2005). Noble gas isotopes suggest deep mantle plume source of late Cenozoic mafic alkaline volcanism in Europe. *Earth and Planetary Science Letters*, *230*(1), 143–162.

Bunge, H.-P., & Grand, S. P. (2000). Mesozoic plate-motion history below the northeast Pacific Ocean from seismic images of the subducted Farallon slab. *Nature*, *405*(6784), 337–340.

Burdick, S., Li, C., Martynov, V., Cox, T., Eakins, J., Mulder, T., Astiz, L., Vernon, F. L., Pavlis, G. L., & van der Hilst, R. D. (2008). Upper Mantle Heterogeneity beneath North America from Travel Time Tomography with Global and US-Array Transportable Array Data. *Seismological Research Letters*, *79*(3), 384–392.

Cadoux, A., Blichert-Toft, J., Pinti, D. L., & AlbarÃšde, F. (2007). A unique lower mantle source for Southern Italy volcanics. *Earth and Planetary Science Letters*, *259*(3), 227–238.

Cao, A., & Levander, A. (2010). High-resolution transition zone structures of the Gorda Slab beneath the western United States: Implication for deep water subduction. *Journal of Geophysical Research: Solid Earth*, *115*(B7).

Chang, S.-J., Ferreira, A. M., Ritsema, J., Heijst, H. J., & Woodhouse, J. H. (2015). Joint inversion for global isotropic and radially anisotropic mantle structure including crustal thickness perturbations. *Journal of Geophysical Research: Solid Earth*, *120*(6), 4278–4300.

Cottaar, S., & Deuss, A. (2016). Large-scale mantle discontinuity topography beneath Europe: Signature of akimotoite in subducting slabs. *Journal of Geophysical Research: Solid Earth*, *121*(1), 279–292.

Crotwell, H. P., Owens, T. J., & Ritsema, J. (1999). The TauP Toolkit: Flexible seismic travel-time and ray-path utilities. *Seismological Research Letters*, *70*(2), 154–160.

Deuss, A. (2009). Global Observations of Mantle Discontinuities Using SS and PP Precursors. *Surveys in Geophysics*, *30*(4-5), 301–326.

Deuss, A., Redfern, S. A. T., Chambers, K., & Woodhouse, J. H. (2006). The Nature of the 660-Kilometer Discontinuity in Earth's Mantle from Global Seismic Observations of PP Precursors. *Science*, *311*(5758), 198–201.

Dziewonski, A. M., & Anderson, D. L. (1981). Preliminary reference Earth model. *Physics of the earth and planetary interiors*, *25*(4), 297–356.

Eagar, K. C., Fouch, M. J., & James, D. E. (2010). Receiver function imaging of upper mantle complexity beneath the Pacific Northwest, United States. *Earth and Planetary Science Letters*, *297*(1), 141–153.

Efron, B. (1992). Bootstrap Methods: Another Look at the Jackknife. In S. Kotz & N. L. Johnson (Eds.), *Breakthroughs in Statistics: Methodology and Distribution* (pp. 569–593). Springer.

Ester, M., Kriegel, H.-P., Sander, J., Xu, X. et al. (1996). A density-based algorithm for discovering clusters in large spatial databases with noise. *Kdd*, *96*, 226–231.

Fichtner, A., vanÂ Herwaarden, D.-P., Afanasiev, M., SimutÄ, S., Krischer, L., Ãubuk-Sabuncu, Y., Taymaz, T., Colli, L., Saygin, E., VillaseÃ±or, A., Trampert, J., Cupillard, P., Bunge, H.-P., & Igel, H. (2018). The Collaborative Seismic Earth Model: Generation 1. *Geophysical Research Letters*, *45*(9), 4007–4016.

Forte, A. M., Mitrovica, J. X., Moucha, R., Simmons, N. A., & Grand, S. P. (2007). Descent of the ancient Farallon slab drives localized mantle flow below the New Madrid seismic zone. *Geophysical Research Letters*, *34*(4).

Forte, A. M., Moucha, R., Simmons, N. A., Grand, S. P., & Mitrovica, J. X. (2010). Deep-mantle contributions to the surface dynamics of the North American continent. *Tectonophysics*, *481*(1), 3–15.

French, S. W., & Romanowicz, B. (2015). Broad plumes rooted at the base of the Earth's mantle beneath major hotspots. *Nature*, *525*(7567), 95–99.

French, S., & Romanowicz, B. (2014). Whole-mantle radially anisotropic shear velocity structure from spectral-element waveform tomography. *Geophysical Journal International*, *199*(3), 1303–1327.

Gao, W., Matzel, E., & Grand, S. P. (2006). Upper mantle seismic structure beneath eastern Mexico determined from P and S waveform inversion and its implications. *Journal of Geophysical Research: Solid Earth*, *111*(B8).

Gilbert, H. J., Sheehan, A. F., Dueker, K. G., & Molnar, P. (2003). Receiver functions in the western United States, with implications for upper mantle structure and dynamics. *Journal of Geophysical Research: Solid Earth*, *108*(B5).

Goes, S., Spakman, W., & Bijwaard, H. (1999). A Lower Mantle Source for Central European Volcanism. *Science*, *286*(5446), 1928–1931.

Grand, S. P. (1994). Mantle shear structure beneath the Americas and surrounding oceans. *Journal of Geophysical Research: Solid Earth*, *99*(B6), 11591–11621.

Grand, S. P., van der Hilst, R. D., & Widiyantoro, S. (1997). High resolution global tomography: A snapshot of convection in the Earth. *Geological Society of America Today*, *7*(4).

Grund, M., & Ritter, J. R. R. (2019). Widespread seismic anisotropy in Earthâs lowermost mantle beneath the Atlantic and Siberia. *Geology*, *47*(2), 123–126.

Hansen, S. E., Evangelidis, C. P., & Papadopoulos, G. A. (2019). Imaging Slab Detachment Within the Western Hellenic Subduction Zone. *Geochemistry, Geophysics, Geosystems*, *20*(2), 895–912.

He, Y., Wen, L., & Capdeville, Y. (2021). Morphology and possible origins of the Perm anomaly in the lowermost mantle of Earth. *Earth and Planetary Physics*, *5*, 1–12.

Hedlin, M. A. H., & Shearer, P. M. (2000). An analysis of large-scale variations in small-scale mantle heterogeneity using Global Seismographic Network recordings of precursors to PKP. *Journal of Geophysical Research: Solid Earth*, *105*(B6), 13655–13673.

Hosseini, K., Matthews, K. J., Sigloch, K., Shephard, G. E., Domeier, M., & Tsekhmistrenko, M. (2018). SubMachine: Web-based tools for exploring seismic tomography and other models of Earth's deep interior. *Geochemistry, Geophysics, Geosystems*, *19*(5), 1464–1483.

Hosseini, K., & Sigloch, K. (2017). ObspyDMT: A Python toolbox for retrieving and processing large seismological data sets. *Solid Earth*, (5), 1047–1070.

Koelemeijer, P., Ritsema, J., Deuss, A., & Van Heijst, H.-J. (2015). SP12RTS: A degree-12 model of shear-and compressional-wave velocity for Earth's mantle. *Geophysical Journal International*, *204*(2), 1024–1039.

Kreemer, C., Blewitt, G., & Davis, P. M. (2020). Geodetic evidence for a buoyant mantle plume beneath the Eifel volcanic area, NW Europe. *Geophysical Journal International*, *222*(2), 1316–1332.

Lekic, V., Cottaar, S., Dziewonski, A., & Romanowicz, B. (2012). Cluster analysis of global lower mantle tomography: A new class of structure and implications for chemical heterogeneity. *Earth and Planetary Science Letters*, *357*, 68–77.

Leonard, T., & Liu, L. (2016). The role of a mantle plume in the formation of Yellowstone volcanism. *Geophysical Research Letters*, *43*(3), 1132–1139.

Li, C., Hilst, R. D. v. d., Engdahl, E. R., & Burdick, S. (2008). A new global model for P wave speed variations in Earth's mantle. *Geochemistry, Geophysics, Geosystems*, *9*(5).

Long, M. D., & Lynner, C. (2015). Seismic anisotropy in the lowermost mantle near the Perm Anomaly. *Geophysical Research Letters*, *42*(17), 7073–7080.

Lu, C., Grand, S. P., Lai, H., & Garnero, E. J. (2019). TX2019slab: A New P and S Tomography Model Incorporating Subducting Slabs. *Journal of Geophysical Research: Solid Earth*, *124*(11), 11549–11567.

Ma, X., & Thomas, C. (2020). Small-Scale Scattering Heterogeneities in the Lowermost Mantle From a Global Analysis of PKP Precursors. *Journal of Geophysical Research: Solid Earth*, *125*(3), e2019JB018736
e2019JB018736 2019JB018736.

Mathar, J. P., Ritter, J. R., & Friederich, W. (2006). Surface waves image the top of the Eifel plume. *Geophysical Journal International*, *164*(2), 377–382.

Menke, W., Skryzalin, P., Levin, V., Harper, T., Darbyshire, F., & Dong, T. (2016). The Northern Appalachian Anomaly: A modern asthenospheric upwelling. *Geophysical Research Letters*, *43*(19), 10, 173–10, 179.

Nelson, P. L., & Grand, S. P. (2018). Lower-mantle plume beneath the Yellowstone hotspot revealed by core waves. *Nature Geoscience*, *11*(4), 280–284.

Ni, S., Tan, E., Gurnis, M., & Helmberger, D. (2002). Sharp sides to the African superplume. *Science*, *296*(5574), 1850–1852.

Obrebski, M., Allen, R. M., Xue, M., & Hung, S.-H. (2010). Slab-plume interaction beneath the Pacific Northwest. *Geophysical Research Letters*, *37*(14).

Pierce, K. L., & Morgan, L. A. (2009). Is the track of the Yellowstone hotspot driven by a deep mantle plume? â Review of volcanism, faulting, and uplift in light of new data. *Journal of Volcanology and Geothermal Research*, *188*(1), 1–25.

Porritt, R. W., Allen, R. M., & Pollitz, F. F. (2014). Seismic imaging east of the Rocky Mountains with USArray. *Earth and Planetary Science Letters*, *402*, 16–25.

Ricker, N. (1943). Further developments in the wavelet theory of seismogram structure. *Bulletin of the Seismological Society of America*, *33*(3), 197–228.

Ricker, N. (1944). Wavelet functions and their polynomials. *Geophysics*, *9*(3), 314–323.

Rickers, F., Fichtner, A., & Trampert, J. (2013). The IcelandâJan Mayen plume system and its impact on mantle dynamics in the North Atlantic region: Evidence from full-waveform inversion. *Earth and Planetary Science Letters*, *367*, 39–51.

Ritsema, J., Deuss, a. A., Van Heijst, H., & Woodhouse, J. (2011). S40RTS: A degree-40 shear-velocity model for the mantle from new Rayleigh wave dispersion, teleseismic traveltime and normal-mode splitting function measurements. *Geophysical Journal International*, *184*(3), 1223–1236.

Ritter, J. R. R., Jordan, M., Christensen, U. R., & Achauer, U. (2001). A mantle plume below the Eifel volcanic fields, Germany. *Earth and Planetary Science Letters*, *186*(1), 7–14.

Rost, S., & Thomas, C. (2002). Array seismology: Methods and applications. *Reviews of geophysics*, *40*(3).

Schmandt, B., Dueker, K. G., Hansen, S. M., Jasbinsek, J. J., & Zhang, Z. (2011). A sporadic low-velocity layer atop the western U.S. mantle transition zone and short-wavelength variations in transition zone discontinuities. *Geochemistry, Geophysics, Geosystems*, *12*(8).

Schmandt, B., Dueker, K., Humphreys, E., & Hansen, S. (2012). Hot mantle upwelling across the 660 beneath Yellowstone. *Earth and Planetary Science Letters*, *331-332*, 224–236.

Schmandt, B., & Humphreys, E. (2010). Complex subduction and small-scale convection revealed by body-wave tomography of the western United States upper mantle. *Earth and Planetary Science Letters*, *297*(3), 435–445.

Schmandt, B., & Lin, F.-C. (2014). P and S wave tomography of the mantle beneath the United States. *Geophysical Research Letters*, *41*(18), 6342–6349.

Sigloch, K., McQuarrie, N., & Nolet, G. (2008). Two-stage subduction history under North America inferred from multiple-frequency tomography. *Nature Geoscience*, *1*(7), 458–462.

Silver, P. G., & Chan, W. W. (1986). Observations of body wave multipathing from broadband seismograms: Evidence for lower mantle slab penetration beneath the Sea of Okhotsk. *Journal of Geophysical Research: Solid Earth*, *91*(B14), 13787–13802.

Simmons, N., Myers, S., & Johannesson, G. (2011). Global-scale P wave tomography optimized for prediction of teleseismic and regional travel times for Middle East events: 2. Tomographic inversion. *Journal of Geophysical Research: Solid Earth*, *116*(B4).

Simmons, N. A., Forte, A. M., Boschi, L., & Grand, S. P. (2010). GyPSuM: A joint tomographic model of mantle density and seismic wave speeds. *Journal of Geophysical Research: Solid Earth*, *115*(B12).

Simmons, N. A., Myers, S. C., Johannesson, G., & Matzel, E. (2012). LLNL-G3Dv3: Global P wave tomography model for improved regional and teleseismic travel time prediction. *Journal of Geophysical Research: Solid Earth*, *117*(B10).

Smith, R. B., Jordan, M., Steinberger, B., Puskas, C. M., Farrell, J., Waite, G. P., Husen, S., Chang, W.-L., & O'Connell, R. (2009). Geodynamics of the Yellow-

stone hotspot and mantle plume: Seismic and GPS imaging, kinematics, and mantle flow. *Journal of Volcanology and Geothermal Research*, *188*(1), 26–56.

Song, A. T.-R., Helmberger, D. V., & Grand, S. P. (2004). Low-velocity zone atop the 410-km seismic discontinuity in the northwestern United States. *Nature*, *427*(6974), 530–533.

Spakman, W., Wortel, M. J. R., & Vlaar, N. J. (1988). The Hellenic Subduction Zone: A tomographic image and its geodynamic implications. *Geophysical Research Letters*, *15*(1), 60–63.

Sun, D., Helmberger, D., Lai, V. H., Gurnis, M., Jackson, J. M., & Yang, H.-Y. (2019). Slab Control on the Northeastern Edge of the Mid-Pacific LLSVP Near Hawaii. *Geophysical Research Letters*, *46*(6), 3142–3152.

Sun, D., Gurnis, M., Saleeby, J., & Helmberger, D. (2017). A dipping, thick segment of the Farallon Slab beneath central U.S. *Journal of Geophysical Research: Solid Earth*, *122*(4), 2911–2928.

Sun, D., Helmberger, D., & Gurnis, M. (2010). A narrow, mid-mantle plume below southern Africa. *Geophysical Research Letters*, *37*(9).

Sun, D., & Miller, M. S. (2013). Study of the western edge of the African Large Low Shear Velocity Province. *Geochemistry, Geophysics, Geosystems*, *14*(8), 3109–3125.

Tao, Z., Li, A., & Fischer, K. M. (2020). Hotspot signatures at the North American passive margin. *Geology*, *49*(5), 525–530.

Taylor, G., Thompson, D. A., Cornwell, D., & Rost, S. (2019). Interaction of the Cyprus/Tethys slab with the mantle transition zone beneath Anatolia. *Geophysical Journal International*, *216*(3), 1665–1674.

Thorne, M. S., Leng, K., Pachhai, S., Rost, S., Wicks, J., & Nissen-Meyer, T. (2021). The Most Parsimonious Ultralow-Velocity Zone Distribution From Highly Anomalous SPdKS Waveforms. *Geochemistry, Geophysics, Geosystems*, *22*(1), e2020GC009467 e2020GC009467 2020GC009467.

Thorne, M. S., Pachhai, S., Leng, K., Wicks, J. K., & Nissen-Meyer, T. (2020). New Candidate Ultralow-Velocity Zone Locations from Highly Anomalous SPdKS Waveforms. *Minerals*, *10*(3), 211.

Tian, Y., Sigloch, K., & Nolet, G. (2009). Multiple-frequency SH-wave tomography of the western US upper mantle. *Geophysical Journal International*, *178*(3), 1384–1402.

Tian, Y., Zhou, Y., Sigloch, K., Nolet, G., & Laske, G. (2011). Structure of North American mantle constrained by simultaneous inversion of multiple-frequency SH, SS, and Love waves. *Journal of Geophysical Research: Solid Earth*, *116*(B2).

Valentine, A. P., & Woodhouse, J. H. (2010). Approaches to automated data selection for global seismic tomography. *Geophysical Journal International*, *182*(2), 1001–1012.

van der Lee, S., & Nolet, G. (1997). Seismic image of the subducted trailing fragments of the Farallon plate. *Nature*, *386*(6622), 266–269.

Vinnik, L. P., Oreshin, S. I., Speziale, S., & Weber, M. (2010). Mid-mantle layering from SKS receiver functions. *Geophysical Research Letters*, *37*(24).

Ward, J., Thorne, M., Nowacki, A., & Rost, S. (2021). Automatic slowness vector measurements of seismic arrivals with uncertainty estimates using bootstrap sampling, array methods and unsupervised learning. *Geophysical Journal International*, *226*(3), 1847–1857.

Ward, J., Nowacki, A., & Rost, S. (2020). Lateral Velocity Gradients in the African Lower Mantle Inferred From Slowness Space Observations of Multipathing. *Geochemistry, Geophysics, Geosystems*, *21*(8), e2020GC009025 e2020GC009025 10.1029/2020GC009025.

Waszek, L., Schmerr, N. C., & Ballmer, M. D. (2018). Global observations of reflectors in the mid-mantle with implications for mantle structure and dynamics. *Nature Communications*, *9*(1), 385.

Waszek, L., Thomas, C., & Deuss, A. (2015). PKP precursors: Implications for global scatterers. *Geophysical Research Letters*, *42*(10), 3829–3838.

Wedepohl, K. H., & Baumann, A. (1999). Central European Cenozoic plume volcanism with OIB characteristics and indications of a lower mantle source. *Contributions to Mineralogy and Petrology*, *136*(3), 225–239.

Wei, W., Zhao, D., Wei, F., Bai, X., & Xu, J. (2019). Mantle Dynamics of the Eastern Mediterranean and Middle East: Constraints From P-Wave Anisotropic Tomography. *Geochemistry, Geophysics, Geosystems*, *20*(10), 4505–4530.

Wortel, M. J. R., & Spakman, W. (2000). Subduction and Slab Detachment in the Mediterranean-Carpathian Region. *Science*, *290*(5498), 1910–1917.

Xue, M., & Allen, R. M. (2007). The fate of the Juan de Fuca plate: Implications for a Yellowstone plume head. *Earth and Planetary Science Letters*, *264*(1), 266–276.

Zhao, D., Hasegawa, A., & Horiuchi, S. (1992). Tomographic imaging of P and S wave velocity structure beneath northeastern Japan. *Journal of Geophysical Research: Solid Earth*, *97*(B13), 19909–19928.

Zhu, H., BozdaÄ, E., Peter, D., & Tromp, J. (2012). Structure of the European upper mantle revealed by adjoint tomography. *Nature Geoscience*, *5*(7), 493–498.

Chapter 5

Discussion and Conclusions

The aim of my thesis is to analyse lateral velocity gradients in the Earth's mantle by observing and quantifying their effect on the seismic wavefield. I quantify this effect by measuring the slowness vector properties of multipathing and diffraction of waves caused by lateral velocity gradients at the boundaries of mantle heterogeneity with array seismology methods. Then, I work to expand the analysis to a global scale. The global observations can then be used to differentiate the unique properties of lateral velocity gradients at the boundaries of heterogeneity which give information about the differing thermal or chemical anomalies. The maps of lateral velocity gradient properties can be used in comparison to hypothetical Earth models and further our understanding of whole Earth dynamics. In this section, I give a brief overview of the chapters (Section 5.1), discuss the key findings of my work (Section 5.2), indicate directions for future work in Section 5.3, discuss the wider impact and contribution of this work (Section 1.3.3), and conclude in Section 5.4.

5.1 Overview of research

5.1.1 Chapter 2

In Chapter 2, I analyse SKS and SKKS multipathing and diffraction from the African LLVP using a beamforming grid search approach to recover the full slowness vectors of the teleseismic wavefield. This allowed areas where multipathing and slowness vector perturbation produced by the interaction of the wave and strong lateral velocity gradients to be identified. I found the first evidence for multipathing being dependent on the frequency which suggests there is a relationship between the velocity gradient length scale and Fresnel zone size to observe multipathing. The frequency multipathing is observed in may be used to constrain the properties of the lateral velocity gradients.

The relative slowness vector properties of the multipathed arrivals may give some

indication of the orientation of the velocity gradient causing them. When plotting the locus separating the multipathed arrivals in slowness space onto a map in comparison to contours from seismic tomography, I find they correlate well (see Section 2.3.2 and Figure 2.8). This shows seismic tomography, while limited in resolution, does constrain the morphology of the African LLVP well in some instances. Through finite frequency forward modelling, the strength of the lateral velocity gradients needed to produce multipathing similar to my observations were estimated. Observations of multipathing from the boundaries of the African LLVPs are extensive (e.g. Ni and Helmberger, 2003a; Ni et al., 2002; Sun and Miller, 2013) which estimate the boundaries have a velocity gradient of -3% δV_S per 50 km or similar which some use as evidence to argue for chemical heterogeneity of the LLVPs. Using finite frequency modelling, we suggest the velocity gradients of the African LLVP may be an order of magnitude lower than previous estimates and is possible from purely thermal or thermochemical structures. Therefore, observation of multipathing is not necessarily evidence for chemical heterogeneity. The main takeaways from this work are multipathing can be observed using array processing and may be able to constrain the spatial properties of the velocity gradient causing the multipathing.

5.1.2 Chapter 3

Chapter 3 outlined the method to automatically identify seismic arrivals in slowness space and measure their slowness vector properties with uncertainty bounds. To my knowledge, there is no other method to identify multiple arrivals automatically and measure slowness vector properties with uncertainties. The method bootstrap samples (Efron, 1992) the seismograms of the array in question. This bootstrap sampling means the stations in the array are also bootstrapped and allows for uncertainties from unaccounted effects of local geology and waveform deformation to be accounted for. For each bootstrap sample, the beamforming is conducted creating a power distribution in slowness space. From the power distributions, the top N peaks are recovered which are the estimated slowness vector measurements of the arrivals in that bootstrap sample. Peaks from all bootstrap samples are collected and clustering algorithm DBSCAN (Ester et al., 1996b) to identify clusters of similar slowness vector properties as arrivals. The location of the cluster gives the slowness vector measurement of the arrival and the scatter of the slowness vectors in the cluster gives uncertainty estimates. This method makes global-scale observations of phenomena identifiable by their slowness vector properties more feasible and uncertainty bounds on slowness vector measurements can now be quantified. The uncertainties quantify the effect of local geology causing waveform complexity, scatter in the arrival time of the wave and the effect of heterogeneous station spacing on the slowness vector measurement. The uncertainties can be translated into uncertainties of the locations of scatterers, reflectors or other structures which cause slowness vector deviation.

5.1.3 Chapter 4

Work presented in Chapter 4 applied the automated technique outlined in Chapter 3 to a global SKS dataset from Thorne et al. (2020) to make slowness vector measurements of multipathed and non-multipathed arrivals. Then, using statistical analysis of variance of slowness vector measurements spatially, I interpret the observations and identify many structures from lower mantle plumes to upper mantle subducted slabs to what may be the Perm anomaly (Lekic et al., 2012). The outcome of this chapter is a multi-regional scale set of observations of multipathing locations and slowness vector perturbations of SKS arrivals in multiple frequency bands. As in Chapter 2 I observe clear frequency dependence of multipathing with low frequencies observing very little and higher frequencies observing much more. Analysing this frequency dependence of multipathing and replicating it with forward modelling studies may allow for general observations of lateral velocity gradients of mantle heterogeneity in the Earth to be made for the first time.

Each of the heterogeneities we interpret to be causing the observations has its own unique slowness vector pattern, whether multipathing is observed and which frequency band multipathing is observable in. The value of analysing the slowness vector properties of waves interacting with mantle heterogeneity is shown here as the differing properties, such as geometry and sharpness of velocity gradients can be constrained. These can then be used to determine the relative difference between the heterogeneities in terms of thermal and chemical characteristics or origins.

This chapter begins the process towards a global map of multipathing and slowness vector deviation which then translate to a map of where strong velocity gradients exist. This map can be used to determine which conceptual Earth models are compatible with the seismic observations.

5.2 Discussion of key findings and outcomes

This section discusses the different key outcomes of the work presented earlier in this thesis. Many of these have been observed over more than one chapter or were not fully discussed in the chapters themselves.

5.2.1 Frequency dependence of multipathing

In Chapters 2 and 4, I conduct the array analysis in multiple frequency bands to vary the length scale the method is sensitive to. In doing so, the possible length scales of the velocity gradients can be constrained and I can investigate a potential relationship between the Fresnel zone size and velocity gradient length scale.

I observe clear frequency dependence of observable multipathing in slowness space.

In some cases, multipathing is observed in a specific frequency band (such as in Figure 2.6 in Chapter 2) and in other cases, multipathing may be observed in several frequency bands. The frequency dependence of multipathing suggests the multipathing is only possible when there is a sufficient proportion of the Fresnel zone perturbed so that multiple regions are moving with different slowness vector properties. By replicating the frequency dependence, one can constrain the spatial scale of the velocity gradient. When analysing the waveforms individually, there appears to be a discrepancy in the amplitude spectra between those which show clear multipathing and those which do not (see Appendix Section A.6). The different amplitude spectra may represent the differing effect the velocity gradient has on the different frequencies where some frequencies may be focused and others defocused depending on the spatial scale of the velocity gradient. Analysing the amplitude spectra could be used to identify multipathing or constrain the spatial properties of the velocity gradients.

A limitation of identifying the frequency dependence of multipathing in slowness space, as done in Chapters 2 and 4, is that for higher frequency bands (>0.15–0.60 Hz and 0.20 – 0.80 Hz in Chapter 2) observations could not be made as a result of the noise conditions. Therefore, for some observations, I could not determine whether multipathing is present or not. This is not the case in all instances, but it is important when interpreting the frequency dependence of multipathing and comparing that to forward modelling efforts.

To my knowledge, the frequency dependence of detectable multipathing has not been observed before, and further study of the frequency dependence of multipathing could constrain the velocity gradient sharpness, velocity perturbations and depths of mantle heterogeneity boundary structure. Investigation of the frequency dependence of multipathing and what conditions are needed to observe it at all is an essential next step in investigating lateral velocity gradients in the mantle. I discuss this further in Section 5.3.1.

5.2.2 Constraining lateral velocity gradient properties

Once the observations in Chapter 2 were made, I used the finite frequency modelling code SPECFEM3D_Globe (Komatitsch and Tromp, 2002a; Komatitsch and Tromp, 2002b) to model the full wavefield propagating through a seismic Earth model (for details, see Section 2.5 in Chapter 2). I found observable multipathing is possible when the wave samples structures with velocity gradients of up to -0.7% per 100 km which is about an order of magnitude lower than the previously reported velocity gradients of -3% per 50 km (Ni et al., 2002). I suggest the reason for the difference in velocity gradient estimates between the work in Chapter 2 and those from studies such as Ni et al. (2002) is the velocity gradient of the boundary is sampled for much longer when finite frequency effects have been accounted for. When the boundary is sampled over a

longer path, the effect of the velocity gradient can be accumulated as the wave travels along the boundary. Therefore, a weaker gradient is sufficient to produce the same result as a stronger gradient that is sampled over a shorter length. Questions remain on the relationship between length sampled and gradient strength are needed to observe multipathing and how this may vary with the depth of the gradient also. I discuss future studies to investigate what conditions are needed to observe multipathing in Section 5.3.1. Despite this trade-off, the finite frequency modelling conducted in Chapter 2 shows the sharpness of the lateral velocity gradients can be estimated by using the slowness space observations of multipathing. This analysis can go further than just the magnitude of the velocity gradient. By trying to replicate the slowness vector properties of the multipathed arrivals, one can recover information about the geometry of the lateral velocity gradient. A limitation of using finite frequency modelling is the computational expense. Ray tracing is much cheaper computationally and may be able to give some information about the velocity gradient causing the slowness vector deviation.

Modelling conducted in Chapter 4 takes a different approach to investigate the properties of velocity gradients observed. There, I used 3-D ray tracing (Simmons et al., 2011; Simmons et al., 2012; Zhao et al., 1992) to infer the qualitative pattern of slowness vector measurements from a wave that has sampled a fast or slow mantle heterogeneity. This modelling allowed the observations made using the method in Chapter 3 to be interpreted. From the 3-D ray tracing, I found slow anomalies produced a diverging slowness vector pattern while fast anomalies produced a converging pattern (see Figure 4.5 in Chapter 4). In both instances, the large magnitude vectors were observed near the boundaries of the structure while negligible magnitude vectors are observed in the centre suggesting refraction plays a small role in slowness vector deviation. This is in line with the interpretation of a slow cylindrical structure causing the radially diverging slowness vector pattern observed in Chapter 2. This shows how non-finite frequency modelling can be useful for determining other properties of velocity gradients in conjunction with slowness vector measurements. However, a comparison with finite frequency modelling is needed to determine whether the assumptions made by ray-tracing modelling affects the slowness vector observation. I discuss a future study using ray tracing and slowness vector measurements to recover information about the slowness vector gradient in Section 5.3.2.

5.2.3 Quantifying the uncertainty of slowness vector measurements

When bootstrapping the waveforms in the method presented in Chapter 3, random sub-arrays are also created in each bootstrap sample. By creating many random sub-arrays, the effect of local geology causing scatter in the travel times, waveform complexity and the effect of heterogeneous station distribution can be estimated. These uncertainty

estimates can be used to determine which observations should be included for interpretation and give uncertainties on properties such as the depths of reflectors. While this is valuable information about the measurement and could be used to provide uncertainty limits on the location of mantle heterogeneity, the uncertainty estimate of the slowness vector properties is affected by the ϵ parameter used to find the clusters in the method.

The method uses DBSCAN, a density-based clustering algorithm, to find dense clusters of slowness vector properties, which are labelled as arrivals. From the cluster's location in slowness space, the slowness vector properties are measured and the scatter of the slowness vector points give the uncertainty estimates. DBSCAN identifies the points which meet the density criterion of having at least $MinPts$ points within a distance ϵ and labels them as core points. Points within ϵ of a core point, but not meeting this density criterion themselves, are classified as a boundary point and added to the cluster. Therefore, having a large ϵ value can bring in more points around the core points of the cluster and may lead to larger uncertainty estimates. Because of this, I describe the uncertainties as estimates because they may change with different DBSCAN parameters. In theory, this may be an issue for the uncertainty estimates, in practice, I have found the points for the arrivals are extremely densely packed around the mean of the cluster with a steep drop off, therefore the uncertainty estimate is not greatly affected by a few more boundary points being added to the edges of the cluster.

5.2.4 Structures at all depths can cause multipathing or slowness vector deviations

In this thesis, I have analysed three different regions in Chapters 2 and 4 with very different mantle structures. The southern African mantle analysed in Chapter 2 is characterised by the LLVP spanning 1000s of kilometres laterally and being over 1000 km high (French and Romanowicz, 2014; Koelemeijer et al., 2015; Ritsema et al., 2011; Simmons et al., 2010) in the lower mantle with known sharp velocity gradients (e.g. Ni and Helmberger, 2003b; Ni et al., 2002; Sun et al., 2010a) and a fast cratonic structure beneath the array. The analysis in Chapter 4 focuses on the European mantle characterised by relatively smaller scale structures such as slabs, plumes and the enigmatic Perm anomaly (Lekic et al., 2012) and also the North American mantle which is dominated by a complex upper mantle with small scale fast and slow anomalies and a large cratonic structure in the east (Sigloch et al., 2008; van der Lee and Nolet, 1997). With three large regional datasets of very different mantle structure, a broad discussion on what structures are resolvable with this technique can be made.

In all three regions, I observe clear radially diverging patterns at a variety of depths indicative of slow anomalies after interpretation of ray tracing modelling in Chapter 4. These anomalies appear to exist in the lowermost mantle beneath Europe in the region of the potential Italian plume and Perm anomaly (Figure 4.16), to a mid mantle cylinder

beneath Africa (Figure 2.9 and upper mantle anomalies beneath the US (Figure 4.28). These also show different depth extents with possible whole mantle anomalies beneath Europe, those confined to the upper mantle beneath the US and those restricted to the lower mantle beneath Africa. These observations show this method is capable of identifying these slow anomalies on a scale of 100s of kilometres and can inform about dynamics such as the potential small scale upper mantle convection in the US or the possible whole mantle upwelling of the Eifel plume (Chapter 4). Some of these structures have been observed in areas where I observe multipathing such as the base of the Italian plume, the possible Perm anomaly, Yellowstone anomaly and the cylindrical structure beneath Africa. On the other hand, some upper mantle slow anomalies such as the upper mantle area of the Eifel plume and the potential Appalachian anomaly have not been observed to cause multipathing. The differential multipathing observations could be indicative of thermal gradients of the plumes, possibly their age and potentially their thermal anomalies. Quantifying these different properties between the structures may lead to an understanding of their relative impact on the dynamics on a regional or global scale.

Two cratonic structures are sampled in this thesis, one beneath Africa (Chapter 2) and one sampling the eastern US (Chapter 4). The US craton is well sampled by the data in Chapter 4 and appears to have very little effect on the slowness vector deviations in the centre of the craton and only cause some (0.5 s/°) slowness vector deviation at the boundaries (Figure 4.28). The craton beneath southern Africa is less well sampled and I suggest the boundaries are not sampled at all by the ray paths to the Kaapvaal array. The relatively negligible effect of the craton body on the slowness vectors observed in Chapter 4 suggests that the effect of refraction through seismic anomalies is very small, supported by results of the ray tracing (Section 4.3). This supports our interpretation that a mainly lower mantle signal is responsible for our observations in Chapter 2. The minimal effect of refraction on the slowness vector measurements suggests that, if very small slowness vector deviations are observed, it does not necessarily mean there is no seismic anomaly, but there are no strong velocity gradients to diffract the wavefield.

Several converging slowness vector patterns are observed in Chapter 4 beneath Europe and the US mainly in the upper mantle but also at the CMB. I interpret these, after the forward modelling in Chapter 4, to be fast anomalies in the mantle and potential cold slab structure. Similar to the slow anomalies described earlier, each heterogeneity causing the converging pattern has unique characteristics. Some fast anomalies cause observable multipathing such as the possible Farallon and Kula slab remnants in the eastern US (see Section 4.4.3.2). While other fast anomalies appear in regions where no multipathing is observed such as the potential Balkan slab in the European lowermost mantle (see Section 4.4.2.3). The slowness vector patterns

themselves are unique like those for the possible alpine anomaly and those from the Hellenic slab region (Figure 4.17) which indicate the geometries of the boundaries of the structures differ. Replicating the anomalies observed for the converging slowness vector patterns and the multipathing observations again can give inferences on the geometry of the structures, their thermal or chemical properties or their ages. These properties can then be used to infer the possible effect they have on the surrounding mantle in the present day and over the history of the mantle.

The African LLVP is unique in the size of mantle heterogeneity I have analysed. It has been shown to cause multipathing from previous studies (e.g. Ni and Helmberger, 2003a; Ni et al., 2002; Sun and Miller, 2013). It offers a different scale of structure to analyse as it spans 1000s of km laterally and 1000 km high (French and Romanowicz, 2014; Koelemeijer et al., 2015; Ritsema et al., 2011; Simmons et al., 2010), therefore I do not expect to have two boundaries of the same structure to be spatially close to each other like for mantle plumes or slabs observed in Chapter 4. This structure then acted as a good test of locating a velocity gradient transitioning from the ambient mantle to the heterogeneity and a velocity gradient that extends for hundreds to thousands of kilometres laterally. My observations of multipathing and the locus of the multipathed arrivals are consistent with each other with a strike of approximately 340° and align well with the velocity contours of tomography model S40RTS (Figure 2.8) for the western boundary striking northwest-southeast. This result shows the geometrical properties of a single lateral velocity gradient or boundary of heterogeneity can be recovered in addition to the relatively small scale structures analysed in Chapter 4.

These results show analysing slowness vector properties of waves sampling lateral velocity gradients can be used to analyse structure on a variety of spatial scales, velocity perturbations and boundary sharpnesses. Future work should focus on linking these observations with the seismic properties of the heterogeneities which can then constrain the thermal or chemical properties of the structures, which in turn allows inferences of their influence on the local and global mantle system.

5.2.5 Implications for constraining Earth models

In Chapter 1, I outlined how seismic phenomena such as scattering and reflections have been analysed to constrain the properties of mantle heterogeneities and how these have been used to discriminate between hypothetical Earth models. In this subsection, I discuss the geodynamic implications my work has with a focus on LLVPs.

Determining whether LLVPs are of a purely thermal nature or are home to some form of chemical heterogeneity has been heavily discussed since their discovery in the 1980s. A commonly used argument in favour of chemical heterogeneity are the ‘sharp’ velocity gradients at the boundaries of LLVPs (e.g. Ni et al., 2002; Sun and Miller,

2013; To et al., 2005). A significant contribution from the work presented in Chapter 2 are my estimates for the velocity gradients at the boundary of the African LLVP are an order of magnitude lower than those commonly cited. This is significant as these gradients are possible with purely thermal LLVP structures (Davies et al., 2012). The weaker estimate suggests the velocity gradients may be the result of a thermal anomaly either a cluster of plumes, superplume or the majority of the LLVP anomaly is caused by thermal anomalies.

Currently, global scale observations of mantle heterogeneity are available for on the broadest scale lengths of 1000s of kilometres from global seismic tomography models (e.g. French and Romanowicz, 2014; Koelemeijer et al., 2015; Ritsema et al., 2011; Simmons et al., 2010) and observations sensitive to some of the smallest structures on scales of 10s of kilometres (Ma and Thomas, 2020). The observations I have made are on the scale of 100s of kilometres. By providing a method that can make these observations automatically in Chapter 3, global-scale observations of structures on the length scale of 100s of kilometres are now possible. These global-scale observations, or maps, such as those in Chapter 4, which locate strong lateral velocity gradients and constrain properties such as morphology or velocity gradient strength. These maps can then be compared with outputs of the location, morphology and velocity gradient strength of heterogeneities in geodynamic simulations therefore providing more constraints to the hypothetical Earth models.

5.3 Future work

It is said a PhD is never finished, only submitted, and I think this is partly because of the abundance of ideas that are inspired by the research undertaken. In this section, I discuss what further investigation would complement work in this thesis.

5.3.1 The frequency dependence and visibility of multipathing

A low proportion ($< 20\%$) of all observations in Chapters 2 and 4 show multipathed arrivals. This highlights the specific criteria that are needed for multipathing to be observed with array methods. The multipathed arrival needs to arrive with sufficiently different slowness vector properties and arrive with enough power relative to the main arrival to be observed in the beamforming power distributions. Factors such as the proportion of the Fresnel zone sampling the velocity gradient, the length over which the wave samples the velocity gradient, the dipping angle of the velocity gradient, the incidence angle of the wave on the velocity gradient, the velocity perturbation of the heterogeneity and the strength of the velocity gradient are all likely to affect whether multipathing is observable with array methods.

In Chapters 2 and 4, there is evidence for observable multipathing to be frequency-

dependent with some multipathing observed in a range of frequency bands and other multipathing observed in just one. A study could analyse the frequency dependence of multipathing and what properties would be needed to observe multipathing in either a single frequency band or in a range of frequencies.

To investigate how observable multipathing is and its frequency dependence, finite frequency modelling is essential but also computationally expensive. The computational cost of finite frequency modelling limits how much of the parameter space can be explored, so investigating all the factors which may influence the visibility of multipathing is not feasible. The goal, therefore, would not be to explore all possible scenarios which may or may not lead to observable multipathing. Instead, the aim would be to determine the weakest velocity gradients and perturbations needed to observe multipathing.

The model setup would aim to create an ideal scenario to observe multipathing with a structure of a certain velocity gradient and perturbation. The parameters to search over would be the velocity gradient strength, velocity perturbation of heterogeneity and length sampled by the wave. The structure would be rooted at the CMB to limit the parameter space to search over as only height above the CMB would need to be explored rather than the depth and length of the structure. The angle of the boundary at each depth would match the angle of the SKS ray path sampling it. If multipathing is not observed under these conditions with the velocity gradient and perturbation and lengths, multipathing will not be observable at all when other factors are included. To reduce the computational cost and allow more of the parameter space to be searched, I would use an axisymmetric seismic modelling code such as AxiSEM (Nissen-Meyer et al., 2014) for most of the investigation. The limitations of the axisymmetric approach are that it will not be able to fully account for the 3-D nature of the problem and possibly overestimate the velocity gradients needed for multipathing at a given sampling length. Therefore, for specific parameters where the observable multipathing to non-observable multipathing transition occurs, I would use a 3D code such as SPECFEM3D Globe (Komatitsch and Tromp, 2002a; Komatitsch and Tromp, 2002b) to validate the results of the axisymmetric modelling.

The results of this would quantify what conditions are needed for lower mantle structure to cause observable multipathing. While this would not necessarily give the velocity gradients which are producing multipathing observed in real data, this study would provide a lower bound for the conditions which could produce the multipathing. Information such as the magnitude of the slowness vector deviation could be used to further quantify the velocity gradient.

5.3.2 Slowness vector magnitudes and velocity gradient

While multipathing has been challenging to observe, there are many observations of slowness vector deviations which I have interpreted to be caused by structures such as LLVPs, plumes or slabs. The next step of using these measurements is to infer the velocity gradients, perturbations, depth extents and morphology of the mantle structure. Like analysing multipathing and its relationship with mantle heterogeneity, ideally, the modelling would use full 3-D finite frequency modelling. To reduce the computational cost, I would use 3-D ray tracing (Simmons et al., 2011; Simmons et al., 2012; Zhao et al., 1992) to search over the majority of the parameter space. Ray tracing assumes the wave has an infinite frequency such that it can be approximated as a ray. In reality, the wave does not have an infinite frequency and at a given depth and frequency is sensitive to an area known as the Fresnel zone. As the wave is sensitive to an area at each depth, and not a point, the velocity gradient will be sampled over a greater length in full wavefield simulations than if the wave is approximated as a ray. Ray tracing may overestimate the velocity perturbations and gradients capable of producing the observed slowness vector deviations.

To validate the observations of the ray tracing, finite frequency modelling code SPECFEM3D Globe (Komatitsch and Tromp, 2002a; Komatitsch and Tromp, 2002b) should be used for models of interest. The finite frequency modelling would show how accurate the 3-D ray-tracing results are in determining the relationship between the parameters and slowness vector deviation. Furthermore, the comparison between ray tracing and finite frequency modelling results would show the viability of ray tracing for inferring the properties of structures causing slowness vector deviation.

5.3.3 Improving the automated method to guard against misidentification of noise

The limitations of the automated method presented in Chapter 3 come from the sensitivity of the output to the parameters chosen for DBSCAN (Ester et al., 1996a). DBSCAN essentially defines a density threshold where a core point in a cluster needs to have $MinPts$ within a radius ϵ to exist. If the density threshold is very low, noise may be misclassified as an arrival, but weaker seismic arrivals may also be identified. On the other hand, if the density threshold is high, noise is less likely to be classified as an arrival, but weaker arrivals are also less likely to be recovered. This limitation highlights the importance of tuning the parameters of DBSCAN to a labelled dataset as I did in Chapter 3 if using the method for automated purposes. If the algorithm is changed to use other information to constrain whether the cluster is an arrival or noise, the density criteria could be lowered allowing weaker arrivals to be identified.

The information which could aid the discrimination of arrivals over noise is the

power values in the grid at the points recovered from each bootstrap sample and travel time estimates using the slowness vector values of each point. The arrival times for each point in the cluster could be estimated by forming the beam using the slowness vector property of the point and then measure the arrival time from the highest amplitude of the beam. The power of each point could be found by integrating along the beam or measured on the power grid directly when the peak is taken.

Once these properties are measured for each point in the cluster, the cluster will have a distribution of power and travel times for the arrival. This could be analysed to investigate what the wavefield has sampled on its path to the array. The distribution of these properties could be used to constrain whether the cluster is noise or an arrival. If the uncertainty of these properties is too high, they could be removed and classified as noise or as too uncertain to use. What limits to put on the uncertainty is challenging to determine and would be up to the user to determine. Preliminary results of this improvement suggest that arrival time uncertainties are often on the order of seconds or lower and uncertainties greater than ten seconds may be too uncertain to use.

5.3.4 Correcting for a curved wavefront

To make observations on a very large seismic array, I developed a method to correct for the curvature of the wavefront as the plane wavefront assumption began to break down and add error to the slowness vector measurements. Our synthetic tests in Chapter 2 showed assuming a plane wavefront causes a backazimuth error of 2.37° and horizontal slowness error of 0.20 $s/°$. Figure A.1 in Section A.1 illustrates the effect of the correction on the slowness vector measurement.

The curved wavefront correction presented in Chapter 2 changes the assumed backazimuth of the wave arriving at each station (see Section 1.2.4.1 for details), but it does not account for the changing horizontal slowness of the wave due to the spherical Earth. The assumption of a constant horizontal slowness across the array may contribute to some of the remaining errors of 0.40° and 0.03 s/° for backazimuth and horizontal slowness respectively. However, correcting for the backazimuth only reduces the error by an order of magnitude suggesting it is the backazimuth assumption that has a greater effect on the slowness vector measurement.

It is not clear what combination of array size, station spacing, phase and wavefront-curvature (i.e. how far the wave is from the source or antipode) the plane wave assumption is no longer valid and how large an error it contributes. To quantify this, ray tracing through a spherical Earth with a 1-D velocity model using PREM (Dziewonski and Anderson, 1981) to a global distribution of arrays of varying apertures and station spacing with different phases such as S, P, ScS, PcP, SKS, Pdiff can be applied. From these travel times, the slowness vector can be estimated using the plane wavefront ap-

proximation and with curved wavefront correction and compare then to the predicted slowness vector from the ray tracing. The result of this analysis should constrain under what conditions the plane wavefront assumption contributes error to the slowness vector measurement and quantify the slowness vector error.

5.4 Conclusion

Lateral velocity gradients in the Earth's mantle can give information about the boundaries of mantle heterogeneity and the length scale of the transition from the ambient mantle to the heterogeneity itself. Multipathing and diffraction occur when a wave is incident on a sufficiently strong lateral velocity gradient, therefore identifying and studying the phenomena may give information about the gradient the wave has sampled. The velocity gradients at the boundaries of different mantle heterogeneities may give some indication of the fundamental differences between them such as the thermal, chemical natures or origin of the anomalies. Furthermore, by understanding the location, morphology and strength of the gradients the observations on a global scale can be used for comparison with hypothetical Earth models, geodynamical modelling investigations and used by tomographic studies. Analysis of multipathing and diffraction caused by boundary structure of mantle heterogeneities has focused on the waveform complexity it creates and trying to replicate it (e.g Ni and Helmberger, 2003c; Ni et al., 2005; Sun et al., 2017; Sun et al., 2010b; Zhao et al., 2015). Analysing the slowness vector properties of the multipathed arrivals can give quantifiable constraints on what the boundary properties of the heterogeneity are. In this thesis, I analyse the slowness vector properties of arrivals sampling lateral velocity gradients to quantify their effect on the wavefield, identify multipathing and work to expand the analysis to a global scale.

I first analyse SKS and SKKS data sampling the African LLVP using beamforming correcting for a curved wavefront to understand the feasibility of observing multipathing in slowness space and determine what information could be recovered by analysing it in this way. I showed observing multipathed arrivals appears to be frequency-dependent which suggests specific criteria between the size of Fresnel zone and velocity gradient spatial scale is needed for multipathing to be observed. Using finite frequency forward modelling I estimated the velocity gradients at the boundary of the African LLVP which were approximately an order of magnitude lower than previous estimates. These gradients were able to be produced by thermal or thermochemical structures (Davies et al., 2012), which suggest observing multipathing is not necessarily evidence for chemical heterogeneity.

Chapter 3 aims to develop a method to automate the measurement of slowness vector properties with uncertainty estimates and identify multipathing. Automating

the measurement means global-scale studies of phenomena such as coherent scattering, surface wave multipathing or mantle reflectors are now more feasible. The uncertainty estimates can quantify the effect of heterogeneous distribution and local geology on the slowness vector measurement, which can then be used to provide estimates on the location of mantle heterogeneity or the source of the wavefield perturbation.

In the final study, the automated method was used to make global-scale observations of SKS multipathing and slowness vector deviation. Using statistical analysis of the variance of slowness vectors, I constrained the depth of mantle heterogeneities and, with comparison to 3-D ray-tracing modelling results, hypothesised their origin. I interpret many different structures beneath Europe and the US from whole mantle plumes, subducted slab material in the upper and mid mantle. Each of these heterogeneities has a unique slowness vector pattern, magnitude, whether they cause multipathing and what frequency band the multipathing is observed in. These differing observations for each heterogeneity show the value in analysing the seismic wavefield with slowness vector measurements. Combined with forward modelling properties such as geometry, velocity perturbation, velocity gradient sharpness can be constrained for each of the structures. This would then create a map of lateral velocity gradient properties which can then give inferences on the thermal anomalies, chemical heterogeneities or ages of the structure and contribute to evaluating different conceptual Earth models.

References

Davies, D. R., Goes, S., Davies, J., Schuberth, B., Bunge, H.-P., & Ritsema, J. (2012). Reconciling dynamic and seismic models of Earth's lower mantle: The dominant role of thermal heterogeneity. *Earth and Planetary Science Letters*, *353*, 253–269.

Dziewonski, A. M., & Anderson, D. L. (1981). Preliminary reference Earth model. *Physics of the earth and planetary interiors*, *25*(4), 297–356.

Efron, B. (1992). Bootstrap Methods: Another Look at the Jackknife. In S. Kotz & N. L. Johnson (Eds.), *Breakthroughs in Statistics: Methodology and Distribution* (pp. 569–593). Springer.

Ester, M., Kriegel, H.-P., Sander, J., Xu, X. et al. (1996a). A density-based algorithm for discovering clusters in large spatial databases with noise. *Kdd*, *96*, 226–231.

Ester, M., Kriegel, H.-P., & Xu, X. (1996b). A Density-Based Algorithm for Discovering Clusters in Large Spatial Databases with Noise, 6.

French, S., & Romanowicz, B. (2014). Whole-mantle radially anisotropic shear velocity structure from spectral-element waveform tomography. *Geophysical Journal International*, *199*(3), 1303–1327.

Koelemeijer, P., Ritsema, J., Deuss, A., & Van Heijst, H.-J. (2015). SP12RTS: A degree-12 model of shear-and compressional-wave velocity for Earth's mantle. *Geophysical Journal International*, *204*(2), 1024–1039.

Komatitsch, D., & Tromp, J. (2002a). Spectral-element simulations of global seismic wave propagationâI. Validation. *Geophysical Journal International*, *149*(2), 390–412.

Komatitsch, D., & Tromp, J. (2002b). Spectral-element simulations of global seismic wave propagationâII. Three-dimensional models, oceans, rotation and self-gravitation. *Geophysical Journal International*, *150*(1), 303–318.

Lekic, V., Cottaar, S., Dziewonski, A., & Romanowicz, B. (2012). Cluster analysis of global lower mantle tomography: A new class of structure and implications for chemical heterogeneity. *Earth and Planetary Science Letters*, *357*, 68–77.

Ma, X., & Thomas, C. (2020). Small-scale scattering heterogeneities in the lowermost mantle from a global analysis of PKP precursors. *Journal of Geophysical Research: Solid Earth*, *125*(3), e2019JB018736.

Ni, S., & Helmberger, D. V. (2003a). Further constraints on the African superplume structure. *Physics of the Earth and Planetary Interiors*, *140*(1-3), 243–251.

Ni, S., & Helmberger, D. V. (2003b). Ridge-like lower mantle structure beneath south Africa. *Journal of Geophysical Research: Solid Earth*, *108*(B2).

Ni, S., & Helmberger, D. V. (2003c). Seismological constraints on the South African superplume; could be the oldest distinct structure on Earth. *Earth and Planetary Science Letters*, *206*(1-2), 119–131.

Ni, S., Tan, E., Gurnis, M., & Helmberger, D. (2002). Sharp sides to the African superplume. *Science*, *296*(5574), 1850–1852.

Ni, S., V. Helmberger, D., & Tromp, J. (2005). Three-dimensional structure of the African superplume from waveform modelling. *Geophysical Journal International*, *161*(2), 283–294.

Nissen-Meyer, T., van Driel, M., Stähler, S. C., Hosseini, K., Hempel, S., Auer, L., Colombi, A., & Fournier, A. (2014). AxiSEM: Broadband 3-D seismic wavefields in axisymmetric media. *Solid Earth*, *5*(1), 425–445.

Ritsema, J., Deuss, a. A., Van Heijst, H., & Woodhouse, J. (2011). S40RTS: A degree-40 shear-velocity model for the mantle from new Rayleigh wave dispersion, teleseismic traveltime and normal-mode splitting function measurements. *Geophysical Journal International*, *184*(3), 1223–1236.

Sigloch, K., McQuarrie, N., & Nolet, G. (2008). Two-stage subduction history under North America inferred from multiple-frequency tomography. *Nature Geoscience*, *1*(7), 458–462.

Simmons, N., Myers, S., & Johannesson, G. (2011). Global-scale P wave tomography optimized for prediction of teleseismic and regional travel times for Middle East

events: 2. Tomographic inversion. *Journal of Geophysical Research: Solid Earth*, *116*(B4).

Simmons, N. A., Forte, A. M., Boschi, L., & Grand, S. P. (2010). GyPSuM: A joint tomographic model of mantle density and seismic wave speeds. *Journal of Geophysical Research: Solid Earth*, *115*(B12).

Simmons, N. A., Myers, S. C., Johannesson, G., & Matzel, E. (2012). LLNL-G3Dv3: Global P wave tomography model for improved regional and teleseismic travel time prediction. *Journal of Geophysical Research: Solid Earth*, *117*(B10).

Sun, D., Gurnis, M., Saleeby, J., & Helmberger, D. (2017). A dipping, thick segment of the Farallon Slab beneath central U.S. *Journal of Geophysical Research: Solid Earth*, *122*(4), 2911–2928.

Sun, D., Helmberger, D., & Gurnis, M. (2010a). A narrow, mid-mantle plume below southern Africa. *Geophysical Research Letters*, *37*(9).

Sun, D., Helmberger, D., & Gurnis, M. (2010b). A narrow, mid-mantle plume below southern Africa. *Geophysical Research Letters*, *37*(9).

Sun, D., & Miller, M. S. (2013). Study of the western edge of the African Large Low Shear Velocity Province. *Geochemistry, Geophysics, Geosystems*, *14*(8), 3109–3125.

Thorne, M. S., Pachhai, S., Leng, K., Wicks, J. K., & Nissen-Meyer, T. (2020). New Candidate Ultralow-Velocity Zone Locations from Highly Anomalous SPdKS Waveforms. *Minerals*, *10*(3), 211.

To, A., Romanowicz, B., Capdeville, Y., & Takeuchi, N. (2005). 3D effects of sharp boundaries at the borders of the African and Pacific Superplumes: Observation and modeling. *Earth and Planetary Science Letters*, *233*(1-2), 137–153.

van der Lee, S., & Nolet, G. (1997). Seismic image of the subducted trailing fragments of the Farallon plate. *Nature*, *386*(6622), 266–269.

Zhao, D., Hasegawa, A., & Horiuchi, S. (1992). Tomographic imaging of P and S wave velocity structure beneath northeastern Japan. *Journal of Geophysical Research: Solid Earth*, *97*(B13), 19909–19928.

Zhao, L., Paul, A., Guillot, S., Solarino, S., Malusa, M. G., Zheng, T., Aubert, C., Salimbeni, S., Dumont, T., Schwartz, S., Zhu, R., & Wang, Q. (2015). First seismic evidence for continental subduction beneath the Western Alps. *Geology*, *43*(9), 815–818.

Appendix A

Supplementary material for Chapter 2

A.1 Plane Circular wavefront comparison

To quantify the effect of the plane wavefront approximation and our correction for a circular wavefront, we placed a Ricker wavelet with a frequency of 0.15 Hz at the PREM Dziewonski and Anderson, 1981 predicted SKS arrival time for each station in the Kaapvaal array for an event on 29 June 1997 and set the amplitude to zero elsewhere. The only arrival with any amplitude arrives at the predicted backazimuth and horizontal slowness, so the observed maximum should be aligned with the prediction in the $\theta - p$ plot. Figure A.1. For the plane wavefront approximation, the observed maximum deviates from the prediction by 2.37° for the backazimuth and 0.20 $s/°$ for the horizontal slowness. After correcting for a circular wavefront using the method outlined above, the deviation from the prediction is reduced to 0.40° for the backazimuth and 0.03 $s/°$ for the horizontal slowness.

A.2 SKKS and S3SK comparison

Most synthetic observations show observable power for the SKKS arrival and S3KS with less than 10 % of the SKKS power with some showing no observable power for S3KS (Figure A.2). We interpret this as SKKS being the dominant signal for these observations, therefore observations with only one observable arrival are interpreted as SKKS. Observations that potentially show other phases such as S3KS arriving in both the time window and any power in the $\theta - p$ plot in both the synthetic and recorded data are labeled as possibly having multipathing. Observations with multiple arrivals in $\theta - p$ plots for recorded data and only SKKS arrivals are observable in the synthetic data are interpreted as multipathing and not S3KS.

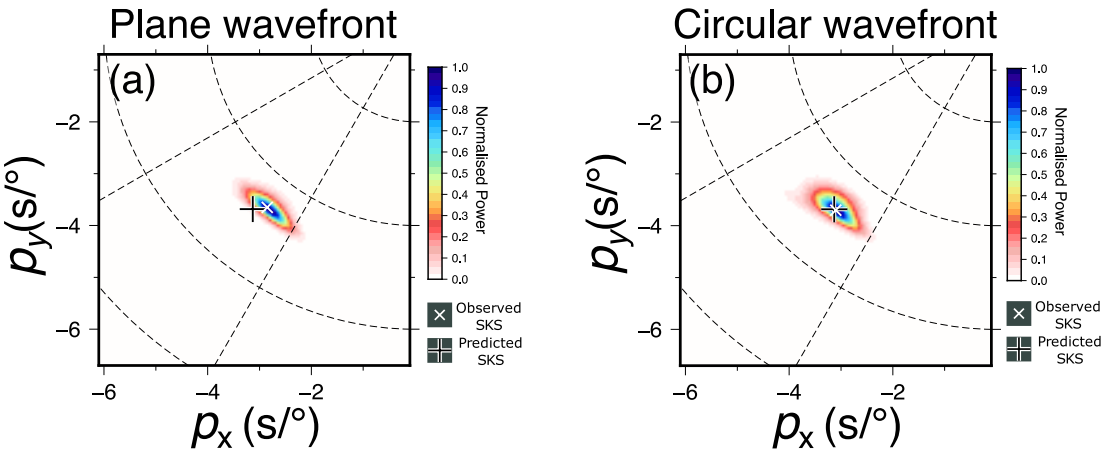

Figure A.1: A comparison of the effect of **(a)** plane and **(b)** circular wavefront approximation on the grid search over slowness vectors. The observed maximum for the plane wavefront approximation has a backazimuth deviation of 2.37° and an horizontal slowness deviation of 0.20 s/°. The circular wavefront approximation reduces these deviations to 0.4° for backazimuth and 0.03 s/° for horizontal slowness. The data are generated by inserting a Ricker wavelet of frequency 0.15 Hz at the PREM predicted arrival time for all stations in the Kaapvaal array. Correcting for a circular wavefront significantly reduces the deviation of the observed arrival from the prediction.

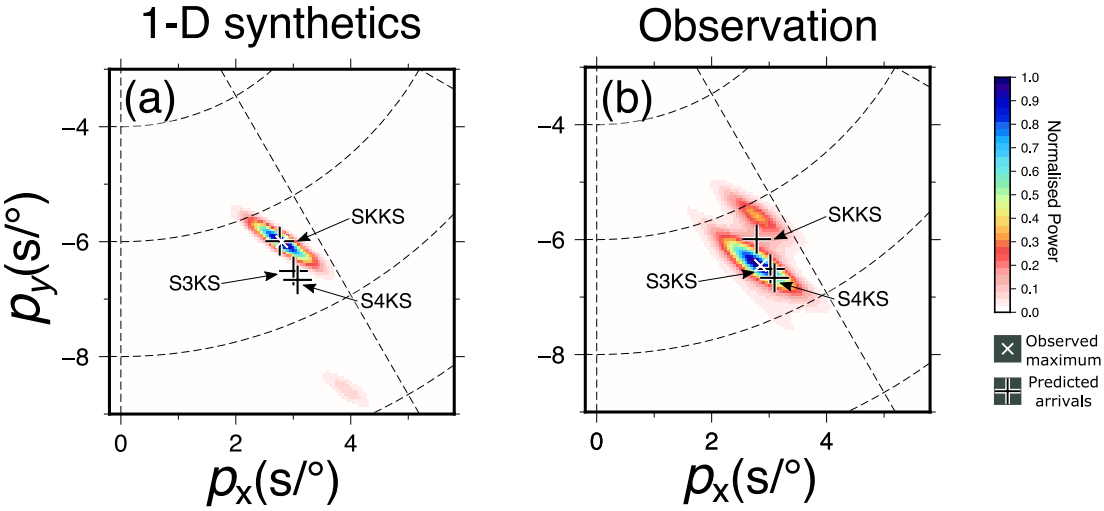

Figure A.2: A comparison of results for synthetic data generated from Syngine using model prem_i_2s Hutko et al., 2017 **(a)** and the recorded data **(b)** from an event on 25 May, 1995. These examples have had the array response function deconvolved. The high power S2KS arrival in the synthetics **(a)** and no visible S3KS power suggest the observation **(b)** shows multipathing and not phases of SmKS reverberations arriving in the time window.

A.3 Noise reduction equations

Phase weighted stacking Schimmel and Paulssen, 1997a weights each time in the linear stack by an amplitude independent weighting and is expressed by

$$c(t) = \frac{1}{N}\sum_{j=1}^{N} s_j(t) \left| \frac{1}{N}\sum_{n=1}^{N} e^{(i\Phi_n(t))} \right|^v , \tag{A.1}$$

where $c(t)$ is the phase weight stack amplitude at time t, N is the number of traces, $s_j(t)$ is the jth real trace, $\Phi_n(t)$ is the nth instantaneous phase at time t and v is the weighting power. A weighting power value of 2 is used as a compromise between reducing noise and visibility of multipathed arrivals.

The F-statistic Blandford, 1974 is applied to the power value of the linear stack to reduce noise. The F statistic is calculated by dividing the power of the beam by the power of the difference between the beam and the individual traces

$$F_{\theta,p} = (N-1)\frac{N\sum_{t=1}^{T} S_{b(\theta,p)}(t)^2}{\sum_{t=1}^{T}\sum_{n=1}^{N}[S_{n(\theta,p)}(t) - S_{b(\theta,p)}(t)]^2} , \tag{A.2}$$

where $F_{\theta,p}$ is the F statistic at a particular backazimuth (θ) and horizontal slowness (p), N is the number of traces that form the beam, $S_{b(\theta,p)}(t)$ is the beam at time t for a given backazimuth and horizontal slowness and $S_{n(\theta,p)}(t)$ is trace n at time t shifted by the time calculated for a particular backazimuth and horizontal slowness.

The array geometry limits our ability to precisely constrain the slowness vectors of the incoming energy. The array response function (ARF) provides a theoretical estimate of the effect of array aperture, inter-station spacing and shape on the power of the arrival Rost and Thomas, 2002. We deconvolve the array response function from the linear $\theta - p$ plot to increase slowness resolution using the Richardson-Lucy algorithm Lucy, 1974; Richardson, 1972. This algorithm iterates towards the most likely deblurred image (in this case the $\theta - p$ plot) taking into account the point spread function (the ARF and therefore the array configuration). The algorithm assumes the starting image is described by

$$g = p * \delta + \mu , \tag{A.3}$$

where g is the observed image ($\theta - p$ plot), p is the matrix describing the point spread function (the ARF in this case), δ is the unblurred image and μ is noise. From this, the deblurred image at iteration i is expressed by

$$\delta_i = \alpha\delta_{i-1}(p^T \frac{g}{p\delta_{i-1}}) , \tag{A.4}$$

where δ_i is the deblurred image at iteration i, δ_{i-1} is the deblurred image of the previous

iteration, α is the inverse of the sum of the columns of the point spread matrix p and acts as a normalising vector, p is the point spreading function (ARF) and g is the original observed image ($\theta - p$ plot). For all of our observations, we used 5 iterations to balance between reducing the noise in the plot and losing the multipathed arrival, which could be removed at higher iterations if it is low amplitude. Figure A.3 shows the effect of each of these techniques.

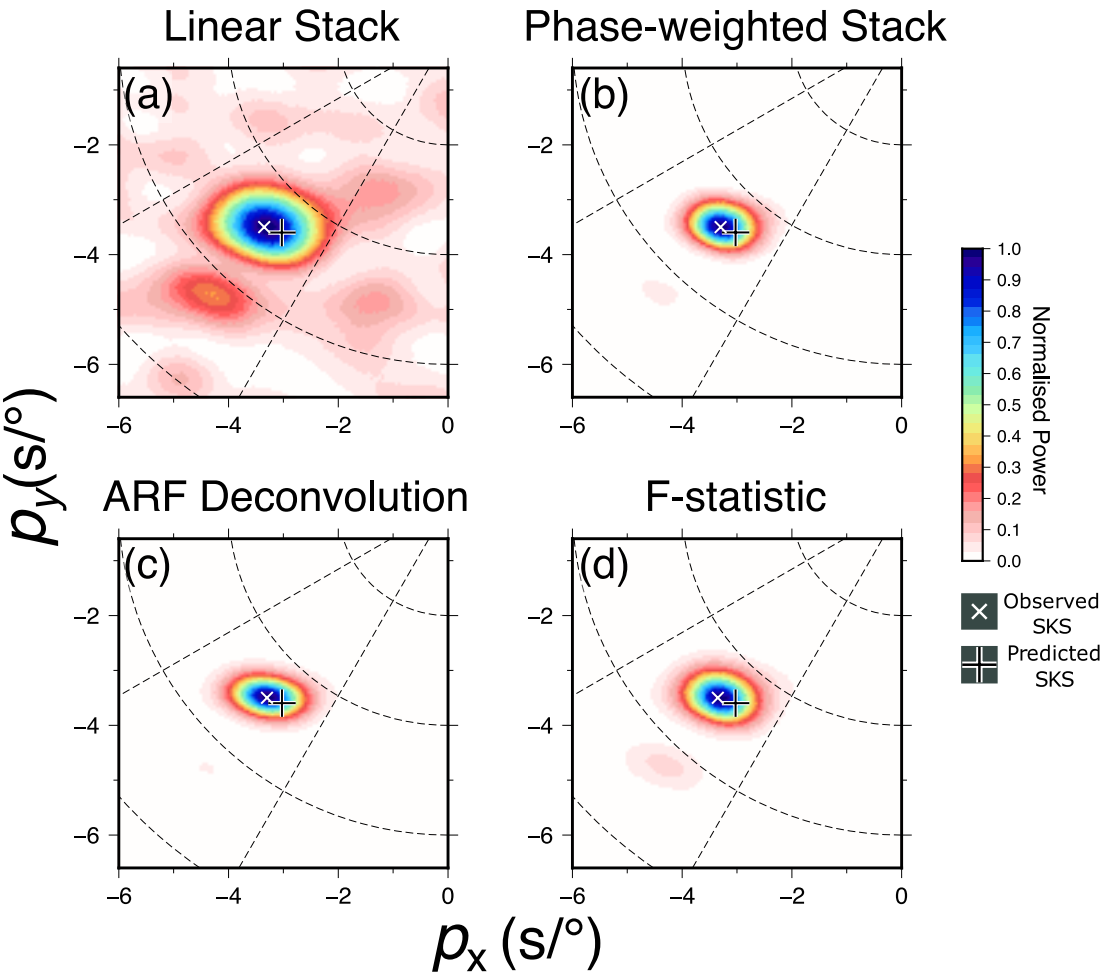

Figure A.3: A comparison of the techniques used to improve the signal-noise ratio and resolution of the $\theta - p$ plots. These examples use all data from an event on the 29 May, 1997. **(a)** uses a linear stack and shows the most background noise. **(b)** uses phase weighted stacking Schimmel and Paulssen, 1997a and shows significant noise reduction. **(c)** is the result of deconvolving the linear plot with the array response function using Richardson-Lucy deconvolution Richardson, 1972 showing significant noise reduction after 5 iterations. **(d)** shows the linear stack with the F-statistic Blandford, 1974 applied showing a reduction in noise.

A.4 Slowness vector descriptions

Figures A.5 to A.8 show the distribution of residuals within the frequency bands.

A.4.1 Backazimuth Residuals

Spatial analysis of backazimuth deviations (Figure A.4) reveals several patterns indicative of structures perturbing the wavefield. The most distinct pattern is to the southeast of Africa (35°S, 27°W) where positive backazimuth residuals (blue, arriving from more clockwise direction than predicted) to negative backazimuth residuals (red, arriving from more anticlockwise direction than predicted) then moving northeast (25°S, 40°W) to negligible backazimuth residuals (white, arriving as predicted).

The transition from positive to negative residuals implies there are two boundaries being sampled causing diffraction in opposite directions. We interpret this as the circular structure southeast of Africa marked by the -1.5% δV_s velocity contours in Figure A.4

We detect more negative backazimuth residuals than positive (Figure A.5) with the negative residuals also spread over a larger area. Some of the negative residuals could be caused by the same circular feature described above, but as the pierce point locations move northeast, the LLVP boundary trending in a northwest-southeast orientation could be contributing. Further north, the negative deviations sharply transition to negligible residuals implying they are not sampling a structure or boundary that would cause the wavefront to change direction.

Either a boundary orthogonal to wave propagation or structures causing the wave to vertically refract with no change to the horizontal propagation direction are possibilities.

A.4.2 Horizontal Slowness Residuals

The spatial distribution of horizontal slowness residuals in Figure A.6 offers a less clear picture than the backazimuth residuals. The circular feature defined by -1.5% δ V_s contours to the southeast of Africa (35°S, 30°W) does show some pattern with the negative residuals lying on the northwest side of the feature, closer to the array, and the positive residuals on the southeast side. Negative residuals mean the wave is arriving more steeply and positive residuals more shallowly, which is expected if the circular feature diffracts the waves.

Residuals west of Africa (25°S, 15°W) are mainly positive, so arrive at a shallower angle, and travel through the body of the LLVP causing the waves to refract. However, there are also several multipathed arrivals in this region with scattered loci (Figure) suggesting the waves also sample a boundary but, because the loci are scattered, it is difficult to constrain exactly what is causing these observations.

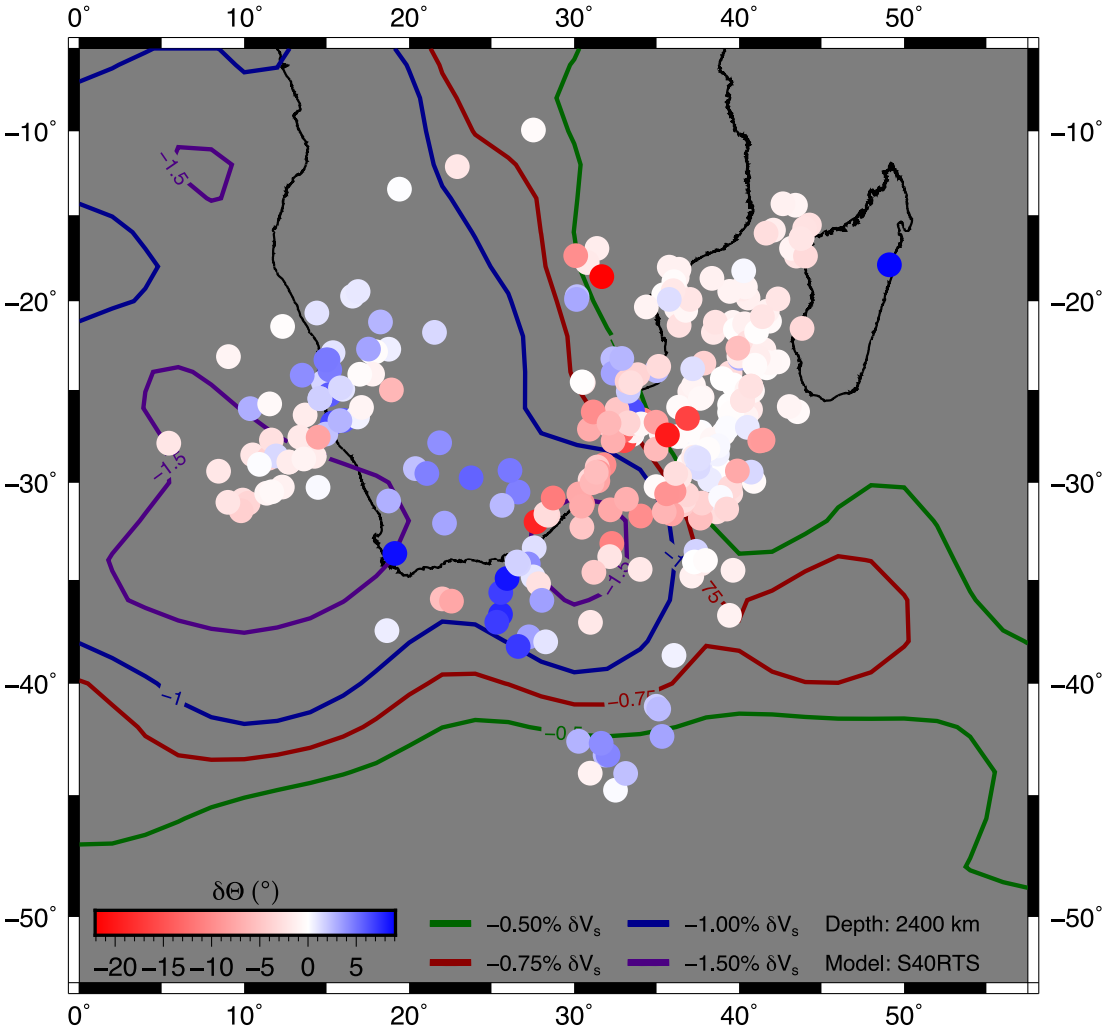

Figure A.4: Pierce points for sub array observations (frequency band 0.13 Hz to 0.52 Hz) at 2400 km depth coloured by backazimuth deviations relative to the great circle path. Blue colours show paths that arrive from a more clockwise direction and red show paths arriving from a more anticlockwise direction than predicted. Contours from S40RTS Ritsema et al., 2011 at a depth of 2400 km are shown to represent potential structures causing the observations. Pierce points are corrected to the measured horizontal slowness and backazimuth.

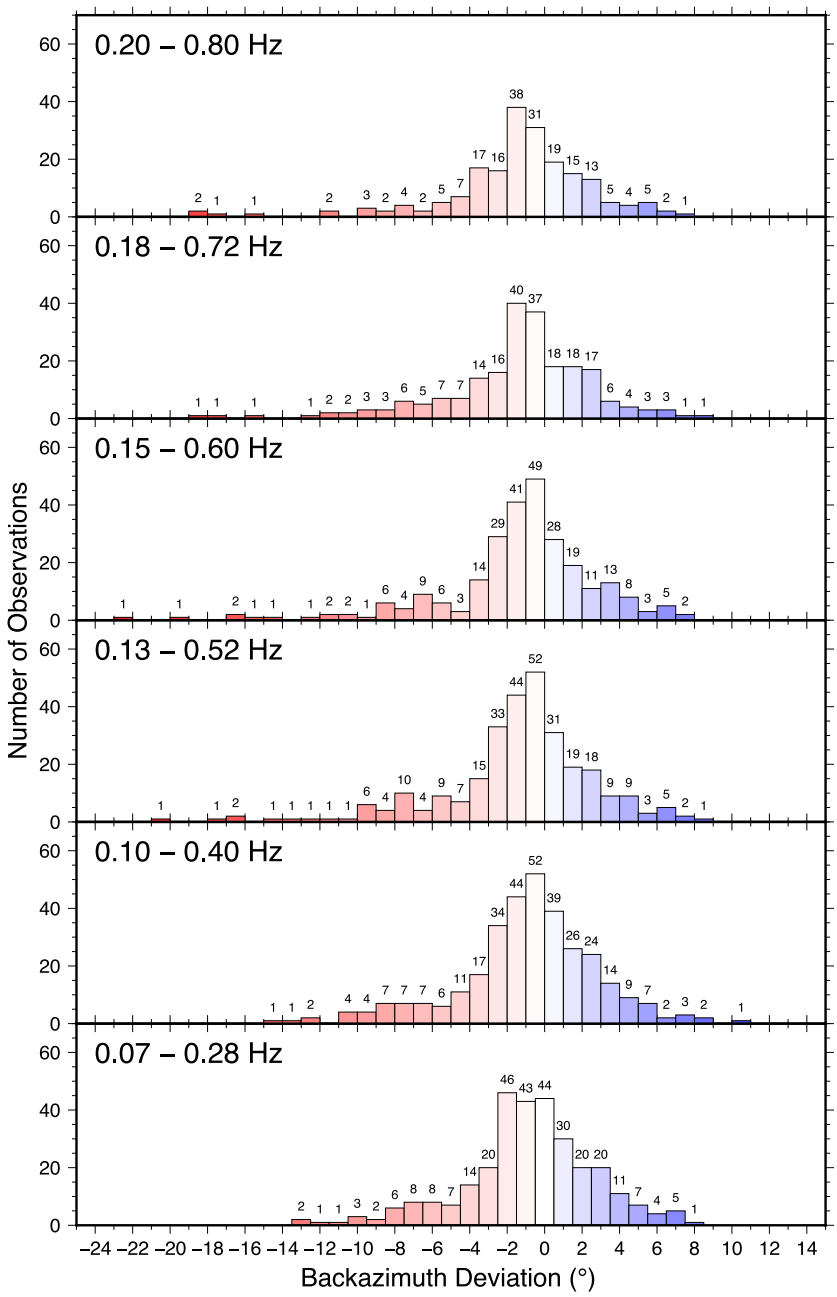

Figure A.5: Histograms of the backazimuth deviations of all observations in each frequency band. The majority of the observations lie close to 0° with maximum observed values of 10° to −22°.

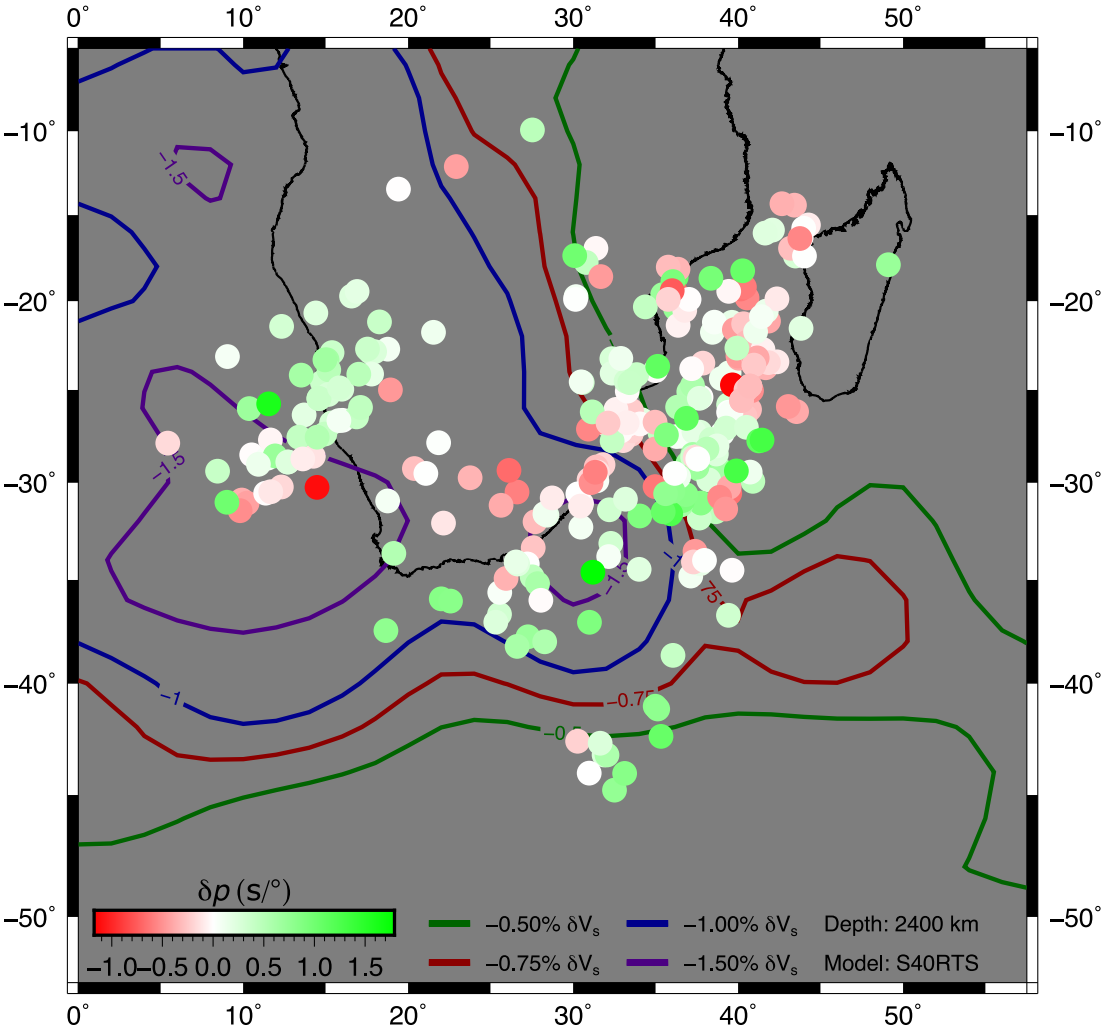

Figure A.6: Pierce points for sub array observations (frequency band 0.13 Hz to 0.52 Hz) at 2400 km depth, coloured by horizontal slowness deviations relative to the PREM predicted ray parameter Dziewonski and Anderson, 1981. Contours from S40RTS Ritsema et al., 2011 at a depth of 2400 km are marked to outline structures potentially contributing to the observations. Pierce points are corrected to match the observed horizontal slowness and backazimuth.

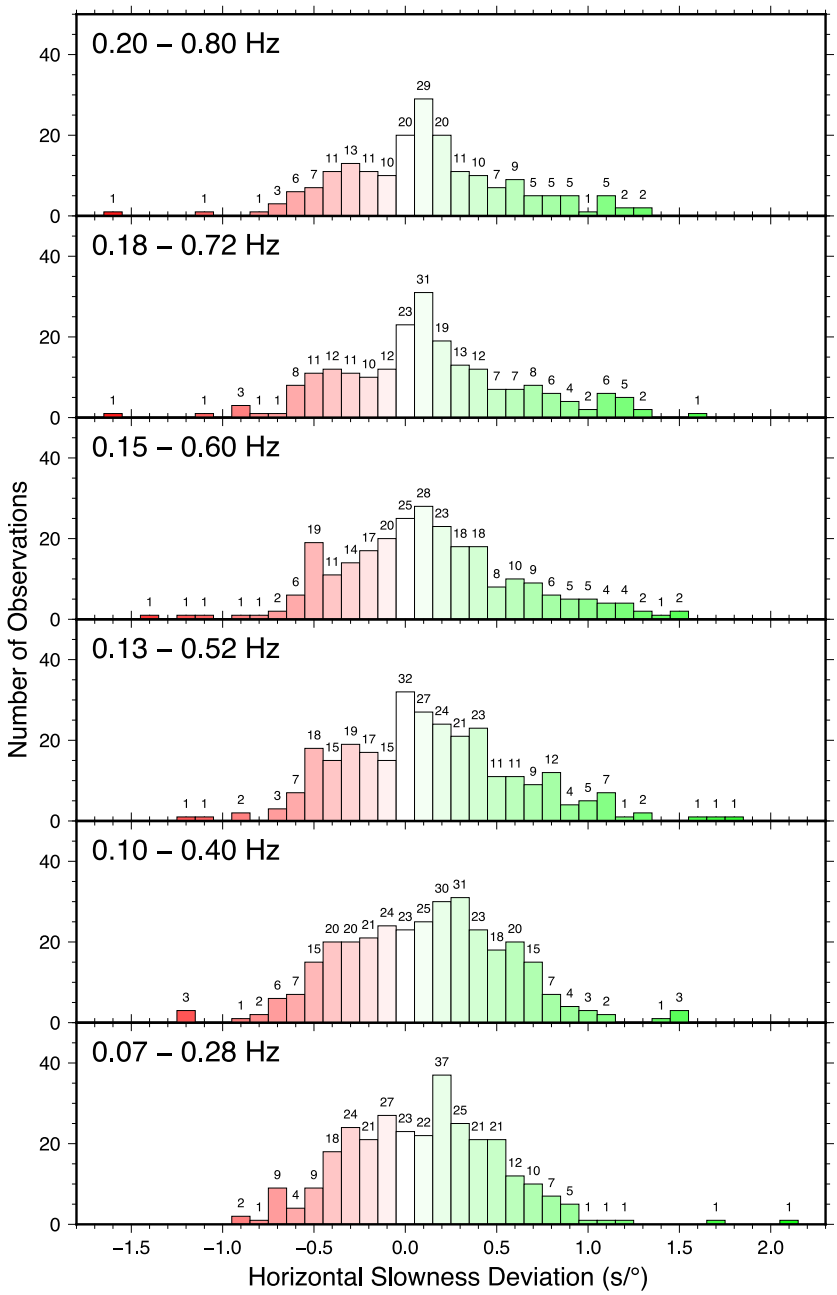

Figure A.7: Histograms of the horizontal slowness deviations of all observations in individual frequency bands. Maximum deviations of 1.2 s/° and −1.0 s/° are observed. More positive than negative deviations are expected due to the dominantly negative velocity mantle structure beneath Africa.

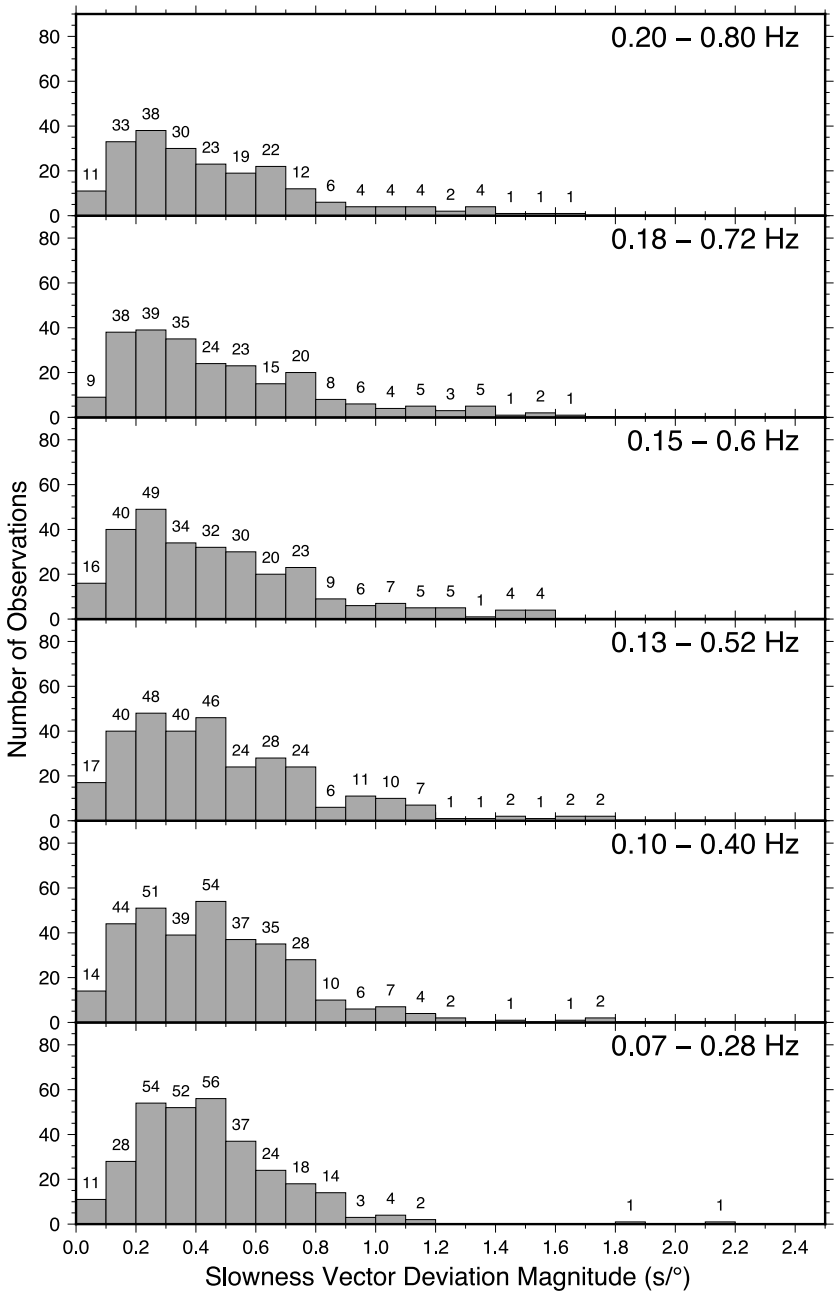

Figure A.8: Histograms of slowness vector deviation magnitude with frequency. Distributions are very similar with frequency, with arguably slightly more high magnitude vectors at higher frequency bands. The smallest slowness vector magnitudes vary from less than 0.1 s/° to 2.1 s/°.

A.5 Effects of crust and mantle models

Figure A.9 shows example $\theta - p$ plots of our tests on the effects of 3-D upper mantle and crustal velocity structure. All runs have the velocity perturbations in S40RTS Ritsema et al., 2011 doubled. Each plot has has the array response function deconvolved and the frequency band used is between 0.13 and 0.18 Hz.

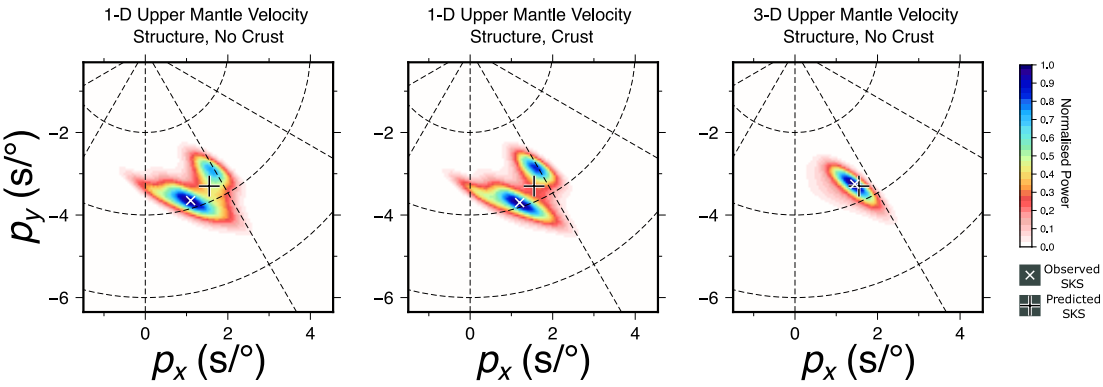

Figure A.9: Three θ-p plots showing synthetic observations with velocity perturbations doubled at depths greater than 1000 km and tapered to a 1-D model at 660 km depth. Left plot is data when using a 1-D upper mantle velocity model and no crustal model. Centre plot uses data when a 1-D upper mantle is used but a crustal model is included. Right plot uses a 3-D upper mantle velocity model from S40RTS Ritsema et al., 2011 and no crustal model. There is very little difference made from adding 3-D crustal structure but a large difference from adding upper mantle structure. Because of this, we include 3-D velocity structure in the upper mantle for all our modelling runs.

A.6 Frequency content multipathed waveforms

We analyse the power spectra of the waveforms for several events to analyse the effects of multipathing. We find evidence for an increase in the power of higher frequencies where multipathing is observed. Figures A.10 to A.12 show examples of waveforms with and without multipathing and their power spectra. Identifying clear evidence of multipathing in the waveforms over background noise is challenging and limiting for expanding the analysis to many other events we use. For event on the 25 May 1997 and 05 April 1999 enough waveforms clearly show either no or clear multipathing to analyse several examples and show the change in power spectra is consistent at least within these events (Figure A.13 and A.14). We hypothesise this could be caused by different frequencies diffracting by different amounts depending on the velocity gradients they sample, leading to some combination of focusing of high frequencies and defocusing of lower frequencies. This is consistent with our interpretation of the slowness vector deviations we observe. Further work is required to fully constrain the effects of velocity gradient on the frequency content of the arrivals and how this relates to the frequencies multipathing is observable in slowness space. This is not the focus of this study so we

do not explore this further.

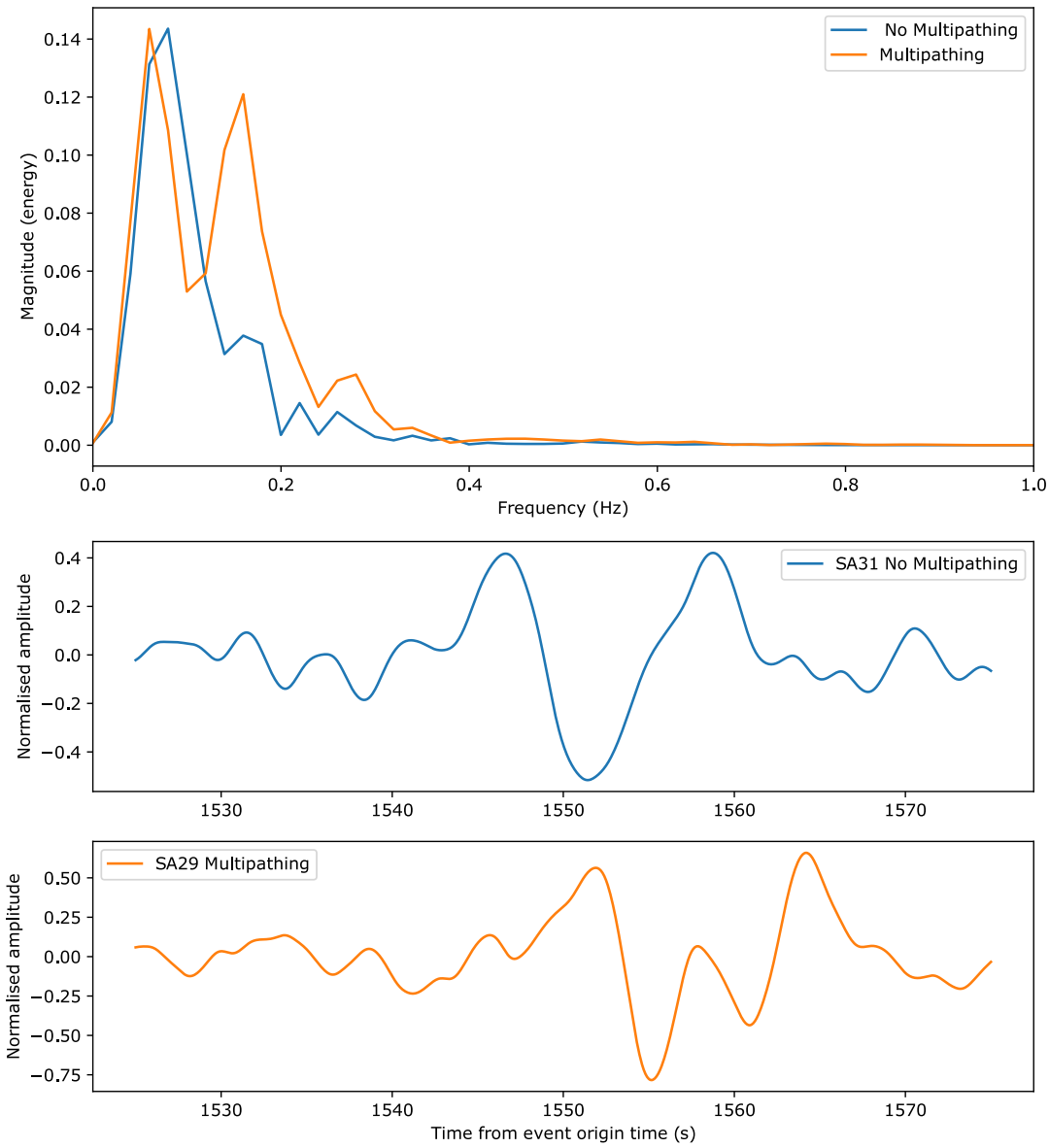

Figure A.10: Top: power spectra of a multipathed (orange) and non multipathed (blue) arrival for data from the 21 May 1997 event. The power spectra are calculated using Welch's method Welch, 1967. Bottom: the waveforms used to calculate power spectra.

A.7 SPdiffKS in synthetics data

Figure A.15 shows the $\theta - p$ plots using waveforms at distances greater than 119° where there is potentially SPdKS in the synthetic waveforms using model M3 (Figure 13 in main document). The $\theta - p$ plots use time windows which, for the plots in the left column, include both SKS and SPdKS and, for the plots in the right column, isolate SPdKS. We find evidence for SPdKS in the synthetics generated using PREM

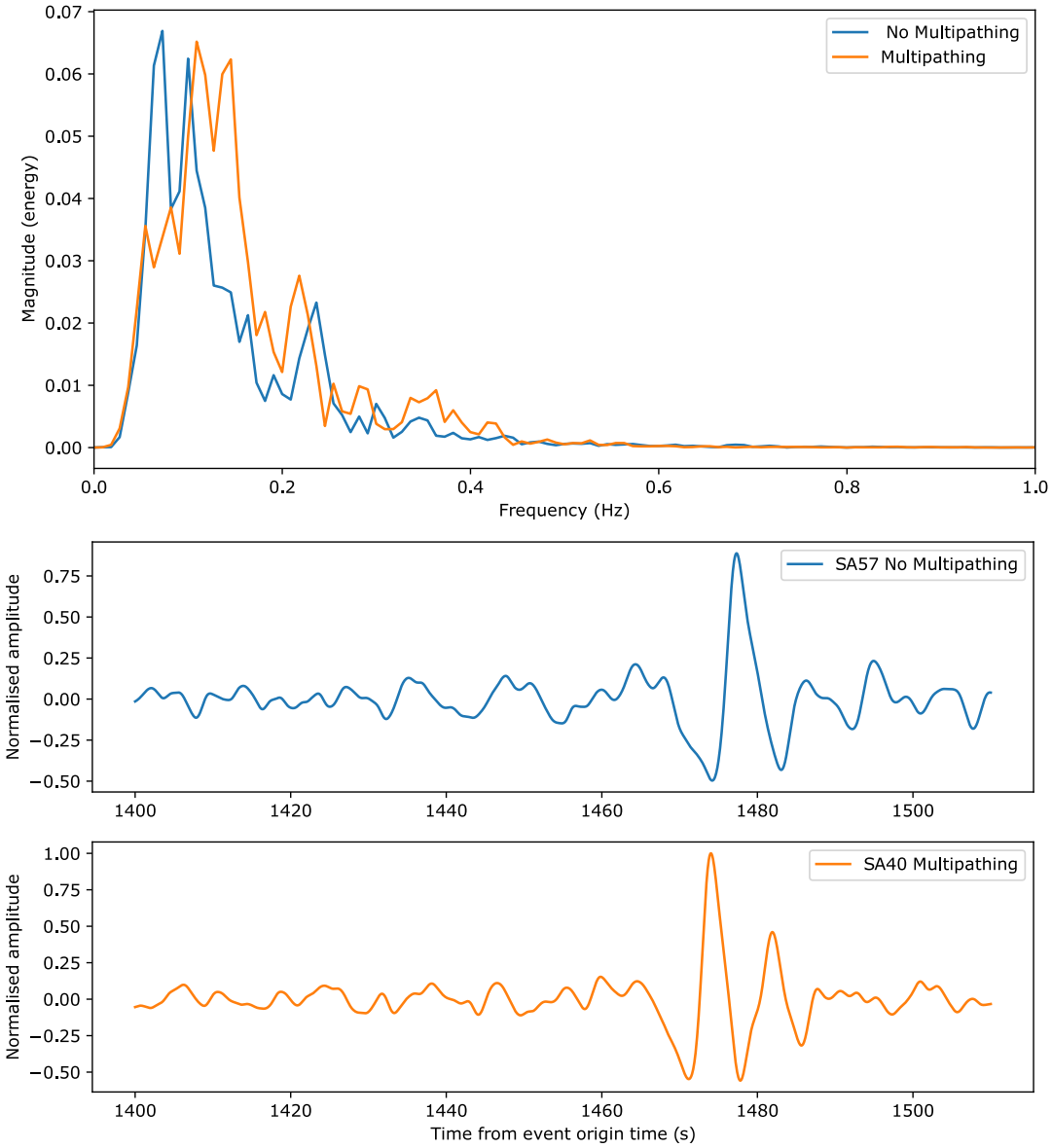

Figure A.11: Top: power spectra of a multipathed (orange) and non multipathed (blue) arrival for data from the 25 May 1997 event. The power spectra are calculated using Welch's method Welch, 1967. Bottom: the waveforms used to calculate power spectra.

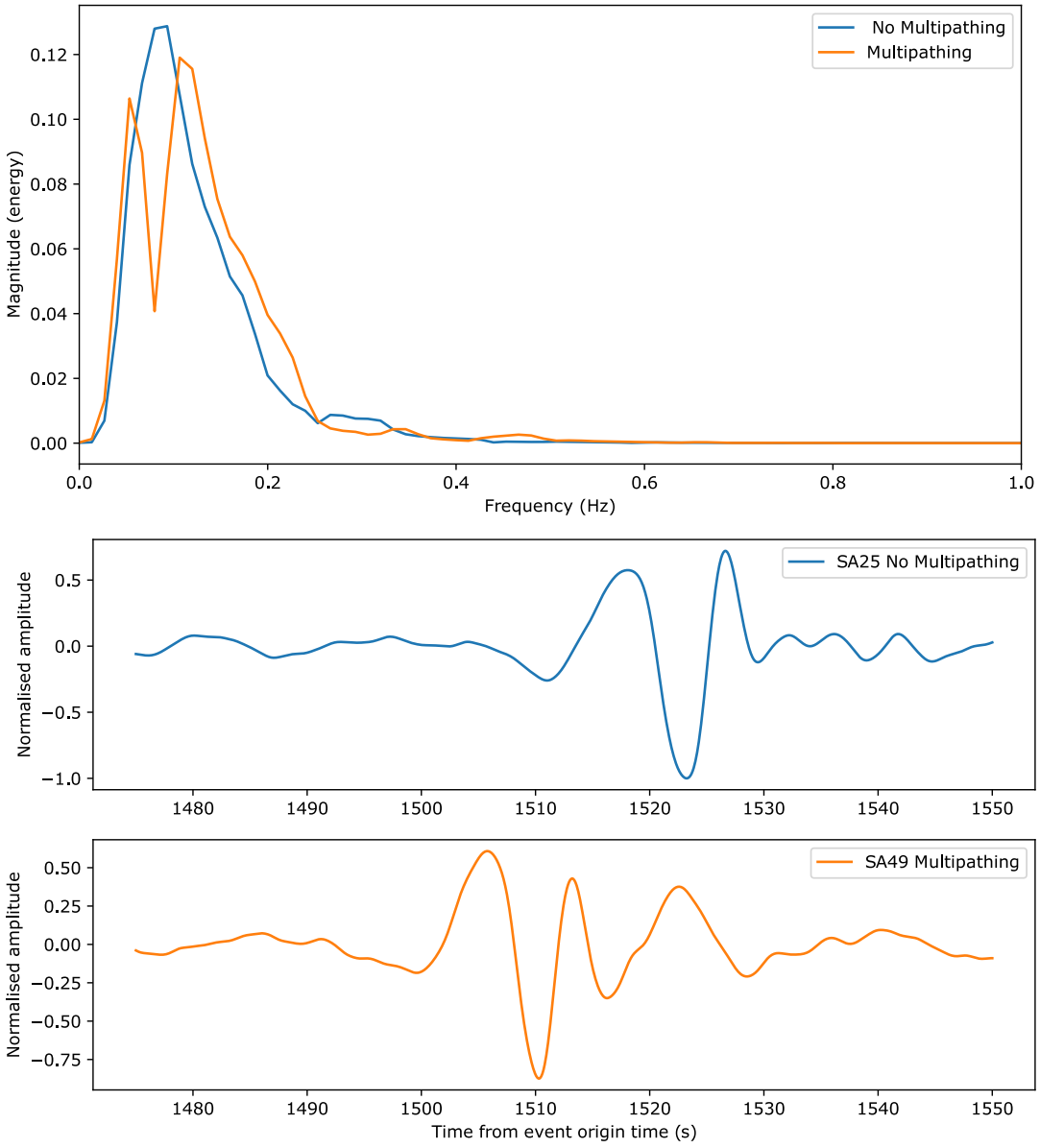

Figure A.12: Top: power spectra of a multipathed (orange) and non multipathed (blue) arrival for data from the 05 April 1999 event. The power spectra are calculated using Welch's method Welch, 1967. Bottom: the waveforms used to calculate power spectra.

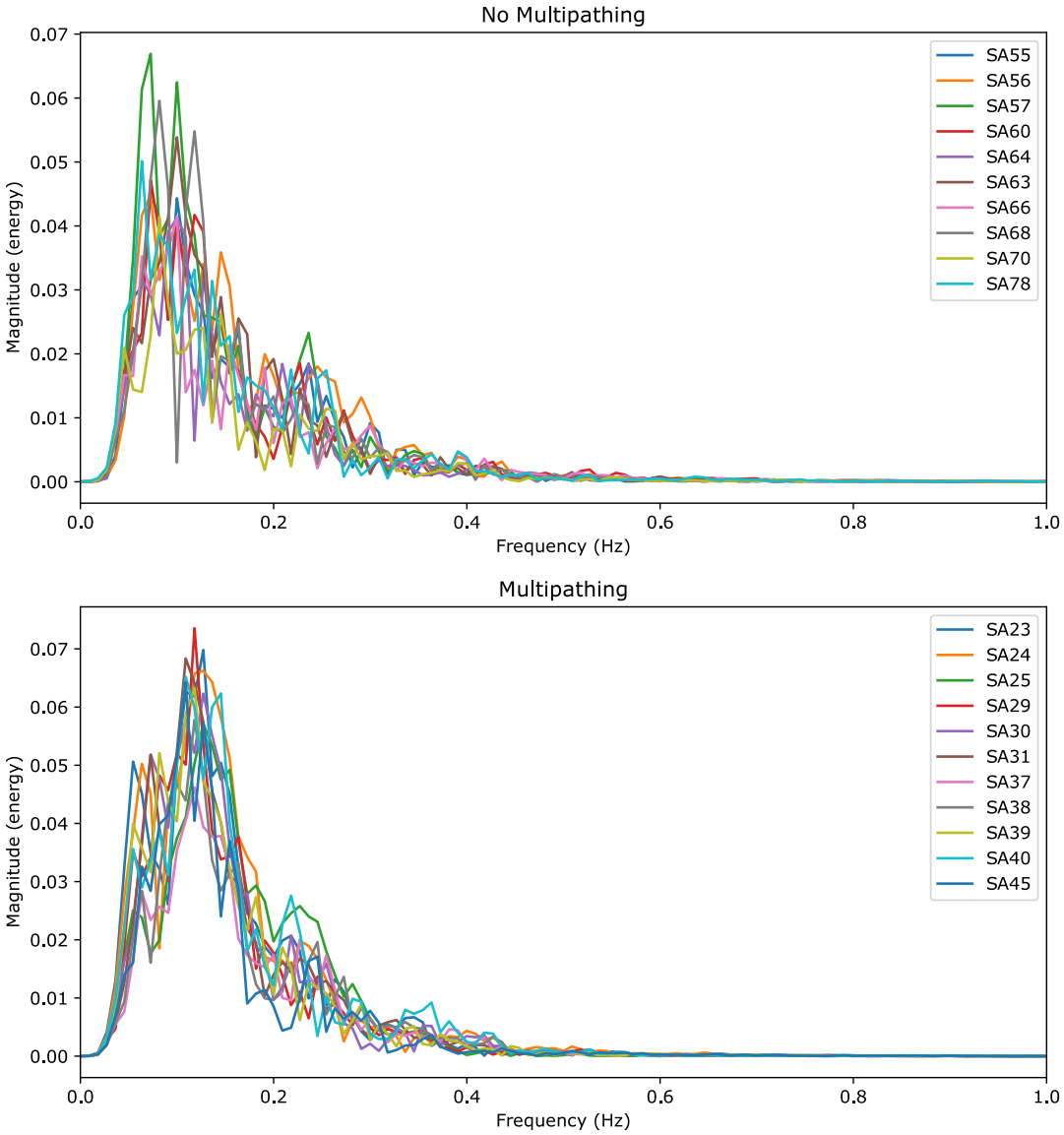

Figure A.13: Power spectra of waveforms recorded by several stations (shown in the legend) which show (top) no multipathing and (bottom) clear multipathing. Data used was recorded from the 25 May 1997 event. Power spectra were calculated using Welch's method Welch, 1967.

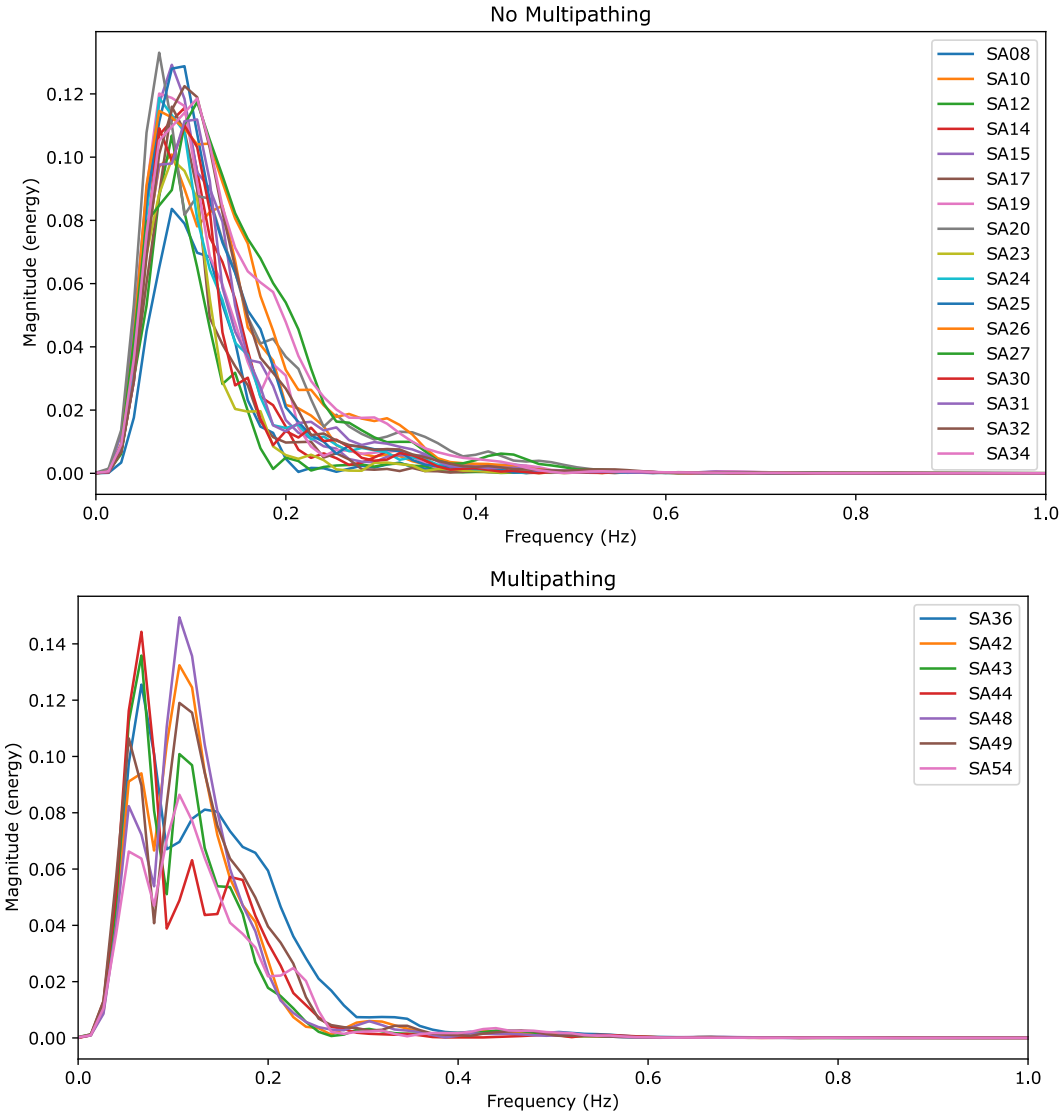

Figure A.14: Power spectra of waveforms recorded by several stations (shown in the legend) which show (top) no multipathing and (bottom) clear multipathing. Data used was recorded from the 05 April 1999 event. Power spectra were calculated using Welch's method Welch, 1967.

Dziewonski and Anderson, 1981 using SYNGINE Hutko et al., 2017; Krischer et al., 2017 only and only when not including SKS. Whenever SKS is included, SPdKS is not observed because of the lower amplitude it arrives with. Because of this, we interpret the second arrival in Figure 11 (in main document) as multipathing and not SPdKS.

In the $\theta - p$ plots using real data there is evidence for multipathing but not in the plots using data from model M3. The multipathed arrival location is different to that observed in the whole array observation suggesting a different structure was sampled. The observation in Figure A.15 uses a small subset of the waveforms recorded at the array, therefore is sensitive to a smaller area. As model M3 is based on the long-wavelength structure in tomography, the structure causing this multipathed arrival may not have been resolved.

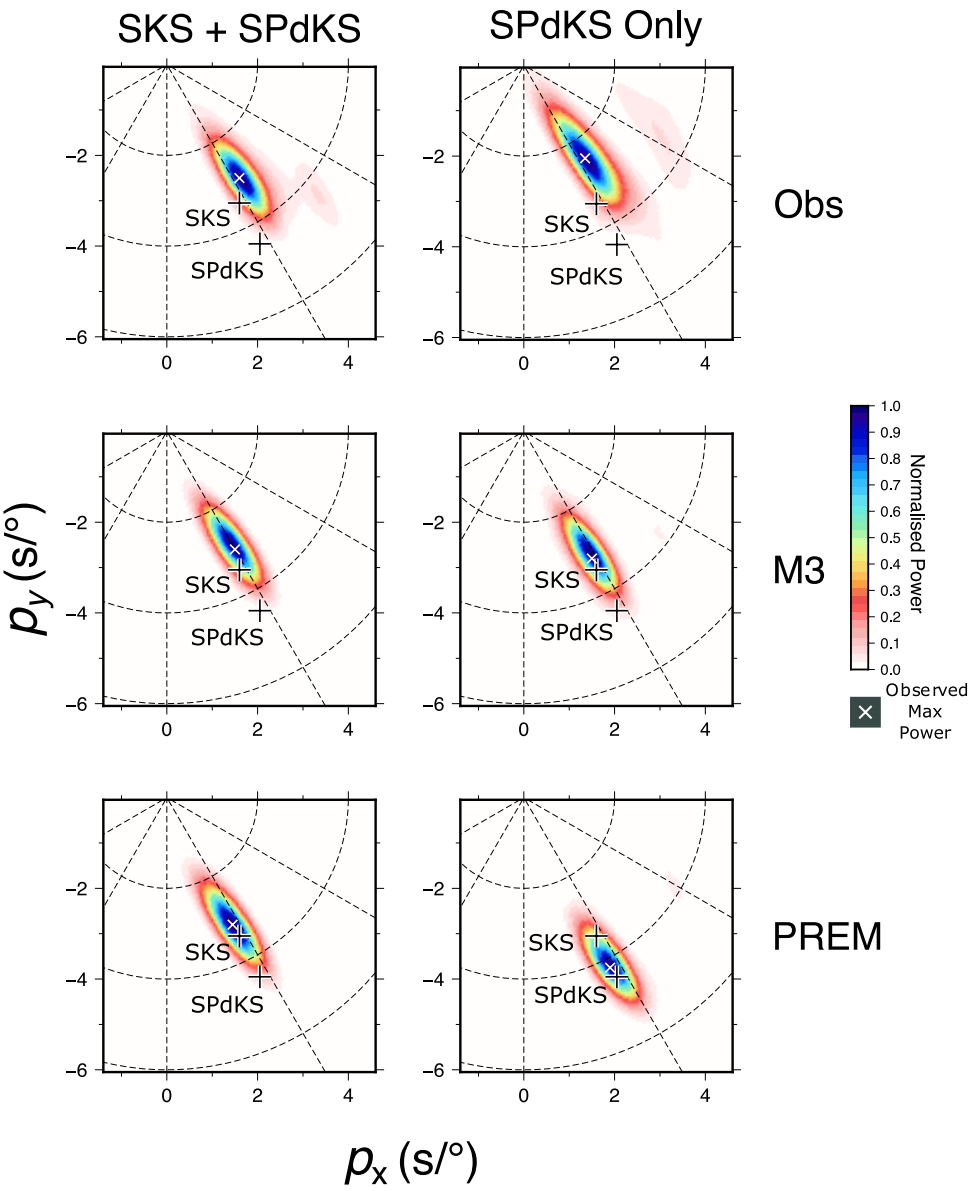

Figure A.15: A comparison of θ-p plots using the observed data (top row), synthetic data from model M3 (middle row) and PREM Dziewonski and Anderson, 1981. The waveforms used have epicentral distances larger than 119° because there is evidence for SPdKS in the waveforms (Figure 13 in main text). These use phase weighted stacking with degree 2.

A.8 Event Metadata Information for Chapter 2

```
date time evlo evla evdp
1997-04-23 19:44:29 144.941 13.9319 114.3
1997-05-03 16:45:55 -179.337 -31.6399 47.8
1997-05-12 13:45:26 121.712 10.2353 33.0
1997-05-21 14:10:28 169.23 -20.3924 69.0
1997-05-25 23:22:32 179.819 -32.1148 322.9
1997-05-29 17:02:38 -102.496 -35.9445 10.0
1997-06-10 21:53:55 -108.096 -35.7475 10.0
1997-06-24 23:04:53 127.934 -1.8877 41.5
1997-06-26 19:21:08 -114.652 -49.761 10.0
1997-07-09 19:24:10 -63.5453 10.5045 3.0
1997-07-20 10:14:19 -66.2225 -22.845 221.7
1997-07-21 23:19:38 -71.912 -30.3136 24.0
1997-07-25 06:47:02 -71.8801 -30.4795 37.05
1997-08-10 09:20:31 124.423 -16.0503 10.0
1997-09-02 12:13:23 -75.6984 3.8794 196.4
1997-09-03 06:22:43 -128.968 -55.267 10.0
1997-09-04 04:23:35 178.319 -26.4997 608.0
1997-09-12 14:09:03 -164.39 -63.1323 10.0
1997-09-15 13:05:44 126.589 8.0938 69.0
1997-09-17 14:50:36 126.61 2.0994 45.2
1997-09-20 16:11:29 -177.575 -28.7375 11.4
1997-09-26 15:48:34 128.984 -5.3669 253.6
1997-09-30 06:27:24 141.99 31.9763 4.7
1997-10-06 12:30:07 125.804 9.7616 124.0
1997-10-15 01:03:33 -71.139 -30.8907 54.1
1997-10-28 06:15:19 -76.6751 -4.3507 127.5
1997-11-10 23:06:43 140.477 31.1512 78.5
1997-11-15 18:59:25 167.344 -15.1272 129.3
1997-11-25 12:14:36 122.562 1.2086 46.3
1997-11-28 22:53:42 -68.7982 -13.772 599.8
1997-11-29 03:42:02 126.657 2.2238 50.9
1997-12-05 18:48:20 161.721 53.7222 16.7
1997-12-07 17:56:17 162.832 54.6374 22.0
1997-12-09 14:23:40 -68.3092 -20.2492 92.3
1997-12-11 07:56:29 -75.7653 3.9729 182.4
1997-12-22 02:05:51 147.838 -5.5589 190.0
1998-01-01 06:11:22 142.02 23.9404 91.3
```

```
1998-01-04 06:11:56 170.909 -22.2306 75.6
1998-01-10 04:54:25 -72.0638 -12.0264 33.0
1998-01-10 08:20:10 -91.5739 14.4023 70.5
1998-01-26 23:05:58 165.494 -47.354 12.0
1998-01-30 12:16:09 -70.1614 -23.838 44.16
1998-02-07 01:19:02 141.84 24.7801 556.1
1998-02-16 23:53:19 -33.6622 52.6815 10.0
1998-02-19 14:14:51 129.055 -4.507 38.6
1998-02-25 19:05:51 -35.2276 53.9275 10.0
1998-03-08 00:35:43 122.156 20.6077 170.1
1998-03-20 21:08:09 162.95 -50.0552 10.0
1998-03-21 16:33:12 2.5307 80.1089 10.0
1998-03-29 19:48:12 -178.99 -17.6585 499.6
1998-04-03 22:01:51 -74.9182 -8.0835 170.1
1998-05-06 01:53:11 120.938 18.8314 45.4
1998-05-21 05:34:23 119.566 0.1811 20.4
1998-05-23 17:44:46 123.788 8.1778 646.0
1998-07-09 14:45:34 -178.97 -30.4781 82.0
1998-07-16 11:56:36 166.173 -11.0892 109.5
1998-07-29 18:00:31 138.966 -2.7226 43.8
1998-08-04 18:59:22 -80.3153 -0.5539 46.6
1998-08-20 06:40:56 139.357 28.9326 442.8
1998-09-02 08:37:31 126.719 5.4038 67.3
1998-09-28 19:23:24 126.41 3.8321 45.1
1998-10-08 04:51:40 -71.3472 -16.0485 111.6
1998-10-28 16:25:04 125.957 0.8201 46.0
1998-11-08 07:25:49 121.45 -9.1338 46.9
1998-11-09 05:30:14 128.994 -6.9466 35.05
1998-11-25 18:05:25 158.663 -7.8883 43.1
1998-11-29 14:10:26 124.882 -1.9808 0.2
1998-12-06 00:47:14 126.272 1.2952 42.9
1998-12-14 19:35:26 167.315 -15.0776 144.2
1998-12-16 17:45:06 126.126 1.1145 51.8
1999-01-24 00:37:06 131.136 30.61 48.2
1999-01-25 18:19:18 -75.682 4.469 24.3
1999-02-22 01:00:32 169.651 -21.383 23.4
1999-02-23 07:27:58 119.483 0.145 50.4
1999-03-01 08:51:00 126.568 -2.925 33.0
1999-03-04 08:51:59 121.923 5.394 15.0
1999-03-05 00:33:41 -68.837 -20.337 62.7
```

```
1999-04-05 11:08:04 149.625 -5.632 152.4
1999-04-06 08:22:15 147.026 -6.532 47.8
1999-04-08 13:10:34 130.413 43.609 564.1
1999-04-13 10:38:39 -176.426 -21.435 85.3
1999-06-06 07:08:11 -90.913 13.927 86.5
1999-06-18 10:55:29 126.69 5.457 66.5
```

A.9 Fresnel Zone and Nyquist Criteria

The range of Fresnel zones for each frequency band along with the range of Nyquist criteria to avoid spatial aliasing in the method. The minimum inter-station spacing usable is approximately 80 km.

Frequency Band (Hz)	Fresnel Zone Range (km)	Nyquist Distance Range (km)
0.07 - 0.28	780 - 390	230 - 60
0.10 - 0.40	650 - 320	160 - 40
0.13 - 0.52	570 - 280	120 - 31
0.15 - 0.60	530 - 260	110 - 27
0.18 - 0.72	480 - 240	90 - 22
0.20 - 0.80	460 - 230	80 - 20

A.10 Example anisotropy correction

Figure A.16 gives an example of how removing anisotropy affects multipathing observations. Once anisotropy is removed, the multipathed arrivals align better and stack more coherently making them easier to observe. For observations with lower signal-noise ratios, correcting for anisotropy makes the observations worse or in some cases unusable.

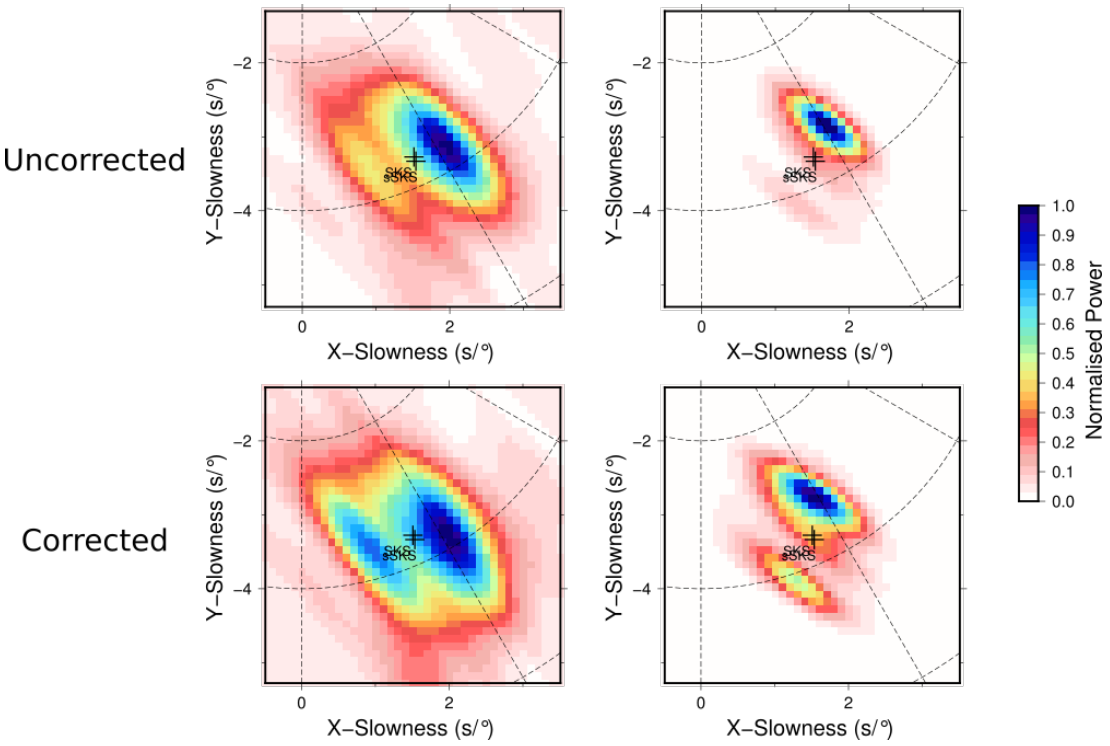

Figure A.16: Example θ-p plots showing how correcting for anisotropy affects multipathing observations. In this example we use data from the 25 May 1997 event recorded at the Kaapvaal array. Plots on the left use a linear stack only and the right hand plots use phase weighted stacking (Schimmel and Paulssen, 1997b).

References

Blandford, R. R. (1974). An automatic event detector at the Tonto Forest seismic observatory. *Geophysics*, *39*(5), 633–643.

Dziewonski, A. M., & Anderson, D. L. (1981). Preliminary reference Earth model. *Physics of the earth and planetary interiors*, *25*(4), 297–356.

Hutko, A. R., Bahavar, M., Trabant, C., Weekly, R. T., Fossen, M. V., & Ahern, T. (2017). Data products at the IRIS-DMC: Growth and usage. *Seismological Research Letters*, *88*(3), 892–903.

Krischer, L., Hutko, A. R., Van Driel, M., Stähler, S., Bahavar, M., Trabant, C., & Nissen-Meyer, T. (2017). On-demand custom broadband synthetic seismograms. *Seismological Research Letters*, *88*(4), 1127–1140.

Lucy, L. B. (1974). An iterative technique for the rectification of observed distributions. *The Astronomical Journal*, *79*, 745.

Richardson, W. H. (1972). Bayesian-based iterative method of image restoration. *JOSA*, *62*(1), 55–59.

Ritsema, J., Deuss, A. A., Van Heijst, H. J., & Woodhouse, J. H. (2011). S40RTS: a degree-40 shear-velocity model for the mantle from new Rayleigh wave dispersion, teleseismic traveltime and normal-mode splitting function measurements. *Geophysical Journal International*, *184*(3), 1223–1236.

Rost, S., & Thomas, C. (2002). Array seismology: Methods and applications. *Reviews of geophysics*, *40*(3).

Schimmel, M., & Paulssen, H. (1997a). Noise reduction and detection of weak, coherent signals through phase-weighted stacks. *Geophysical Journal International*, *130*(2), 497–505.

Schimmel, M., & Paulssen, H. (1997b). Noise reduction and detection of weak, coherent signals through phase-weighted stacks. *Geophysical Journal International*, *130*(2), 497–505.

Welch, P. (1967). The use of fast Fourier transform for the estimation of power spectra: a method based on time averaging over short, modified periodograms. *IEEE Transactions on audio and electroacoustics*, *15*(2), 70–73.

Appendix B

Supplementary material for Chapter 3

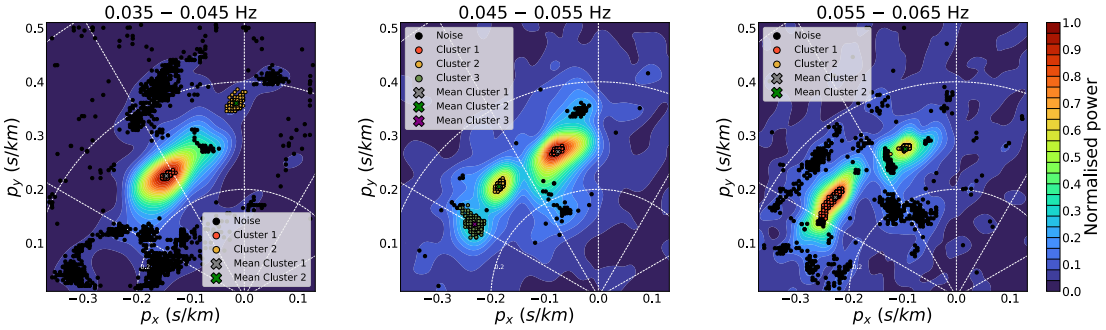

Figure B.1: Three results when using the automated method on Rayleigh wave data in three different frequency bands do investigate the effect of dispersion. Data is from the 05 January 2013 event recorded at the Southern California Seismic Array (CI).

Appendix C

Supplementary material for Chapter 4

The following subsections show the depth slices for slowness vector and multipathing observations. They are presented in order of frequency band.

C.0.1 Europe

C.0.2 0.10 – 0.20 Hz band

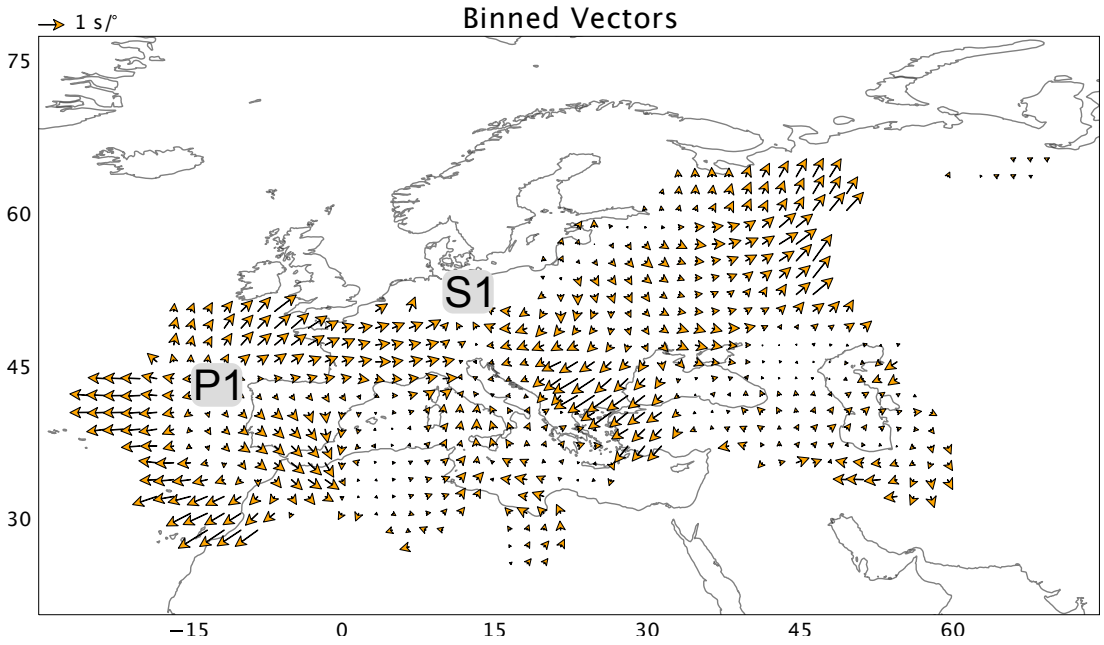

Figure C.1: Map of slowness vector bins in the 0.10 – 0.20 Hz frequency band using pierce points at 2891 km depth beneath Europe. The bins have a radius of 200km with a spacing of 100 km.

C.0.3 0.15 – 0.30 Hz band

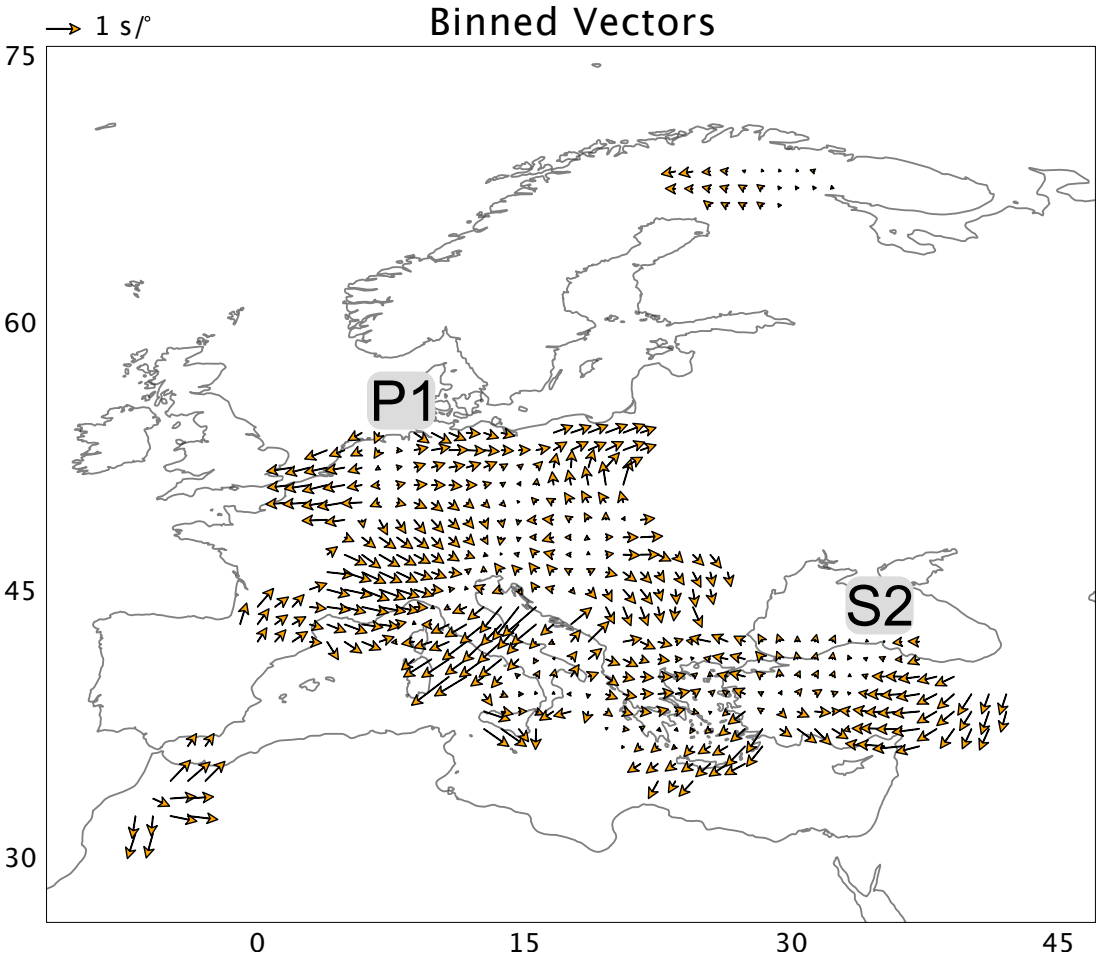

Figure C.2: Map of slowness vector bins in the 0.15 – 0.30 Hz frequency band using pierce points at 500 km depth beneath Europe. The bins have a radius of 200km with a spacing of 100 km.

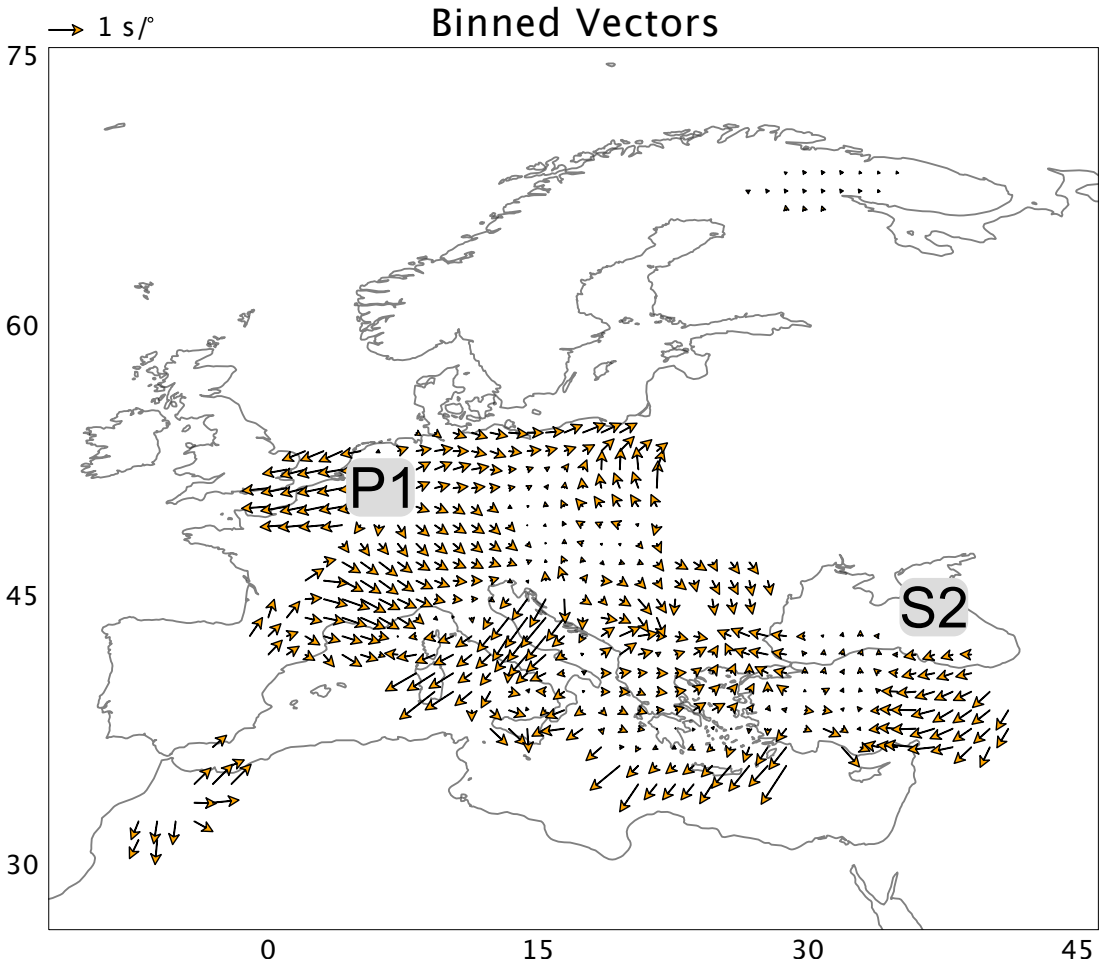

Figure C.3: Map of slowness vector bins in the 0.15 – 0.30 Hz frequency band using pierce points at 800 km depth beneath Europe. The bins have a radius of 200km with a spacing of 100 km.

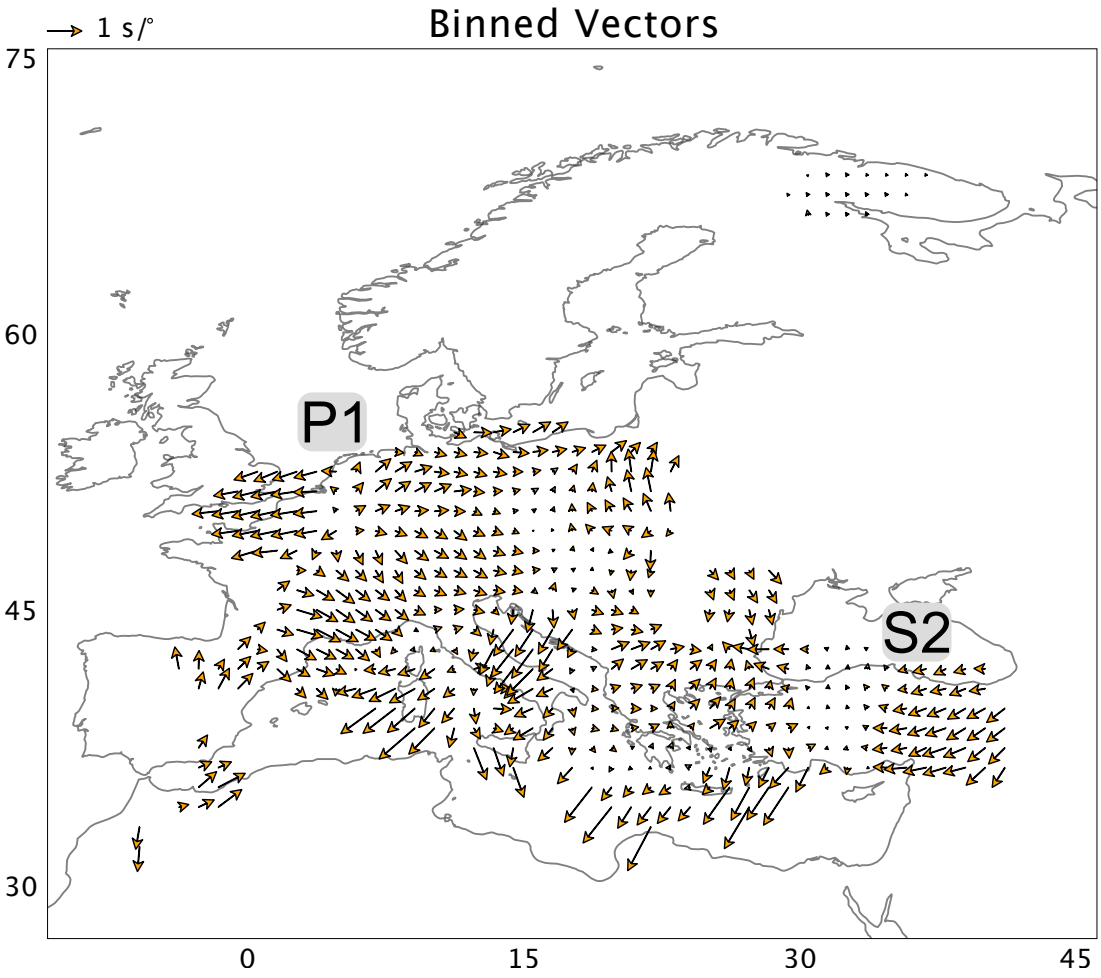

Figure C.4: Map of slowness vector bins in the 0.15 – 0.30 Hz frequency band using pierce points at 1000 km depth beneath Europe. The bins have a radius of 200km with a spacing of 100 km.

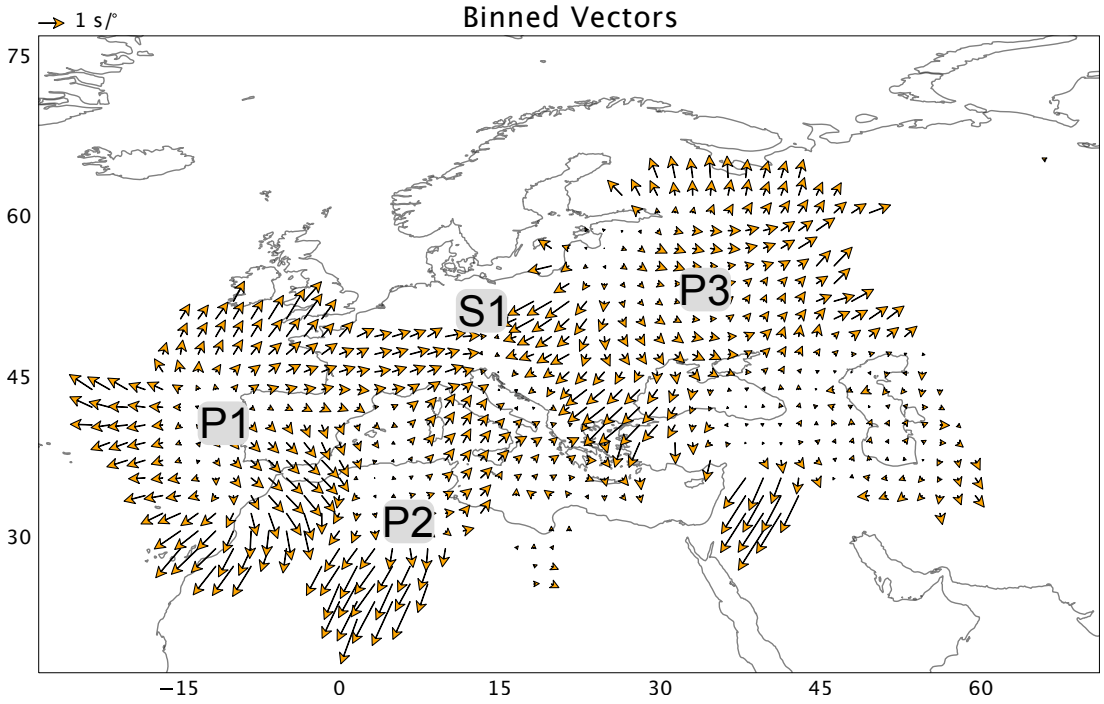

Figure C.5: Map of slowness vector bins in the 0.15 – 0.30 Hz frequency band using pierce points at 2891 km depth beneath Europe. The bins have a radius of 200km with a spacing of 100 km.

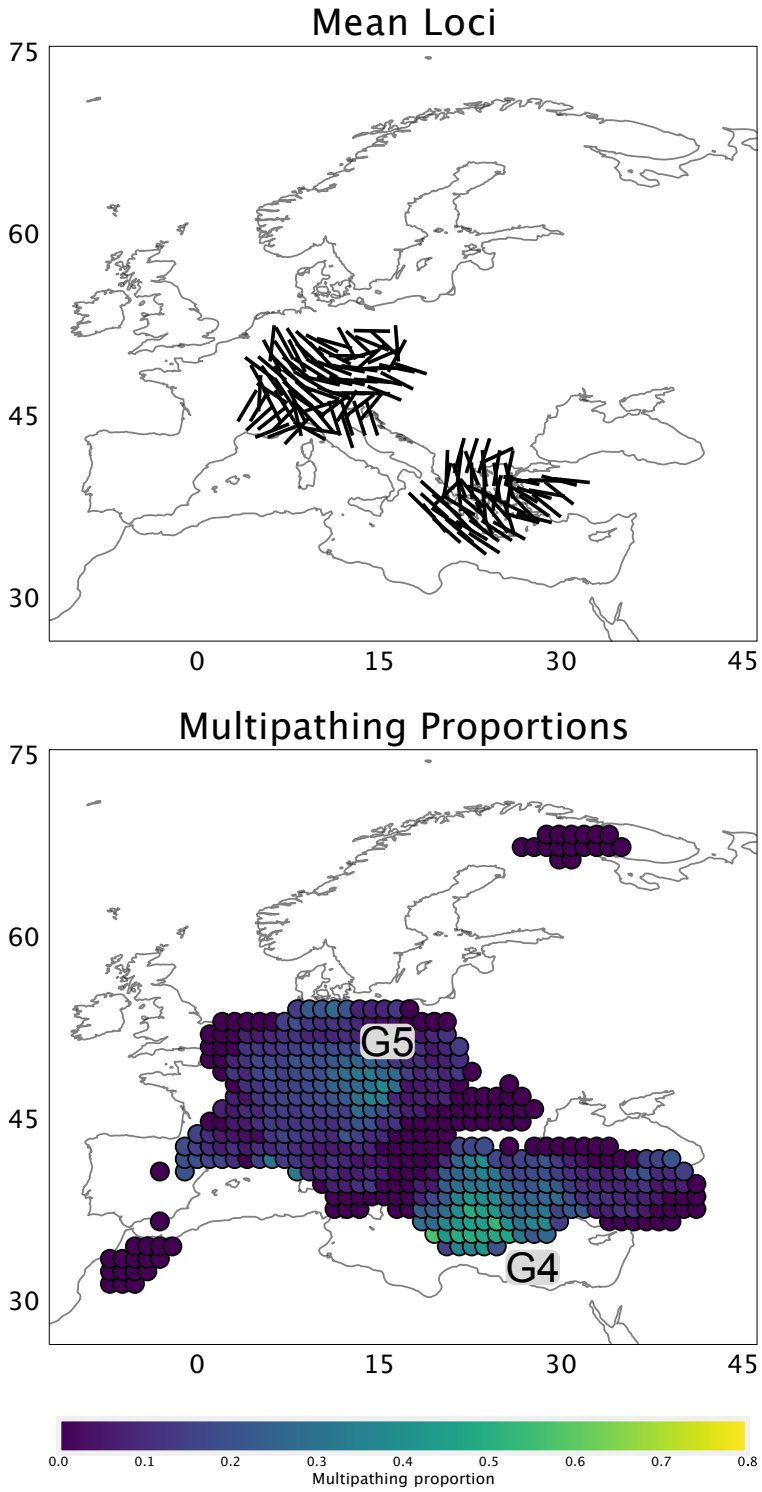

Figure C.6: Figure summarising multipathing observations using data in the 0.15 – 0.30 Hz frequency band and pierce points at 800 km depth. The top figure shows the mean loci in bins of 200 km radius in increments of 100 km. The bottom figure shows the proportion of multipathing relative to the total number of observations in the bin. Bins for the multipathing proportion measurements are 200 km radius spaced with increments of 100 km.

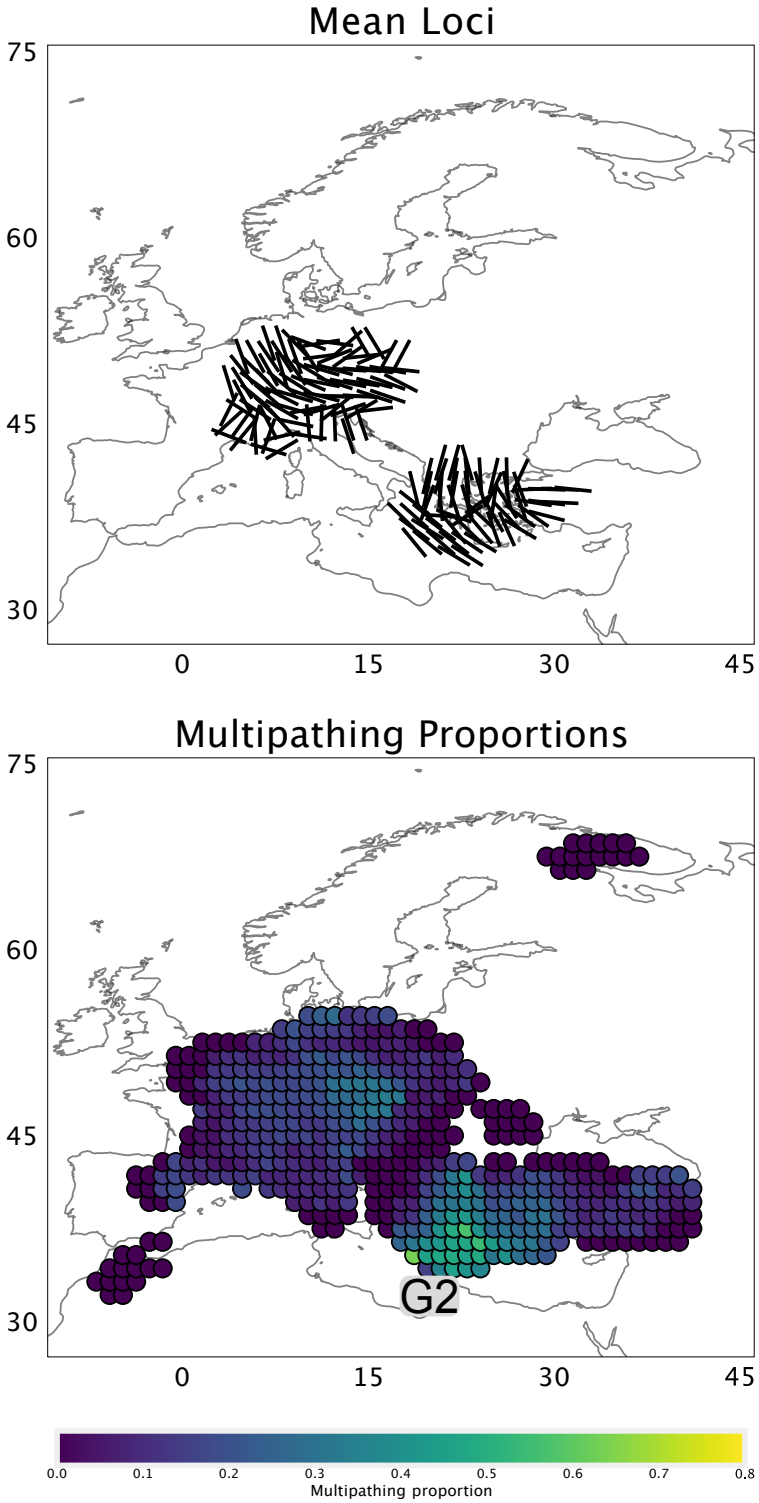

Figure C.7: Figure summarising multipathing observations using data in the 0.15 – 0.30 Hz frequency band and pierce points at 1000 km depth. The top figure shows the mean loci in bins of 200 km radius in increments of 100 km. The bottom figure shows the proportion of multipathing relative to the total number of observations in the bin. Bins for the multipathing proportion measurements are 200 km radius spaced with increments of 100 km.

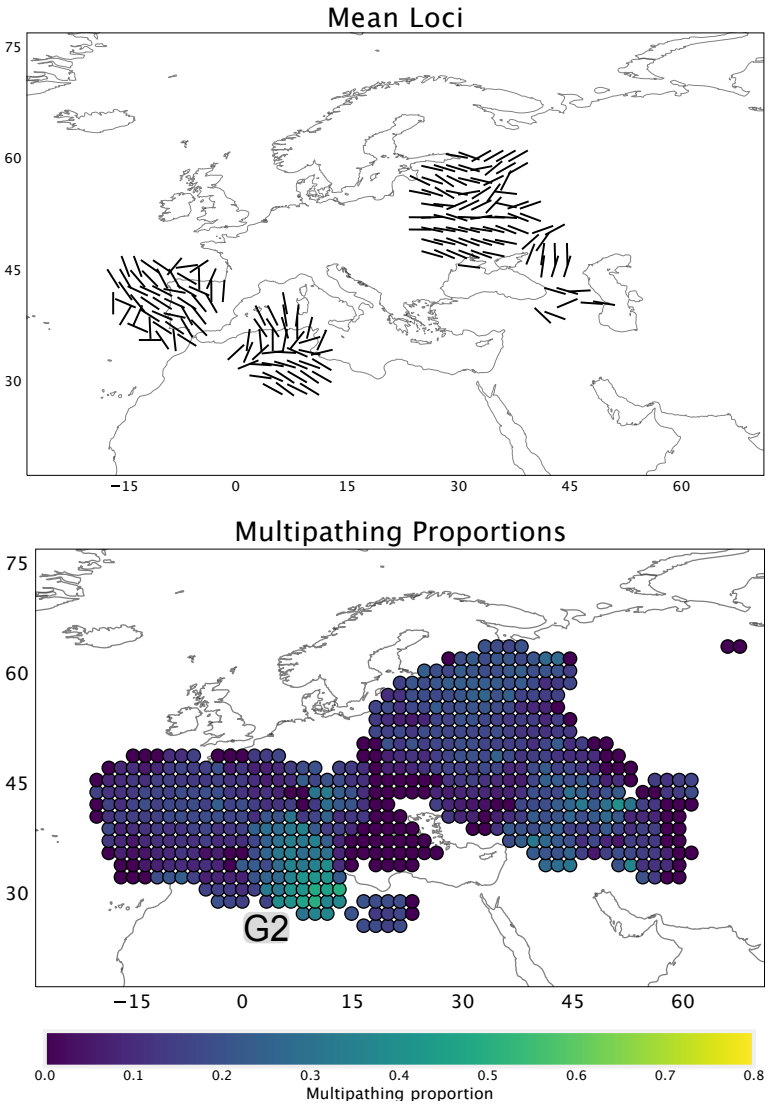

Figure C.8: Figure summarising multipathing observations using data in the 0.15 – 0.30 Hz frequency band and pierce points at 2891 km depth. The top figure shows the mean loci in bins of 200 km radius in increments of 100 km. The bottom figure shows the proportion of multipathing relative to the total number of observations in the bin. Bins for the multipathing proportion measurements are 200 km radius spaced with increments of 100 km.

C.0.4 0.20 – 0.40 Hz band

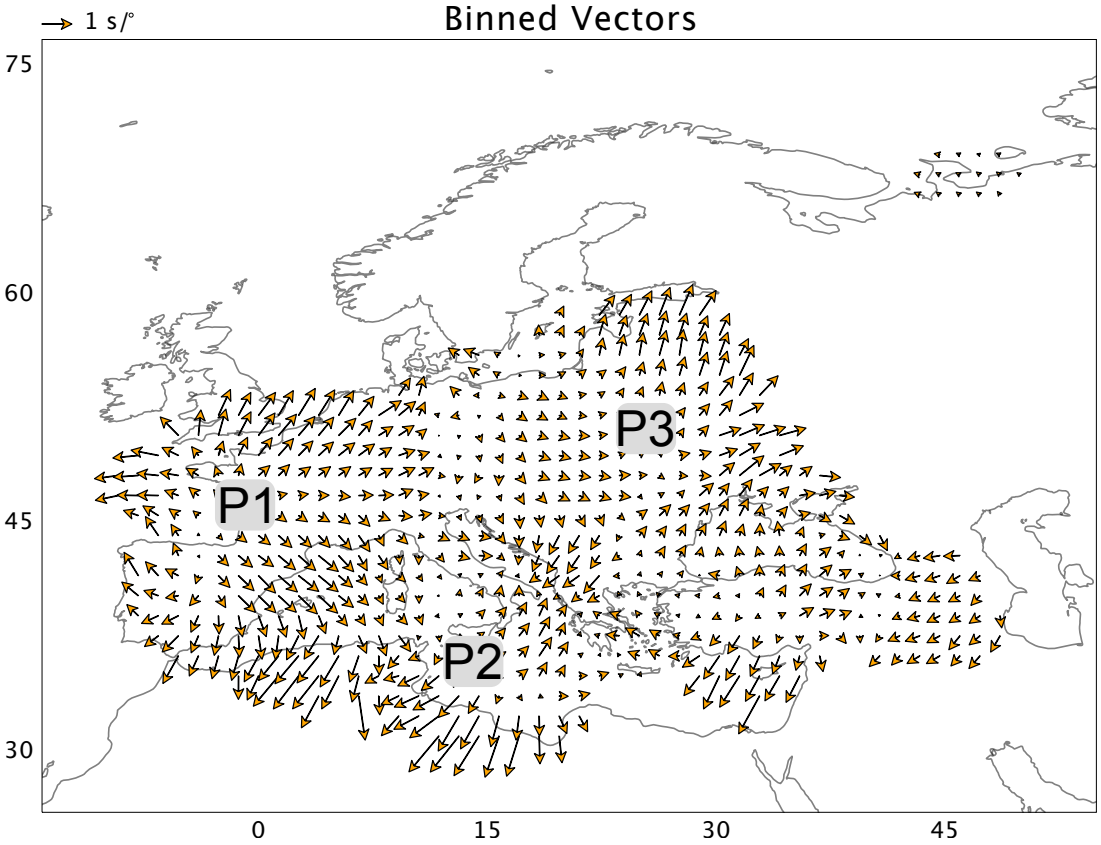

Figure C.9: Map of slowness vector bins in the 0.20 – 0.40 Hz frequency band using pierce points at 2000 km depth beneath Europe. The bins have a radius of 200km with a spacing of 100 km.

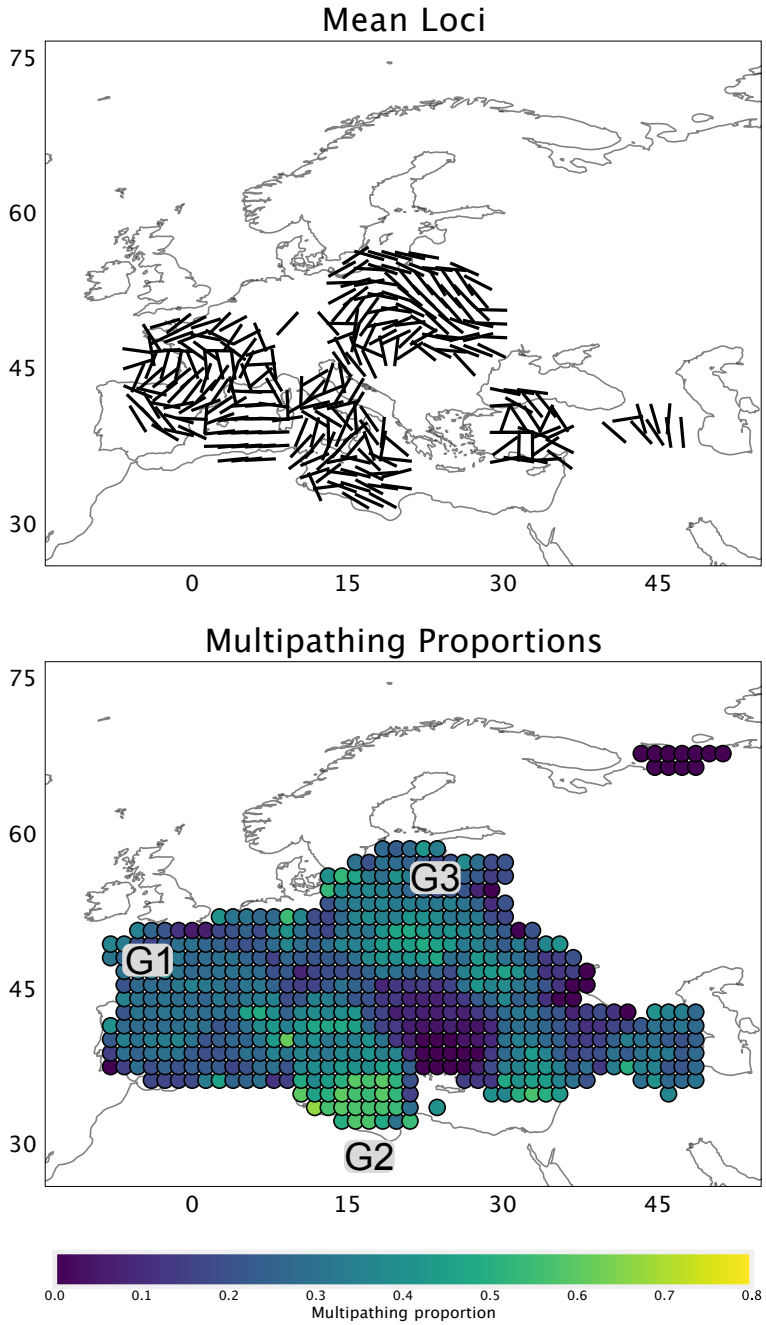

Figure C.10: Figure summarising multipathing observations using data in the 0.20 – 0.40 Hz frequency band and pierce points at 2000 km depth. The top figure shows the mean loci in bins of 200 km radius in increments of 100 km. The bottom figure shows the proportion of multipathing relative to the total number of observations in the bin. Bins for the multipathing proportion measurements are 200 km radius spaced with increments of 100 km.

C.0.5 North America

C.0.6 0.10 – 0.20 Hz band

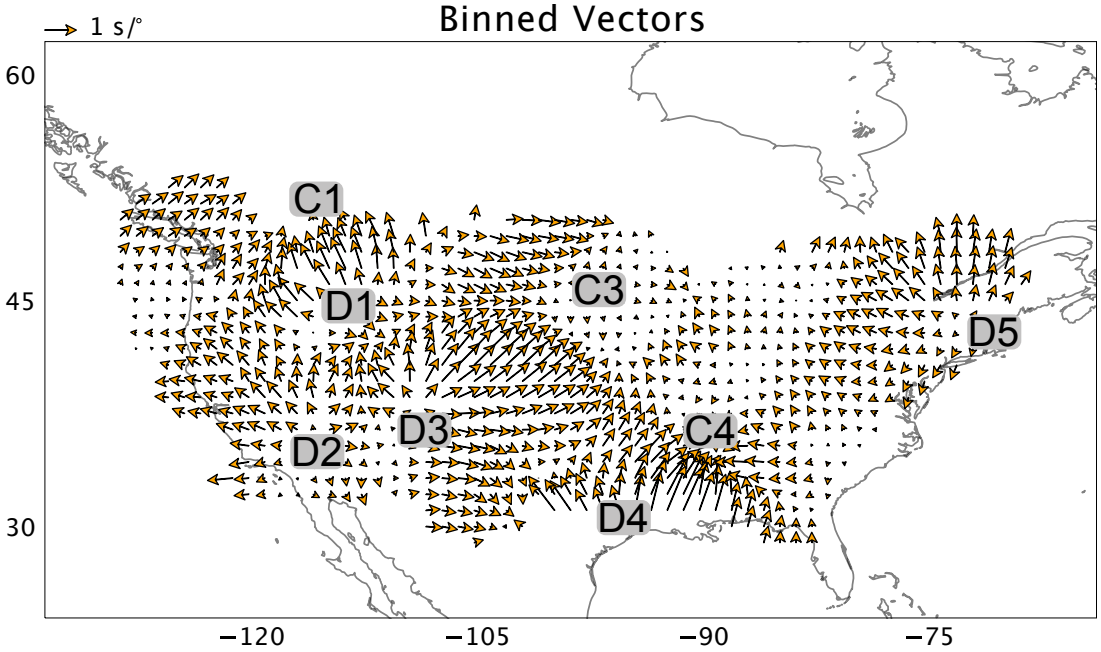

Figure C.11: Map of slowness vector bins in the 0.10 – 0.20 Hz frequency band using pierce points at 1000 km depth beneath the US. The bins have a radius of 200km with a spacing of 100 km.

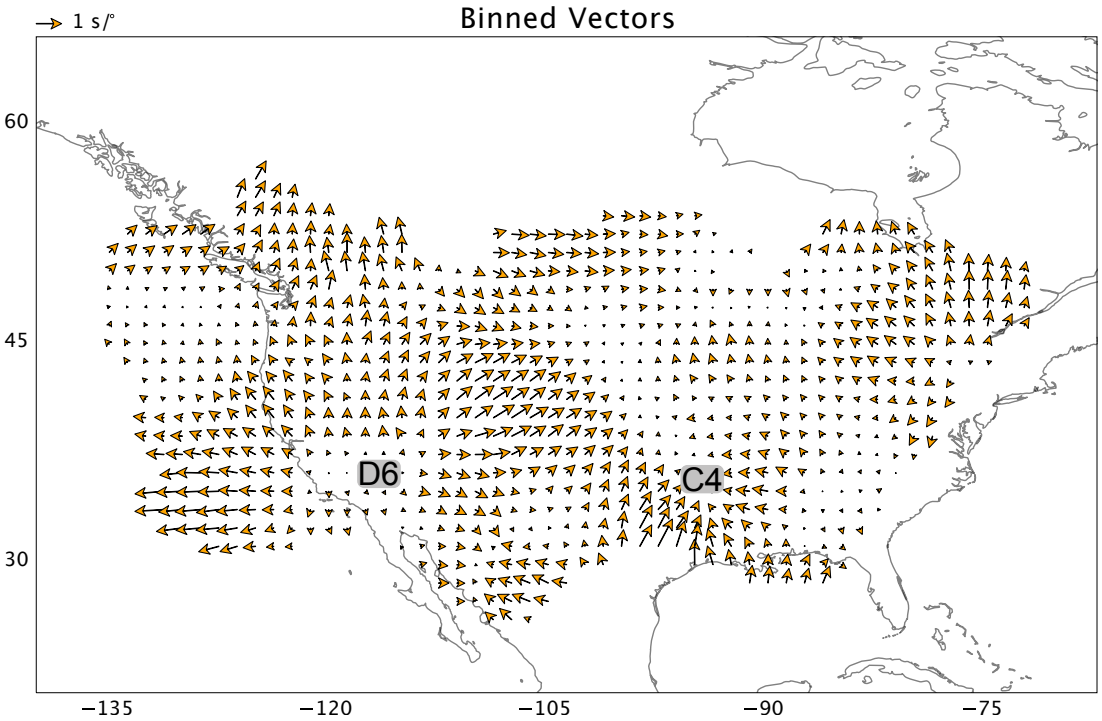

Figure C.12: Map of slowness vector bins in the 0.10 – 0.20 Hz frequency band using pierce points at 1800 km depth beneath the US. The bins have a radius of 200km with a spacing of 100 km.

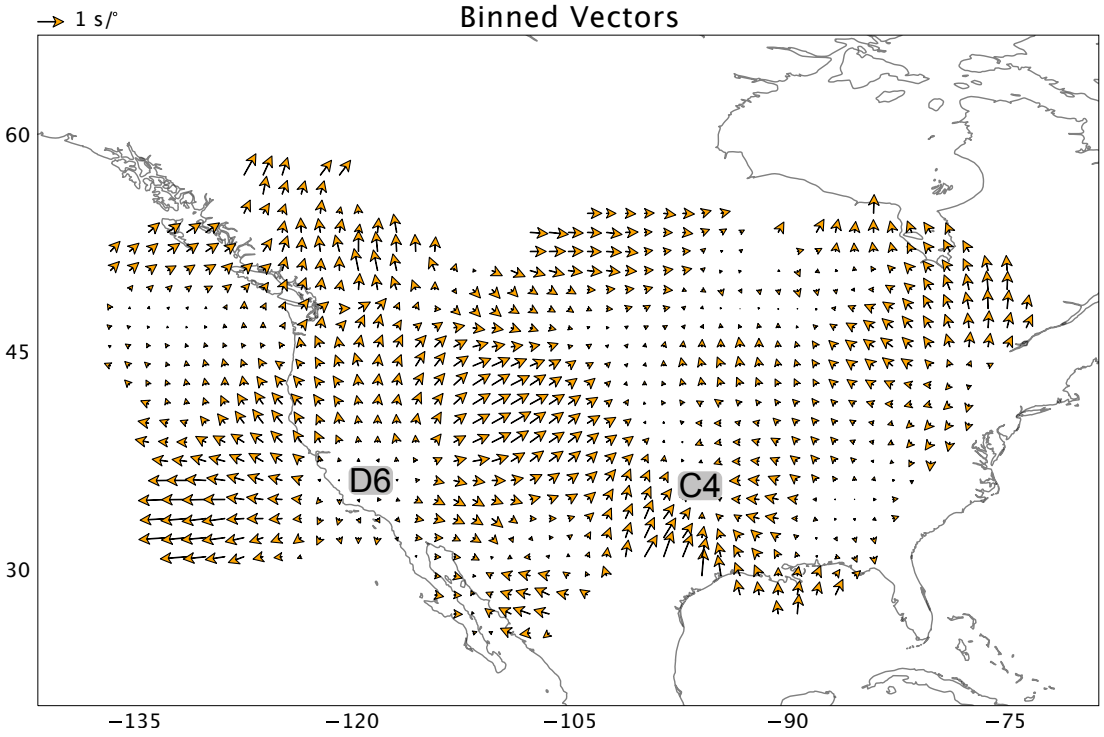

Figure C.13: Map of slowness vector bins in the 0.10 – 0.20 Hz frequency band using pierce points at 2000 km depth beneath the US. The bins have a radius of 200km with a spacing of 100 km.

C.0.7 0.15 – 0.30 Hz band

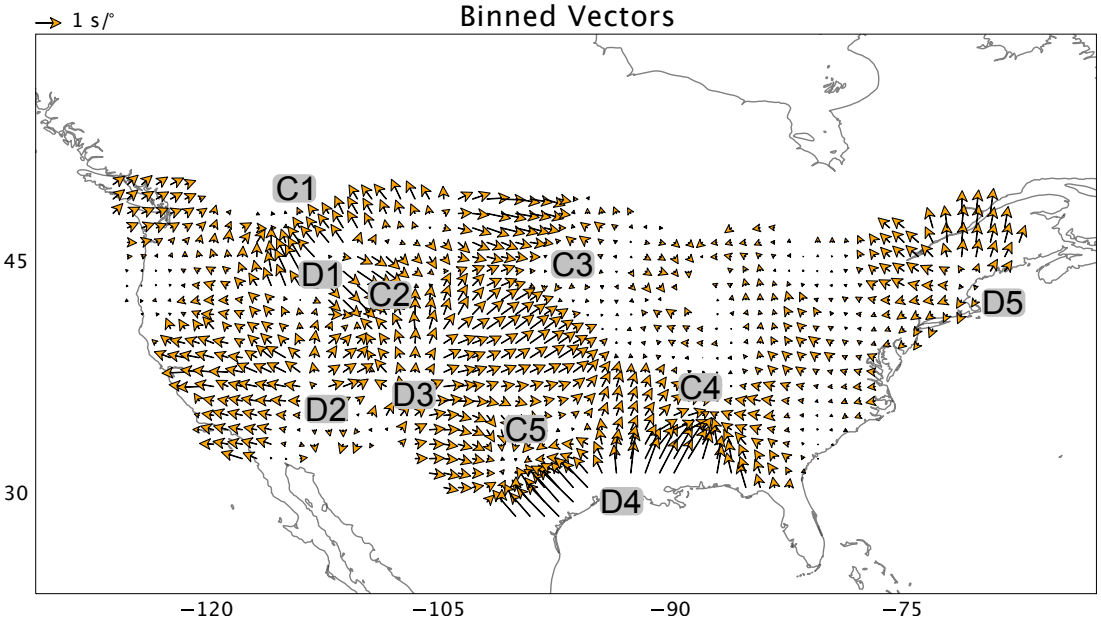

Figure C.14: Map of slowness vector bins in the 0.15 – 0.30 Hz frequency band using pierce points at 200 km depth beneath the US. The bins have a radius of 200km with a spacing of 100 km.

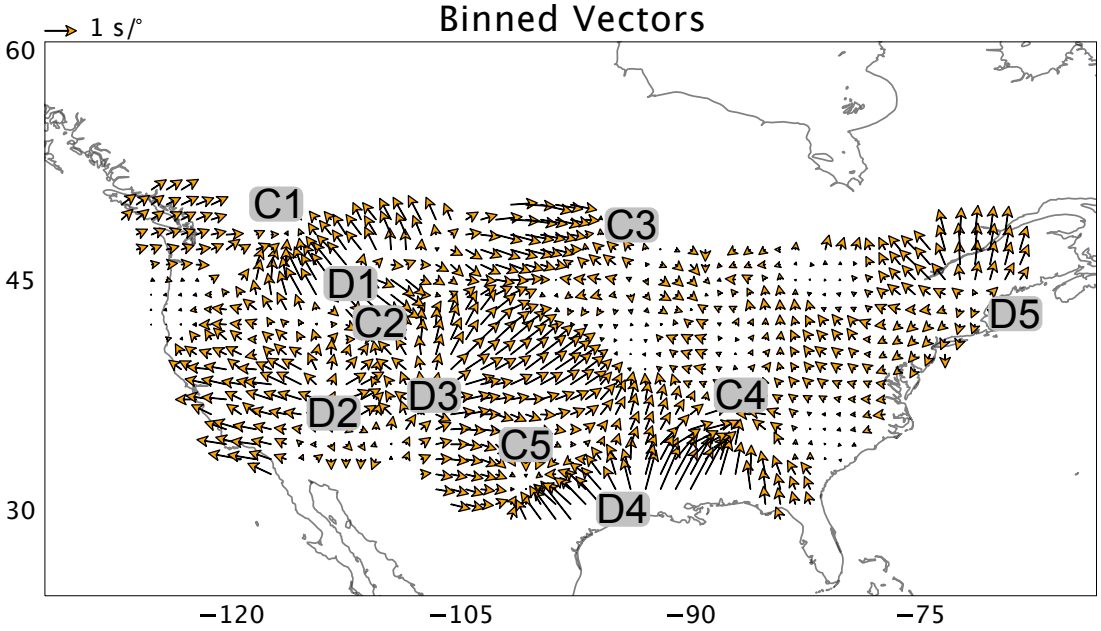

Figure C.15: Map of slowness vector bins in the 0.15 – 0.30 Hz frequency band using pierce points at 500 km depth beneath the US. The bins have a radius of 200km with a spacing of 100 km.

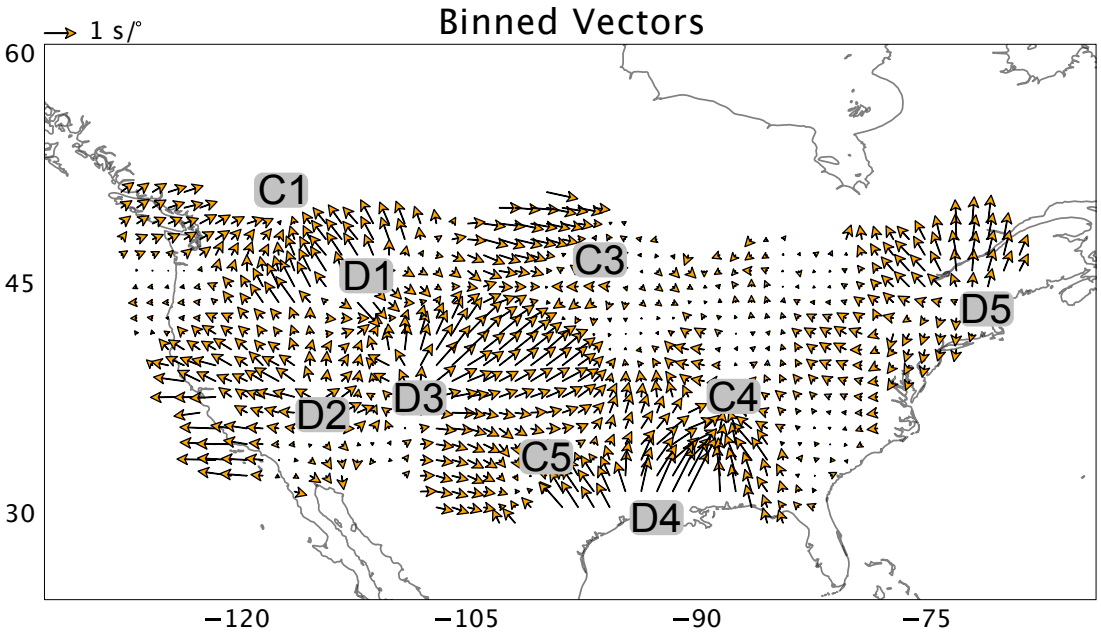

Figure C.16: Map of slowness vector bins in the 0.15 – 0.30 Hz frequency band using pierce points at 800 km depth beneath the US. The bins have a radius of 200km with a spacing of 100 km.

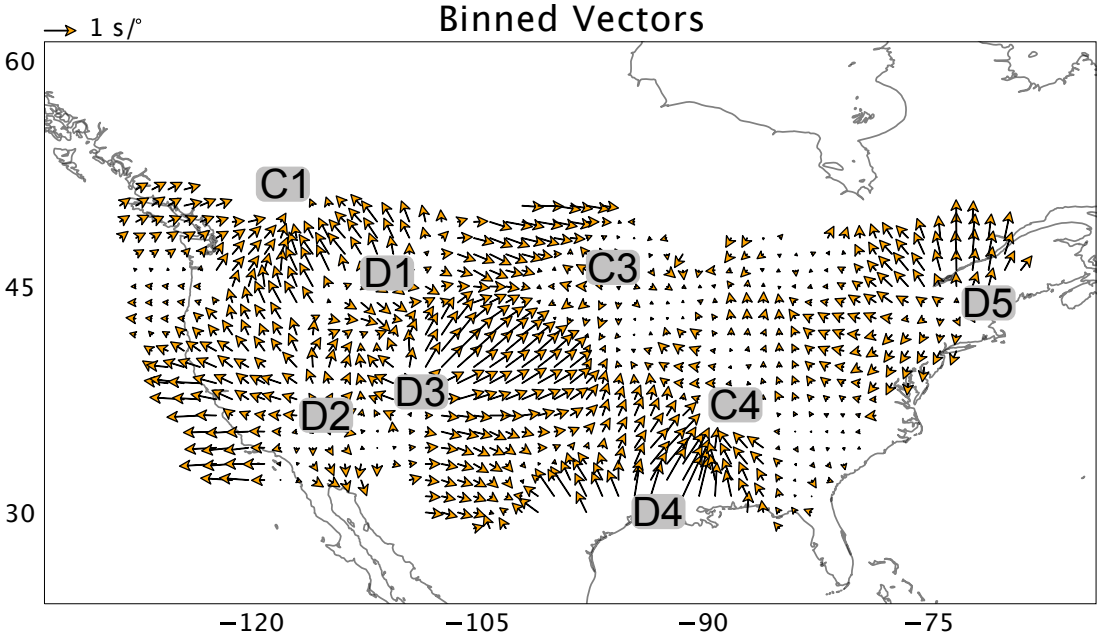

Figure C.17: Map of slowness vector bins in the 0.15 – 0.30 Hz frequency band using pierce points at 1000 km depth beneath the US. The bins have a radius of 200km with a spacing of 100 km.

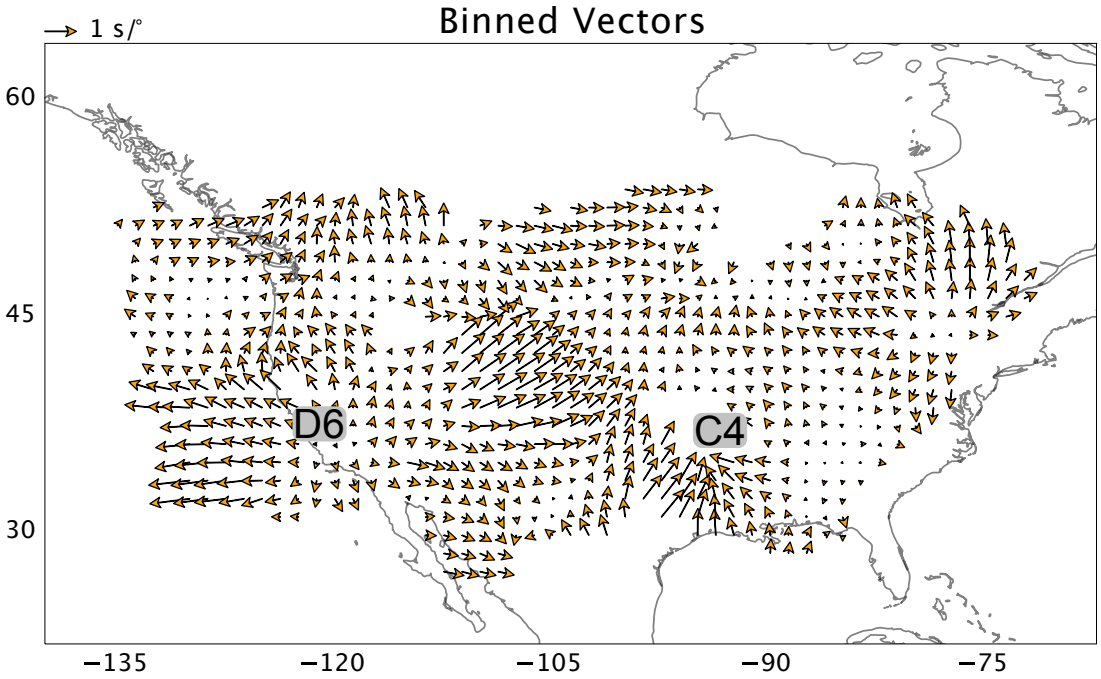

Figure C.18: Map of slowness vector bins in the 0.15 – 0.30 Hz frequency band using pierce points at 1800 km depth beneath the US. The bins have a radius of 200km with a spacing of 100 km.

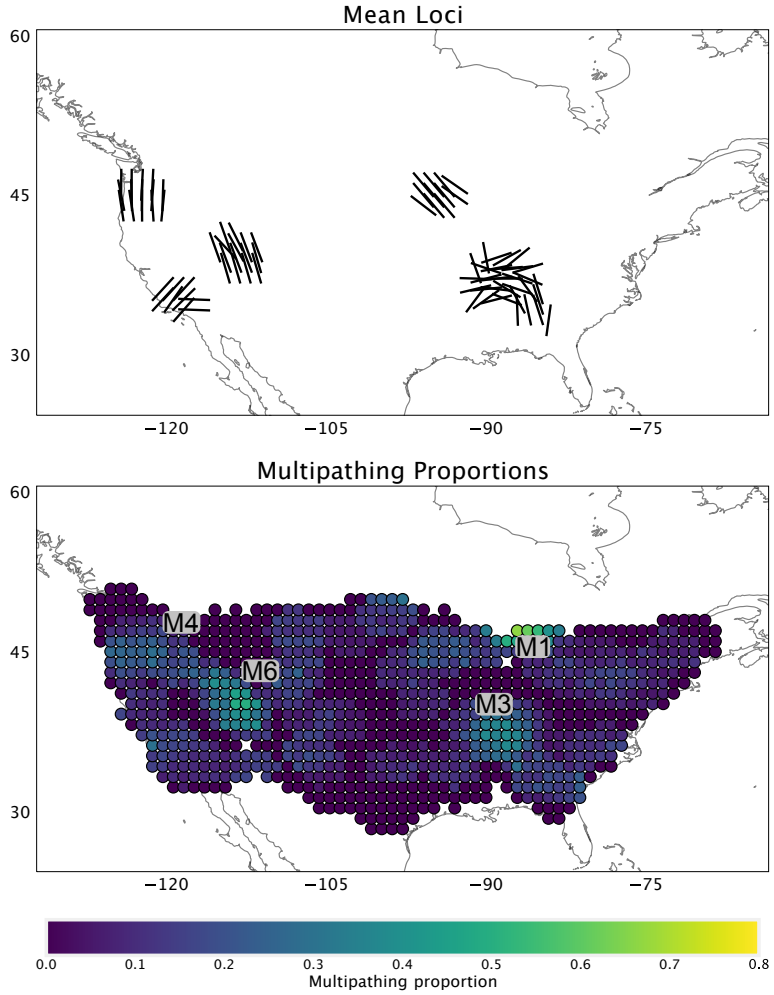

Figure C.19: Figure summarising multipathing observations using data in the 0.15 – 0.30 Hz frequency band and pierce points at 500 km depth. The top figure shows the mean loci in bins of 200 km radius in increments of 100 km. The bottom figure shows the proportion of multipathing relative to the total number of observations in the bin. Bins for the multipathing proportion measurements are 200 km radius spaced with increments of 100 km.

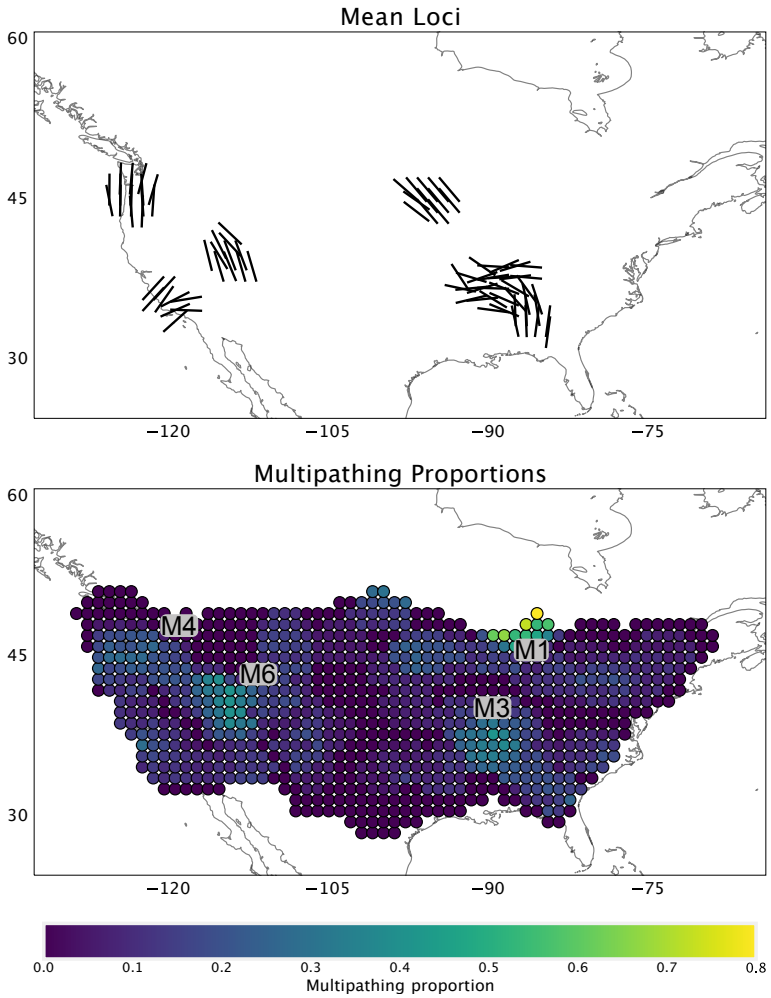

Figure C.20: Figure summarising multipathing observations using data in the 0.15 – 0.30 Hz frequency band and pierce points at 800 km depth. The top figure shows the mean loci in bins of 200 km radius in increments of 100 km. The bottom figure shows the proportion of multipathing relative to the total number of observations in the bin. Bins for the multipathing proportion measurements are 200 km radius spaced with increments of 100 km.

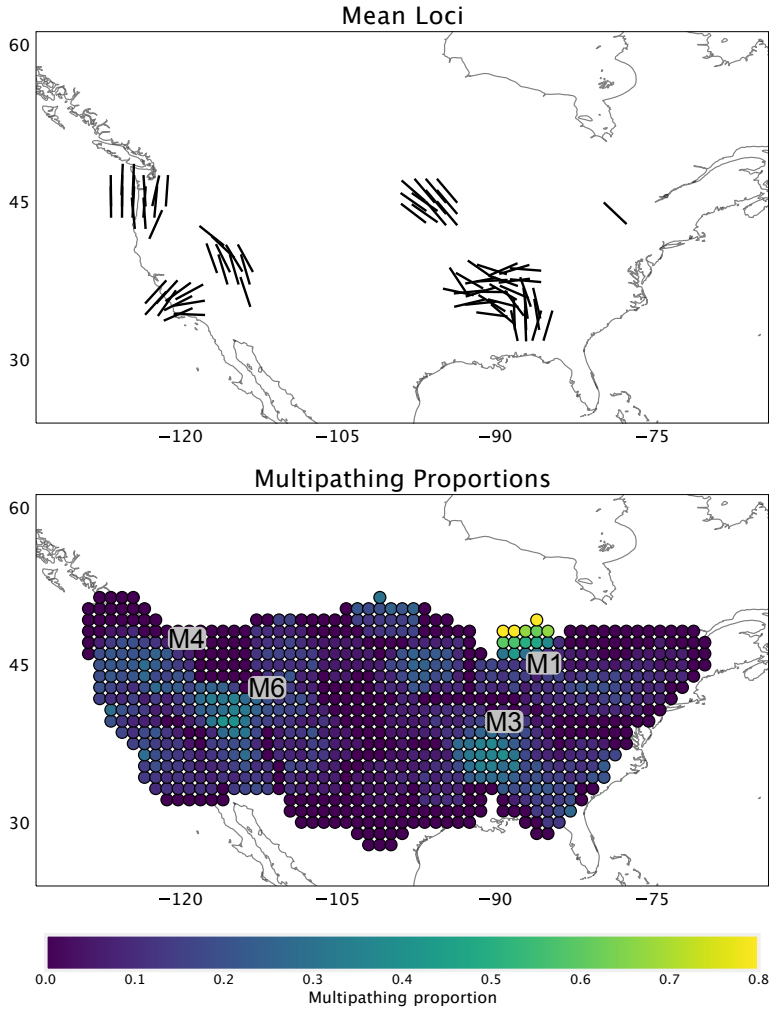

Figure C.21: Figure summarising multipathing observations using data in the 0.15 – 0.30 Hz frequency band and pierce points at 1000 km depth. The top figure shows the mean loci in bins of 200 km radius in increments of 100 km. The bottom figure shows the proportion of multipathing relative to the total number of observations in the bin. Bins for the multipathing proportion measurements are 200 km radius spaced with increments of 100 km.

C.0.8 0.20 – 0.40 Hz band

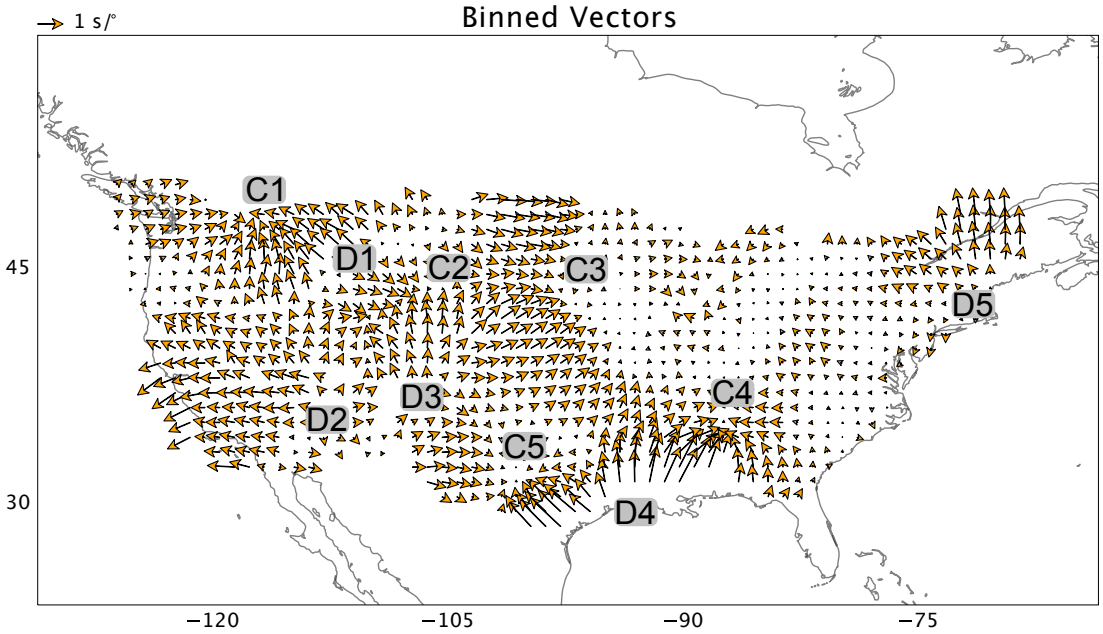

Figure C.22: Map of slowness vector bins in the 0.20 – 0.40 Hz frequency band using pierce points at 300 km depth beneath the US. The bins have a radius of 200km with a spacing of 100 km.

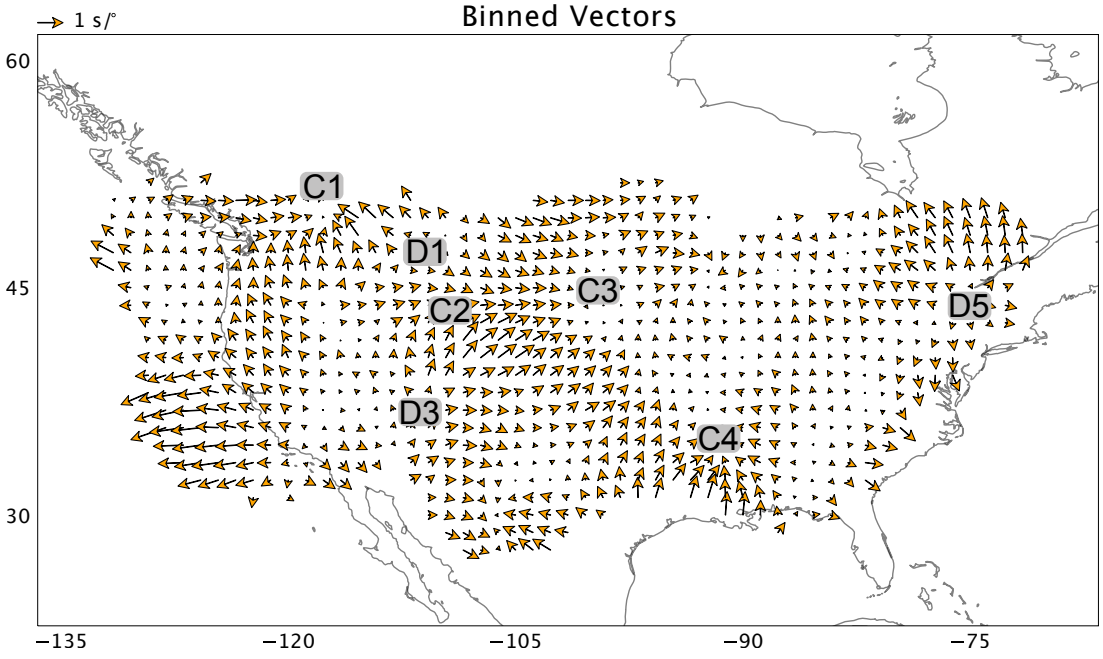

Figure C.23: Map of slowness vector bins in the 0.20 – 0.40 Hz frequency band using pierce points at 1400 km depth beneath the US. The bins have a radius of 200km with a spacing of 100 km.

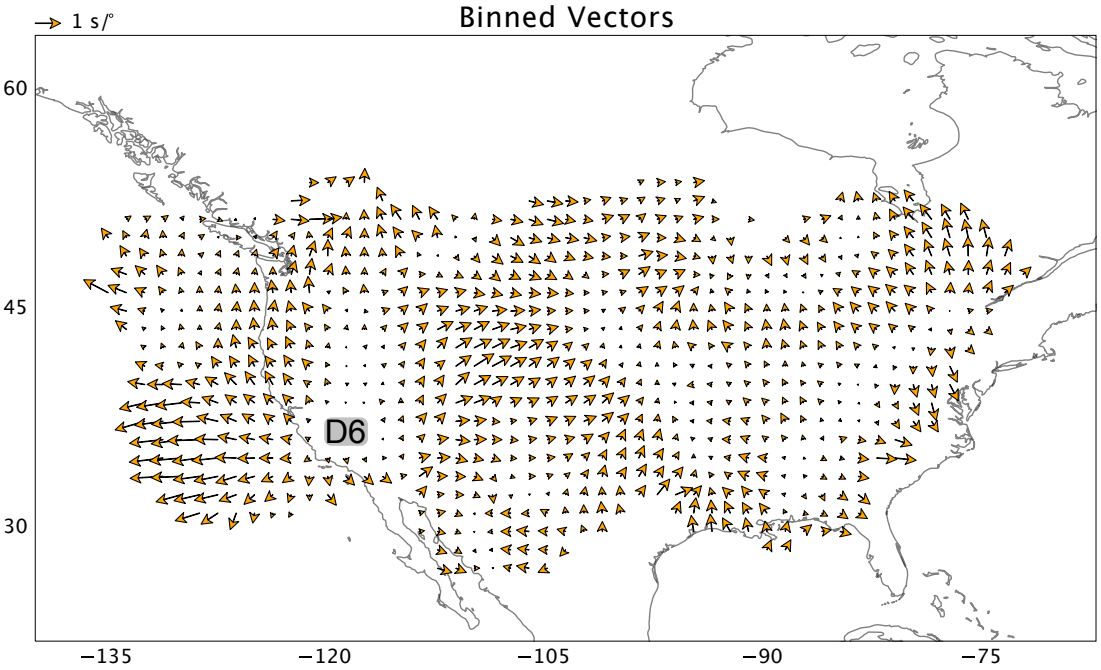

Figure C.24: Map of slowness vector bins in the 0.20 – 0.40 Hz frequency band using pierce points at 1800 km depth beneath the US. The bins have a radius of 200km with a spacing of 100 km.

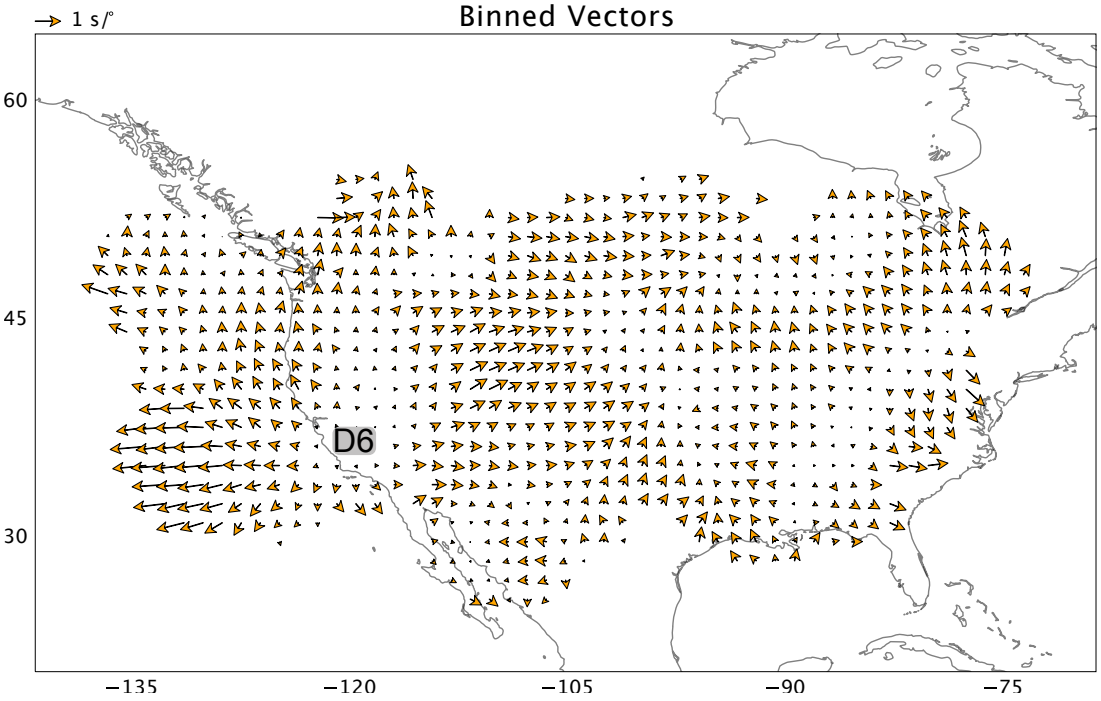

Figure C.25: Map of slowness vector bins in the 0.20 – 0.40 Hz frequency band using pierce points at 2000 km depth beneath the US. The bins have a radius of 200km with a spacing of 100 km.

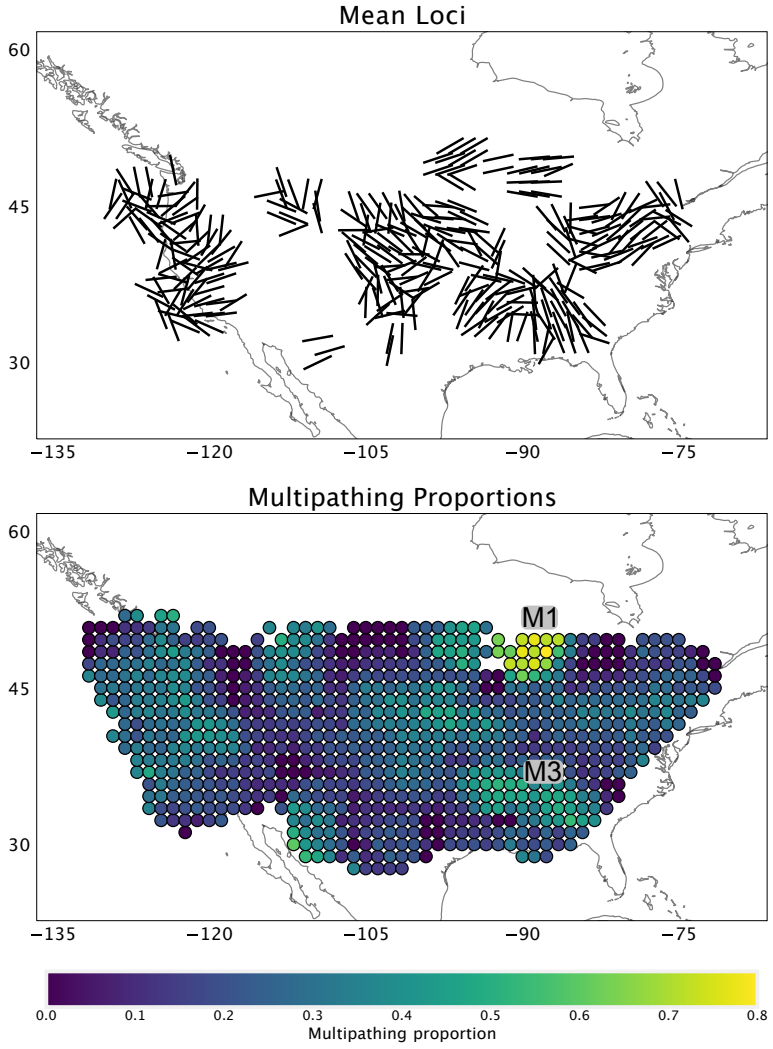

Figure C.26: Figure summarising multipathing observations using data in the 0.20 – 0.40 Hz frequency band and pierce points at 1400 km depth. The top figure shows the mean loci in bins of 200 km radius in increments of 100 km. The bottom figure shows the proportion of multipathing relative to the total number of observations in the bin. Bins for the multipathing proportion measurements are 200 km radius spaced with increments of 100 km.

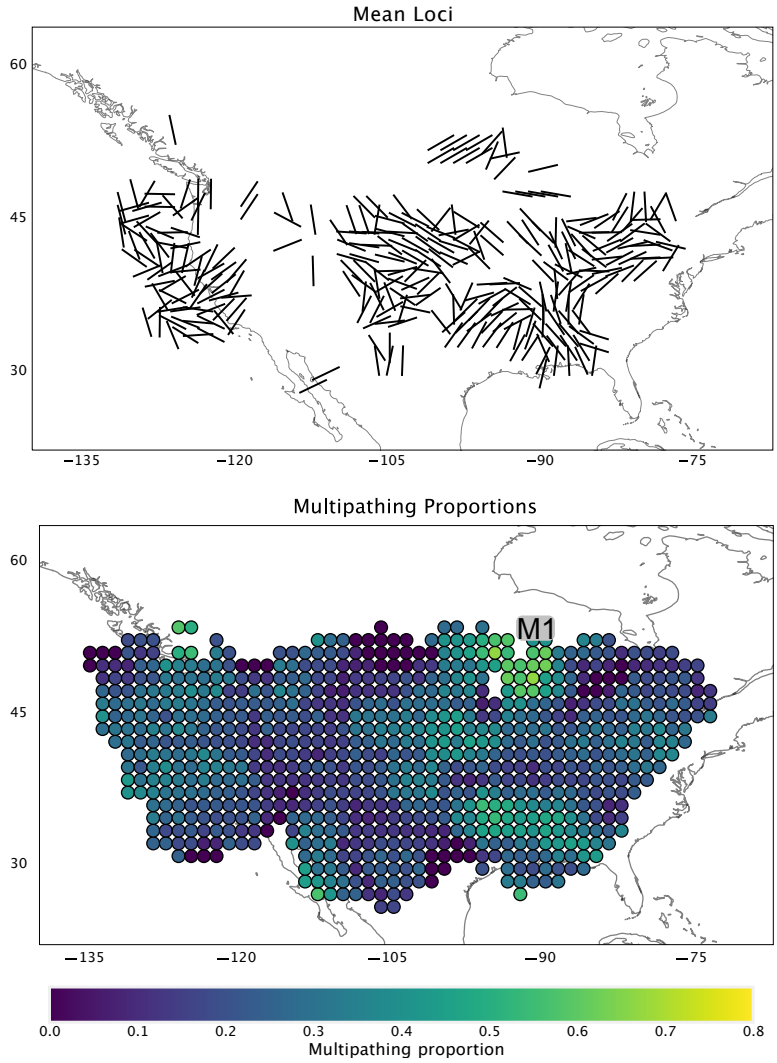

Figure C.27: Figure summarising multipathing observations using data in the 0.20 – 0.40 Hz frequency band and pierce points at 1800 km depth. The top figure shows the mean loci in bins of 200 km radius in increments of 100 km. The bottom figure shows the proportion of multipathing relative to the total number of observations in the bin. Bins for the multipathing proportion measurements are 200 km radius spaced with increments of 100 km.

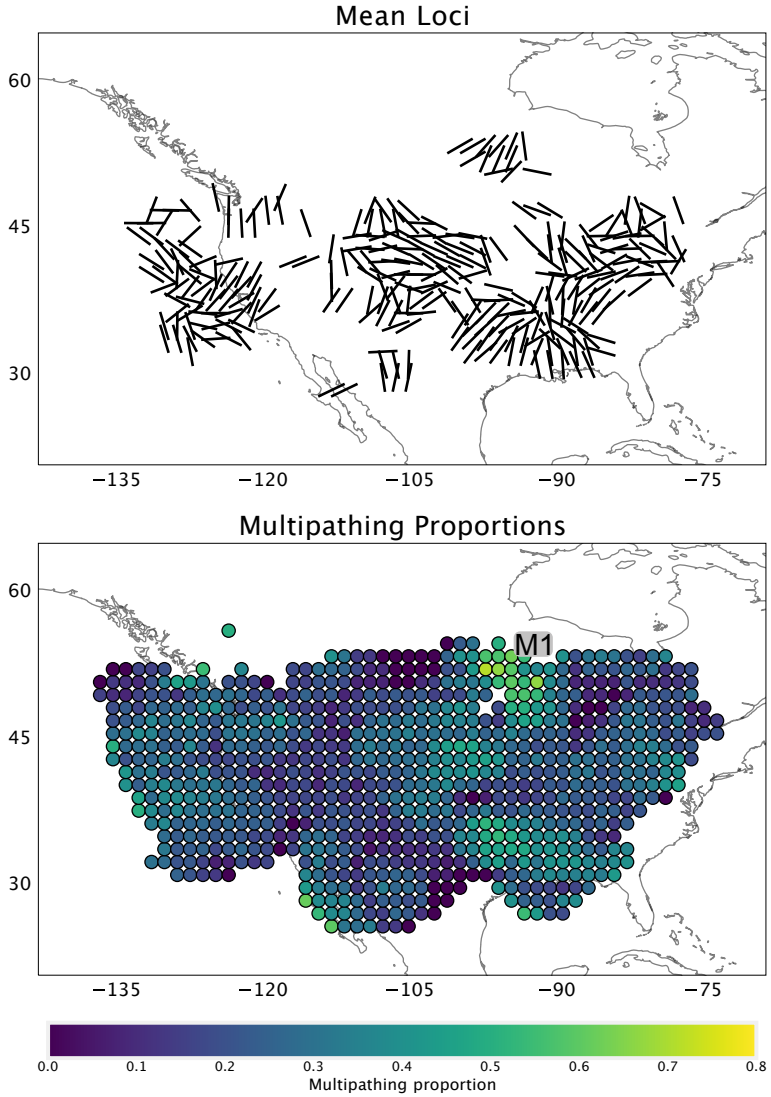

Figure C.28: Figure summarising multipathing observations using data in the 0.20 – 0.40 Hz frequency band and pierce points at 2000 km depth. The top figure shows the mean loci in bins of 200 km radius in increments of 100 km. The bottom figure shows the proportion of multipathing relative to the total number of observations in the bin. Bins for the multipathing proportion measurements are 200 km radius spaced with increments of 100 km.

Appendix D

Summary of chapters for non experts

D.1 General Premise

The inner workings of the Earth can directly impact the surface we live on. The convection of the Earth's rocky mantle, which is the layer between the crust and the core, drives plate tectonics leading to earthquakes, tsunamis and the convection of mantle plumes or hotspots can lead to volcanism on continents and create island arcs. Understanding how the Earth's interior operates in terms of the structures that are inside it and how they influence the wider convection of the mantle can therefore aid us in answering wider spread questions about how plate tectonics may facilitate life, how the Earth evolved to its current state or is there an adverse effect of glacial rebound on the surrounding oceans? Seismology, particularly the study of waves generated by earthquakes, is crucial in analysing the Earth's interior as it can make observations of structures 1000s of km below the surface. Analysing the properties of waves travelling from an earthquake to a recording station like the time taken for it to arrive, or even if it arrives at all has lead to discoveries such as the inner and outer core and the crust's varying depths. As more recording stations have become available and techniques have improved, seismologists have made maps of the whole Earth at various depths of whether the material will speed up or slow down the wave. Knowing whether material speeds up or slows down waves can give an indication about it's temperature and what it's made of in comparison to laboratory experiments. Seismic observations of what the Earth looks like and the properties of the structures within it, such as their temperature, density or composition, can then be used to discriminate between proposed models/cartoons of what the interior workings of the Earth are.

While this has really pushed forward our understanding of the Earth greatly, there,

as always, is more information waiting to be analysed. One property I am interested in is the transition length from the rocky mantle to the structure itself which can be translated to temperature gradients or again give inferences of the make-up of the structure. Fortunately, some weird stuff happens when a wave hits a sharp enough boundary. When I say 'sharp' i mean a big change in wave speed over a relatively short distance. Like when you move into a really warm room you immediately notice the temperature change.

When a wave moves past or hits the boundary of a structure with a sharp transition from the rocky mantle to the structure it begins to diffract (change direction) and arrive at the recording station from a direction different to that travelled from the earthquake to the receiver. Sometimes, you can observe multiple arrivals when this happens, one which is outside the structure and diffracts/changes direction and another which just goes through the structure. Previous studies have yet to analyse the direction or horizontal speeds of the waves arriving at the surface, which can give inferences on how 'sharp' the boundary is, its orientation (angle from north) or how much the structure speeds up or slows down the wave. This is where I swoop in with this thesis. I use commonly used seismological techniques to measure the direction and speeds of waves at the surface and then map the measurements to structures in the Earth. Ideally, this would be done on a global scale so maps of where boundaries of structures are and how 'sharp' they are can be made. So, I also try to semi-automate the measurements (automate just means I don't have to look at each measurement to tell if it is awful or usable). The next sections outline how I try to make these measurements, estimate the properties of structures causing the observations and then try to expand the observations to a global scale and begin the process of making this map.

D.2 Chapter 2

We begin our adventure in southern Africa, not like I actually went there but that's where my data samples...

So, in the 80s, the first maps of where the material speeds up/slows down waves are were made. In these maps, seismologists noticed a giant blob of slow material beneath Africa. Since this discovery, many, many, many papers and different approaches have tried to figure out what the slow material is and where it came from. Because of its size, it undoubtedly affects the convection of the mantle and the surface. This structure is of particular interest to me because many studies have observed evidence for multiple arrivals caused by 'sharp' changes in material properties. This structure, therefore, acts as the perfect laboratory to test whether measurements of the directions and horizontal speeds of waves are useful for analysing the properties of the 'sharp' boundaries.

To make the measurements, seismologists decide which paths they want the waves to approximately take to make their lives easier. I decided to use waves that travel through the core and out the other side (Figure 1.10). This path was chosen because it makes interpretation of what structures may be causing the measurements easier. It is easier because you assume only structures between where the wave emerges from the core and the stations will affect the wave.

Anyway, I made a bunch of observations changing the frequency band of the waves to vary what length of boundaries I am sensitive to. When I say frequency, think more about the pitch of a sound wave, the higher the pitch of a sound, the higher the frequency. Higher frequencies are more sensitive to smaller structures or sharper boundaries. If our measurements change with frequency, it could be used to infer the spatial properties of the boundary (how sharp it is basically).

Incredibly, I observe a frequency dependence and observe multiple arrivals. The benefit of using direction and horizontal speed measurements is they can give some idea of the orientation of the boundary structure causing them, which I somewhat confirm in later chapters.

To round off this study, I investigate what structures could reproduce some of my observations by simulating a wave travelling through the Earth and changed the structures inside it. This is very computationally expensive (it takes 5000 computers 1 hour to do the simulation for 1 Earth), so I couldn't do many tests. What I did find was a relatively smooth transition from the rocky mantle to the anomalous structure can produce multiple arrivals which previous studies suggested only very sharp transitions are capable of it.

These observations show the African anomaly could still really be anything, but these observations can give real constraints to the shape of the anomaly and the sharpness of its boundaries. The results motivate similar analysis to be conducted on other mantle heterogeneities such as hotspots or ancient crust material near the core.

D.3 Chapter 3

Now that the value of these measurements has some support, I begin the journey to make these measurements without the need for a person to look at each measurement.

To do this, I bootstrap sample the seismograms. Bootstrap sampling is essentially sampling your data a certain number of times, usually 500 or 1000. The important thing is that when you randomly sample the data, you do not remove the thing you sampled. Easier to explain with an example. So, let's say we have 5 letters A, B, C, D, E and I bootstrap sample the letters 10 times. I could end up with 10 As because after each random sample I put the letter back into the pile so it can be sampled again.

Hopefully, that makes sense.

I've deliberately avoided exactly explaining how you make the direction and horizontal speeds measurements because it would be long and arduous. I still won't explain the details but I will say you essentially make the measurements from a 2-D graph. If you imagine this graph is of some mountains like an OS map and the peaks of the mountains give the measurements of direction and horizontal velocity. For each random sample, you conduct the standard analysis to create the graphs and take the peaks. I randomly sampled the data 1000 times so I ended up with 1000 graphs and thousands of peaks representing the direction and horizontal speed measurements. I collected the peaks and made the assumption that if there is a seismic arrival, the peaks in each random sample should roughly be in the same place. When collecting the peaks, these should be regions where there are loads of peaks in a small area. In other words, these are 'dense' regions of peaks.

To find these dense regions of peaks, which we assume are caused by seismic waves arriving from a particular direction and horizontal speed, I use a clustering algorithm. Specifically, I use the DBSCAN algorithm which has won awards like the 'test of time' award for being so good. Essentially you, the user, define a minimum number of points that need to be in a certain area for a region to be a cluster. i.e. if a region is dense enough it will be a cluster. If there are multiple regions dense enough and separated well enough then multiple clusters will be found.

From the cluster's location on the graph, the direction and horizontal speed measurements can be made from the average location of the peaks. The distribution of the peaks in the cluster gives an estimate of the uncertainty of the measurement. For example, the direction measurement could be a wave arriving 30° from North, give or take 5° so I think it is 30°, but it could be between 25° and 35°.

This method could be used to automatically measure the direction and horizontal speeds of any waves really. Sound waves, waves generated by ice fractures, waves from volcanic activity just to name a few. My application would be to understand the inner workings of the Earth, but who knows maybe I'll expand it to analyse other things like storms or icequakes.

D.4 Chapter 4

This chapter is somewhat straightforward in its strategy. I have the first method to automatically measure the direction and horizontal speeds of a wave and Mike Thorne at the University of Utah has a very big dataset... So I applied the method to the big dataset.

This resulted in a lot of measurements, like >11,000. Essentially, with such a large

dataset, you can have different branches of analysis and more than is really necessary for a study. As a result of this, I only tried to interpret what could be the cause of the measurements focusing on the structures beneath North America and Europe as that is where there are the majority of the observations and it reduces my workload.

Analysing the observations revealed a whole variety of mantle structures. I interpret several mantle plume/upwellings/hotspots beneath Europe all of which have a base on the top of the core. I find that some of these actually may share the same lower mantle origin location. There is a plume/hotspot beneath the Eifel region which has made its way from the top of the core to the surface. I locate its lower mantle origin and several other studies found the same location may produce a plume that is connected to the Icelandic plume. The Iceland plume is typically shown as a vertical structure extending beneath Iceland to the core. The structure I propose as a second plume fueling Iceland actually migrates northwards from west of Spain (at the core) under the UK and eventually to Iceland at the surface. I think it's really cool.

Beneath the US, the mantle structure has been heavily analysed through a variety of techniques so most of what I find has already been imaged by other means. The contribution of my observations, other than recovering information about the 'sharpness' of the boundaries of these structures, is how different the measurements are for each anomalous region. I believe the differences are because of the sensitivity of the measurements to the shape of the structures and the length over which the boundaries 'diffuse' to the surrounding Earth (how sharp the boundary is). Anyway, the many unique measurements of different anomalies show the potential power of analysing the Earth in this way. While this is not the end result of a global map of where 'sharp' boundaries are and what their shape is, it's the initial step towards it and motivates future studies to build upon it.

D.5 Final thoughts

Well there you have it, 3–4 years worth of work using waves from earthquakes to analyse the edges of blobs in the Earth. I hope the above made some sense to you and thank you for being interested at all in what I have accomplished. This may be the beginning of a career working on this and similar stuff or maybe I will go off into a totally different field and leave academia. Irrespective of what the future holds, I am glad I did this PhD it has been incredibly interesting and enjoyable. I'll be interested to see where I am in 10 years and may open this thesis and read these words. Until then, have a good one reader!